3-2021

Characterization and Analysis of BOMARC Accident Debris

Aaron J. Heffelfinger

CHARACTERIZATION AND ANALYSIS OF BOMARC ACCIDENT DEBRIS

THESIS

Aaron J. Heffelfinger, Major, USA
AFIT-ENP-MS-21-M-121

DEPARTMENT OF THE AIR FORCE
AIR UNIVERSITY

AIR FORCE INSTITUTE OF TECHNOLOGY

Wright-Patterson Air Force Base, Ohio

AFIT-ENP-MS-21-M-121

CHARACTERIZATION AND ANALYSIS OF BOMARC ACCIDENT DEBRIS

THESIS

Presented to the Faculty

Department of Engineering Physics

Graduate School of Engineering and Management

Air Force Institute of Technology

Air University

Air Education and Training Command

In Partial Fulfillment of the Requirements for the

Degree of Master of Science

Aaron J. Heffelfinger, BS

Major, USA

March 2021

AFIT-ENP-MS-21-M-121

CHARACTERIZATION AND ANALYSIS OF BOMARC ACCIDENT DEBRIS

THESIS

Aaron J. Heffelfinger, BS

Major, USA

Committee Membership:

Dr. Gaiven Varshney
Chair

Dr. Abigail A. Bickley
Member

Dr. James C. Petrosky
Member

Abstract

Accidents involving nuclear weapons, such as the Boeing Michigan Aeronautical Research Center (BOMARC) accident in 1960, always pose a significant risk of allowing particles composed of nuclear materials to enter the environment. These particles often differ in characteristics and can be of greatly varying sizes; some are large enough to see with the naked eye and others are so small they pose a substantial inhalation risk. While numerous government agencies have conducted soil remediation/surveys at the BOMARC site, radioisotopes remain behind in the soil. Gamma ray analysis was conducted on the soil sample and calculations based on the presence of ^{241}Am confirmed the weapons grade plutonium activity listed by the organization that collected the sample. While testing two very different non-destructive methods for the separation of actinide bearing particles, this research located 70 actinide particles ranging in diameter from 1 to 34 μm from a sample resultant from the conflagration of a nuclear weapon and subsequent firefighting. These particles underwent analysis that included both morphological and elemental characterization. Morphological trends indicated particles across the four evaluated size distributions had similar circularity, and found three major particle classes present based on shape, angularity, and surface features. Elemental analysis indicated the presence of uranium in all 70 particles and identified trends of other major and trace elements within these particles.

Acknowledgements

I would like to express my deep sense of respect and sincere gratitude to my thesis advisor, Dr. Gaiven Varshney, for having the patience to help guide me through this research at every phase. Dr. Varshney's encouragement, attention, insight, and willingness to push me toward impactful research made this a phenomenal experience, and most importantly, an enjoyable one. I also would like to express a heavy debt of gratitude to my committee, Prof. James Petrosky and Prof. Abigail Bickley, for their continual input, guidance, and support to ensure my research stayed on task and was scientifically founded. I would like to especially thank Dr. George Peterson and Maj James Bevins, for providing me with excellent guidance on equipment capabilities, theory, and how to draw conclusions from the data, and challenging me to always make the research my own. I would also like to thank Mr. Eric Taylor and Mr. Connor Gautam, who from the very beginning offered both their time and resources to aid me in my pursuit of knowledge. I would be remiss not to thank the scientists at both USAFSAM and AFRL, especially Mr. Michael Velez, for allowing me access to their state-of-the-art equipment during a pandemic and limited lab access to analyze my soil sample. I would also like to thank Dr. Richard Gostic for the advice and guidance he provided to make my research more successful.

Most importantly, I would like to thank my lovely wife for her love and support through this whole process, ensuring our son was cared for while I was consumed with my studies and research, and for constantly reminding me "the sky is not falling." Without my family I would not be where I am today.

Aaron J. Heffelfinger

Table of Contents

Page

Page

List of Figures

List of Tables

Table Page

List of Abbreviations

Abbreviation		Page
AEC	Atomic Energy Commission	3
AFRL	Air Force Research Laboratory	42
BOMARC	Boeing Michigan Aeronautical Research Center	iv
BSE	Backscattered Electrons	21
CRS	Congressional Research Service	52
DAR	Digital Autoradiography	7
DU	Depleted Uranium	3
EOD	Explosive Ordnance Disposal	3
FDF	Fermi Distribution Function	15
FWHM	Full Width Half Max	36
HEU	Highly Enriched Uranium	3
HGMS	High Gradient Magnetic Separation	11
HPGe	High Purity Germanium	7
LANL	Los Alamos National Laboratory	61
LIBS	Laser Induced Breakdown Spectroscopy	6
NaI	Sodium Iodide	7
NDA	Nondestructive Analysis	7
PMT	Photo Multiplier Tube	14
RDD	Radiological Dispersion Device	2
SAM	Surface to Air Missile	2
SDD	Silicon Drift Detector	43

Abbreviation		Page
SE	Secondary Electrons	21
SEM/EDS	Scanning Electron Microscopy/ Energy Dispersive X-Ray Spectroscopy	2
SIMS	Secondary-Ion Mass Spectroscopy	6
SNM	Special Nuclear Materials	3
TIMS	Thermal Ionization Mass Spectroscopy	6
USAFSAM	U.S. Air Force School of Aerospace Medicine	4
µXRF	Micro X-Ray Fluorescence	19
WGPu	Weapons Grade Plutonium	3
XRF	X-ray Fluorescence	2

CHARACTERIZATION AND ANALYSIS OF BOMARC ACCIDENT DEBRIS

I. Introduction

1.1 Motivation

Releases of radioactive materials into the environment occur from several sources such as nuclear weapons accidents, nuclear weapons tests, and accidental releases from nuclear reactors [1]. Nuclear detonations have been shown to distribute radionuclides across the entire globe through fallout, and there are many documented instances of nuclear accidents contaminating surrounding areas; most famously the meltdown and subsequent explosion at the Chernobyl nuclear power station. The radionuclides can be deposited into the soil in many ways, from both detonations and nuclear related accidents. After accidental or intentional release of radionuclides into the environment, their transport continues via different migration processes from atmosphere to soil, sediments, and water systems. The factors that determine the threat and extent of the material include physical properties of the emission (explosion, dispersion, particle size, particle composition, etc.) and the method of exposure (inhalation/ingestion/external radiation). Results from years of research have shown that particle characteristics, such as elemental composition, depend on the source [2]. In addition, characteristics such as particle size distribution, structure, and oxidation state influence ecosystem transfer and depend on the release scenario [3]. Based on literature related to former nuclear weapons test sites or sites associated with nuclear accidents, it could be concluded that a significant fraction of the distributed radioactive material remains localized in the form of discrete particles of various size,

composition, and structure long after its release where the soil and sediments can act as a transient for deposited particles [4]. Due to particle weathering and remobilization, particle contaminated soil and sediments may act as a potential diffuse source. Thus, there is a need for knowledge with respect to particle characteristics and processes influencing particle weathering and remobilization of associated radionuclides to assess long-term impact from radioactive particle contamination [3].

An in-depth analysis of the soil containing radioactive particles can give valuable insights into the elemental composition and morphology of the particles as well as the conditions in which the particles may have formed. In a real-world scenario, such as the interdiction of nuclear materials, a nuclear detonation, or the use of a radiological dispersal device (RDD), particles must be located and analyzed quickly to allow state and federal officials to make informed decisions. By using available state-of-the-art technologies such as X-ray Fluorescence (XRF) and Scanning Electron Microscopy/ Energy Dispersive X-Ray Spectroscopy (SEM/EDS) these particles can be quickly located within a sample and analyzed to gather critical data (post detonation samples would need to be collected away from ground zero to reduce overall activity of the soil). Utilizing an organized and effective methodology to identify and find a single (or few) actinide bearing particle(s) within a large bulk particulate sample can reduce the associated time and costs.

1.2 Background

Before surface to air missiles (SAMs) had the technological ability to achieve kinetic energy hit-to-kill intercepts on aircraft and ballistic missiles, most of these defensive systems employed a conventional or nuclear warhead that would be detonated in the

vicinity of the target. One such system was the BOMARC missile that was employed by the United States Air Force to defeat these strategic bomber threats. Approximately 16 miles southeast of Trenton, NJ at McGuire Air Force Base, a BOMARC missile site protected the Eastern United States against these threats. On June 7, 1960, a helium tank within a BOMARC shelter exploded, causing the liquid fueled missile inside to catch fire [5]. This intense fire burned for approximately 30 minutes uninhibited before firefighting efforts commenced. Although the high explosives within the W40 nuclear warhead burned, no fission explosion occurred, with the gravest risk being the loss of special nuclear materials (SNM). The fire was fought for 15 hours using water to prevent the nuclear materials from being lost through aerosolization. The water then carried these materials under the shelter doors where it flowed down a paved surface and into a drainage ditch outside the boundary fence [5]. The primary concern from the accident was the release of weapons grade plutonium (WGPu), highly enriched uranium (HEU), and depleted uranium (DU) that could be absorbed into the surrounding environment. Since then, numerous attempts were made to remediate the soil, with initial remediation conducted by USAF Explosive Ordnance Disposal (EOD) teams and the Atomic Energy Commission (AEC) to remove the debris that contained a significant amount of the weapon material. Post-remediation estimates show that up to 300 grams of SNM remained. Remediation was once again conducted from 2002 to 2004 by private companies, resulting in the removal and disposal of almost 22,000 cubic yards of waste [5]. Further radiation surveys were conducted in 2006 that indicated the continued presence of radioisotopes, and samples were taken for further analysis. A number of studies, such as those conducted by Dr. Richard Gostic and Dr. James Bowen, have since been conducted on independently collected

BOMARC samples, and a trend of identifying larger particles containing actinides is evident [6,7]. While other research identified and analyzed particles smaller than 100 microns, there has been a lack of in-depth statistical analysis of these BOMARC particles (e.g. Bowen studied only two particles smaller than 30 microns, with the smallest being 23 microns; Gostic studied zero particles smaller than 30 microns) [7, 6]. Work with particles from other nuclear accidents and tests also shows a lack of in-depth analysis of smaller particles (e.g. Cezeaux studied only three particles smaller than 30 microns) [1]. This research has extended the analysis to collect > 50 particles, focusing on as small of particles as 1 μm where the statistical similarities and differences are highlighted with respect to their elemental composition and morphology.

1.3 Problem Statement

The primary goal of this research is to study the post-accident debris from the BOMARC site and develop techniques and procedures that will allow expeditious identification of actinides within soil samples that may contain plutonium and uranium isotopes. The specific focus of the research is to investigate <90 micron size actinide bearing particles that have been in the environment more than 50 years and understand their statistical variability with respect to chemical and physical features. The secondary objective is locating, characterizing, and conducting elemental analysis of very small particles to demonstrate that environmental remediation efforts have left behind a significant amount of small actinide particles. To achieve these objectives, the research was divided into numerous segments, as follows.

1. Identify activity of interest within the soil sample using gamma spectroscopy.
2. Develop a method to locate these actinide particles such that:
   (a) the method must be organized and allow one to quickly return to the particle for further analysis and study (particle location and relocation method).
   (b) the method must be entirely non-destructive to preserve the integrity of the particle, to include attachment to/inclusion within other soil particles.
   (c) the method must allow future studies to remove actinide bearing particles for further scientific analysis.
3. Once located, conduct detailed analysis of the actinide bearing particles as follows:
   (a) Utilize both XRF and EDS to determine elemental composition to include trace elements.
   (b) Utilize SEM to study morphological characteristics (shape, size, and associated properties) of actinide bearing particles.
4. Identify elemental trends of the actinide bearing particles.

1.4 Leading Questions Resolved by this Study

1. Can nuclear fuel particles from a non-critical accident be identified and characterized using only non-destructive, commercial off the shelf products/ technologies to inform environmental remediation efforts and the nuclear forensics community?
2. Are gamma and alpha spectroscopy conducted on the soil subsamples sufficient to indicate the presence of low intensity actinide particles within the particulate?

3. Can the sample be prepared using a method that not only allows for quick identification of actinide particles, but also is repeatable and organized to allow further analysis of individual particles?
4. Will the actinide bearing particles identified within the sample be composed of either plutonium or uranium or both?
5. Does the composition of the actinide bearing particles demonstrate elemental trends that may be exploited for further soil remediation efforts?

1.5 Hypothesis

Techniques and experimental methodology can be developed to identify and characterize nuclear fuel particles released into the environment from a non-critical accident using only non-destructive equipment and modern technology to aid in future environmental remediation and nuclear forensic endeavors.

1.6 Research Limitations

A key limitation of this research was the use of non-destructive techniques to find and analyze the actinide bearing particles. This was put in place so that the particles' interaction within the soil could be studied as well as to preserve the particles' forensic information for future research studies. This limitation eliminated proven techniques of isolating actinides such as chemical separation [1]. It also greatly reduced the number of procedures that could be utilized to analyze the elemental and isotopic composition of the particles. Techniques such as Thermal Ionization Mass Spectroscopy (TIMS), Secondary-Ion Mass Spectroscopy (SIMS), and Laser Induced Breakdown Spectroscopy (LIBS) that consume

or destroy all or part of a particle were not utilized to preserve the full integrity of the particles. While elemental composition can still be determined using technologies such as XRF and EDS, these systems are limited to mostly qualitative analysis in this research because they do not probe the entire mass of the particle, whereas the others give very precise quantitative data.

Another limitation of the research was the focus on soil particulate less than 90 microns in size. This limit was imposed to focus on the smallest remaining actinide bearing particles within the environmental soil sample, as most of the published research on samples collected from this site have focused on a larger size domain [6]. This research focus resulted in numerous small actinide bearing particles being discovered, but did not reveal larger particles with actinide inclusions that previous researchers analyzed and compared to the smaller particles found.

The effects of COVID-19 also had a significant impact on the research, most importantly restricting the access to key equipment that was to be utilized for the research. Key instruments that were to be utilized for digital imaging, such as Digital Autoradiography (DAR), were unavailable for use due to the inability of technicians to gain access to facilities to service the equipment. Access to equipment such as the SEM/EDS at the Air Force Research Laboratory was also limited due to COVID related access requirements, greatly reducing the amount of time available to identify and analyze particles.

1.7 Approach

The focus of this study is on performing nondestructive analysis (NDA) of actinide contaminated soil particles using laboratory-based methods. First, the sample was processed through sieving to separate it by particle size distribution. Gamma spectroscopy was then conducted on each size distribution within the sample. Both sodium iodide (NaI) and high purity germanium (HPGe) detectors were utilized to analyze the overall activity and to determine the presence of radioisotopes of interest. Alpha and gamma spectroscopy were also utilized to attempt to sequentially split the sample and locate actinide bearing particles. A flip test was conducted using the HPGe detector to confirm that the activity was homogeneously distributed through the sample. Thereafter, the sample was prepared and analyzed utilizing both the XRF and SEM/EDS systems to determine the morphological and elemental composition as well as image each individual particle. This data was then processed and analyzed to make the conclusions included in this thesis.

II. Literature Review

This chapter discusses the soil composition of the BOMARC site, outlines some of the previous research done on BOMARC accident debris and the Clean Slate II safety test and illustrates the background knowledge necessary to understand the physics and concepts governing both the equipment and techniques used for this research. First, gamma spectroscopy is discussed focusing on the science as well as the detectors used in the research. Second, is a brief overview of alpha particle detection available and used for this research. Then, the concept of XRF and the information of the utilized equipment is discussed. Following this, the concepts governing SEM/EDS for surface morphology and elemental composition is covered in detail. To interpret the results from these non-destructive techniques, it is also imperative to properly understand the techniques as well as methodology behind peak analysis.

2.1 Composition of BOMARC Soil

The location of the BOMARC missile site is within the Pine Barrens Preserve of east-central New Jersey as indicated by the green square in Figure 1.

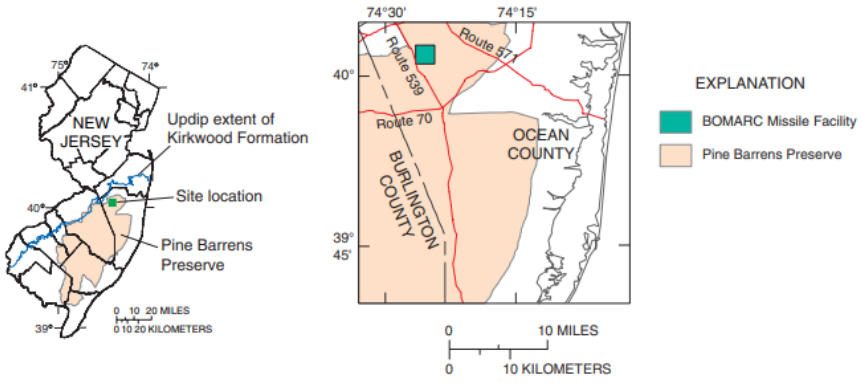

Figure 1. Location of BOMARC site within New Jersey [8]

The soil at the site is composed of the sediments natural to the Kirkwood-Cohansey aquifer system, which is dominated by light-colored fine to coarse quartz sand, silty sands, and clays interbedded with sand and gravel [8]. Most of the soil in the BOMARC location is comprised of over 97% sand by weight, with particles greater than 53 μm in size [9]. The water in this aquifer system is slightly acidic. The aquifer has poor sorption capacity, leading to radioactive colloids having relatively high mobility within this aquifer system [8]. This is of particular concern because it is known that the firefighting efforts greatly contributed to the actinides being dispersed throughout the site.

2.2 Previous Analysis of BOMARC and other Environmental Debris

Previously, research has been done to study the BOMARC accident site debris with the goal of developing different methods to locate the actinide bearing soil particles and characterize the presence and activity of actinide bearing (primarily WGPu) particles. The research in the following paragraphs highlights the previous work that was impactful to this thesis.

In 2010, Gostic conducted characterization of plutonium particles originating from the BOMARC accident via gamma spectroscopy to determine the presence and isotopic composition of WGPu and ^{235}U within the soil sample [6]. This research also highlighted the gamma analysis of plutonium using the ^{241}Am isotope as a surrogate, assuming isotopes would be collocated within the soil and therefore finding americium would be indicative of plutonium presence [6]. He also highlighted the use of both SEM/EDS to image and map the particle to conduct further surface morphology classification as well as determine elemental composition and distribution, demonstrating the presence of numerous actinides

including plutonium and uranium occurring as inclusions on larger particles [6]. The actinide bearing particles (17 in total) identified in this research varied in size, ranging from 150 to 1000 microns along their longest axis. Elemental mapping of these particles indicated the presence of Pu, U, and Am within particles, with ^{239}Pu presence detected on most particles having high ^{241}Am gamma spikes along with elements such as Ga in minor quantity/trace [6]. This research demonstrated the use of gamma ray detection and digital imaging techniques to successfully analyze and identify actinide bearing particles.

In other research of BOMARC debris in 2013, Bowen's research primarily focused on the physiochemical properties of the WGPu particles to predict their fate in the environment and ultimately address the issues of both radiation protection and nuclear security concerns [7]. The research used gamma spectrometry, DAR, and SEM/EDS for locating actinide bearing particles. The research also used gamma spectrometry to determine the presence of actinides and demonstrate sequential splitting to reduce soil sample sizes for locating particles [7]. As with Gostic's work, gamma detection of ^{241}Am was utilized to locate actinide bearing particles and determine the presence of plutonium within the sample. EDS mapping of particles in this research demonstrated the technique's utility to map both uranium and plutonium content on a particle's surface [7]. In total, seven actinide bearing particles were identified, ranging in size from 23 to 64 microns along the major axis, with six particles being crystalline in texture and one being amorphous [7].

In 2014, Greb utilized a high gradient magnetic separation (HGMS) technique for the location of actinide bearing particles from contaminated WGPu soil. While the identification of the particles was done primarily with DAR, he also utilized a collimated alpha particle detection technique [10]. Gamma detection was also utilized to identify

radioisotopes within the soil and calculate the amount of each isotope within a sample [10]. The results of the HGMS illustrated the greatest separation occurred in soil samples with a measured activity greater than 55 pCi (pico- Curie), likely due to the separation of solid individual WGPu particles. In contrast, the small WGPu inclusions on soil particles passed through the HGMS without significant separation [10].

In 2018, Cezeaux identified a set of explosively generated nuclear weapons particles and objectively described the range of detailed morphologies of particles formed during controlled non-critical nuclear weapon tests (Clean Slate II) [1]. To locate actinide bearing particles, he utilized a sequential splitting method to find the subsample with the highest activity, and therefore an actinide bearing particle contained within it. He also demonstrated techniques to mount soil subsamples to carbon tape for analysis utilizing SEM/EDS [1]. Important to this research was the in-depth particle analysis conducted, covering the elemental analysis, size and circularity trends, quantitative morphology, applying an identification lexicon, and the conclusions that would be drawn from a conflagration (BOMARC) versus a non-critical safety test detonation (Clean Slate II). The research identified 68 total actinide bearing particles containing Pu, U and Am, and ranging from 9 to 425 microns in diameter, where most of the particles contained inclusions of U and Pu on soil [1].

2.3 Gamma Spectroscopy

When radioisotopes undergo decay, their daughter isotopes are often left in an excited nuclear state. This very often occurs in the case of β^+ and β^- decays, but can also be a result from an α decay. The excited nucleus of these isotopes then releases a gamma photon that

allows the nucleus to return to a less energetic state, most typically the nucleus' ground state. The gamma photon, of a distinct characteristic energy for the decay, can then be detected. The characteristic gamma rays of interest to this research, as well as their branching percent (the percent of decays that result in that gamma ray's emission), are listed below in Table 1. Assuming secular equilibrium, where daughter isotopes with shorter half-lives will have the same activity as the parent after a period of time, the ^{234}Pa metastable gamma ray can be used to calculate the ^{238}U activity. For the ^{238}U decay series, this secular equilibrium is achieved after a 6-month period [11].

Table 1. Characteristic Gamma Ray Energies for Actinides of Interest [12, 13]

Isotope	Gamma Energy [keV]	Percent Branching
^{234}Pa	1001	0.8
^{235}U	143.76	10.96
	185.7	57.2
	205.31	5.01
^{239}Pu	51.63	0.0271
	129.29	0.00631
^{240}Pu	45.23	0.045
	104.24	0.00708
^{241}Am	59.5	35.9
	98.95	0.0203

With the branching percentages very low for most of these isotopes, the dominant gamma rays from ^{235}U and ^{241}Am are expected to be the strongest indicators of U and/or Pu presence within the soil sample analyzed in this research. The presence of ^{241}Am is also a strong indicator of plutonium presence (to include WGPu that will contain trace amounts of ^{241}Pu), as ^{241}Am is a decay product of plutonium as illustrated in equation (2.1) [5].

$$^{241}Pu \rightarrow {}^{241}Am + e^{-} + \bar{\nu} \quad (2.1)$$

One method of gamma detection is an NaI inorganic scintillator. Scintillators use materials, such as an NaI crystal, that produce a spark or scintillation of light when ionizing radiation passes through them [14]. These alkali crystals typically contain a small amount of an impurity, such as thallium, which acts as an activator and is responsible for the overall luminescence of the crystal [14]. This light is then captured in a photomultiplier tube (PMT) connected to the detector as illustrated in Figure 2.

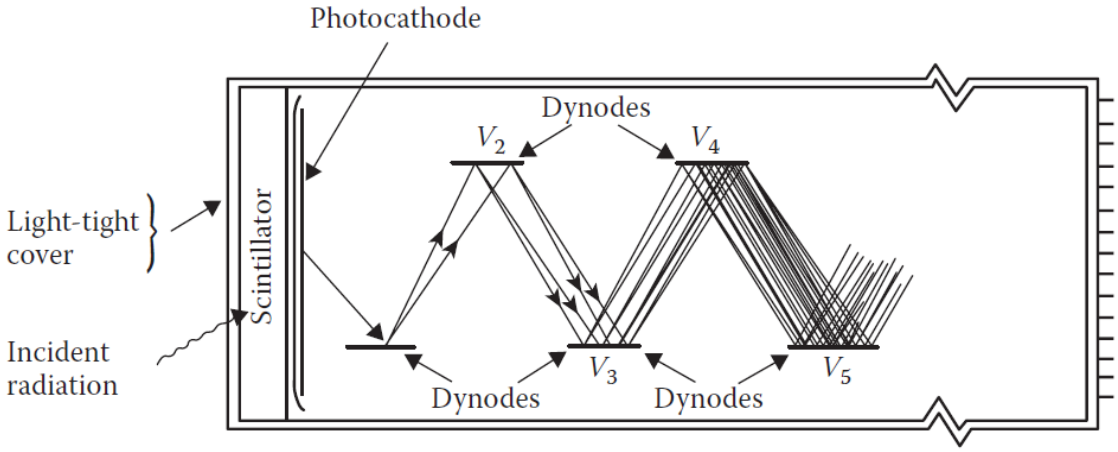

Figure 2. Diagram of a PMT [14]

First, the photons of light created in the crystal contact the photocathode where they are converted from light to electrons. These electrons are then amplified between dynodes within the PMT and leave the PMT as an electrical signal that is registered as a count in the detection equipment. The NaI scintillator has numerous benefits as well as limitations. With a relatively high density and high atomic number, the NaI detector has a very high efficiency for detecting gamma rays and is therefore an effective tool to calculate the overall activity of a sample. The efficiency is simply a measurement of the number of

pulses recorded divided by the amount of radiation emitted by the source. However, a PMT lacks the energy resolution of other detectors to be useful for determining isotopic content of a soil sample.

The other type of detector utilized for this research is the HPGe semiconductor detector. This semiconductor detector works on the principles of electrons and "holes" as charge carriers, where a hole is simply a lack of electron and is treated as a particle with a positive charge [14]. To understand the movement of electrons within a semiconductor, one must first understand the Fermi Distribution Function (FDF) as depicted in Figure 3.

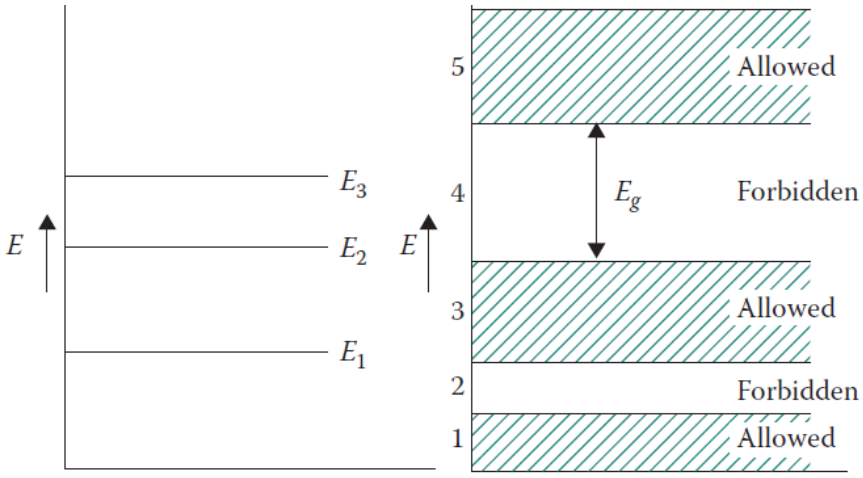

Figure 3. Atomic Energy Levels of Solid Depicted as a Band [14]

In a solid, this FDF is represented by energy bands, where electrons may be present in allowed bands separated by forbidden bands. When radiation imparts enough energy, the electron can cross this forbidden gap and move to a higher energy band where it is more mobile. In a semiconductor, the lower energy band (the valence band) is full while the higher energy band (the conduction band) is empty [14]. As temperature of the semiconductor increases, thermal energy can cause electrons to jump to the conduction

band because germanium has a relatively low energy gap between the valence and conduction band (hence why HPGe detectors are either cryogenically cooled or mechanically cooled to reduce electrons in the conduction band, reducing the signal to noise ratio). A semiconductor doped with donor atoms (atoms that can give an electron) has many electrons and a small number of holes, thus being considered an *n*-type semiconductor, while one doped with acceptor atoms (atoms that receive an electron) has many holes and a small number of electrons, called a *p*-type. These two types of semiconductors, when brought together form a *p*-*n* junction with a large electric field, **E**. When radiation is incident upon the *p*-*n* junction, the **E** creates the electron-hole pairs. The overall efficiency is governed by equation (2.2) [14].

$$\frac{(Radiation\ energy\ in\ eV)}{3\ eV/pair} = number\ of\ electron - hole\ pairs \qquad (2.2)$$

By applying a reverse bias, the **E** separates the electrons and holes, and the charge produces a pulse that is recorded by the detection equipment [14]. Semiconductor gamma detectors have benefits and shortfalls. The HPGe detector's benefit is its energy resolution, the ability of the detector to resolve counts at a specific energy. This resolution is dependent on the gamma's energy and is therefore measured for both low energy and high energy gamma rays. With a higher resolution, the HPGe detector can distinguish between contributions from radioisotopes that may have gammas only a few keV apart in energy, allowing conclusions to be made as to what isotopes are present within a sample. A shortfall of the HPGe detector is its lower efficiency, meaning that subsamples must be analyzed for a longer period to obtain the necessary counting statistics, especially when analyzing subsamples with low activity.

One point that must be considered with both semiconductor and scintillating detectors is the introduction of background radiation. Background radiation can range from cosmic rays to gamma radiation originating from natural sources, such as the ^{40}K isotope found naturally. This background, if not managed, can make the analysis of low activity subsamples difficult. To reduce the background counts, high Z materials such as lead and tungsten can be used to shield the detector and sample, greatly reducing the overall background, and increasing peak detection.

Another important consideration for the use of gamma detection equipment is the proximity of the source to the detector. The solid angle, and thus, the surface area of a unit sphere covered by the surface's projection onto the sphere, is directly affected by the source's distance to the detector [15]. For a very strong source, proximity of the source to the detector can result in considerable dead time and non-Gaussian peaks. For low activity subsamples, proximity to the detector will maximize the solid angle, therefore increasing counts and allowing peaks above the background [16].

2.4 Alpha Particle Detection

Very high Z actinides such as uranium and plutonium undergo α-decay to become a more stable daughter product. The neutron and proton rich nuclei eject an α-particle, a heavy charged particle consisting of a ^{4}He nucleus. Like characteristic gamma rays, these particles also have a distinct energy they are emitted with, and that energy corresponds to the different excited states of the daughter products the isotope can decay to [17]. Isotopes of interest to this research and their alpha particles' characteristic energies are listed in Table 2. Detection of these particles, however, can be a difficult process when there is no

ability to put the sample under vacuum conditions to utilize typical detectors. Because of their sheer size (relative to other charged particles), α-particles tend to lose their kinetic energy over a very short distance, meaning that very thin materials as well as air itself can stop these particles.

Table 2. Characteristic Alpha Particle Energies for Actinides of Interest [18]

Isotope	α-Particle Energy [MeV]	Percent Branching
^{238}U	4.196	77
	4.149	23
^{235}U	4.598	4.6
	4.401	56
	4.374	6
	4.365	12
	4.219	6
^{239}Pu	5.1554	73.3
	5.1429	15.1
	5.1046	11.5
^{240}Pu	5.16830	76
	5.12382	24
^{241}Am	5.48574	85.2
	5.44298	12.8

In air, the mean range of a heavy charged particle is given by equation (2.3) [14]:

$$R(mm, air) = \exp\left[1.61\sqrt{T(MeV)}\right], 1 < T \leq 4$$
$$R(mm, air) = [0.05T(MeV) + 2.85]T(MeV)^{2/3}, 4 < T, T \leq 1 \qquad (2.3)$$

In (2.3) T is the kinetic energy of the alpha particle. The mean range is the distance the particle will have traveled when it has lost 50% of its kinetic energy, with the maximum range usually falling within 5% of the mean range [14]. This, for example, indicates the mean range of the most intense alpha particle from ^{239}Pu is only 9.27 mm. Therefore, under normal temperature and pressure, the detector must be < 9.27 mm for the particles to reach the detector. Also, the sample must be spread extremely thin, because the alpha particles

can also be self-absorbed in the soil. Furthermore, actinide inclusions within larger particles must be facing the detector or they will likely not be counted [19]. A benefit of these principles is the inherent ability to block background counts with readily available materials and resources.

2.5 Micro X-Ray Fluorescence

Micro X-ray Fluorescence (μXRF) Spectroscopy is an analysis technique that utilizes X-rays to non-destructively determine the elemental composition of a sample. The X-rays most common to these instruments (including the one utilized in this research) results from the excitation of a rhodiumtarget. The X-rays are focused by an aperture. The size of the aperture is selected by the user, with an aperture of 100 microns or greater being more appropriate for bulk or mass sampling and an aperture of 10 microns or smaller being utilized for analysis of singular particles. The X-rays interact with the atoms of the sample and excite the electrons. If the incident X-ray's energy is great enough to ionize the atom and eject an inner-shell electron, an outer shell electron from a higher energy level replaces it. The energy difference is released as an X-ray photon, called fluorescent radiation [20]. This radiation is of a characteristic energy for each element's electron orbitals. A spectrometer is then used to detect this X-ray as a count in an energy bin, and as interrogation of the sample continues, these counts will build an elemental spectrum of the sample.

The XRF technique has very distinct strengths and limitations. It is very well-suited for the analysis of bulk samples and, by using higher energy incident X-rays, it can capture the higher X-ray spectrum of a sample [20]. Furthermore, the XRF instruments calibrate

quickly compared to other instruments. Limitations of the technique can often be tied directly to the instrument on hand. XRF instruments utilize an optical camera to align the aperture on the portion of the sample to be analyzed. In the case of the instrument used in this research, the optical camera was unable to distinguish particles smaller than 40 μm in diameter. Another limitation directly tied to the instrument is the size of the aperture. Analyzing a very small particle only a few microns in diameter that is not isolated from the other particulate can be challenging as a larger aperture will also likely lead to sampling the surrounding material.

The penetration depth of the incident X-Rays generated by the XRF offer a maximum depth for the measurement. The average range of a photon in matter is the inverse of its mass attenuation coefficient [14]. This implies that while the beam from the instrument may probe the sample beyond the outermost layers, the generated characteristic X-rays (especially those lower in energy) may not escape the sample to be detected.

2.6 Scanning Electron Microscopy/Energy Dispersive X-ray Spectroscopy

Scanning Electron Microscopy is one of the most versatile instruments available for the examination and analysis of microstructure morphology and elemental composition of materials. An SEM works by generating and accelerating electrons at a sample target, as illustrated in Figure 4. These electrons are generated by a source material that is subjected to a high electrical bias, resulting in emitted electrons once their thermal energy overcomes the work function of this source material [21].

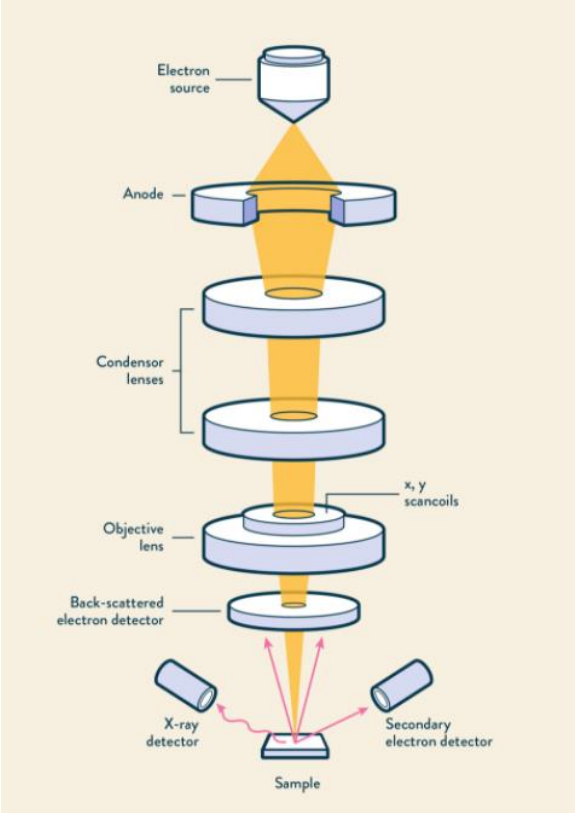

Figure 4. Schematic Diagram of an SEM [22]

The positively charged anode then attracts and accelerates these electrons, where they enter a series of electromagnetic lenses that focus the beam of electrons down to a user specified resolution. The instrument utilizes this beam in a raster pattern to analyze the sample. The electrons interact with the sample and produce two types of electrons, backscattered electrons (BSE) and secondary electrons (SE), depending on the interaction depth [21]. The areas of the sample from where these electrons often originate can be seen in Figure 5.

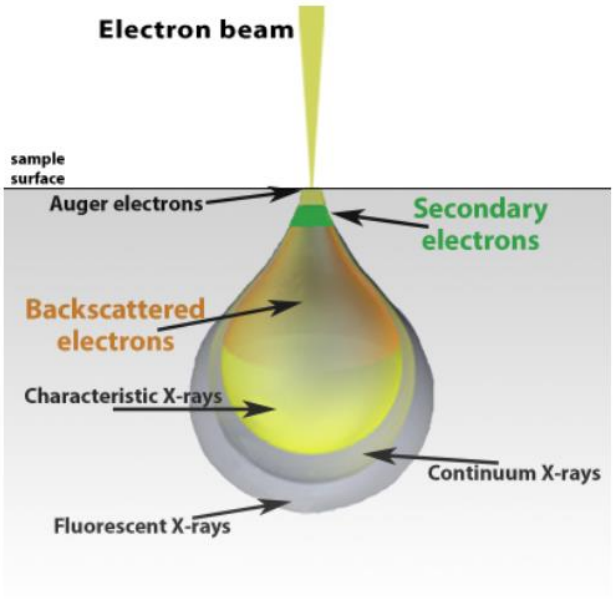

Figure 5. Principle of SEM: Electron Beam Sample Interactions [23]

BSEs originate from the incident electron beam, being reflected toward the source of the beam after undergoing an elastic collision (electron-nucleus) and are detected utilizing a solid-state detector placed above the sample. These electrons originate from deeper within the sample that the SEs, and are indicative of the atomic number of the material being sampled. The higher the atomic number, the more BSEs will be detected causing these materials to appear much brighter in the backscatter electron image [21]. SEs in contrast, result from inelastic collisions (electron-electron) between the electrons of the incident beam and sample and originate from the atom itself. These electrons are generated near the surface of the sample and are utilized to generate a more detailed image of the sample's surface. They are detected using a scintillator within a Faraday cage placed at an angle to increase the detection efficiency [21].

SEM analysis also produces characteristic X-rays from deeper within the sample that can then be detected using Energy Dispersive X-ray Spectroscopy. The ability to detect

these characteristic X-rays is dependent on many factors. First and most importantly, is the voltage of the electron beam being used. The incident beam energy, E_0, must exceed the critical ionization energy, E_c, for the specific atomic shell whose ionization generates the characteristic X-ray [24]. This ratio, called the overvoltage (U_0), is written in (2.4) [24].

$$U_0 = E_0/E_c > 1 \tag{2.4}$$

Importantly, when U_0 is high enough to produce X-rays from inner electron shells, X-rays will also be produced for the lower energy shells. For example, if U_0 is high enough to generate K-shell X-rays, then it will produce them from the L and M shells as well [24]. While these X-rays may be generated, the overvoltage must also be high enough for that characteristic peak to be visible above the background spectrum. This visibility of the characteristic peak to continuum background, *P/B*, is approximately represented in (2.5) [24].

$$\frac{P}{B} = (U_0 - 1)^{0.5} \tag{2.5}$$

Formula (2.5) indicates there is direct relationship between the overvoltage and the visibility of the peak above the background; as U_0 is lowered the *P/B* drastically decreases [24]. It is also important to consider the absorption of these characteristic X-rays within the sample while utilizing EDS. A photon has a very high probability of being absorbed (there will exist a large mass absorption coefficient) if it lies in a range of approximately 1 keV above the critical ionization energy of another element present in the analyzed sample volume [24]. For particles with high uranium content, this could make it difficult to determine a 14.28 keV plutonium peak with the 13.61 keV uranium peak within that 1 keV range (even though the higher energy uranium peaks at 16.43 and 17.22 keV are visible in the spectrum). However, particles of very small size likely would not provide enough

material for attenuation to fully absorb these X-rays, as the interaction volume is greater than the size of the particle [25].

2.7 Peak Analysis Methodology

Conducting peak analysis on spectra is vitally important to correctly understanding the acquired data and drawing conclusions from it. Depending on an instrument's resolution, a peak may be viewed as a single source or as having contributions from numerous sources. The first step in the peak analysis is to correctly remove the background counts. In the case of the HPGe detector, a background must be collected with no sample for the same amount of time as the samples. The background counts are then subtracted from the overall sample counts, giving a true representation of the isotopes and their gamma emissions within the sample. In the case of HPGe analysis, various isotopes can contribute counts to a peak if they have gammas of similar energy. Examples important to this research are the ^{235}U 185.7 keV and ^{226}Ra 186.1 keV gamma rays, which are close enough in energy that they do not form two separate peaks; as the best full-width half-max (FWHM) energy resolution the detector in this research provides is 0.681 keV as measured for the 122 keV ^{57}Co gamma rays. The ^{235}U is expected to be within the soil sample due to the nature of the accident, but the ^{226}Ra cannot be discounted because it lies within the ^{238}U decay chain, so would also be present in trace amounts [26]. In this case, other characteristic gamma rays must also be examined, such as the 143.76 and 205.31 keV gammas from ^{235}U, and using their intensities, the number of expected counts for a single isotope under the double peak can be calculated. By subtracting these counts from the total peak, one can also then determine the counts from the second isotope.

These same principles of peak fitting can be applied to both the XRF and EDS X-ray spectra as well. With the difficulty in taking a background using these techniques, it becomes more advantageous to use peak-fitting software (such as OriginLab's Origin 2020) to remove the background. By first defining the background, it can then be subtracted or utilized as the analysis baseline, leaving only the counts under peaks for further manipulation. By using the software's Peak Analyzer feature, Gaussian curves can be fit to the spectrum, and peak centroids, FWHM, and counts can be fixed. This is especially useful for deconvolution of peaks that may have multiple isotopes contributing counts, such as the uranium 3.34 keV M_β and plutonium 3.35 keV M_α (where M_β and M_α are M family X-ray lines) X-rays. These X-rays not only depend on the overvoltage and peak to background ratio as discussed above, but also the relative intensities of X-ray lines in each family. By comparing the counts of these peaks with those of other intensities, conclusive analysis can be done to either show the presence of, or lack of, other elements. The relative intensities of X-rays utilized for the peak analysis in this research can be seen in Table 3.

Table 3. X-Ray Relative Intensities by Electron Shell [27]

X-Ray Lines (M and L Family)	Relative Intensity (%) Within Family
M_α	100
M_β	60
M_ξ	6
M_γ	5
$M_{II}N_{IV}$	1
L_α	100
$L_{\beta1}$	70
$L_{\beta2}$	20
$L_{\gamma1}$	8
$L_{\gamma2}$	3
$L_{\gamma3}$	3
Ll	4
L_η	1

It is also important to determine whether the peak is statistically significant or not as a part of element deconvolution and peak fitting. For a peak to be statistically significant at the 99% confidence level (and therefore must be identified), the criteria in (2.6) must be met.

$$I_A > 3(I_B)^{1/2} \tag{2.6}$$

In (2.6) I_A is the counts under the Gaussian peak and I_B is the background counts over the same energy bins [27].

III. Methodology

3.1 Soil Sample Sieving

3.1.1 Sample Overview

This research focused on particulate from a BOMARC sample (Sample ID BC-SS-4040-01) which was collected by Cabrera in 2007 from the BOMARC site [6]. The reported sample weight is 304 grams, and the total measured activity is 6.451 nCi (nanocurie) with 5.427 nCi resultant from Pu content within the sample. While handling the sample, gloves, eye protection, and a dust mask were always worn to limit the exposure or inhalation of radioactive materials.

3.1.2 Dry Sieving

The sieving process began with the removal of the bulk soil sample from the large blue puck (shown in Figure 6) in which the sample was originally packaged. The bulk sample indicated the presence of moisture due to clumped particulate and was thus placed within a Kimax 600 mL beaker subsequently to be broken up as sample dehydration techniques were not available. Prior to sieving the soil samples, the entire sample was weighed on a calibrated Mettler Toledo ME104E scale with the weight of 280.5 grams. The sieving process was then performed to fractionate the soil according to particle size with sequential stacking of six sieves (Advantech 3" Sonic Sifter Separator Sieves) with the largest sieve size (425 μm) on the top and smallest (25 μm) on the bottom as shown in Figure 6.

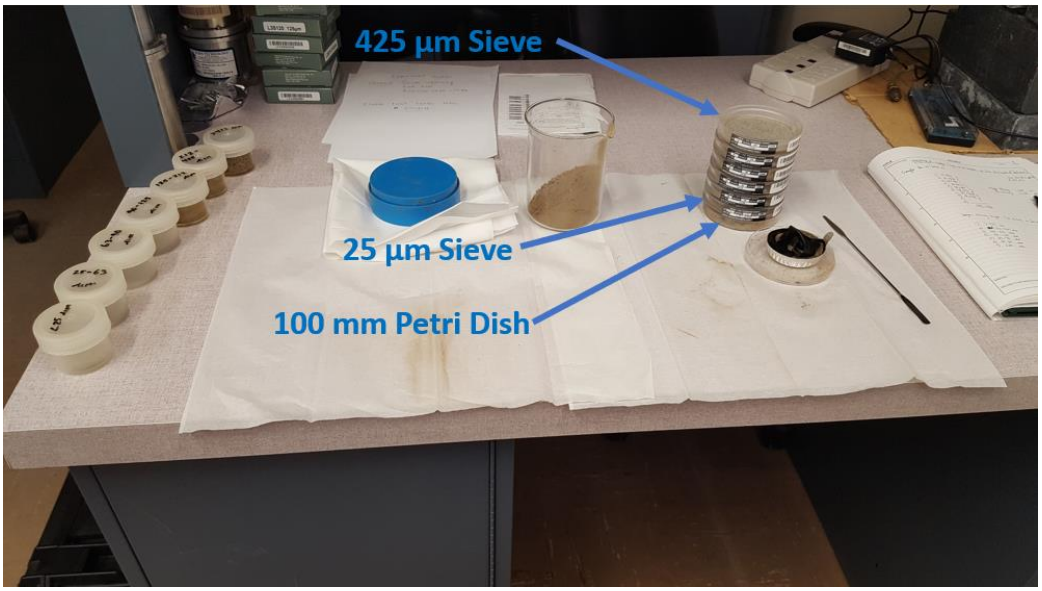

Figure 6. Sample Preparation and Sieving

A Fisherbrand 100 x 15 mm polystyrene petri dish (the type used throughout the research) was kept below the smallest sieve. Approximately 10 grams of particulate was sieved at a time, with each hand sieving lasting between 6 to 8 minutes depending on whether the sieve screens were clogged and needed to be cleaned. During sieving, particulates were removed from the sieves and placed in Nalgene 60 mL wide mouth lidded jars, labeled according to the particulate size fraction to store the samples. Once the entire sieving process was completed, the sample was weighed by sieve size fractionates as shown below in Table 4.

Table 4. Particle Size Distribution and Weight Measurements of the Sample

Sieve Size [µm]	Weight [g]	% of Total Sample Weight
> 425	126.9	45.2
212 – 425	64.5	23.0
125 – 212	36.4	13.0
90 – 125	25.3	9.0
63 – 90	13.5	4.8
25 – 63	13.2	4.7
< 25	0.68	0.2

3.2 Gamma Spectroscopy

3.2.1 Overview

Gamma spectroscopy was conducted to determine the presence of the ^{241}Am (daughter nuclide of ^{241}Pu) 59.5 keV gamma ray which indicates Pu presence, the ^{235}U 185 keV gamma ray, and other radioisotopes in the different sample size distributions. Each sample size distribution (as shown in Table 4) was analyzed separately to determine actinide concentrations by particle size. Energy calibration was conducted utilizing the Maestro software and Genie 2000 for the NaI detector and HPGe detector, respectively [28, 29].

3.2.2 NaI Scintillator Sample Analysis

3.2.2.1 NaI Scintillator Equipment Setup

A Saint-Gobain 3M3/3 NaI detector utilizing a NIM bin, bias supply, amplifier, and preamplifier manufactured by Ortec was used for counting. The detector was placed within an Ortec lead shield 115 mm thick to minimize background and rested on top of a piece of sheet lead with a 77 mm hole to allow sufficient room for the petri dish under the detector as seen in Figure 7. The lidless petri dish containing the sample was placed 17 mm below the detector cladding to maximize the solid angle. A similar procedure was repeated for all the subsamples.

Figure 7. NaI Scintillator within Lead Shielding

3.2.2.2 NaI Calibration and Counting Process

The NaI detector calibration and peak FWHM determination was performed using a ^{137}Cs test source with an initial activity of 10 µCi on September 1, 2000. The current activity was calculated using (3.1) [1].

$$Activity = A_0 e^{-\lambda t} \tag{3.1}$$

In (3.1) A_0 is the initial activity, λ is the characteristic decay constant of the isotope (7.31E-14 s^{-1}), and t is time in seconds, yielding an activity of 6.34 µCi the day of the experiment. The calibration utilized the 661 keV gamma peak where the counting lasted for 60 seconds, producing a well-defined Gaussian curve allowing for proper calibration using the Maestro

software. The peak produced a calculated FWHM of 44.5 keV, suggesting that it lacks the resolution needed for true isotope analysis. Following the calibration, each full subsample was analyzed. These subsamples were again placed in the 100 mm petri dishes and vibrated to evenly distribute the sample in the dish, and then placed centered under the NaI detector within the closed lead shield. The counting continued for between 900 and 2100 seconds dependent on the amount of sample present for a particular size, followed by a background spectrum taken for the same allotted time. Next, the analysis of the potential ^{241}Am peak was conducted after subtracting the corresponding background count. No isotope specific activity calculations were conducted due to the poor resolution of the peaks.

3.2.3 HPGe Sample Analysis

The sample was next analyzed using a high purity germanium (HPGe) semi-conductor detector. While the HPGe detector has a lower efficiency and the experiment must run for a longer duration to get strong counting statistics, the energy resolution is fine enough that the specific radioisotopes within the soil can be identified. Of interest in this experiment were not only the photo-peaks of the actinides of interest, but also possible daughter products of these actinides, such as the numerous actinium, radium, bismuth, and lead isotopes.

3.2.3.1 HPGe Equipment Setup

The HPGe detector utilized throughout this experiment was an Ortec coaxial detector system with an 81.8 mm germanium crystal with an operating bias of 2500 volts. Each sample was analyzed in a 100 mm petri dish constructed of 0.5 mm thick polystyrene

plastic. Because the petri dish separates the soil and the detector's crystal, the attenuation of the gamma ray through the petri dish must be calculated. To determine the gamma intensity passing through the plastic without interaction, (3.2) was used [17].

$$I = I_0 e^{-(\frac{\mu}{\rho})\Delta x \rho} \tag{3.2}$$

In (3.2) I is the intensity, I_0 the initial intensity, (μ/ρ) the mass attenuation coefficient of the gamma rays for the energy of interest through the specified material obtained from linear interpolation of data from NIST, Δx is the thickness of the material (in cm), and ρ the density of the material (1.05 g/cm^3 for polystyrene). The intensity ratio $(I/I_0)\cdot 100\%$, indicates the percentage of the gamma rays passing through the plastic container. The % intensity was calculated for the dominant ^{241}Am and ^{235}U isotopes as shown in Table 5.

Table 5. Intensity Ratio (I/I_0) Values for Actinide Isotopes of Interest [30]

Isotope	Gamma Energy [keV]	Mass Attenuation Coefficient(μ/ρ) [cm^2/g]	I/I$_0$ [%]
^{241}Am	59.5	0.19	99.0
^{235}U	185.7	0.14	99.3

Due to the very high values of I/I_0, loss of gamma rays due to attenuation through the petri dish is minimal and is not expected to be a significantly detrimental factor to the experiment. Prior to being placed within the detector's lead shield, the petri dish was gently vibrated to ensure the sample had uniform thickness in the dish. In addition, to ensure the greatest solid angle value for this experiment, the petri dishes were placed in the center directly on top of the detector housing as shown in Figure 8.

Figure 8. The Soil Sample was placed within the HPGe Detector to Maximize the Solid Angle.

3.2.3.2 HPGe Calibration and Counting Process

The HPGe detector was calibrated before each use using a ^{22}Na source. This source was chosen due to its low activity, therefore not requiring collimation or solid angle reduction to prevent dead time and poor Gaussian peaks. The source's activity was 0.88 µCi calibrated on February 15, 2003, yielding an activity of 0.0086 µCi from equation 3.1 at the start of the analysis. The counting was done for 3 minutes, and the 1274.5 keV gamma and 511 keV positron annihilation emission peaks were used for the calibration in Genie 2000 software. Due to the very low total activity of the sample, each sub sample was measured for 39 hours to maximize the isotopic counts for further analysis. A 39-hour background count was also taken and subtracted from the subsamples' counts prior to peak analysis. The background spectrum contained the expected gammas from lead (Pb) isotopes inherently contained within the detector's shield as well as the other isotopes shown in Figure 9 [31].

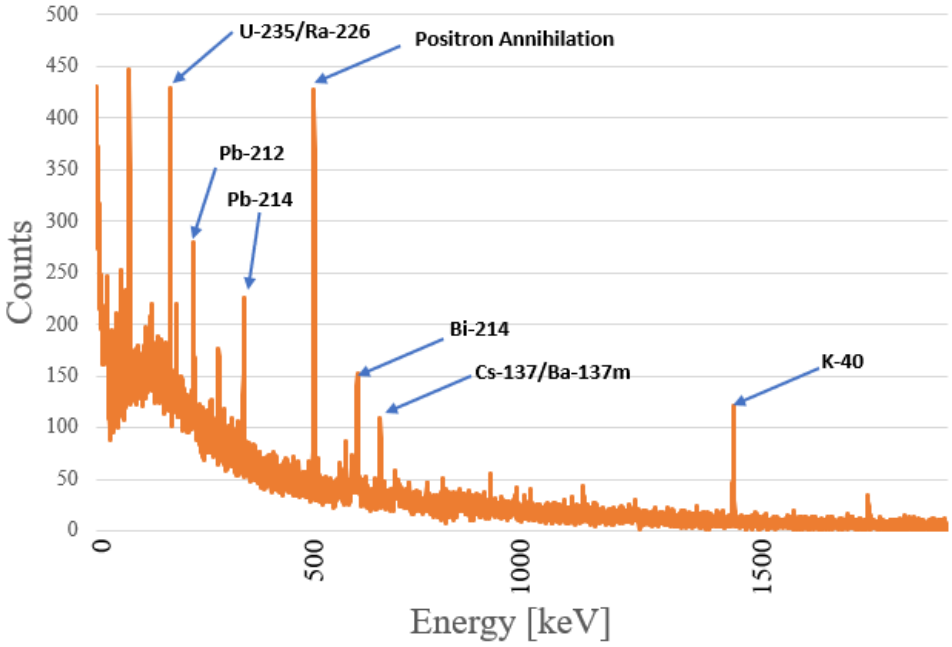

Figure 9. HPGe Background Spectrum

3.2.3.3 Activity and Mass Calculations

Two methods were utilized to determine the activity of reported radioisotopes within the sample. First, the Genie 2000 software's peak locate tool was utilized with all spectra. This tool was able to identify all major and minor peaks, as well as calculate the gross and net counts under each peak. Spectrum labels were added to each peak from the nuclide library within the software to identify the isotope of interest. Although this is a time effective analytical tool, three major drawbacks exist with this method of peak analysis. First, the background counts are subtracted with the assumption that the background continuum is a relatively flat or linear line with no peaks, which is not always true. For example, the ^{40}K peak from Figure 9 is not subtracted out of the counts obtained in other spectra, therefore peaks may contain considerably more counts than the sample itself is producing. Second, the software does not classify peaks as containing more than a single

isotope, such as the closely overlapping ^{235}U and ^{226}Ra peaks centered near 186 keV. The third concern with the technique is associated with the number of energy bins the software pulls counts from. Often, the peak widths of the automatically classified peaks extended well into the background spectrum energy bins instead of only counting the bins under the Gaussian peak, falsely inflating the counts. Although this tool was of value, it was necessary to conduct manual peak analysis by first subtracting the true background then using tools such as Origin to analyze the data and deconvolute peaks due to discussed reasons.

For each isotope of interest, the specific activity was first calculated before the mass could be determined. The specific activity (the activity per unit mass), represented in this research as Bq/g, was calculated using (3.3) [10].

$$Specific\ Activity = \frac{\lambda A_v}{M} \tag{3.3}$$

In (3.3) λ is the decay constant of the isotope, A_v is Avagadro's number, and M is the molecular weight for the isotope of interest. Next, the measured activity of the isotope was calculated using (3.4) [10].

$$Activity = \frac{N}{T}\frac{1}{\varepsilon_{det}\cdot\varepsilon_{photon}\cdot\varepsilon_{geo}} \tag{3.4}$$

In (3.4) N is the net counts of the photopeak, T is the live time of the detector, ε_{det} is the measured detection efficiency of the photopeak, ε_{photon} is the photon yield at the measured energy, and ε_{geo} is the geometric efficiency of the detector. Once both the specific activity and activity have been calculated, the mass of that isotope can be calculated by dividing the measured activity by the specific activity [10]. This was done for each subsample and

the results were compared to identify the differences of activities as a function of particle size for the bulk subsample.

3.2.4 Homogeneity Test

The next step in the research was to locate the actinide bearing particles. To do this, sequential splitting was employed focusing on the dominant ^{241}Am peak. Using sequential splitting, subsamples were separated into two parts of nearly equal mass and specific activities of each part were determined. The subsample which had the highest activity was further split into two subsamples, and the procedure of splitting was continued until the bulk particulate was reduced to a desired small fraction size that other methods could be utilized to find the actinide bearing particle. This method was tested with small subsamples of approximately 0.1 g, where the length of the detection time was varied between five minutes and three hours, with all tests resulting in poor counting statistics. Due to the research focusing on very small soil particulate (< 90 micron), this process would have been extremely time consuming because even very small subsamples could have contained a very large number of individual actinide bearing particles.

To circumvent this problem, it was hypothesized that for subsamples ≤ 63 microns the actinide bearing particles would be homogeneously mixed throughout the sample. If the activity in the soil contamination is homogeneously distributed, regardless of sample orientation, the measured activity is constant. If the activity is heterogeneously distributed within each sample, then the measured activity is highly dependent upon sample orientation [7]. To confirm this hypothesis, two different tests were conducted. First, the 25-63 micron sample was split into two equal subsamples, A1 and B1, of approximately 6.58 g, where

each half was measured for 39 hours using the HPGe detector to measure the ^{241}Am activity. The sample was then recombined, shaken, and the test repeated (sample halves A2 and B2). To ensure portions of the background spectra were not also counted using the Genie 2000 software's peak analysis tool, the FWHM counts were utilized for the analysis as shown in Table 6.

Table 6. HPGe Homogeneity Test Results

Test	Sample Half	FWHM Counts	FWHM Count Difference [%]
1	A1	3144	4.2
	B1	2888	
2	A2	2919	1.98
	B2	3037	

To further confirm the hypothesis, a Flip Test was also conducted. In a Flip Test, the activity is determined first with the bottom of the dish in contact with the detector, then repeated with the top of the dish in contact with the detector. The 25-63 micron sample was placed in a sealed petri dish and then measured for 39 hours. Once complete, the sample was flipped to the lid of the petri dish, and the sample was measured. The results showed only a 3.1% ^{241}Am count difference and a 1.9% difference when analyzing the FWHM of the peaks, supporting the hypothesis that the activity is homogeneous through the particulate. This conclusion is supported by previous research that also confirmed the homogeneity of Pu within samples obtained from the BOMARC site [32].

3.3 Alpha Particle Detection

3.3.1 Overview

Alpha particle detection was another method used for sequential splitting of the subsamples. The actinides of interest all undergo alpha decay with a 100% branching ratio (with the low probability of spontaneous fission as with ^{240}Pu) with half-lives shown in Table 7.

Table 7. Half-lives and Daughter Products of Actinides of Interest [33]

Isotope	Half-Life [years]	Daughter Product
^{235}U	704,000,000	^{231}Th
^{238}U	4,468,000,000	^{234}Th
^{239}Pu	24,110	^{235}U
^{240}Pu	6,561	^{236}U
^{241}Am	432	^{237}Np

3.3.2 Alpha Particle Equipment Setup

The detector used for this research was a Ludlum 2360 α/β counter utilizing a Ludlum 43-89 detector probe. The probe is a ZnS(Ag) scintillator adhered to a 0.3 mm thick plastic scintillator with a 1.2 mg/cm^2 metalized polyester window. Over the window is a 0.76 mm thick stainless steel hex screen that is 79% open. The detector has a rated 20% efficiency for detection of ^{239}Pu alpha particles, with a background count of three counts per minute or less [34]. Without the ability to perform the experiments under vacuum, attenuation through air was a major concern as demonstrated in equation 2.3. The soil subsamples were spread thinly on 0.5 mm thick, 50 mm diameter aluminum disks to minimize self-absorption, then placed within a wooden conical collimator to maximize the solid angle

and reduce background counts. The sample was placed 5 mm from the top of the collimator and the detector rested on the collimator as shown in Figure 10.

Figure 10. Alpha Particle Detection Experiment Configuration

3.3.3 Alpha Particle Counting Process

For alpha particle detection to be used for a sequential splitting technique in the experiment, it needed to provide results in a timely manner as numerous splits of the sample would consume a large amount of time to locate a single actinide bearing particle. Therefore, an analysis time of 8 minutes was selected. First, a background count was taken with no sample placed within the collimator. Following this, seven subsamples were prepared from the 63-90 micron subsample (due to high ^{241}Am activity), ranging in total weight from 0.02 to 0.43 g, and each sample was analyzed for 8 minutes. The background counts were then subtracted out to yield net counts for each sample.

3.4 Sample Particle Mounting

3.4.1 Initial Sample Analysis and Elemental Mapping

Subsamples utilized for initial XRF sampling and elemental mapping were prepared using Ted Pella 1/2” aluminum circular SEM stubs with precut Pelco Tab 12mm double sided carbon tape adhered to the stub. Three strips of Ted Pella double sided carbon tape were applied to a 100 mm petri dish, with the white Teflon tape backing left intact on the tape. The soil particulate was then removed from the jar utilizing a Ted Pella micro spatula, held approximately 15 cm above the petri dish, and the handle was tapped gently to allow small amounts of the particulate to fall onto the Teflon backing within the petri dish. The SEM stub with affixed carbon tape was then gently placed on the particulate to adhere the particles to the stub.

3.4.2 Particle Analysis

The analysis of particles required that a more detailed technique be developed. The primary goal of this technique was to ensure that any particles identified could easily be identified later in time for further analysis. A simple circular SEM stub is far from ideal for such a solution. To solve this issue, a Pelcotec Silicon SFG12 Finder Grid Substrate was utilized. This silicon grid consists of 144 1x1 mm individual grids, each with a laser etched alphanumeric indicator in the top left corner. These individual grids contain no carbon tape the particles can adhere, so a method had to be developed to adhere the carbon tape to the grid squares. Utilizing a straight razor, a 1mm thick ribbon of double-sided carbon tape was cut from the roll. Under a magnify lens, one end of the ribbon was grasped

with a tweezer while the other end was applied within the square utilizing pressure from an EMS 0.5mm diameter high precision fine diamond scriber. Once adhered, the straight razor was utilized to cut the ribbon, thereby adhering a 1 x 0.5 mm piece of carbon tape in each grid (to ensure the alphanumeric indicator was not covered) as shown in Figure 11.

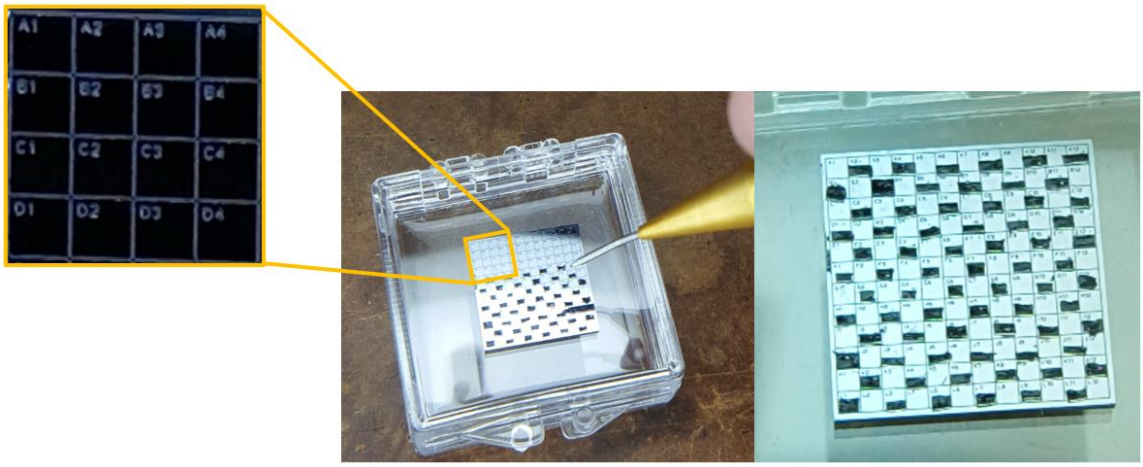

Figure 11. Finder Grid Preparation

The particulate was applied in the same manner as for the initial XRF sampling and mapping; however, less particulate was placed on the Teflon tape for these studies than for the initial analysis. For SEM analysis these finder grids were then adhered to an SEM stub to ensure the grids did not move during analysis. Particles located were labeled by their grid indicator followed by the number of that particle within the grid.

3.5 Scanning Electron Microscopy

3.5.1 Backscatter Imaging

The first set of SEM imaging done in this research was conducted at the U.S. Air Force School of Aerospace Medicine (USAFSAM), 711 High Performance Wing, utilizing a

JEOL 6610LV SEM/EDS microscope. The EDS which could provide elemental analysis on this microscope was not functioning, therefore it was only utilized for backscatter imaging to locate high density particles on the prepared finder grids. The JEOL microscope's electron beam was set at 15-20 kV to ensure the interaction volume produced and escape depth were large enough to produce sufficient backscattered electrons from throughout the particles while still being low enough to observe surface features by secondary electrons [24]. No SE images were taken of individual particles using this microscope as their composition as actinides could not be confirmed. Also, as high magnification images were not being taken, the probe current was decreased to ensure the images were bright enough and had a higher sharpness [24]. Further, to maintain the forensic information intact, the particles were not sputter coated with gold or carbon coated. A representative high Z (atomic number) particle (bright in color due to the higher number of electrons backscattered back into the detector) identified using this microscope's BSE detector is shown in Figure 12 .

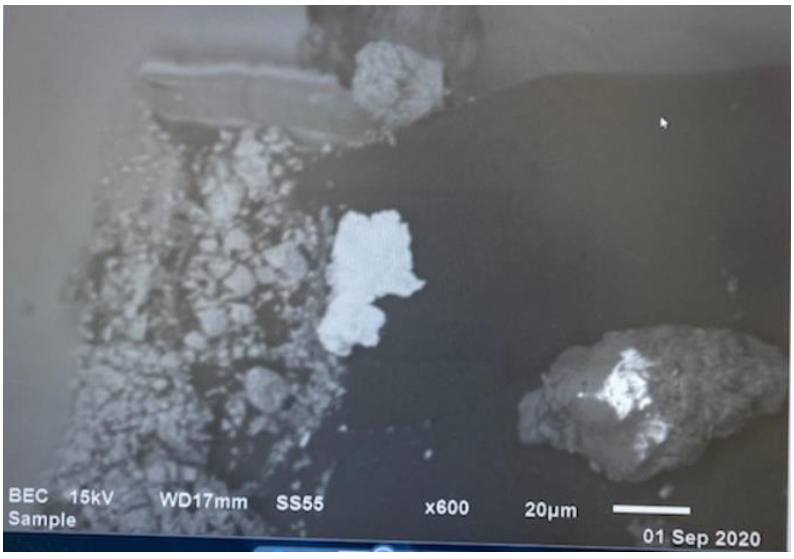

Figure 12. High Z Particle Located Using JEOL 6610V SEM/EDS Microscope

3.5.2 EDS and Particle Imaging for Microscopy

After the initial high Z particles discovered at USAFSAM were confirmed as actinide bearing using XRF, access was granted to the Air Force Research Laboratory (AFRL) microscopy facilities to utilize their SEM with functioning EDS capability. A ThermoFisher Scientific Apreo C SEM microscope, as shown in Figure 13, was served to conduct both high magnification imaging as well as EDS analysis simultaneously.

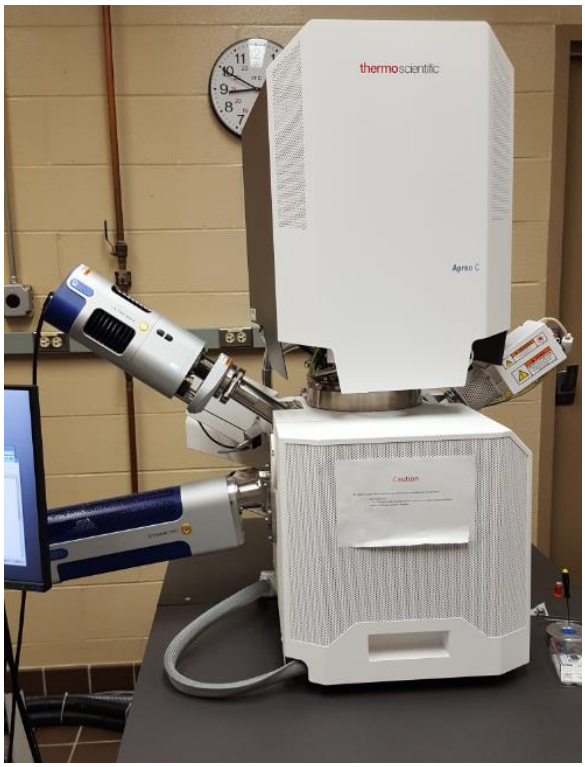

Figure 13. ThermoFisher SEM Utilized for Particle Imaging and EDS Analysis

The voltage was set at 26 kV to approximately double the ionization energy of the U and Pu L-shell X-rays of interest, providing enough overvoltage to create an optimal peak to background ratio described in equation 2.5. Because the number of secondary electrons produced by the beam increases with lower voltage due to a reduced beam range, this

voltage was not ideal for SE imaging but necessary for EDS [24]. The probe current was also set to 1.6 nA to obtain the higher resolution at the magnification levels being used. The working distance between the sample and electron gun was 10 mm to maximize the X-rays entering the EDS and backscattered images. Both BSE and SE images of all found actinide bearing particles are reported in Appendix C.

3.6 Energy Dispersive X-Ray Spectroscopy

Once particles containing high Z elements were identified using BSE imaging, they were analyzed utilizing an Oxford Instruments Ultim Max 65 silicon drift detector (SDD) EDS (shown in figure 14) that utilizes the Aztec 4.4 software for data analysis.

Figure 14. Oxford Instruments EDS Utilized for Research

Individual particles were examined to determine the elemental composition of major, minor, and trace elements using area and point analysis tools available in AZtec. The area analysis was utilized primarily for particles greater than 10 microns in diameter to ensure most of the particle was sampled, while the point analysis tool was utilized for the smaller particles to reduce sampling of surrounding materials and for particles that warranted

numerous samplings (such as those particles with obvious fines or grains attached to the surface). This EDS is capable quantifying a particle's composition at a rate of 400,000 counts/s, therefore a 30 second counting time was initially utilized for each particle [35]. The AZtec software was utilized to generate a full spectrum (as well as retrieve the raw data counts) for each particle and generate a report containing qualitative atom percentage elemental composition. Elemental mapping of select actinide bearing particles was also conducted to ascertain if the elements were homogeneously distributed.

After the initial data was obtained, further EDS analysis of particles was warranted to investigate the presence of both trace elements and plutonium. To do this, run time was increased to two minutes to achieve better counting statistics and to allow possibly hidden peaks to emerge above the background spectrum. Finally, EDS was utilized to conduct a grid analysis on an individual particle (particle A1-1). With previous research suggesting Pu content on U bearing particles, it was necessary to test this particle that had possible Pu counts in the generated X-Ray spectrum [10]. To test for Pu, 110 individual point analysis were taken on particle A1-1 and each spectrum analyzed for Pu content.

It is also important to consider the depth these X-Rays are penetrating the individual particles, and therefore the interaction volume being analyzed. Using the Kanaya-Okayama formula, the interaction volume (represented as the radius of a hemisphere centered on the beam impact point that contains 95% of the trajectories) $R_{K\text{-}O}$ is determined using equation (3.5) [24].

$$R_{K-O}(nm) = 27.6\left(\frac{A}{Z^{0.89}\rho}\right)E_0^{1.67} \tag{3.5}$$

In (3.5) A is the atomic weight (g/mol), Z is the atomic number, ρ is the density (g/cm^3), and E_0 is the incident beam energy (keV). At 26 kV, this results in an interaction volume of 1.42 µm for uranium, meaning that the interaction volume consists of the outer surface of each particle, with the interior not being sampled.

3.7 X-Ray Fluorescence

XRF was utilized to analyze the particulate after the subsamples were determined to have homogeneous activity. The initial subsamples affixed to the circular SEM stubs were analyzed utilizing the Horiba XGT-7200V at AFIT as seen in Figure 15. The XRF can analyze subsamples using either a 10 or 100-micron aperture and has the capability to conduct elemental mapping of particles [36].

Figure 15. Horiba XGT-7200V XRF

Before high Z particles were found using SEM, the feasibility of utilizing mapping to identify actinides on the particulate was explored. First, the XRF was calibrated utilizing standard Ga and W test sources to ensure proper identification of X-Ray peaks. SEM stubs with particulate were placed within the XRF under vacuum and were approximately 2 mm from the aperture during examination. The software was set to conduct two iterations of mapping at the highest resolution for each sample which lasted for approximately 1 hour each. Subsequently, an elemental map of particulate (shown in Figure 16) from a UO_2 fuel pellet was collected utilizing the same setting.

Figure 16. XRF Optical Image of Fuel Pellet Dust

The elemental map generated from the uranium sample available at AFIT confirmed that the XRF can identify actinides, even though much of the fuel pellet particulate did not appear on the generated elemental map. Also, with XRF mapping limited to a small area of 1x1 mm (the whole stub cannot be mapped simultaneously), it is possible that only soil particles with no actinides present are mapped and therefore it must be repeated until the

entirety of the stub is mapped; increasing the mapping time for each area to ensure actinides are identified.

High Z particles discovered from the initial BSE imaging of particulate on the finder grids at USAFSAM were analyzed using XRF due to the unavailability of EDS at that time. Only the particles over 25 μm in diameter could be seen with the optical camera of the XRF, which made centering the aperture crosshairs precisely over the particle difficult. Therefore, the location of the particle within the finder grid on the BSE image was measured and that measurement scaled to the optical camera's image of the finder grid on the XRF computer's screen, allowing the aperture to be directly over the particle without physically being able to see it. This technique was able to quickly confirm or deny actinide presence on these particles and collect qualitative elemental data for further analysis. Using 50 kV X-Rays, the interaction volume in the uranium particle calculated from (3.5) is three times larger than that of the 26 kV peak utilized with the EDS, demonstrating the XRF's ability to sample deeper within the particle than EDS.

3.8 Image J Software for Microscopy

To analyze the size and circularity of the identified actinide bearing particles, Image J image analysis software was utilized [37]. Once an SEM image was opened within the program, the pixel scale was calibrated with the scale of each image, making the measurements accurate for all particles as scales varied based on the SEM magnification used. Next, the particles were measured along the major and minor axis to determine their general size. Lastly, the polygon tool was used to outline the particle and calculate both the

perimeter and the area of the particle. Using these measurements, the circularity, *C*, was then calculated using (3.6) [1].

$$C = \frac{4\pi * A}{P^2} \tag{3.6}$$

In (3.6) *A* is the calculated area and *P* the calculated perimeter of the particle. The diameter *D* was then calculated using (3.7) [1]

$$D = \frac{D_1 + D_2}{2} \tag{3.7}$$

The values of D_1 and D_2 are found using (3.8) and (3.9).

$$D_1 = \sqrt{\frac{4 * A}{\pi}} \tag{3.8}$$

$$D_2 = \frac{P}{\pi} \tag{3.9}$$

These measurements could then be utilized to correlate size and circularity, as well as correlation to elemental composition of the particles.

IV. Results and Analysis

4.1 Radiation Detection

4.1.1 HPGe Detection

4.1.1.1 Am/Pu Analysis

The assessment of Am and Pu content within the environmental subsamples was conducted using an HPGe detector as shown in Appendix F with the data processed using OriginLab software [38]. With Pu being the actinide most frequently identified from BOMARC soil in previous research, the initial focus was on identifying gamma ray signatures of the Pu isotopes within the soil particulate [6,7]. To maximize the detection of Pu, gamma rays of interest with the highest intensities were identified in different energy ranges as shown in Table 8 [13].

Table 8. Pu Gamma Rays of Interest

Energy Region [keV]	Isotope	Gamma Energy [keV]
40-60	^{239}Pu	51.6
	^{240}Pu	45.2
90-105	^{239}Pu	98.8
	^{240}Pu	104.2
120-450	^{239}Pu	129.3
	^{240}Pu	160.3

A background spectrum was collected and did not contain gamma ray counts at the energy values in Table 8; therefore, the results did not require a background subtraction. For all subsamples analyzed with the HPGe detector, there were no counts attributed to any of these six gamma ray energies (possibly due to their low intensities). Pu content in environmental samples is typically quantified by analyzing its daughter product ^{241}Am.

This daughter produces a 59.5 keV gamma, and these counts were used to assess the Pu content [39]. For a 59.5 keV gamma, the total detector efficiency, ε, for the geometry in this research is 2.0% [14]. With a gamma ray intensity, I, of 35.9%, and no background counts detected, the ^{241}Am activity and mass were calculated using (3.3) and (3.4) utilizing counts obtained with Origin software as shown in Table 9.

Table 9. ^{241}Am Activity and Mass Calculations

Subsample Size [µm]	HPGe Counts	Counts (ε factored)	Activity [Bq]	Activity (I factored) [Bq]	Specific Activity [Bq/g]	Mass [g]
< 25	80.3	4015	0.029	0.080	0.12	6.28×10^{-13}
25 – 63	861.7	43235	0.31	0.86	0.065	6.77×10^{-12}
63 – 90	771.0	38550	0.28	0.77	0.057	6.04×10^{-12}
90 – 125	1197.6	59880	0.43	1.19	0.047	9.3×10^{-12}
125 – 212	1976.4	98820	0.70	1.96	0.054	1.55×10^{-11}

This data suggests that the total amount of ^{241}Am present increases as particulate size increase. However, the specific activity of the isotope increases as particulate size of the sample decreases as also shown in Figure 17 with single standard deviation error bars.

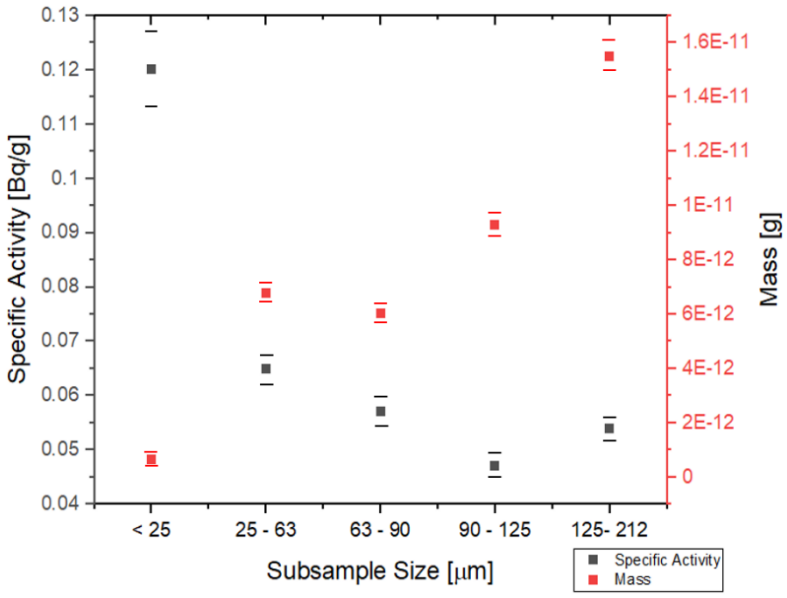

Figure 17. ^{241}Am Mass and Specific Activity by Particulate Size

With an estimated pit production date of 1958, the ratio of ^{241}Am:^{239}Pu and ^{241}Am:^{240}Pu by mass can be calculated [5]. With the date of Pu chemical separation not known, the assumption is being made that it was performed immediately before pit production (therefore these calculations are assuming there was no ^{241}Am content when the pit was produced). The calculations in this research do not utilize classified information regarding the specific weapon's pit design, instead using data from a Congressional Research Service (CRS) report's isotopic definition of WGPu and expected in-growth of ^{241}Am [40]. First, the mass of ^{241}Am in each subsample was calculated using (4.1).

$$Mass\ (g) = \frac{N}{MAW} \tag{4.1}$$

In (4.1) N is the number of atoms and MAW is the molar atomic weight (g). The value of N is found using (4.2).

$$N = C * \frac{1}{\varepsilon} * \frac{1}{I} * \frac{1}{t} * \frac{1}{\lambda} \tag{4.2}$$

In (4.2) C is the counts obtained using the Origin software, ε is the total detector efficiency, I is the gamma ray intensity, t is the total collection time (s), and λ is the decay constant. Extrapolation of the CRS ^{241}Am mass percentage data adjusted for 62 years after pit production yields an ^{241}Am mass percentage of 0.21%. The theoretical mass of WGPu within the subsample is then found using (4.3).

$$Mass_{WGPu} = \frac{Mass_{^{241}Am}}{0.0021} \tag{4.3}$$

This total mass accounts for all isotopes of Pu, Np, and U that would be present in the WGPu 62 years after pit production. The mass and activity of ^{239}Pu and ^{240}Pu was

calculated using extrapolated mass percentages from the CRS report as shown in Table 10 [40].

Table 10. ^{239}Pu and ^{240}Pu Mass and Activity

Subsample Size [µm]	WGPu [g]	^{239}Pu [g]	^{240}Pu [g]	Activity ^{239}Pu [Bq]	Activity ^{240}Pu [Bq]	Activity $^{239+240}$Pu [Bq]
< 25	3.0×10^{-10}	2.8×10^{-10}	1.8×10^{-11}	0.64	0.15	0.79
25 – 63	3.2×10^{-9}	3.0×10^{-9}	1.9×10^{-10}	6.89	1.60	8.49
63 – 90	2.9×10^{-9}	2.7×10^{-9}	1.7×10^{-10}	6.18	1.44	7.62
90 – 125	4.44×10^{-9}	4.2×10^{-9}	2.7×10^{-10}	9.58	2.23	11.81
125 – 212	7.4×10^{-9}	6.9×10^{-9}	4.4×10^{-10}	15.78	3.69	19.47

Utilizing the total theoretical mass of WGPu as 1.8×10^{-8} g, the mass and activity for all isotopes within the WGPu of the environmental sample (all particulate < 212 µm) was calculated as shown in Table 11 using extrapolated mass percentages from the CRS report [40].

Table 11. Theoretical WGPu Isotopic Mass and Activity

Isotope	Initial Mass %	Extrapolated Mass %	Mass [g]	Activity [Bq]
^{241}Am	0	0.21	3.8×10^{-11}	4.9
^{238}Pu	0.01	0.01	1.9×10^{-12}	1.12
^{239}Pu	93.77	93.61	1.7×10^{-8}	39.1
^{240}Pu	6.0	5.96	1.1×10^{-9}	9.11
^{241}Pu	0.20	0	0	0
^{242}Pu	0.02	0.02	3.6×10^{-12}	5.3×10^{-4}
^{237}Np	0	0.012	2.3×10^{-12}	5.9×10^{-5}
^{235}U	0	0.16	2.9×10^{-11}	2.3×10^{-6}
^{236}U	0	0.037	6.8×10^{-12}	1.6×10^{-5}
TOTAL			**1.8×10^{-8}**	**54.2**

This calculation predicts that for particulate < 212 µm, the theoretical total activity from WGPu will be 54.2 Bq (1.46 nCi), which accounts for 26.9% of the total WGPu

activity measured by Cabrera for the entire sample. These calculations are based off the assumption that the Am and Pu are still located together within the sample. After 62 years in the environment, it is also possible that the Am is no longer within the Pu matrix and is moving freely in the soil (and vice versa) [41].

4.1.1.2 Uranium Analysis

The HPGe spectra also suggest a significant presence of U within the environmental subsamples. As an isotope that undergoes α-decay, but also emits gamma rays, ^{235}U presence is directly detectable utilizing the HPGe detector. As previously mentioned, the primary gamma ray at 185.7 keV must first be deconvolved with the 186.2 keV gamma ^{of} ^{226}Ra before mass calculations can be made. To do this, the next most intense ^{235}U gamma ray was first analyzed. At 143.76 keV with a 13.2% intensity, and total detector efficiency of 5.1%, this peak can be analyzed to determine overall activity of the isotope, thereby allowing deconvolution of the 185.7 keV peak [42]. The analysis results of the 143.76 keV peak using (4.1) and (4.2) are shown in Table 12.

Table 12. ^{235}U Mass and Activity Calculation

Subsample Size [μm]	^{235}U Counts	^{235}U Activity [Bq]	^{235}U Mass [g]
< 25	1039	0.0074	9.3×10^{-8}
25 – 63	7856	0.056	7.0×10^{-7}
63 – 90	3530	0.025	3.1×10^{-7}
90 – 125	8272	0.059	7.4×10^{-7}
125 – 212	7916	0.056	7.0×10^{-7}
TOTAL		**0.20**	**2.5×10^{-6}**

This total activity of 0.20 Bq (5.5 pCi) from Table 12 is low in comparison to the theoretical WGPu overall activity, however, the mass of ^{235}U present is two orders of magnitude higher.

^{238}U should also be present within the subsamples. The overall activity of ^{238}U must be calculated utilizing the activity of its daughter, metastable ^{234}Pa, since there would be substantial in-growth. When the spectra were analyzed , the counting statistics did not allow an accurate calculation of the total counts. Utilizing Origin's Fit Peaks (Pro) the background counts were first removed. The peaks produced from the data were not Gaussian shaped and therefore produced extremely poor representations of the data as demonstrated in Figure 18.

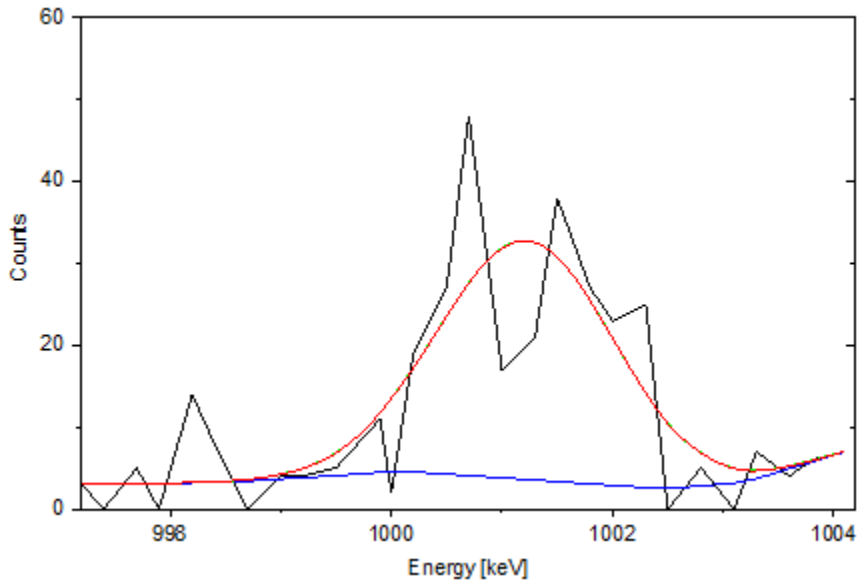

Figure 18. Metastable ^{234}Pa 1001 keV Peak

Significantly increasing the analysis time would improve the counting statistics and perhaps allow an accurate calculation of ^{238}U within the sample.

4.1.1.3 Analysis of Other Isotopes

The subsamples in this study contained several more radioactive isotopes than those analyzed above. Many of the isotopes identified are possible daughter products from Pu or U. One isotope that must be considered is ^{226}Ra. As a naturally occurring isotope in the decay chain of ^{238}U, its presence within the sample cannot be discounted. Using the data from the previously calculated ^{235}U mass and activity in Table 12, the ^{226}Ra can be analyzed using Origin's Fit Peaks (Pro) from the remaining counts under the 186 keV double peak as shown in Figure 19 for the 125-212 µm subsample.

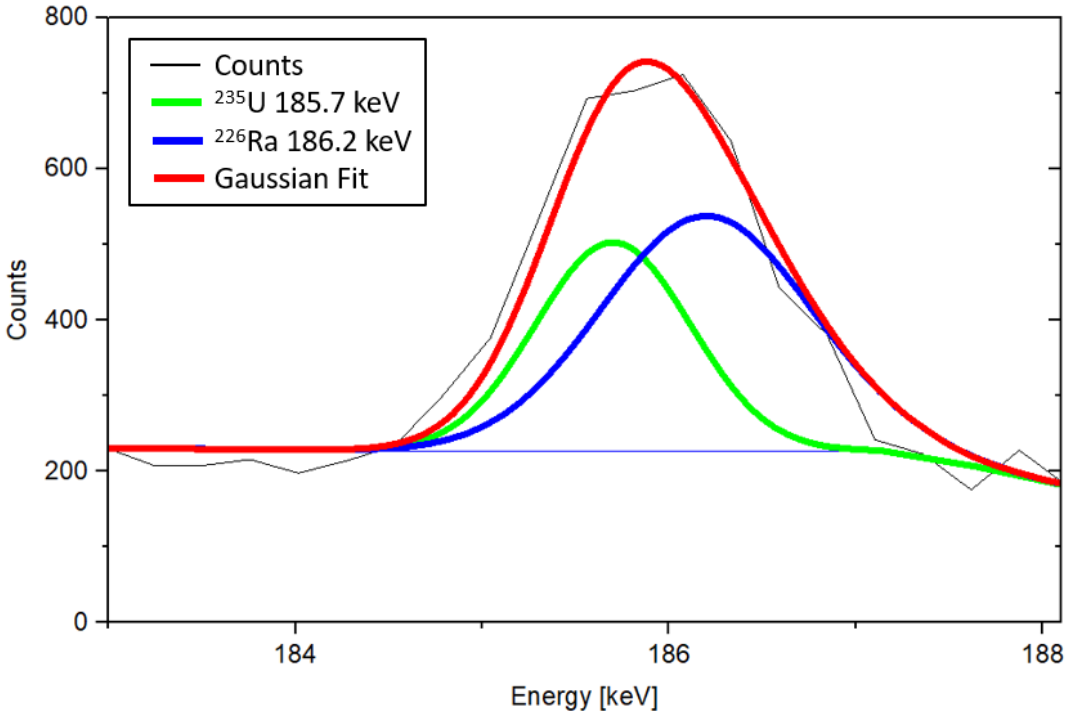

Figure 19. ^{235}U/^{226}Ra 186 keV Double Peak Deconvolution

This double peak was analyzed for all subsamples, and the activity and mass of the ^{226}Ra within the subsamples calculated using (4.1) and (4.2) as shown in Table 13. While the ^{226}Ra 186.2 keV gamma ray has a lower intensity than the ^{235}U 185.7 keV gamma ray, the

shorter half-life allows it to contribute more activity under this double peak even with a smaller total mass present.

Table 13. ^{226}Ra Activity and Mass Calculation

Subsample Size [µm]	^{226}Ra Counts	^{226}Ra Activity [Bq]	^{226}Ra Mass [g]
< 25	0	0	0
25 – 63	118348	0.8	2.3×10^{-11}
63 – 90	164547	1.2	3.2×10^{-11}
90 – 125	151901	1.1	3.0×10^{-11}
125 – 212	192105	1.4	3.8×10^{-11}
TOTAL		**4.5**	**1.2×10^{-10}**

Spectra analysis using Fit Peaks (Pro) was conducted for all other daughter products that had significant counts within the subsamples, with the results shown below in Table 14.

Table 14. Daughter Product Activity and Mass Calculation

Isotope	γ Energy [keV] [31]	Parent Isotope [43, 44]	Half-life [33]	Activity [Bq]	Mass [g]
^{234}Th	92.7	^{238}U	24.1 d	2.6	3.1×10^{-5}
^{212}Pb	238.8	^{240}Pu	10.6 h	3.6	7.0×10^{-17}
^{228}Ac	338.4	^{240}Pu	6.2 h	3.3	4.0×10^{-17}
^{214}Pb	352.0	^{238}U	26.8 m	4.1	3.4×10^{-18}
^{208}Tl	583.4	^{240}Pu	3.1 m	1.3	1.2×10^{-19}
^{214}Bi	609.3	^{238}U	19.9 m	4.7	2.9×10^{-18}
TOTAL				**19.6**	**3.2×10^{-15}**

^{137}Cs, a product of nuclear fission (from both weapons testing and spontaneous fission), also had a significant peak within the HPGe spectra. (4.1) and (4.2) were used along with Fit Peaks (Pro) to calculate the total ^{137}Cs activity of 1.8 Bq and a total mass of 5.6×10^{-13} g. The activity and specific activity of these non-WGPu isotopes in each analyzed subsample is shown in Figures 20 and 21, respectively.

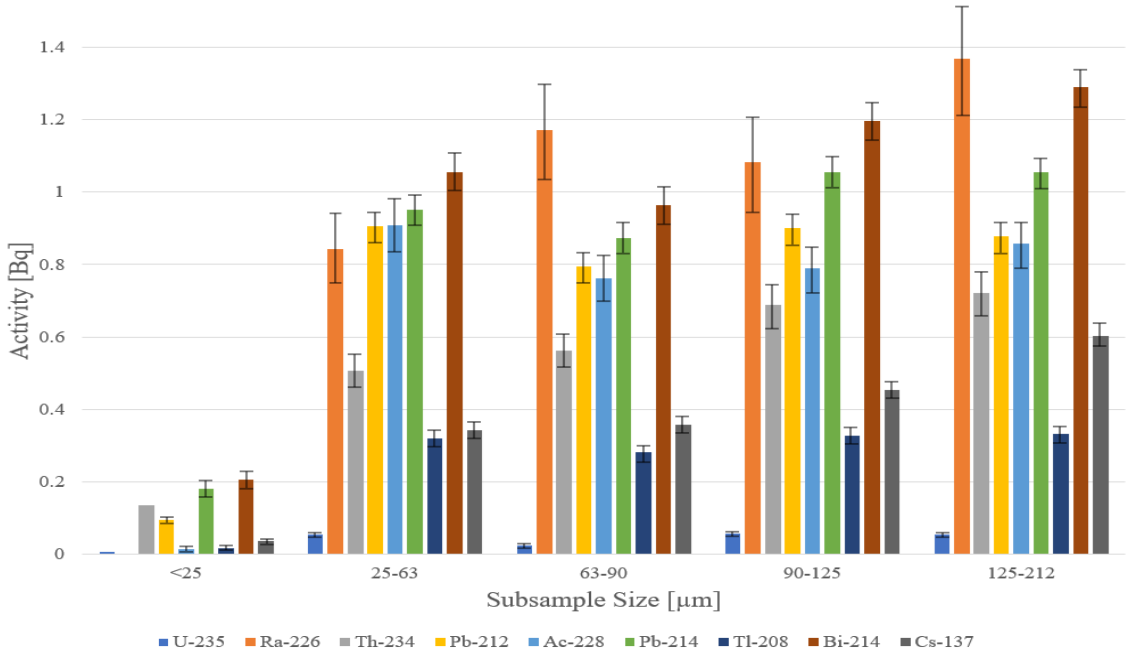

Figure 20. Non-WGPu Isotope Activity

Figure 20 shows that total activity of each isotope generally increases as particulate size increases.

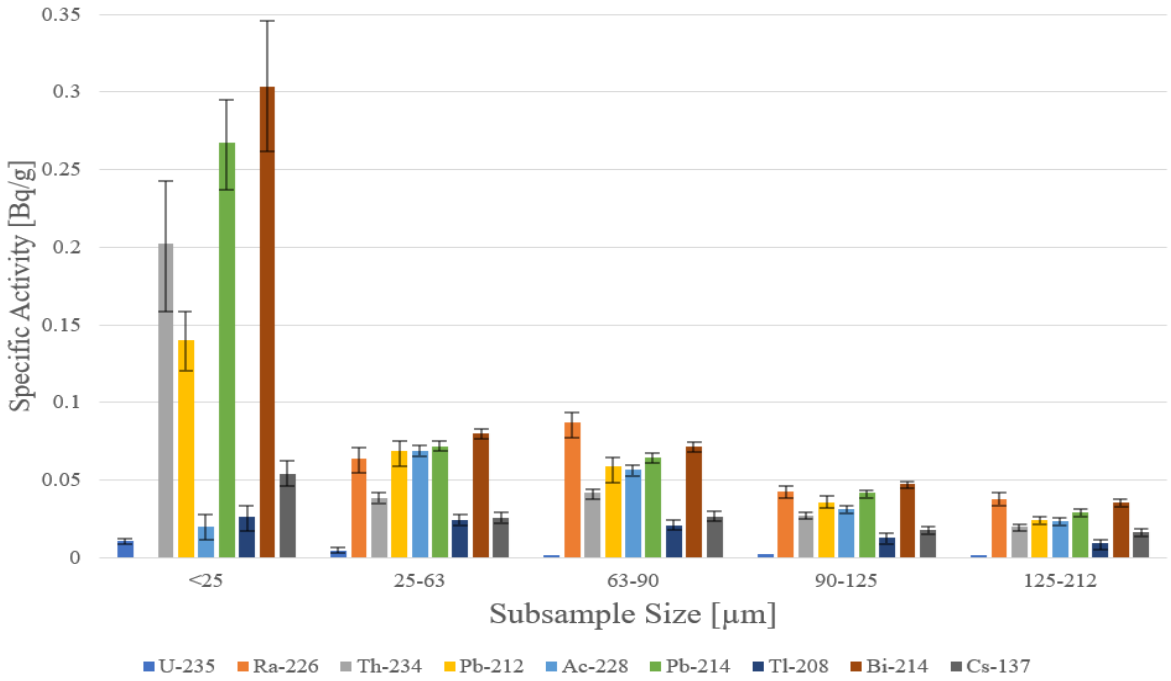

Figure 21. Non-WGPu Isotope Specific Activity

While the total activity of all isotopes is higher in the particulate > 25 μm, the specific activity for many of them (such as ^{214}Bi) is higher in the particulate < 25 μm as shown in Figure 21. This is significant because the smaller particulate pose a serious health concern because the smallest particulate also pose an inhalation hazard.

4.1.2 Alpha Particle Detection

The alpha particle detection used to reduce the sequential splitting process was first conducted with very small subsamples of varying masses of soil on the aluminum disks. The background was measured twice for accuracy, with both 8-minute background counts producing 26 counts. The seven subsamples were examined and produced the counts shown in Table 15.

Table 15. Alpha Particle Detection Results

Sample	Mass [g]	Gross Counts	Net Counts
1	0.024	35	9
2	0.030	37	11
3	0.038	27	1
4	0.065	29	3
5	0.028	21	0
6	0.027	28	2
7	0.43	23	0

While this data may suggest that Sample 2 had the highest number of actinides, further splitting of that sample yielded 23 and 25 counts, both below that of the background. It is likely that the split samples' counts were inaccurate due to self-shielding. Sample 1 was also further split yielding similar results, discounting this method's effectiveness for locating actinide bearing particles.

4.2 Morphological Characterization (SEM/Image J)

Morphological characterization was completed using the SEM images taken of each actinide bearing particle shown in Appendix C. The particles were first measured along their major and minor axes. Using the perimeter and area measurements, the average diameter was calculated using equations (3.7) - (3.9). The particle size distribution is shown in Figure 22.

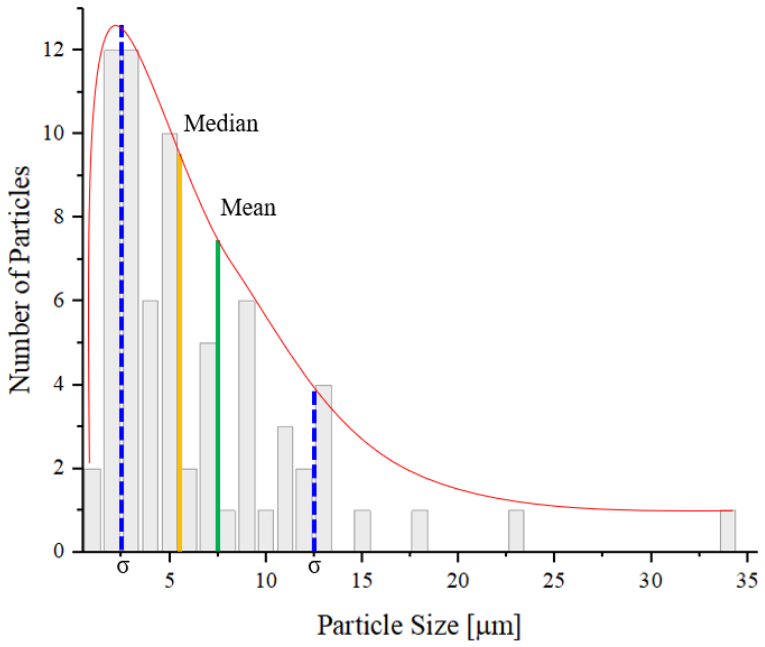

Figure 22. Size Distribution of Identified Actinide Bearing Particles

The mean value of 7 µm demonstrates the small average size of these actinide bearing particles, but is higher than the median value of 5.2 µm. This is important because the median value indicates that 50% of all particles are larger or smaller than its value. The standard deviation of +/- 5.5 µm describes the particle size interval around the mean value where 68% of all particles fall. This standard deviation assisted in determining the particle bins, with these four large particles contained within a single bin and the other 66 particles

divided into three bins of roughly equal number of particles. These four particle size bins are shown in Table 16.

Table 16. Actinide Bearing Particle Size Classes for Morphology Characterization

Particle Size [µm]	Number of Particles
0 – 4	26
4 – 8	22
8 – 14	18
14 – 35	4

4.2.1 Particle Circularity

The first characterization conducted on the individual particles was circularity. After using Image J to measure the perimeter of the particles, equation (3.6) was utilized to determine the circularity of individual particles, shown in Tables 18 and 19 of Appendix A. The circularity by particle size bin as examples from this research are shown in Figure 23.

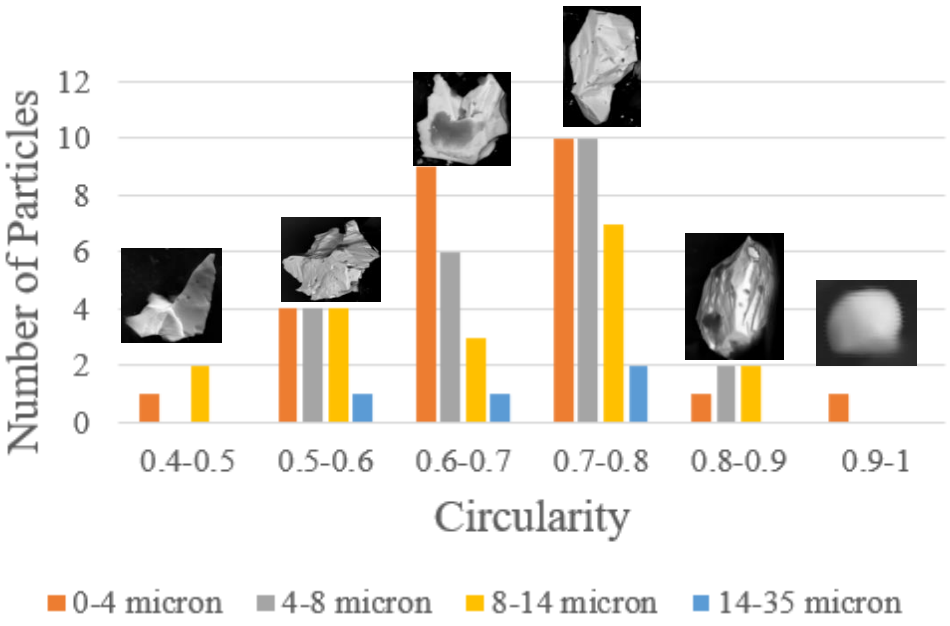

Figure 23. Particle Circularity by Size Distribution

The trend evident from Figure 23 is that for all size distributions, the highest number of particles had a circularity of 0.7 – 0.8. This is significant because it indicates these actinide bearing particles did not reach their melting point which would have resulted in highly spherical particles with higher values of circularity.

4.2.2 Particle Morphology Characterization

Particle morphology was characterized using the lexicon developed by Los Alamos National Laboratory (LANL) for the consistent description of images for nuclear forensics [46]. Steps 1-4 (particle nature and morphology) and 7-9 (surface features and appearances) of this process were used to describe the characteristics of all actinide bearing particles identified in this research. First, the particles' overall morphology was classified by the degree they contained crystalline or faceted faces as shown with examples from the research in Figure 24 [46].

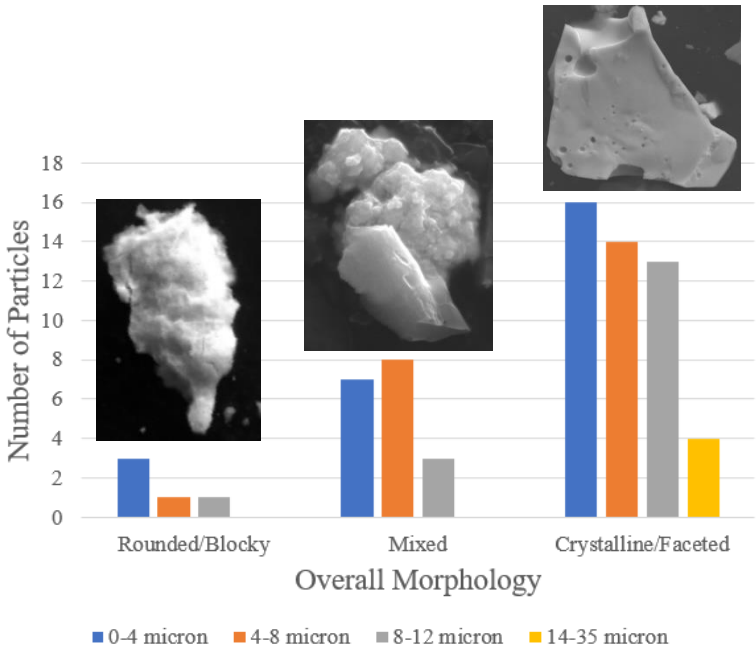

Figure 24. Particle Overall Morphology by Size Distribution

This step illustrates that for each size distribution, the highest number of particles (and all in the 14-35 micron size) have a crystalline/faceted overall morphology, with 67% of all particles falling into this category. The third step in the lexicon was to classify the angularity of the particles, ranging from well-rounded whose edges are smoothly curved and/or rounded to very angular who edges are sharp and distinct [46]. The angularity by particle size distribution is shown with examples in Figure 25.

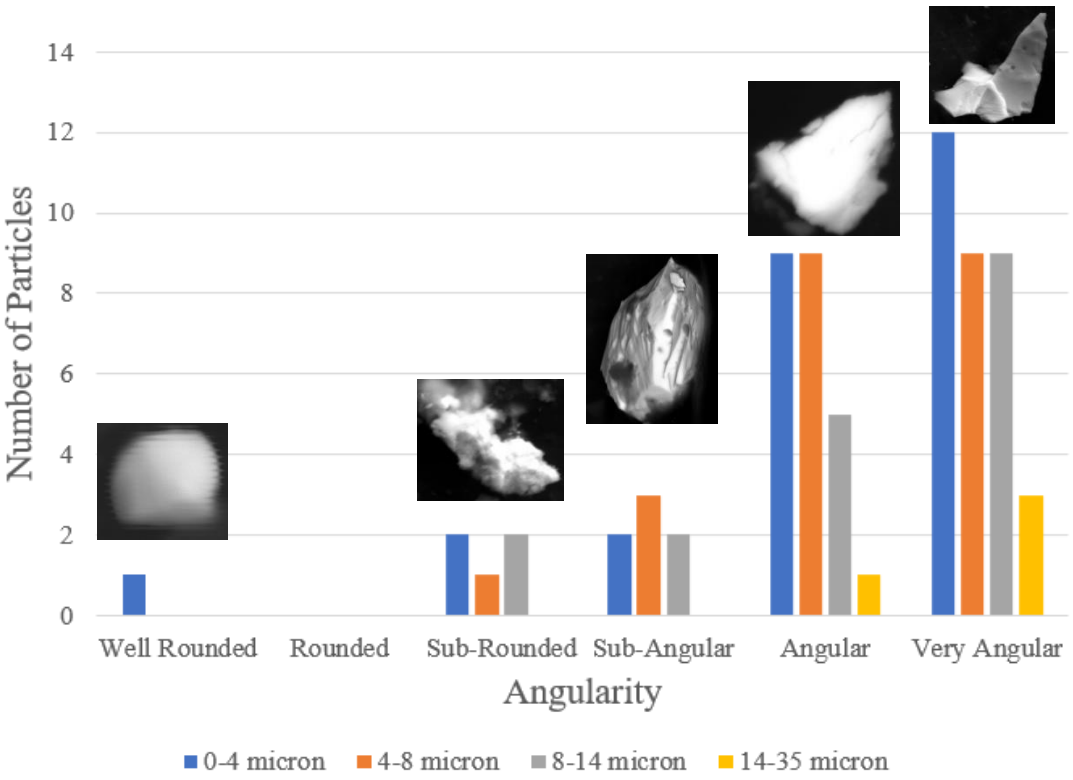

Figure 25. Particle Angularity by Size Distribution

The fourth step in the lexicon was to classify the sphericity and overall shape of the particle. In this context, sphericity is an indication of how equal the size of the particle is in all three dimensions; high sphericity is not necessarily an indication of being round as a

cube would have high sphericity [46]. The sphericity was classified by subsample and is shown in Figure 26 with examples.

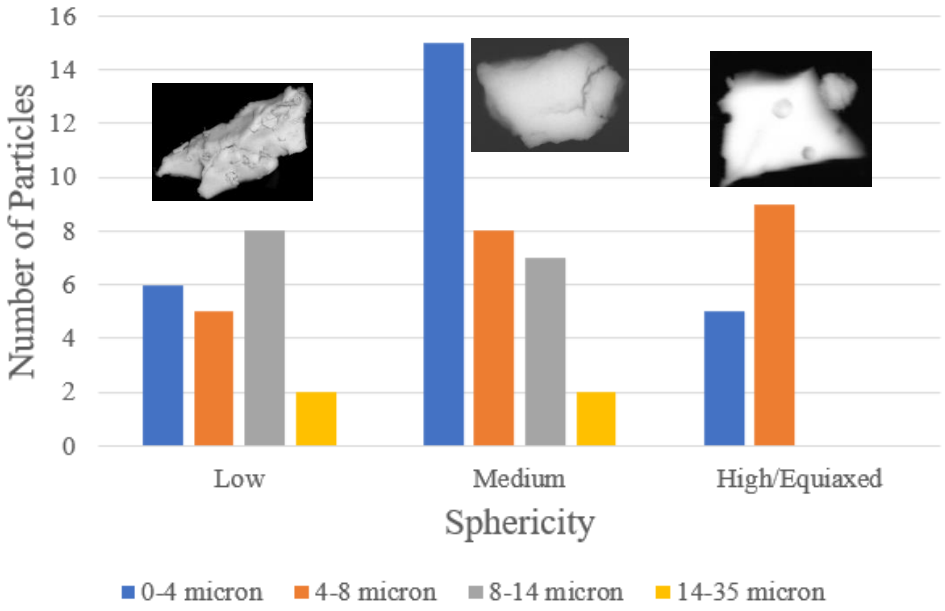

Figure 26. Particle Sphericity by Size Distribution

While there are particles in each sphericity category, 46% of all particles fall in the medium sphericity, with 76% being either low or medium sphericity. The next area to be analyzed was step 7 of the lexicon, describing the overall surface of the particles for projections, coarseness, and unevenness as shown in Figure 27 with examples [46].

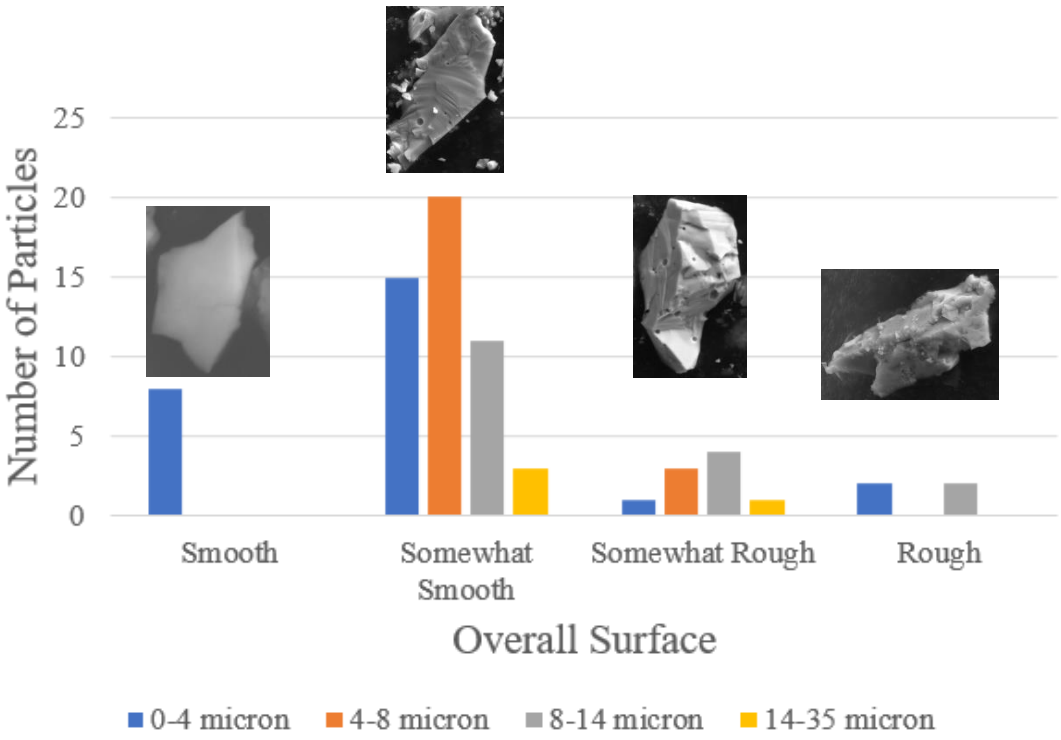

Figure 27. Particle Overall Surface by Size Distribution

The results from this step of the lexicon show 70% of all particles classified as somewhat smooth. It is also noteworthy that the only particles with smooth surfaces are smaller than 4 microns. The final step of the process was to describe the surface features of the particles. This included four categories as outlined in the lexicon: surface indentations, surface patterns, surface decorations, and surface appearance [46]. Most particles had features from one or more of these categories, although there were particles with no visible surface features (almost entirely those classified as smooth in the previous step). Features such as pits, striations, and cracks/fractures allowed particle classes to be determined based on morphology. The results from this surface characterization are shown in Figure 28 and can be seen in greater detail from the individual particles images contained in Appendix C.

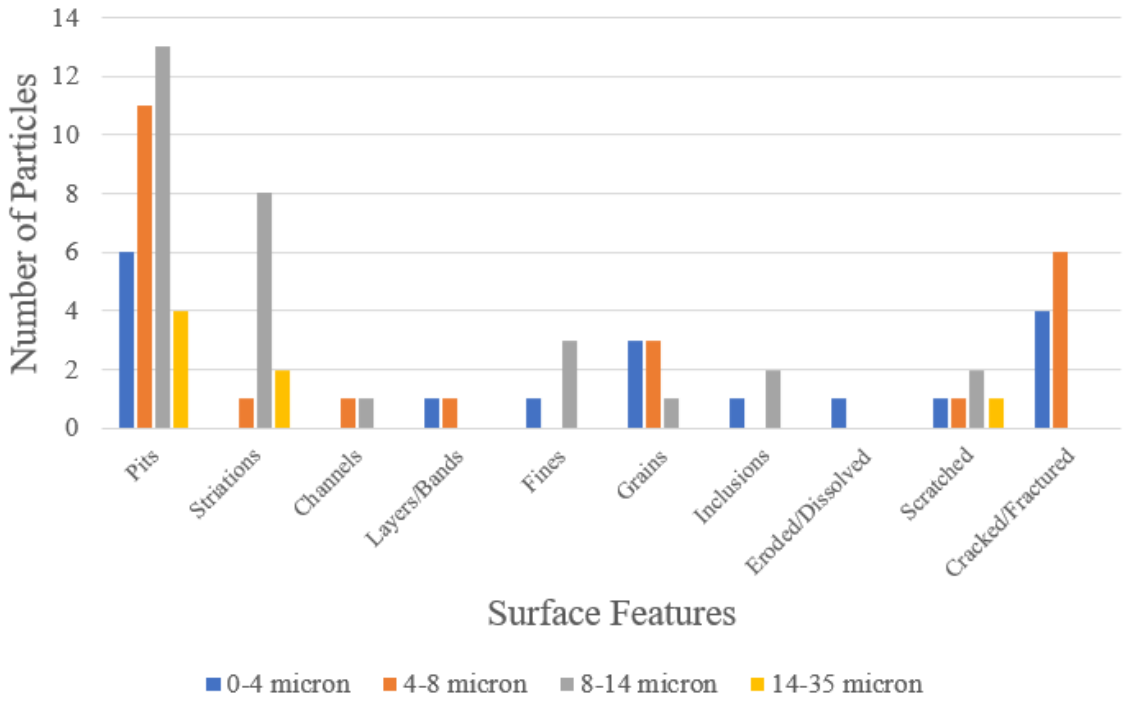

Figure 28. Particle Surface Features by Size Distribution

After the steps utilized from the lexicon were completed and the trends analyzed, three general classes of particles were identified. The first type is a mixed or crystalline/faceted particle (no size trend) with angular or very angular edges, varying sphericity, and a somewhat smooth to somewhat rough surface. These particles are dominated by surface pitting, striations, fines, and grains. The second type of particle is a mixed or crystalline/faceted particle that is 7 microns or smaller with sub-angular to very angular edges, varying sphericity, and a smooth to somewhat smooth surface. These particles have cracks or fractures on the surface and tend to have no other distinguishable surface features. The third type is a rounded/blocky particle that is 10 microns or smaller with no distinct angularity, varying sphericity and an irregular shape, and a somewhat rough to rough

surface. These particles can have surface cracks or fractures, and tend to have grains on the surface.

4.3 Elemental Composition

4.3.1 EDS Analysis

EDS analysis was conducted on all previously suspected actinide bearing particles and those identified as high Z for elemental composition using the SEM BSE imaging at AFRL. This analysis resulted in 70 total particles being identified as actinide bearing from the prepared silicon grids by analyzing their total spectra as shown in Appendix H. Figure 29 shows an EDS area analysis conducted on particle G6-1 (spectrum 32 in the SEM image).

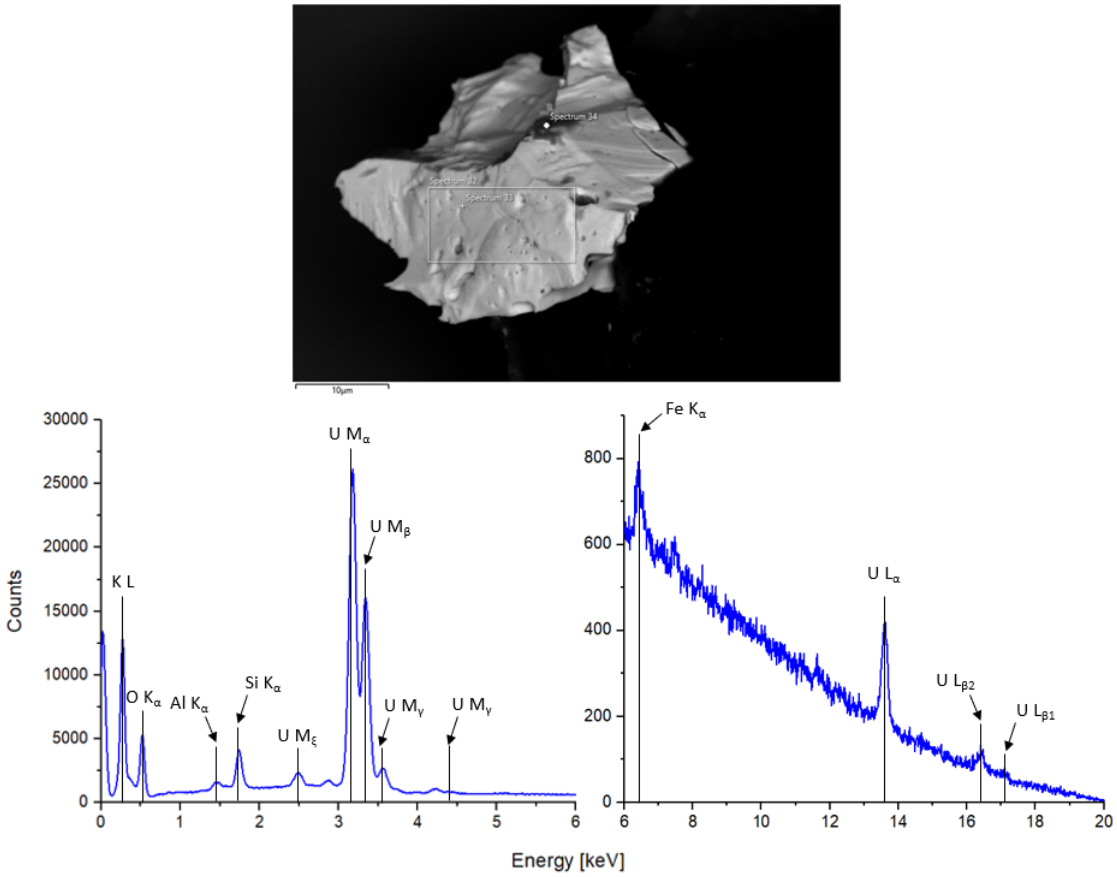

Figure 29. Full EDS Spectrum

The particles were analyzed for their atom perecentage (at%) composition which resulted in five elements being common in most or all of the particles, and 16 total trace elements occurring in one or more particles, as shown in Tables 24 and 25 of Appendix E. These results were analyzed using the same size classes defined in Table 16. It is important to note that the at% result generated in the EDS reports is a qualitative analysis and not necessarily quantitatively accurate. The EDS at AFRL was calibrated using a mixed copper and aluminum reference standard at the beginning of the analysis. However, for correct quantitative analysis spectra from elements of interest must be taken and a new calibration standard built within the AZtec software [47]. The standards should be close in composition to samples, homegeneous, well characterized, and pure elements or compounds. For proper calibration, actinide calibration samples would have to be utilized for the analysis to be quantitatively correct, which were not available. With small sample sizes being considered, the 95% confidence intervals for the five most common elements' at% was calculated using (4.1) [48].

$$t = \frac{\pm t_{0.025,\nu} S_x}{n^{1/2}} \tag{4.1}$$

In (4.1) $t_{0.025,\nu}$ is the *t*-distribution value, S_x is the calculated standard deviation, n is the number of values sampled, and $\nu = n\text{-}1$. Elements occurring in a singular particle within a size distribution will have no confidence interval as S_x cannot be calculated. The results of the EDS analysis of the major elements can be seen in Figure 30. The values in Figure 30 represent the mean for each of the elements with 95% confidence intervals as error bars. Also, as particle size increases, the EDS analysis will be sampling a lower total percentage of the particle's volume, which can contribute to a greater margin of error as well. For

oxygen, it must also be stated that the system is not operating under a perfect vacuum, so there will be inevitable sampling of the oxygen left within the chamber as well.

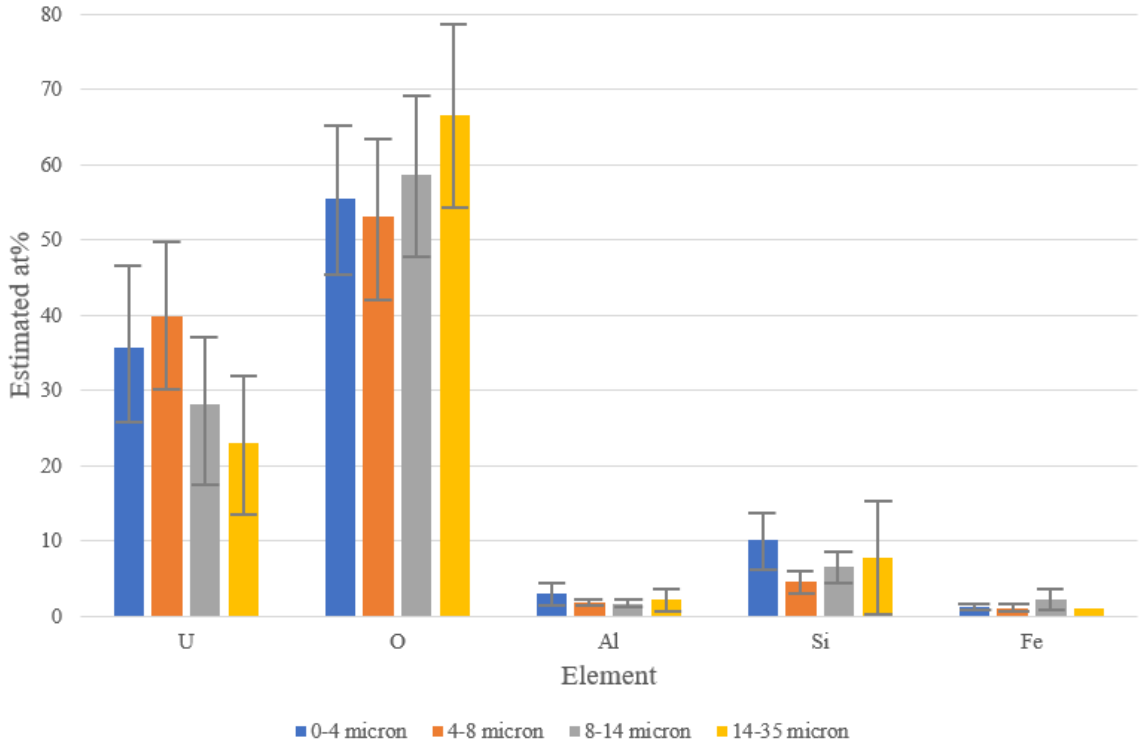

Figure 30. EDS Analysis of Most Common Elements

The trace elements were next analyzed. Using (4.1) with an 80% confidence interval (with $t_{0.1,\nu}$ as the *t*-distribution value, due to less particles containing trace elements), the mean values with appropriate error bars for the five most common trace elements and those of particular interest are shown in Figure 31. The 80% confidence interval of Cr was not added due to its extreme value that was far outside of the actual data range. The EDS analysis also showed trace amounts of Ca, S, Cu, Ti, Cs, F, Zr, V, and Mn contained within 1-4 of these actinide bearing particles. Figure 32 shows an EDS point analysis conducted on particle G10-2 (spectrum 36 in the SEM image) of an inclusion on the larger particle that contained numerous trace elements.

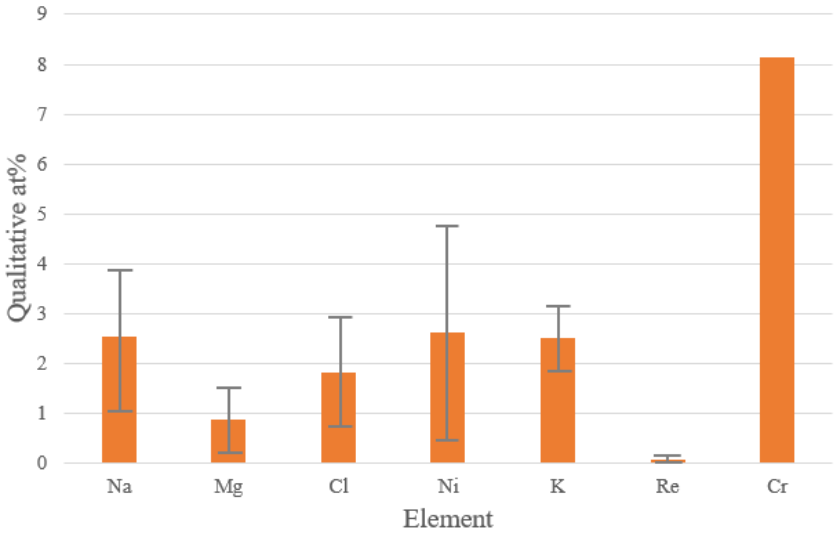

Figure 31. EDS Analysis of Trace Elements

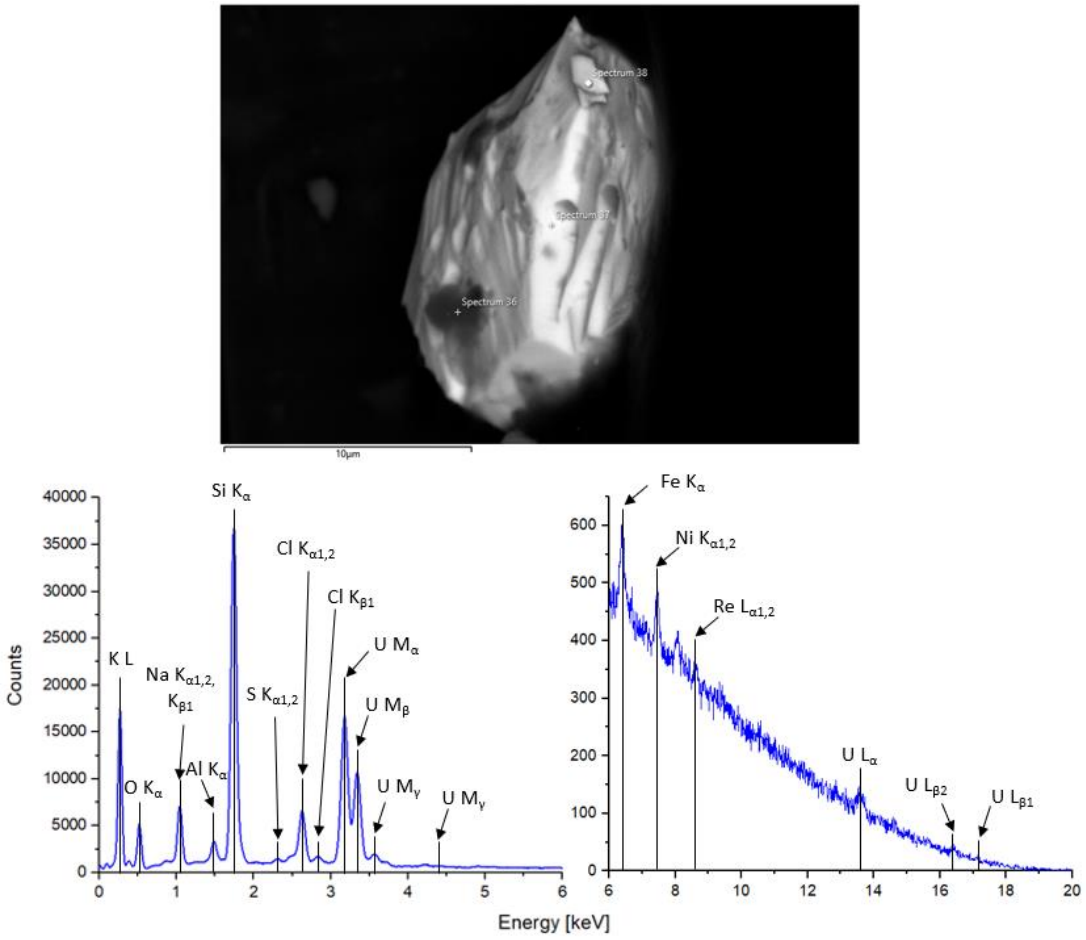

Figure 32. Full EDS Spectrum with Trace Elements

In addition to EDS point and area analysis, elemental mapping was also conducted on particle A1-1 (only 1 particle because of very limited access to the SEM/EDS due to COVID restrictions). The intent of the mapping analysis was to determine whether the elements detected were homogeneously distributed throughout the particle. The SE SEM image of the particle as well as the elemental maps are shown in Figure 33.

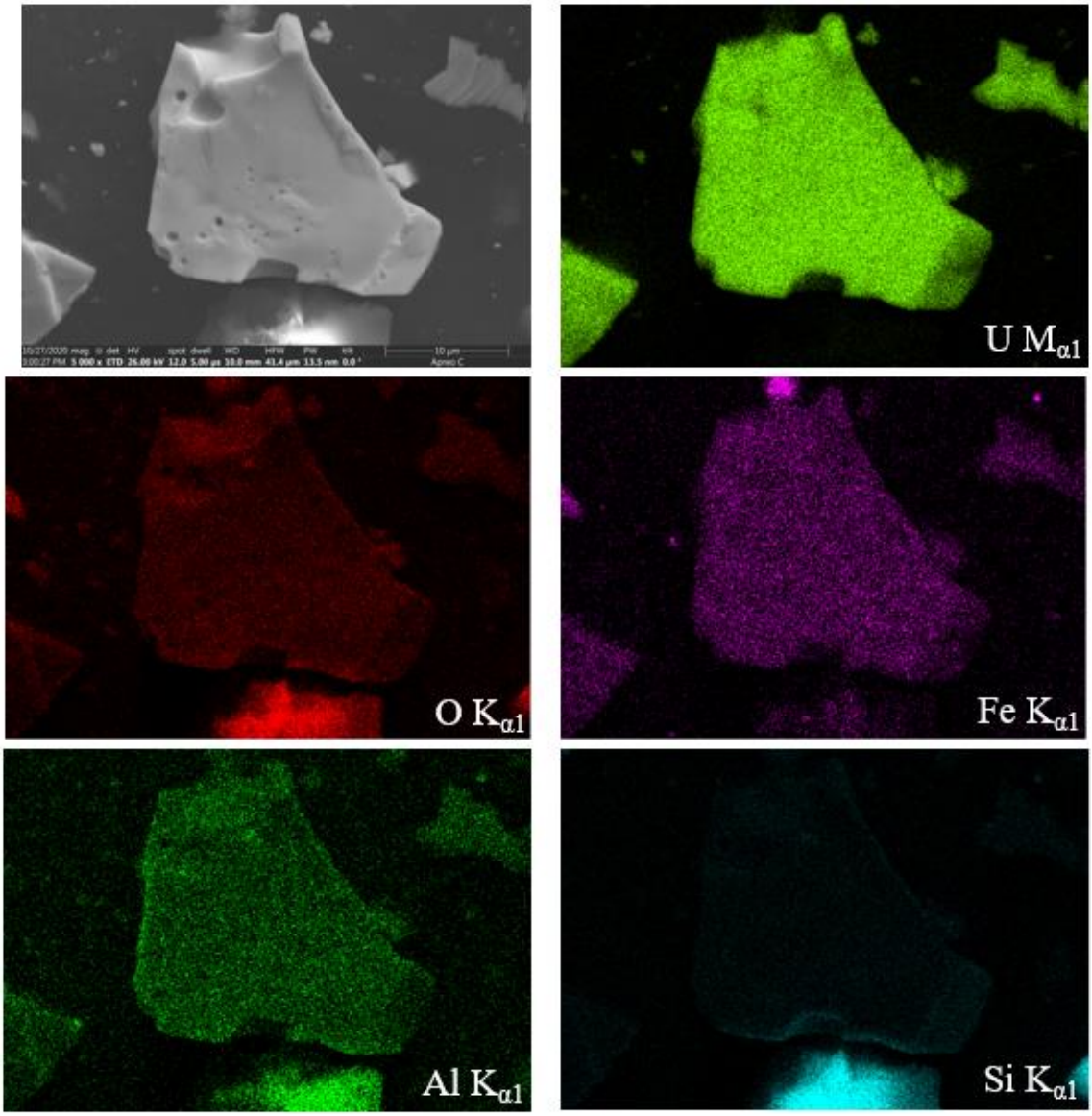

Figure 33. SEM Image and Corresponding Elemental Maps of Particle A1-1

The elemental maps illustrate that the elements present on this actinide bearing particle are homogeneously distributed. Of note, Pu was included as an element to map for this particle and produced a map showing no content within the particle. This alone, however, does not disprove that Pu is present within the particle. Origin software was used to further analyze the spectra for Pu content that the EDS may have automatically classified as U utilizing the characteristic X-rays found in Table 17.

Table 17. U and Pu Characteristic X-Rays

Element	X-Ray Lines	Energy [keV]	Intensity [%]
U	M_α	3.17	100
	M_β	3.34	60
	M_γ	3.56	5
Pu	M_α	3.35	100
	M_β	3.525	60
	L_α	14.28	100

Of particular interest is the deconvolution of the 3.34/3.35 keV peak that the EDS resolution is not sufficient to distinguish between the U M_β and Pu M_α X-Rays. Using Origin, the 60% intensity counts attributed to the U M_β X-Ray line can be determined from the total counts under the 3.17 keV U M_α peak. For numerous particles, this left a second, statistically significant peak contributing counts at 3.34/3.35 keV. An example of the peak deconvolution conducted in Origin software for all 70 particles is shown in Figure 34 for particle L12-5 (due to this particle having 61% more U M_β counts at 3.34/3.35 than should be present from only U). This peak deconvolution involved two tasks. First, if the peak at 3.34/3.35 keV had a second statistically significant peak possibly from Pu, other Pu X-Ray peaks had to be analyzed to prove or disprove the element's presence. Second, if the counts were not from Pu, the identity of the element contributing the counts had to be determined.

For particle L12-5, the two major peaks at 3.17 and 3.34/3.35 keV were first analyzed and the counts recorded. Based off the expected counts, the rest of the peaks in the 3-4 keV range for both U and Pu were added as seen in Figure 34. The Pu M_β peak at 3.53 keV was set at 60% intensity of the counts under the M_α peak.

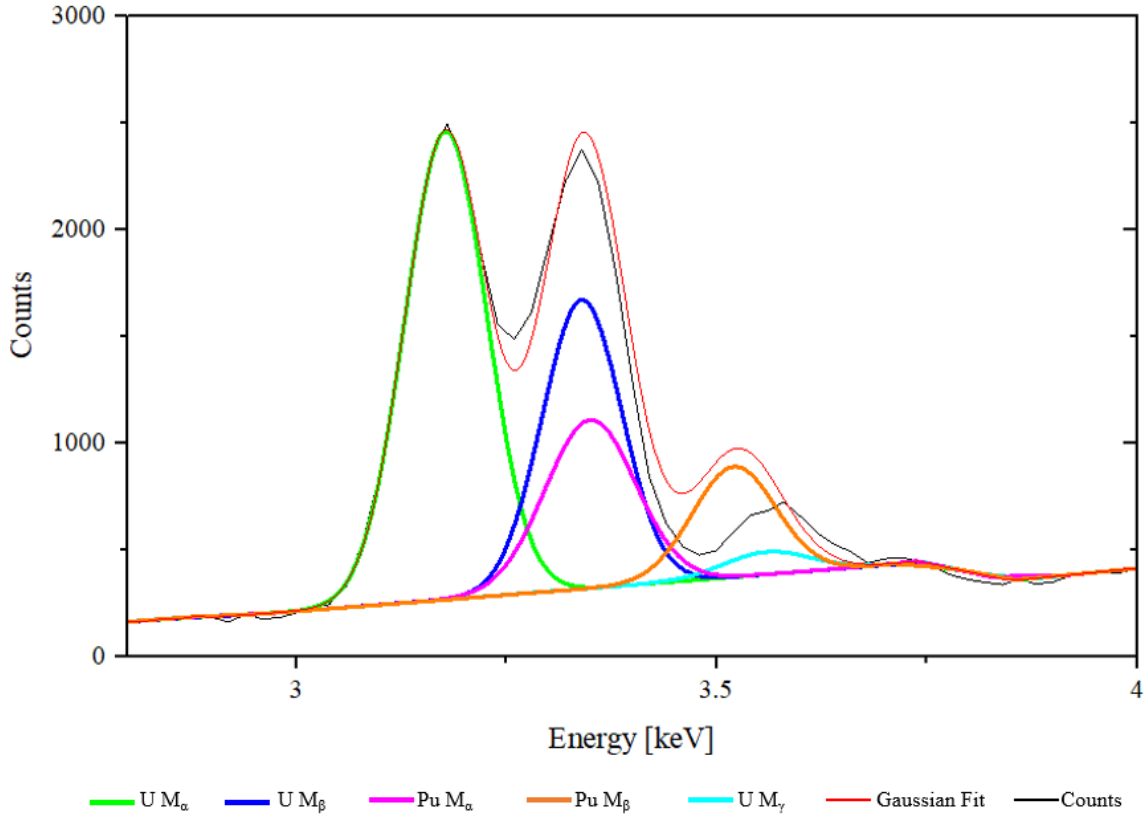

Figure 34. Deconvolution of U/Pu 3.34 keV X-Ray Peak

Figure 34 shows the expected Pu M_β peak well above the actual counts in the spectrum, although there is a small shoulder in this general area. With a lack of any peak above the background for plutonium's L_α line at 14.28 keV, the conclusion cannot be made that Pu is contributing counts to the 3.34/3.35 peak. Potassium also produces characteristic X-rays in this analyzed energy range, with its K_α at 3.31 keV and the K_β at 3.59 keV, and therefore

it must be considered in this peak deconvolution as well [49]. Once again, Origin software was utilized to conduct the analysis of these peaks as shown in Figure 35.

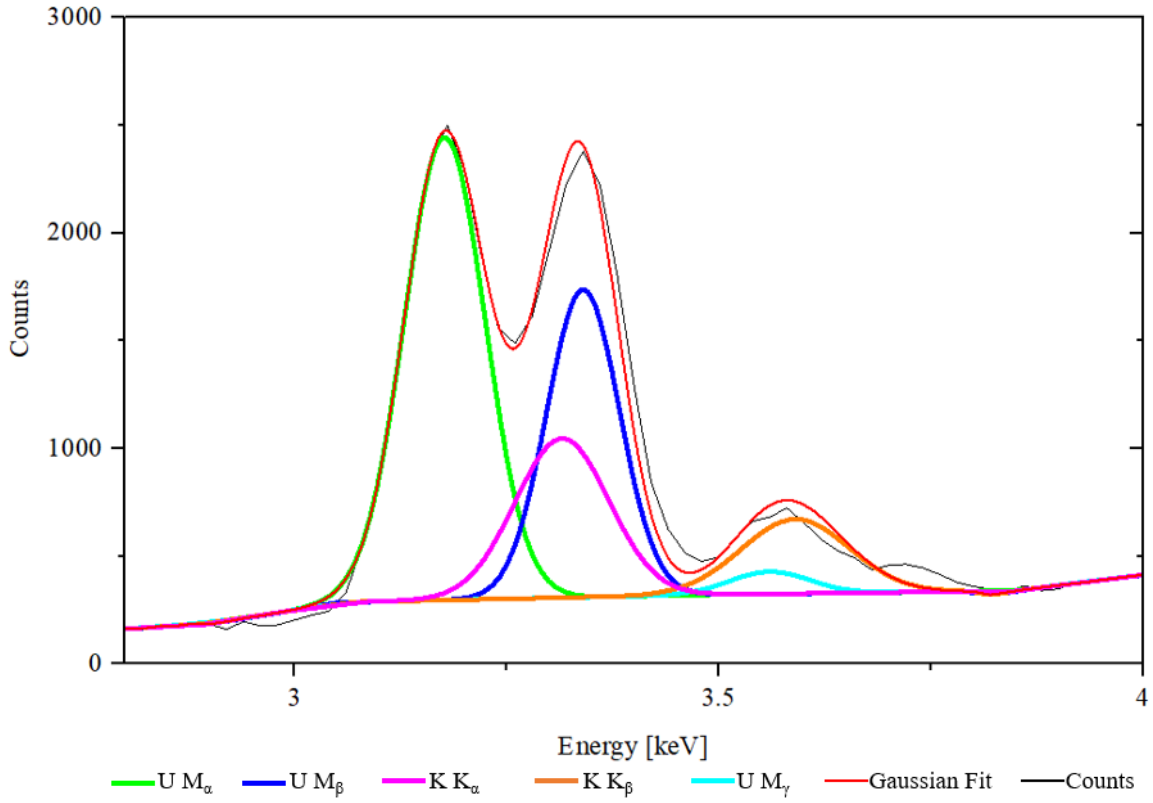

Figure 35. Deconvolution of U/K 3.34 keV X-Ray Peak

Comparing Figures 34 and 35 draws the conclusion that the element contributing counts to the 3.34 keV peak is more likely to be K than Pu.

A literature review of the solubility of Pu and U within soil was conducted. Previous research was conducted on the storage of nuclear waste and the associated groundwater hazards in both the United States and Canada. The research conducted for the U.S. Yucca Mountain site studied the calculated and experimental solubility of Pu compounds in groundwater [50]. The Canadian study researched the storage of spent nuclear fuel in deep underground vaults and the solubility of U compounds in the surrounding groundwater

[51]. Slightly acidic ground water has been reported at the BOMARC site. For the purposes of this research it is assumed that this means the ground water has a pH in the range of 5 to 6. At this pH $Pu(OH)_4$ (s) and PuO_2 (s) have an experimentally calculated solubility of 10^{-8} to 10^{-6} mol/L dependent on the Pu oxidation state [50]. This compares to a maximum U solubility of 10^{-10} mol/L for total uranium concentrations expected within ground waters at this pH [51]. These values indicate that the lack of Pu found within the subsamples of this research could be resultant from its dissolution within the ground water prior to the samples being collected.

4.3.2 XRF Analysis

XRF analysis was also conducted on the high Z particles originally identified using SEM BSE. This analysis identified 12 total high Z actinide bearing particles (all of which were also further analyzed using EDS) and the full spectrum taken for each as shown in Appendix G, with an example shown in Figure 36.

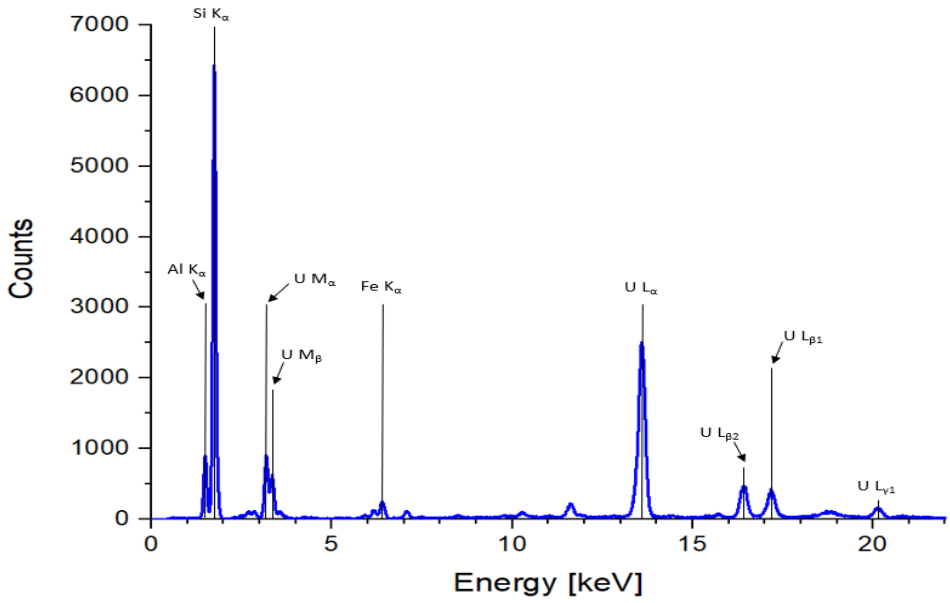

Figure 36. Full XRF Spectrum

With only 12 particles, size distributions were not considered during this analysis as the focus was only on identifying actinide presence. It is important to note that the results shown in Figure 37 are also qualitative and represent the mean at% for all the particles. Because these particles are all larger than the mean particle size, these at% numbers are not a sampling of the entire particle, only a region of the surface and its associated interaction volume. The confidence intervals were again calculated using formula 4.1 for elements present in at least three of the 12 particles (to again prevent unrealistic confidence intervals).

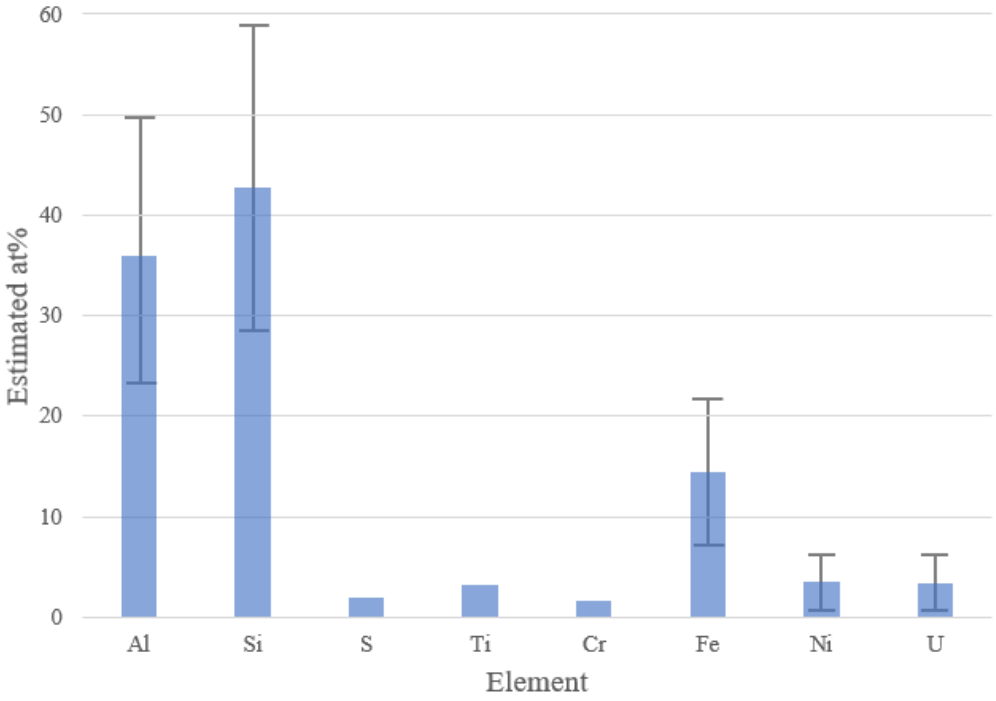

Figure 37. XRF Analysis of Actinide Bearing Particles

While the method did not prove effective for elemental mapping (at least over a 1-hour period) and the smallest aperture (10 µm) available for use also allowed the surrounding materials to be sampled, it provided a rapid method to confirm or deny actinide presence

in particles. Origin software was again utilized to analyze each particle's spectrum and confirm the XRF's uranium classification. Peak deconvolution was completed for each particle as well to investigate the possible presence of Pu, with the same results as the EDS analysis, indicating the additional counts were likely due to potassium (which was not classified in any of the 12 particles by the XRF's software). It is also important to note that the 50 kV X-rays generated by the instrument are energetic enough to penetrate the entirety of the particles, but the characteristic X-rays generated by this interaction may not have enough energy to escape the particle and be detected.

V. Conclusions

Locating actinide bearing particles and their subsequent analysis and characterization from the BOMARC nuclear accident were the two major goals set at the start of this research. By implementing numerous techniques, multiple routes to locating particles were explored and proved successful. Once these actinide bearing particles were located, they were analyzed for elemental composition and their morphology described using a highly descriptive particle lexicon. Unique to this research was the focus on only the smaller soil particulate, which resulted in most of the discovered actinide bearing particles being much smaller than in previous research.

5.1 Locating Actinide Bearing Particles

Two methods of locating actinide bearing particles were explored during this research to determine which would be the most effective method. Both HPGe gamma spectroscopy and alpha particle detection can be utilized for sequential splitting techniques, but require high activity to be conducted in a timely process and provide sound counting statistics. Locating actinide bearing particles using SEM/EDS and XRF required that the particles be mounted in an organized manner that allows easy return to the particle for further analysis.

Sequential splitting using both HPGe gamma spectroscopy and handheld alpha particle detection proved ineffective to locate an actinide bearing particle in a sample with a total activity of less than 7 nCi. The HPGe detector required more than five hours to identify peaks in the spectrum, and this time increased linearly as the sample size decreased from splitting. While gamma spectroscopy did prove that actinide bearing particles exist within the sample, the shear time it would require isolating a singular particle ruled it out for

further use in the research. The handheld alpha particle detection also proved ineffective for isolating an actinide bearing particle. Even with collimation, the counts registered in the detector were not substantially higher than the background. This method was unable to detect substantial alpha activity within very small, thinly spread subsamples or bulk particulate; a problem that was only compounded without the sample being under vacuum.

Mounting the particles to the silicon finder grid and utilizing SEM/EDS and XRF proved a timely method to locate the actinide bearing particles. By applying a small piece of carbon tape to each alphanumeric square and then loading the grid with particulate, these environmental subsamples could be quickly examined using BSE imaging in the SEM to find high Z particles. Initial XRF examination of the high Z particles took approximately 12 hours, identifying 12 total particles. The efficiency and timeliness of the XRF analysis would be greatly improved by utilizing a smaller aperture (approximately 1 μm) and a more powerful optical camera, reducing both the sampling of other materials within the sample and the time necessary to locate the particle on the grid. The SEM/EDS combination proved the most effective method for isolating the actinide bearing particles. When a high Z particle was identified, it could quickly be analyzed using the EDS to confirm or deny actinide presence without having to move the sample to another instrument as with the XRF. Using this method, 58 additional particles were found and analyzed within the sample over an 8-hour period. This method could be used efficiently for analysis of future nuclear accident debris and within the nuclear forensics community for sample analysis.

5.2 Elemental/Morphological Characterization

A total of 70 particles were subjected to analysis of their elemental composition and morphology. The BSE and SE images of each particles were analyzed, and Image J utilized to measure the particles' diameter, area, and perimeter. The lexicon for describing particles developed by LANL was then used to characterize the particles' shape, structure, and surface features so correlations among the particles by size distribution could be determined. Elemental analysis of each particle was done using EDS and spectra collected for all particles. While the EDS software automatically identifies elements, individual peak analysis was done on all 70 particles using Origin software to verify actinide presence and determine if other elements not identified by the software contributed to the counts.

The analysis of the SEM imagery using Image J and the lexicon was done for all particles across four size distributions. The 70 actinide bearing particles identified range in size from 1 to 34 μm, with an average particle size of 7 μm where 34% of the particles are between 2 and 4 μm. The morphology of the particles resulted in two dominant classes of particles being identified that are crystalline/faceted, of high angularity and are dominated by pits, striations, and fractures on the surface.

The elemental analysis of these 70 particles conducted with the EDS at AFRL confirmed that all particles had significant uranium and oxygen content, with aluminum, silicon, and iron present in most of the particles. The qualitatively estimated elemental at% of these elements is indicative of the oxidation of U, Al, Si, and Fe on the surface of the actinide bearing particles. Because previous research into BOMARC debris found Pu, and the ^{241}Am present in the HPGe results is also indicative of Pu presence, each particle's

spectrum was analyzed using Origin software to determine if Pu was present. This peak analysis found no conclusive evidence of Pu content on any of the 70 particles.

5.3 Implications and Consequences

The presence of these U bearing particles within the subsamples shows that actinide particles can remain in the soil long after an accident or release. Even after decades of exposure to the environment and millions of dollars spent on soil remediation, these particles can still be found in the soil and analyzed. Within these subsamples, the dominant form of particles had easily identifiable features and demonstrated no evidence of reaching their melting temperature during the conflagration.

Actinide bearing particles in the 1-10 μm range are capable of being carried by the wind. In the event of an accident at a uranium production or enrichment site, soil samples from the downwind area could be analyzed later in time and still provide crucial evidence of activities at the accident location to include the enrichment levels of the particles. The research also reinforced environmental concerns that actinide debris remains within the soil even after numerous attempts to remediate the soil.

5.4 Future Work

The 70 particles identified during this research, as well as the rest of the environmental sample would benefit from further research and analysis. While morphology and elemental characteristics have been determined for these particles, there is still a large portion of the sample that has not been analyzed. The particulate greater than 212 μm from this sample that has not been analyzed yet accounts for 68.2% of the sample by mass. Gamma

spectroscopy of the larger particulate would give further insight to the isotopic content of the sample, and SEM/EDS analysis using the silicon grid finder would likely lead to additional U (or even Pu) particles being found. Also, considerably more analysis of the rest of the smaller particulate may reveal different actinides and particles with very different morphology. Different technologies, such as DAR, may also prove effective at identifying particles containing both actinides and concentrations of other radioisotopes that BSE SEM imaging is not capable of finding.

It would also be beneficial to conduct further analysis on these 70 particles to obtain more information that may give insight into their forming and the effects of 60+ years in the environment. First, the particles need to be removed from the carbon tape on the finder grid through a developed particle picking technique to free the particles. Raman spectroscopy of the particles could then be conducted to determine the oxidation states of the uranium and other metals. Backscattered diffraction (EBSD) could be used to study the crystalline structures of the particles. There are several destructive techniques that could be used to analyze these particles. With uranium already identified within the particles, in-depth analysis utilizing either TIMS or SIMS would be able to determine the exact isotopic ratio of ^{235}U:^{238}U to determine whether the particles contain HEU, DU, or natural uranium.

Appendix A. Individual Particle Data

A total of 70 particles with actinide presence were isolated in this research. The tables below list the dimensional measurements and calculations for all the particles.

Table 18. Circularity and Diameter of Particles A1-1 through A1-15

Particle	Major Axis [µm]	Minor Axis [µm]	Area [µm^2]	Perimeter [µm]	Circularity	D_1 [µm]	D_2 [µm]	Avg. Diam. [µm]
A1-1	27.89	18.97	355.75	77.79	0.74	21.28	24.76	23.02
D8-1	5.01	2.75	11.61	15.34	0.62	3.84	4.88	4.36
F10-1	9.63	9.29	69.24	32.74	0.81	9.39	10.42	9.91
F10-2	14.21	8.76	116.01	43.66	0.76	12.15	13.90	13.03
F10-3	12.6	4.83	47.49	33.54	0.53	7.78	10.68	9.23
F10-4	19.44	8.78	109.61	50.69	0.54	11.81	16.14	13.97
F10-5	8.21	8.18	41.47	26.11	0.76	7.27	8.31	7.79
F10-6	6.57	5.51	21.28	18.7	0.76	5.21	5.95	5.58
L8-1	20.81	11.94	171.73	53.82	0.75	14.79	17.13	15.96
L8-2	14.49	13.59	115.8	47.9	0.63	12.14	15.25	13.69
G6-1	33.86	29.94	673.73	125.04	0.54	29.29	39.80	34.55
G10-1	22.21	12.9	224.41	64.55	0.68	16.90	20.55	18.73
G10-2	16.36	9.51	115.74	41.26	0.85	12.14	13.13	12.64
E4-1	3.48	2.9	6.18	10.06	0.77	2.81	3.20	3.00
A6-1	2.66	1.07	1.97	6.84	0.53	1.58	2.18	1.88
B7-1	4.13	2.52	6.4	14.21	0.4	2.85	4.52	3.69
B7-2	3.28	2.21	4.38	10.4	0.51	2.36	3.31	2.84
I6-1	2.77	1.81	3.58	8.54	0.62	2.13	2.72	2.43
A1-2	13.71	12	97	39.44	0.78	11.11	12.55	11.83
A1-3	12.3	7.2	63.08	32.06	0.77	8.96	10.21	9.58
A1-4	3.8	2.11	5.3	10.16	0.65	2.60	3.23	2.92
A1-5	3.52	3.44	8.19	11.78	0.74	3.23	3.75	3.49
A1-6	5.65	5.41	16.48	18.81	0.59	4.58	5.99	5.28
A1-7	3.69	3.33	8.17	11.99	0.71	3.23	3.82	3.52
A1-8	5.68	4.69	16.62	18.29	0.62	4.60	5.82	5.21
A1-9	4.08	2.55	7.14	11.8	0.64	3.02	3.76	3.39
A1-10	19.98	6.72	96.17	51.74	0.45	11.07	16.47	13.77
A1-11	2.5	1.58	2.93	6.7	0.82	1.93	2.13	2.03
A1-12	15.6	10.47	111.83	43.97	0.73	11.93	14.00	12.96
A1-13	15.82	8.25	81.23	41.26	0.6	10.17	13.13	11.65
A1-14	1.86	1.78	2.22	5.54	0.91	1.68	1.76	1.72
A1-15	8.78	4.69	29.52	26.4	0.53	6.13	8.40	7.27

Table 19. Circularity and Diameter of Particles A1-16 through L12-7

Particle	Major Axis [µm]	Minor Axis [µm]	Area [µm^2]	Perimeter [µm]	Circularity	D_1 [µm]	D_2 [µm]	Avg. Diam. [µm]
A1-16	5.61	5.37	14.94	18.82	0.53	4.36	5.99	5.18
A1-17	6.26	5.35	20.08	18.86	0.71	5.06	6.00	5.53
A1-18	13.32	8.47	64.16	41.24	0.47	9.04	13.13	11.08
A1-19	3.28	2.36	4.41	8.98	0.69	2.37	2.86	2.61
A1-20	6.27	4.36	22.69	20.19	0.7	5.37	6.43	5.9
A9-1	14.02	4.84	57.28	37.76	0.5	8.54	12.02	10.28
A9-2	3.81	2.63	6.47	10.47	0.74	2.87	3.33	3.10
D8-2	3.75	2.64	7.38	11.28	0.73	3.07	3.59	3.33
F2-1	9.86	6.69	45.44	26.89	0.79	7.61	8.56	8.08
G1-1	2.84	2.24	4.15	8.24	0.77	2.30	2.62	2.46
I11-1	5.64	3.94	15.6	17.76	0.62	4.46	5.65	5.05
I11-2	2.84	2.14	4.83	9.02	0.75	2.48	2.87	2.68
I11-3	4.73	4.19	11.41	14.8	0.65	3.81	4.71	4.26
I11-4	6.3	5.16	18.1	17.81	0.72	4.80	5.67	5.23
K5-1	8.36	3.45	18.16	21.47	0.5	4.81	6.83	5.82
K5-2	4.33	2.95	9.2	13.55	0.63	3.42	4.31	3.87
K5-3	5.63	3.34	13.48	14.95	0.76	4.14	4.76	4.45
K5-4	2.55	2	3.82	8.36	0.69	2.21	2.66	2.43
L2-1	8.17	5.68	34.81	24.04	0.76	6.66	7.65	7.15
L2-2	3.61	2.51	7.4	11.91	0.66	3.07	3.79	3.43
L8-3	14.09	5.25	53.58	34.88	0.55	8.26	11.10	9.68
L8-4	7.59	6.25	30.98	23.67	0.69	6.28	7.53	6.91
L8-5	12.23	8.94	52.17	32.79	0.61	8.15	10.44	9.29
L8-6	10.39	5.94	38.42	26.61	0.68	6.99	8.47	7.73
L8-7	6.74	4.93	22.4	19.15	0.77	5.34	6.10	5.72
L10-1	11.11	7.18	58.77	30.8	0.78	8.65	9.80	9.23
L10-2	10.08	6.91	42.29	26.85	0.74	7.34	8.55	7.94
L10-3	8	5.84	34.16	22.65	0.84	6.59	7.21	6.90
L10-4	4.16	2.81	6.83	11.28	0.67	2.95	3.59	3.27
L10-5	4.99	1.84	5.73	11.3	0.56	2.70	3.60	3.15
L10-6	2.51	1.88	3.16	7.31	0.74	2.01	2.33	2.17
L12-1	4.93	3.8	15.65	15.6	0.81	4.46	4.97	4.71
L12-2	5.27	3.28	14.3	15.55	0.74	4.27	4.95	4.61
L12-3	3.29	2.89	5.62	9.96	0.71	2.67	3.17	2.92
L12-4	2.88	2.15	3.9	8.3	0.71	2.23	2.64	2.44
L12-5	4.22	1.94	4.58	10.33	0.54	2.41	3.29	2.85
L12-6	4.22	2.84	7.8	12.1	0.67	3.15	3.85	3.50
L12-7	6.34	3.01	13.96	15.22	0.76	4.22	4.84	4.53

Appendix B. Morphological Codes and Particle Characterization

The following codes were utilized to characterize the morphology of the 70 particles isolated in this research [1]. The process involved the characterization of individual particles using path A as defined in the Lexicon process, consisting of steps 1-4 and 7-9 [46].

Table 20. Morphology Code Assignment for Lexicon Steps 1-4

Step	Code	Term
1- Particle Type	1	Individual Particle
	2	Conglomerate
	3	Agglomerate
2- Crystal Structure	1	Rounded/Blocky
	2	Mixture
	3	Crystalline/Faceted
3- Angularity	1	Well Rounded
	2	Rounded
	3	Sub-Rounded
	4	Sub-Angular
	5	Angular
	6	Very Angular
		High
4- Sphericity/Shape	1	Sphericity/Equiaxed
	2	Medium Sphericity
	3	Low Sphericity
	A	Blocky
	B	Oblate
	C	Lenticular
	D	Prolate
	E	Fibrous
	F	Ribbon-like
	G	Irregular
	H	Straight
	I	Curved
	J	Bent
	K	Twisted
	L	Flattened
	M	Elongated

Table 21. Morphology Code Assignment for Lexicon Steps 7-9

Step	Code	Term
7- Surface Texture	1	Smooth
	2	Somewhat Smooth
	3	Somewhat Rough
	4	Rough
8- Surface Features	A	Pits
	B	Holes
	C	Pores
	D	Concavity
	E	Striations
	F	Ripples
	G	Channels
	H	Conchoidal Fracture
	I	Layers/Bands
	J	Shell
	K	Fibers
	L	Scale
	M	Crust
	N	Fines
	O	Grains
	P	Inclusions
	Q	Other "Crud"
	R	Eroded/Dissolved
	S	Melted
	T	Scratched
	U	Smeared
	V	Cracked/Fractured
	W	Friable
	X	Mud Flats
	Y	Glass-like
	Z	Vitreous
9- Processing Effects	A	Extruded
	B	Sintered
	C	Solution-Grown
	D	Spray-Dried
	E	Crushed
	F	Sieved
	G	Other

Table 22. Morphology Codes for Particles A1-1 through D8-2

Particle	Step 1	Step 2	Step 3	Step 4	Step 7	Step 8	Step 9
A1-1	1	3	5	2A	2	A	
D8-1	1	3	4	3A	2	V	E
F10-1	1	2	5	1A	3	A,N	
F10-2	1	3	6	3A	3	A,E,N	E
F10-3	1	2	6	3G	4	N	
F10-4	1	3	5	3A	2	A	
F10-5	1	3	6	1A	2	A	
F10-6	1	3	6	1A	2	A	
L8-1	1	3	6	3G	3	A,E	
L8-2	1	3	6	1A	2	A,G,P	
G6-1	1	3	6	2A	2	A, E	
G10-1	1	3	6	3A	2	A,T	
G10-2	1	3	4	2D	3	A,P,T	
E4-1	1	3	5	2A	2	I,V	
A6-1	1	1	3	3G	3	R	
B7-1	3	1	5	2A	4	O	E
B7-2	1	2	5	3G	4	A,O	
I6-1	1	3	5	3A	2	V	
A1-2	1	3	5	2A	2	A,E,T	
A1-3	1	3	4	2A	2	A,E	
A1-4	1	3	6	2A	1	V	
A1-5	1	3	4	1A	2	A	
A1-6	1	3	5	2A	2	V	
A1-7	1	3	6	1A	2	T	
A1-8	1	2	5	2A	2	V	
A1-9	1	3	5	2A	1		
A1-10	1	3	5	3A	2	A,E	
A1-11	1	3	6	2A	1		
A1-12	1	3	6	2A	2		
A1-13	1	3	6	3A	2	A	
A1-14	1	1	1	1A	1		
A1-15	1	1	4	3G	3	V	
A1-16	1	3	6	1A	2	A	
A1-17	1	3	6	1A	2	A	
A1-18	1	3	6	3A	2	A,E	
A1-19	1	3	6	2A	2	A	
A1-20	1	2	6	2A	2		
A9-1	1	1	3	3G	4	O	
A9-2	1	3	6	1A	1		
D8-2	1	2	5	2A	2	P	

Table 23. Morphology Codes for Particles F2-1 through L12-7.

Particle	Step 1	Step 2	Step 3	Step 4	Step 7	Step 8	Step 9
F2-1	1	2	3	1G	3		
G1-1	1	2	6	2A	2		
I11-1	1	2	5	2A	2	A	
I11-2	1	3	6	1A	1		
I11-3	1	2	6	1A	2	V	
I11-4	1	3	6	1A	2	O	
K5-1	1	2	5	3G	3	O,T	E
K5-2	1	2	4	2A	2	O	
K5-3	1	2	3	3A	2	I	
K5-4	1	2	3	2A	1		
L2-1	1	2	5	2A	2	V	
L2-2	1	2	5	2A	2	V	
L8-3	1	3	6	3A	2	A,E	
L8-4	1	3	5	1A	3	O	
L8-5	1	3	6	2A	2	A,E	
L8-6	1	3	6	2A	2	A	
L8-7	1	3	6	2A	2	A	
L10-1	1	3	5	2A	2	A,E	
L10-2	1	3	4	2A	2	A,G	
L10-3	1	3	6	1A	2	A	
L10-4	1	3	6	3A	2	A	
L10-5	1	3	6	3A	2		
L10-6	1	3	6	2A	1		
L12-1	1	3	5	1A	2	A	
L12-2	1	3	5	3A	2	A	
L12-3	1	3	6	2A	2	A	
L12-4	1	2	5	2A	2	N	
L12-5	1	3	6	3A	2	A	
L12-6	1	3	5	2A	2		
L12-7	1	2	5	2A	2	E	E

Appendix C. SEM Images of Particles in BSE and SE

For each particle, both a BSE and SE SEM image were taken. The BSE will be the top image and the SE the bottom image.

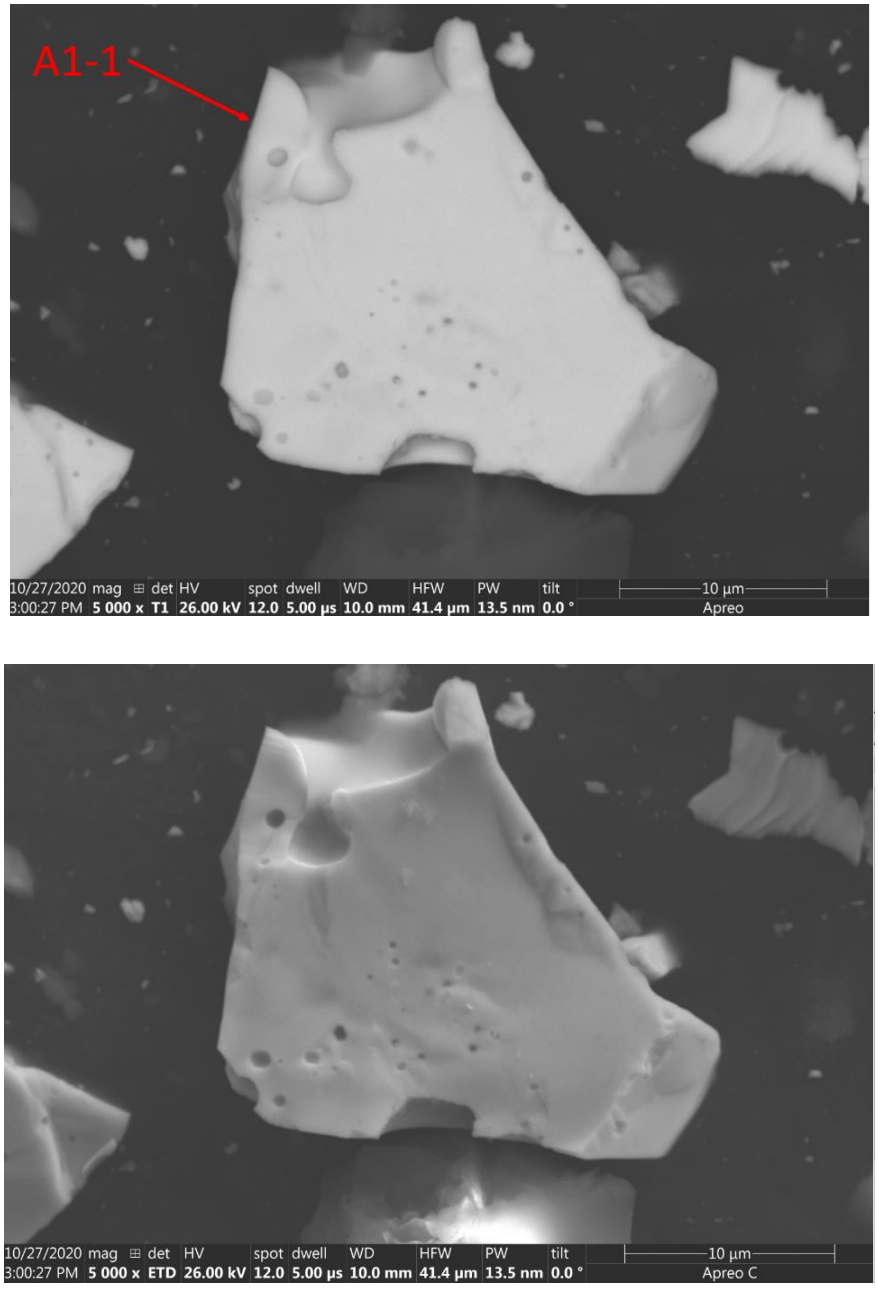

Figure 38. Particle A1-1 SEM Images

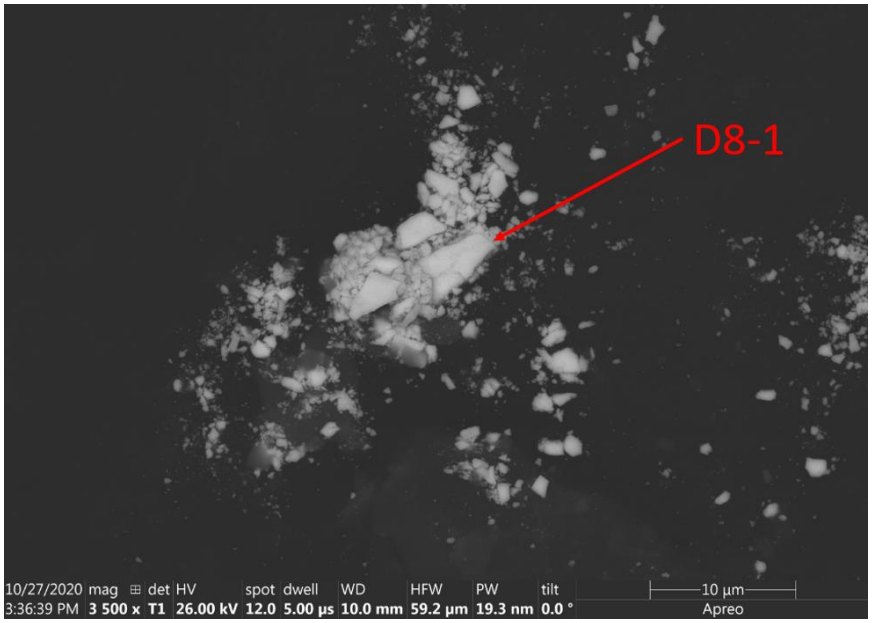

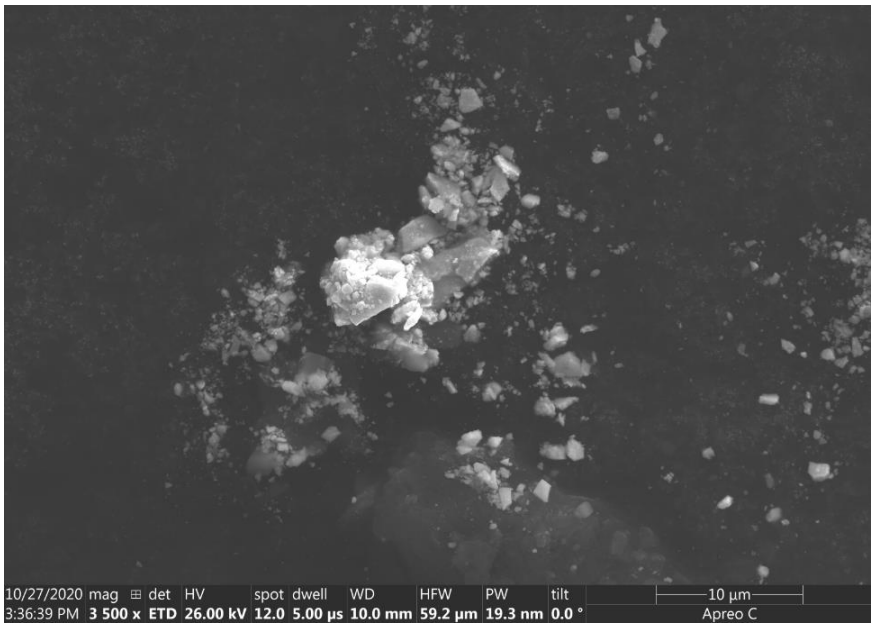

Figure 39. Particle D8-1 SEM Images

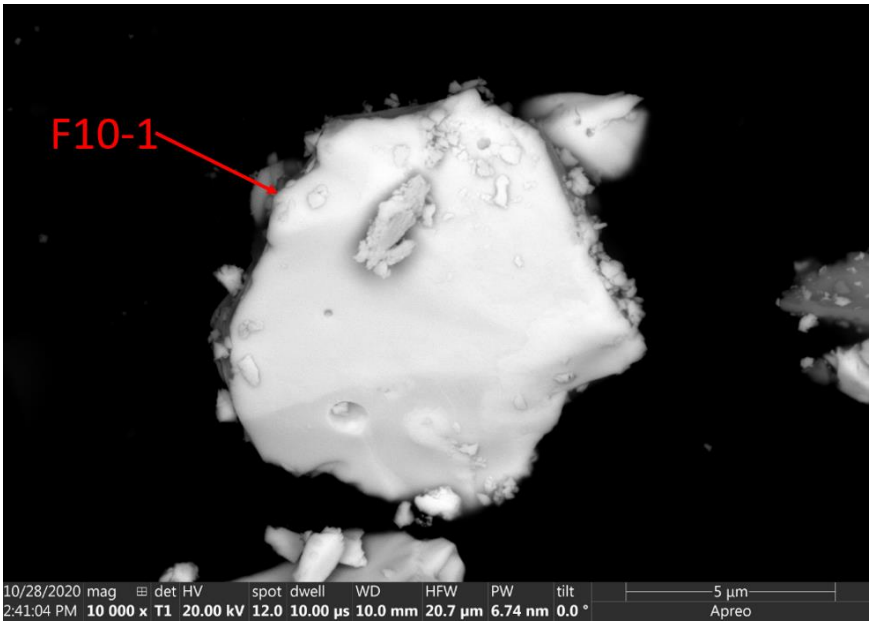

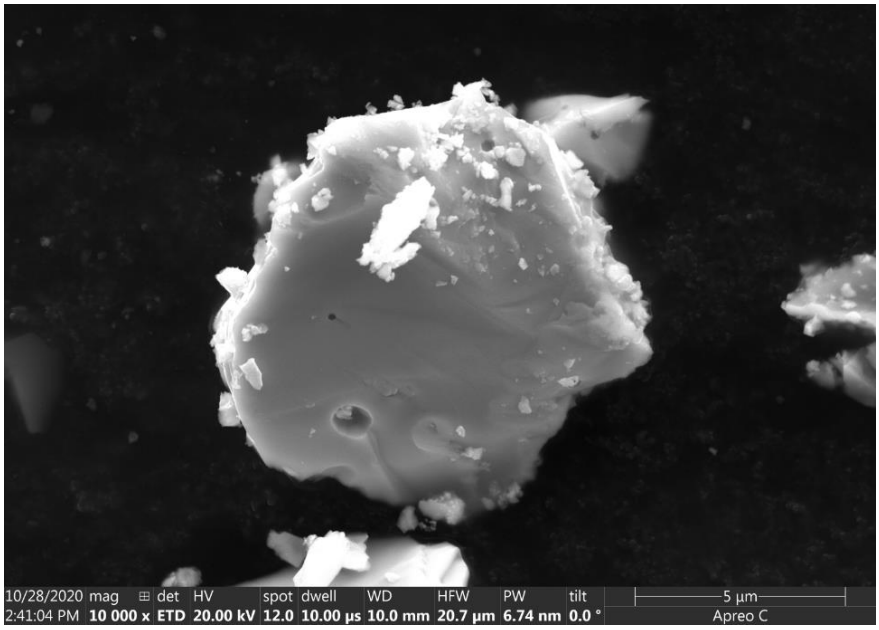

Figure 40. Particle F10-1 SEM Images

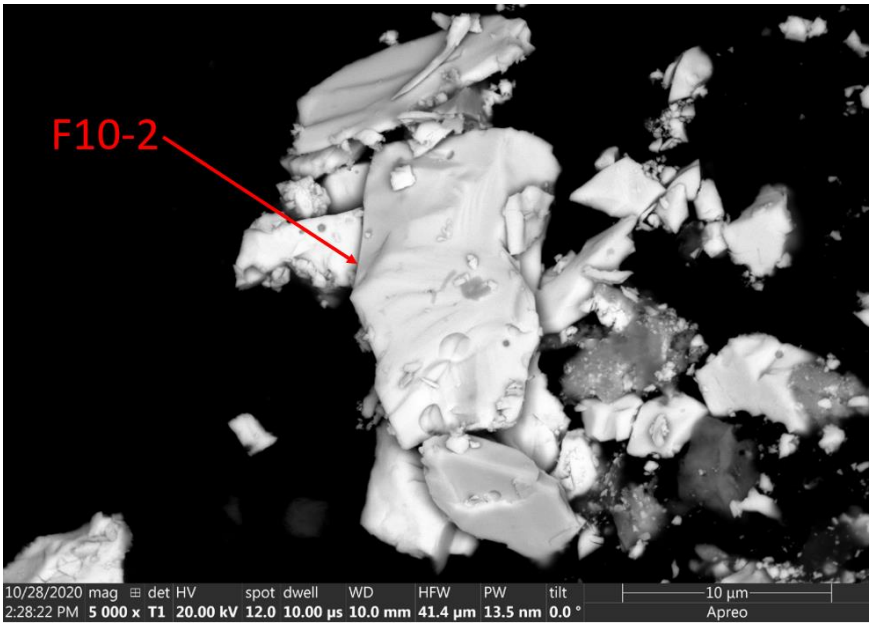

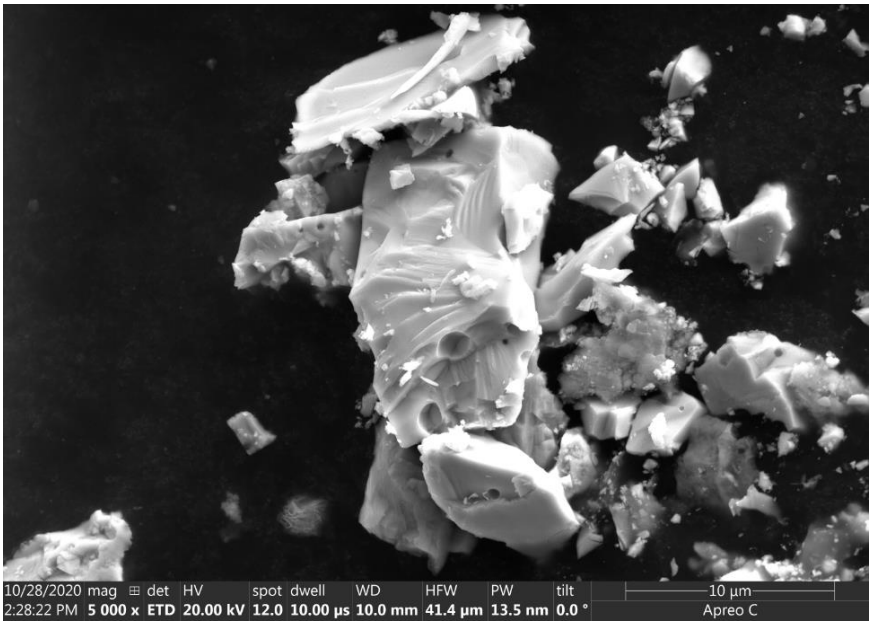

Figure 41. Particle F10-2 SEM Images

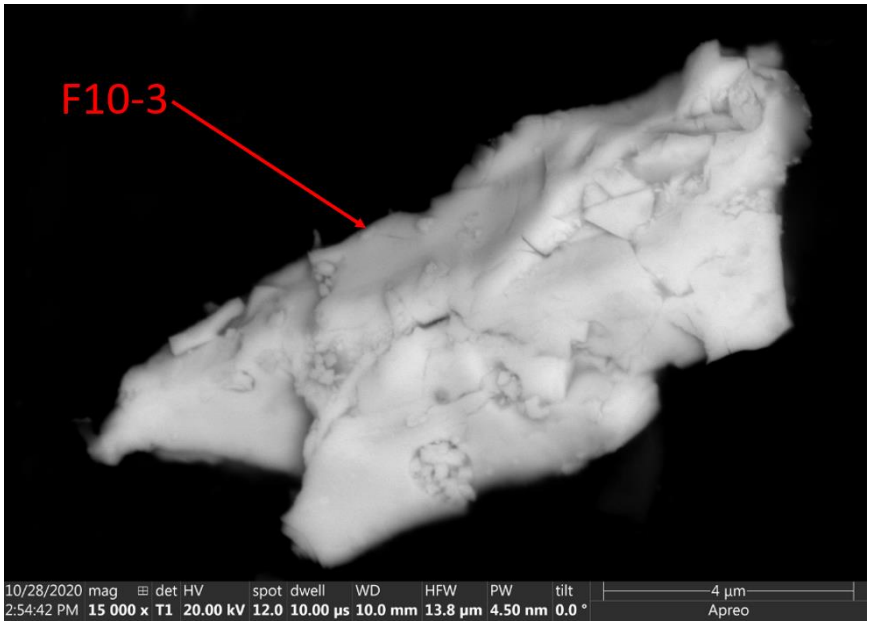

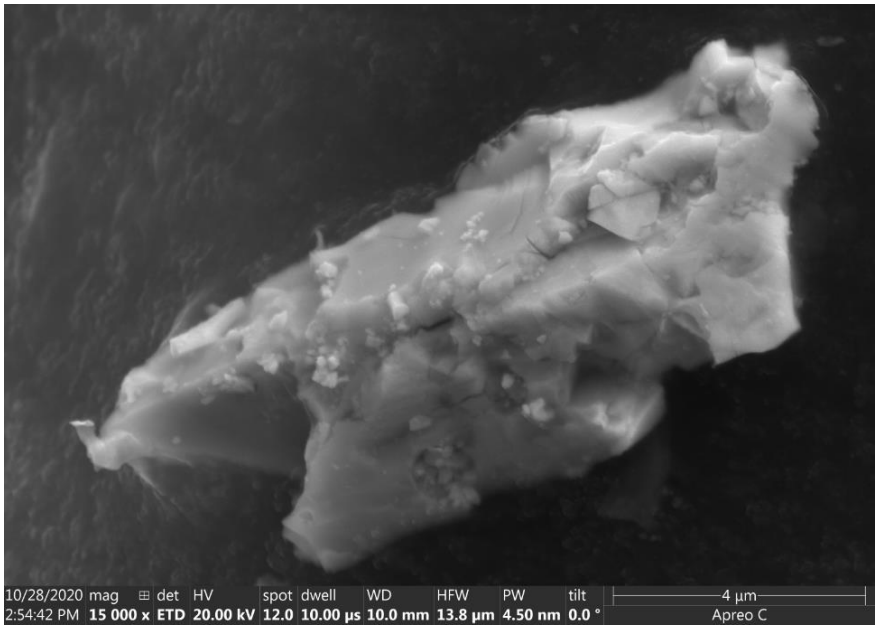

Figure 42. Particle F10-3 SEM Images

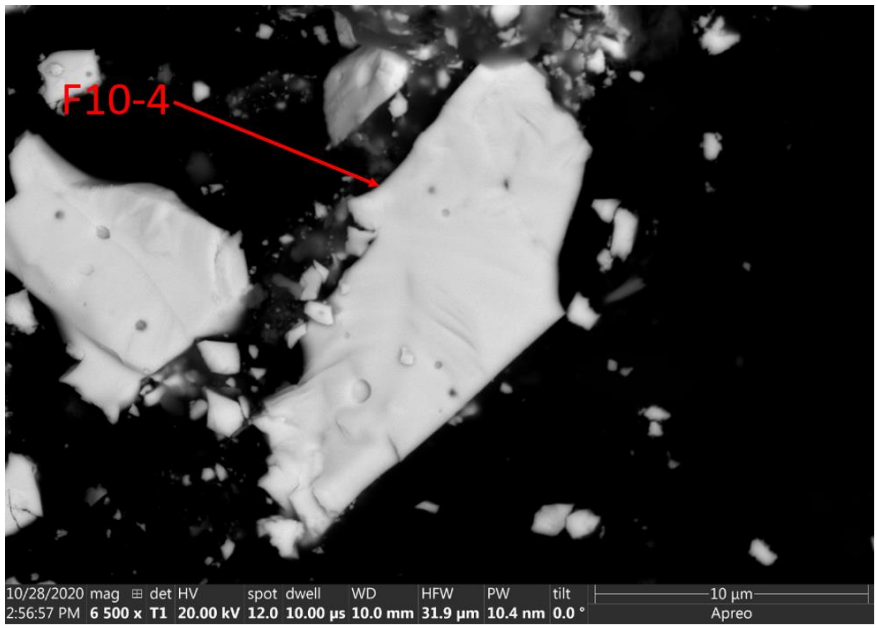

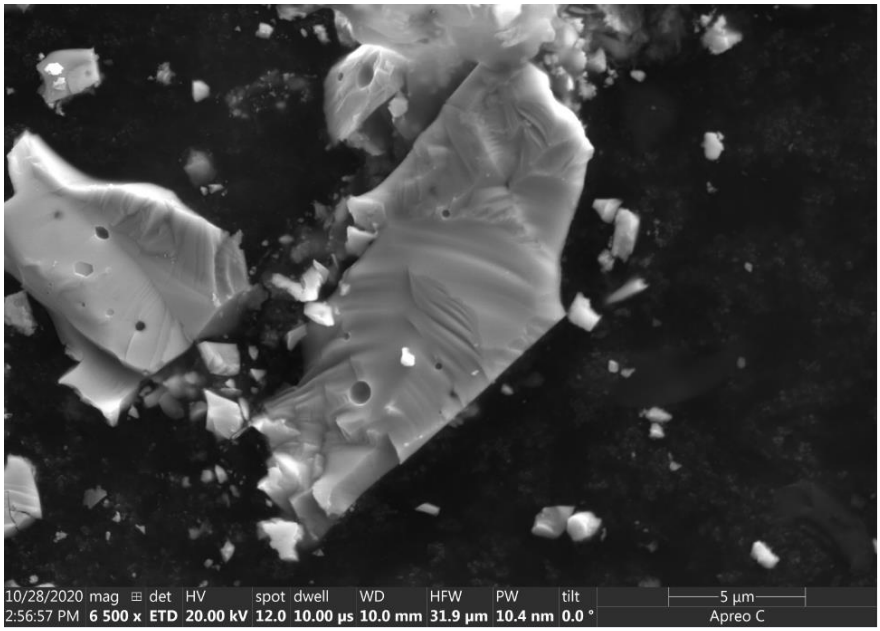

Figure 43. Particle F10-4 SEM Images

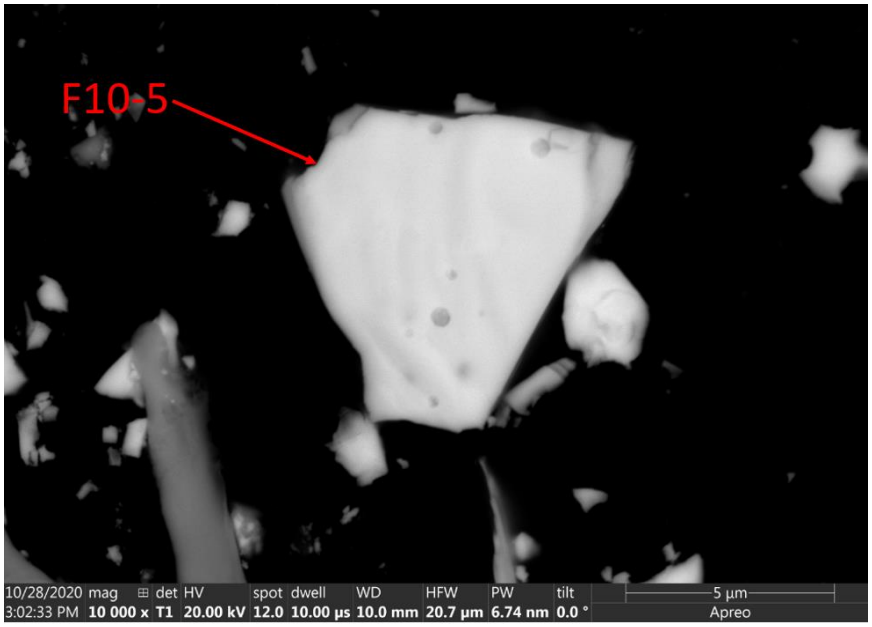

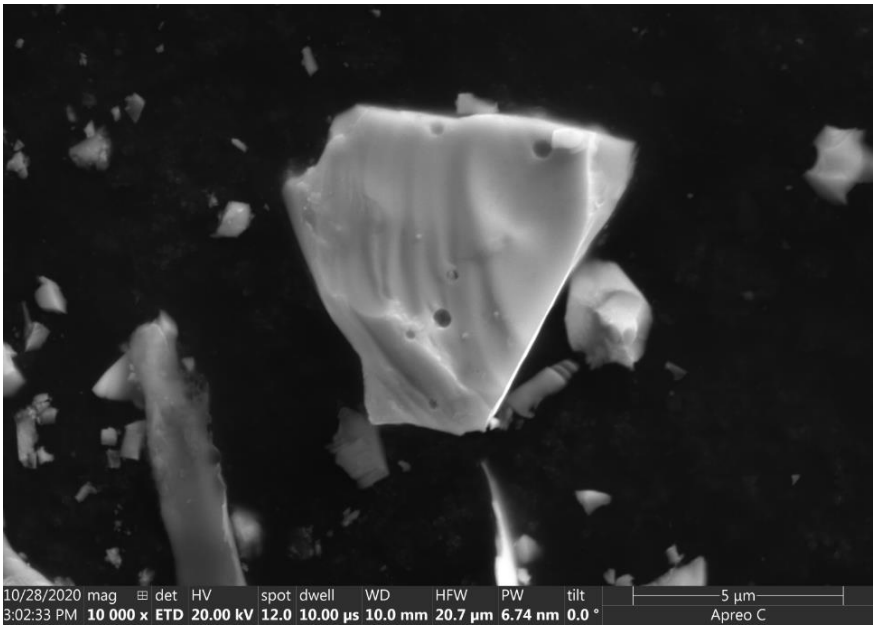

Figure 44. Particle F10-5 SEM Images

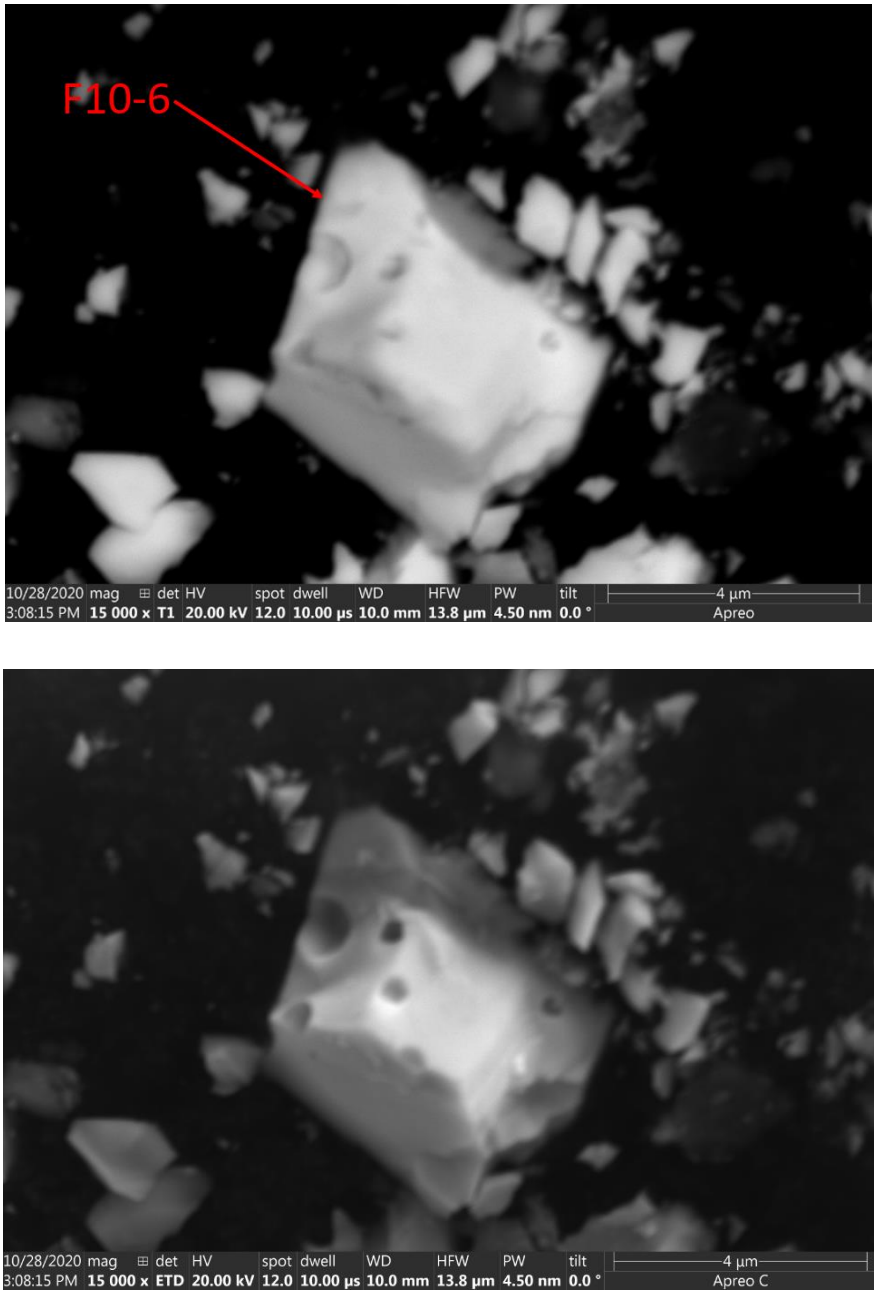

Figure 45. Particle F10-6 SEM Images

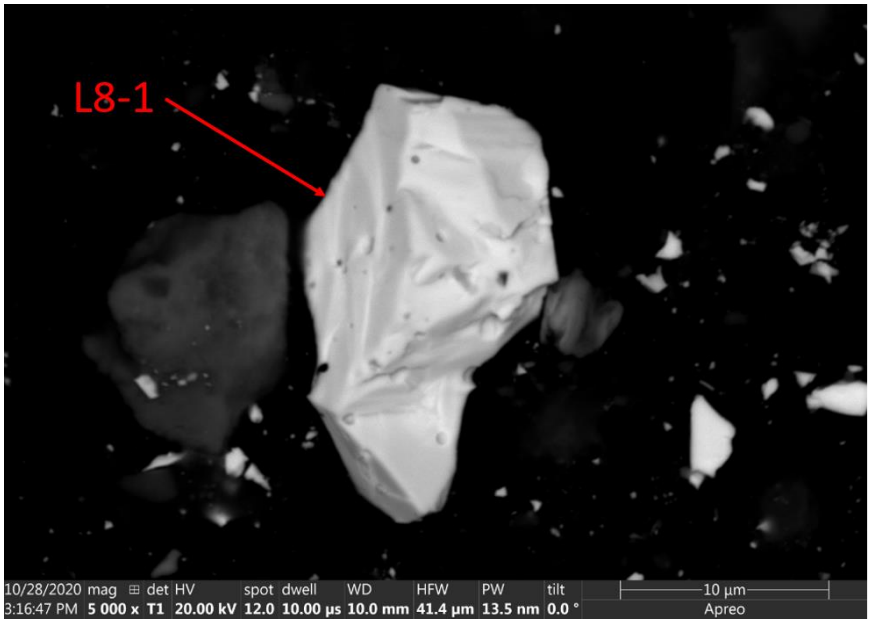

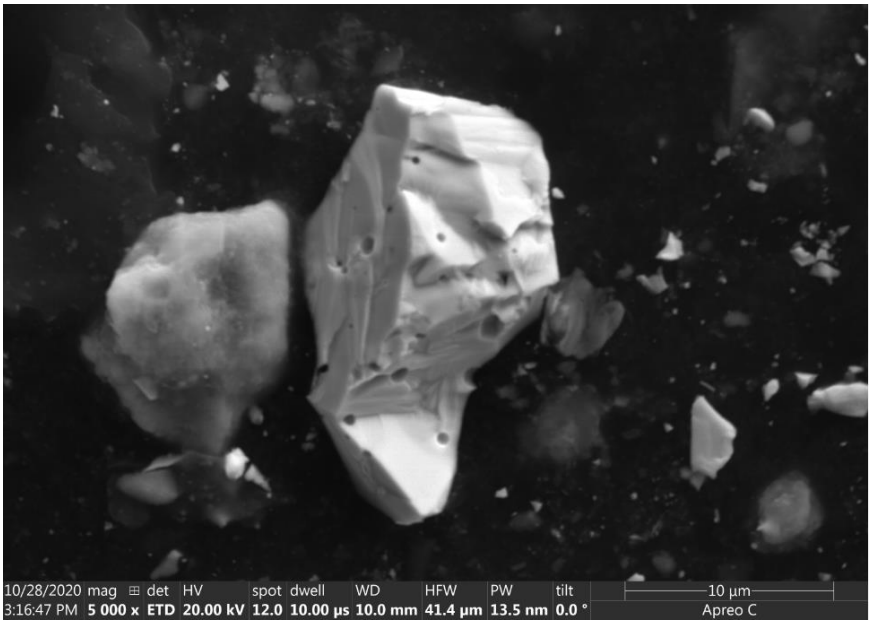

Figure 46. Particle L8-1 SEM Images

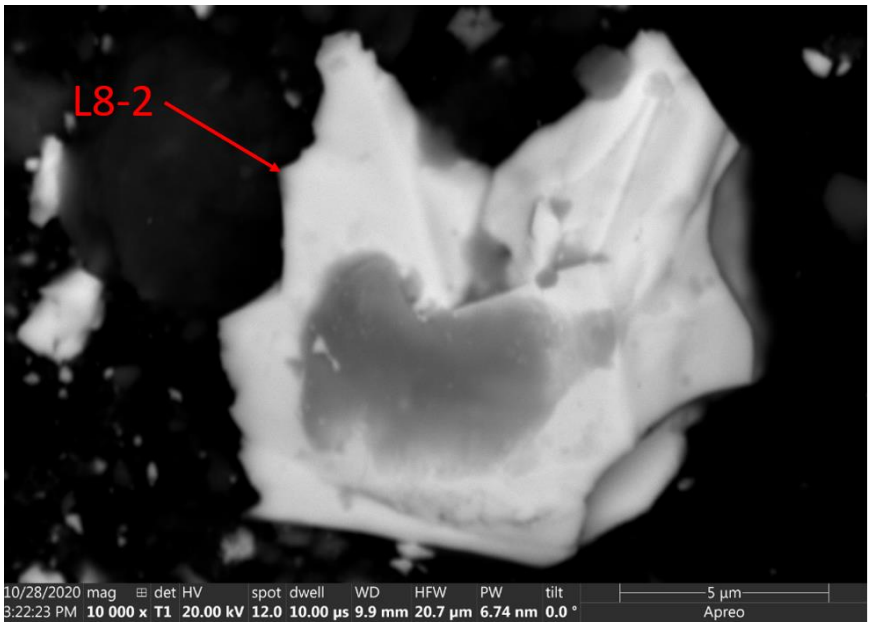

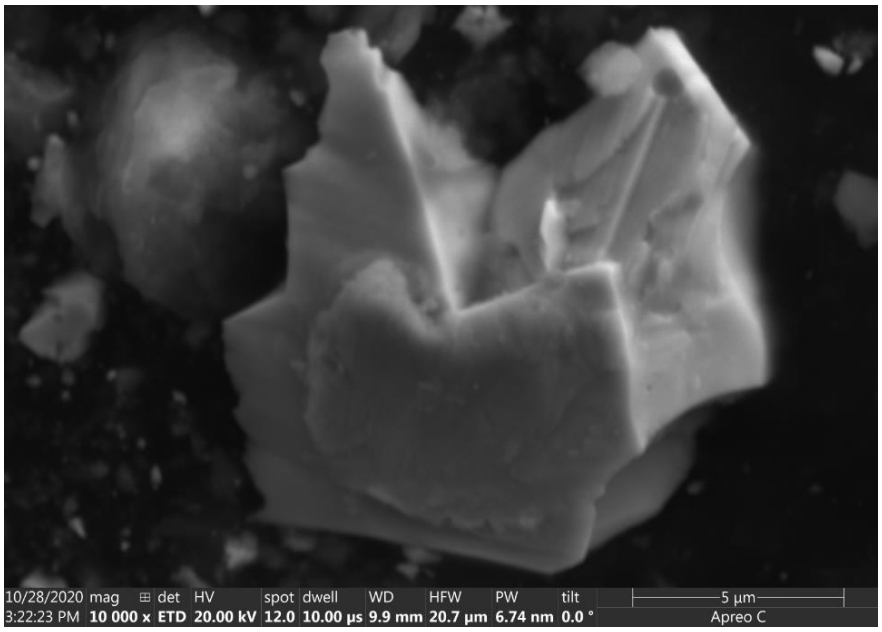

Figure 47. Particle L8-2 SEM Images

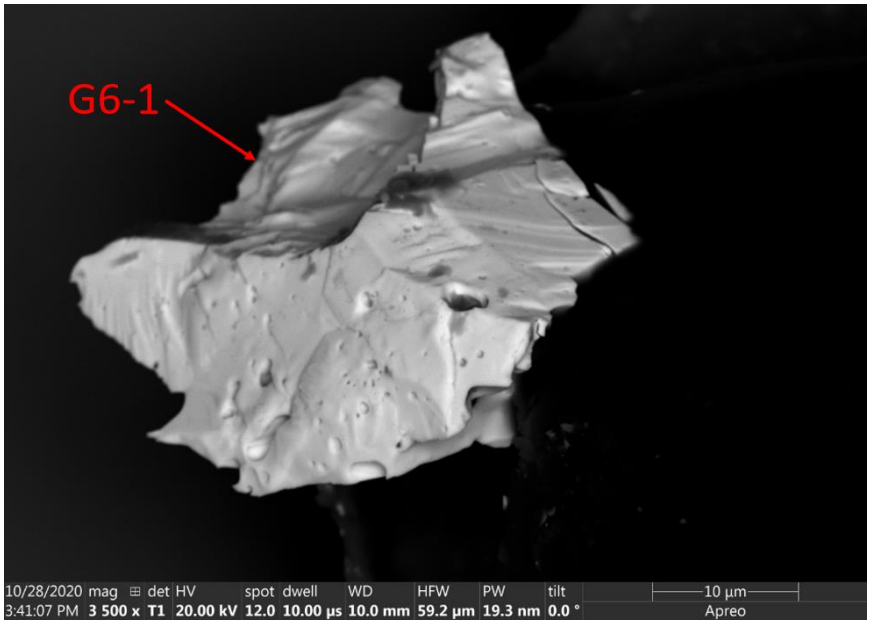

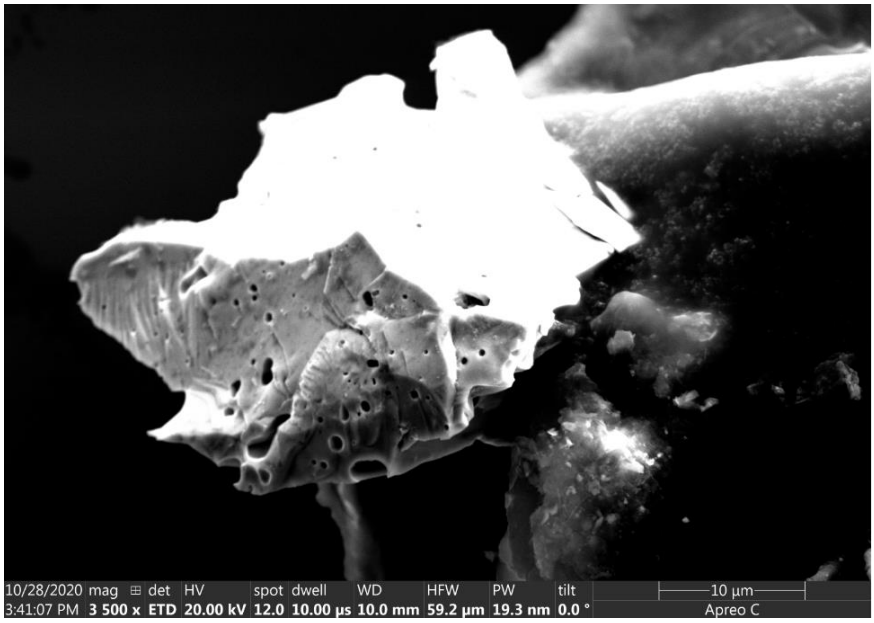

Figure 48. Particle G6-1 SEM Images

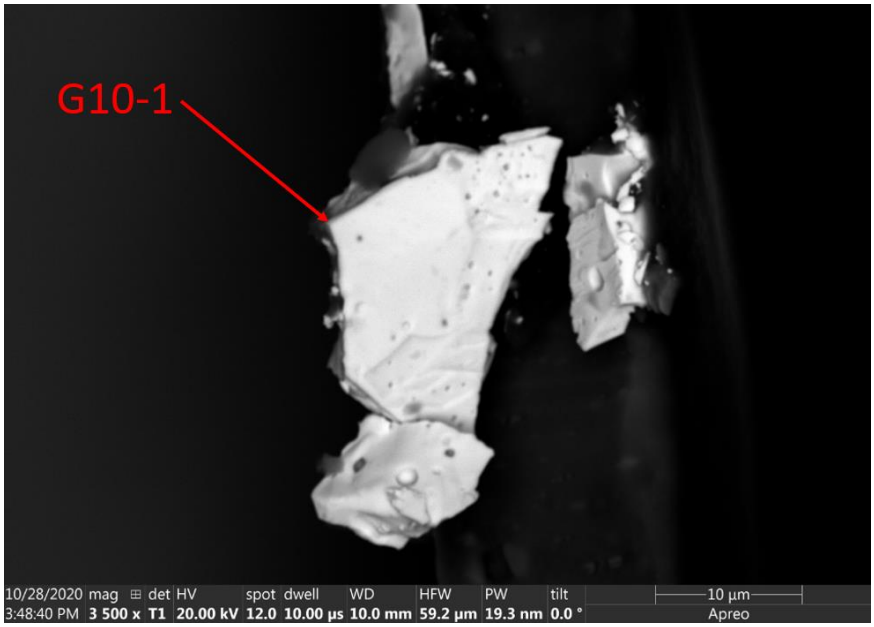

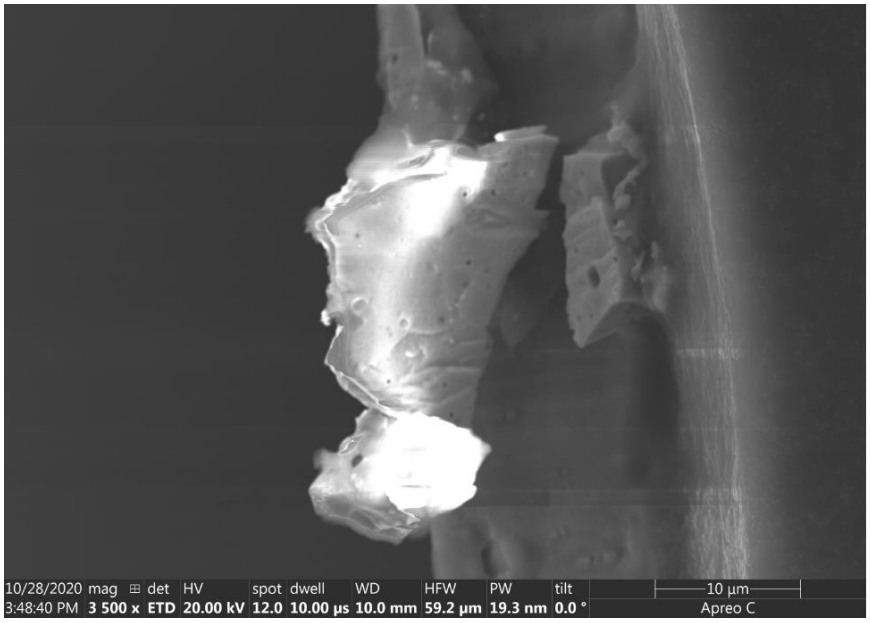

Figure 49. Particle G10-1 SEM Images

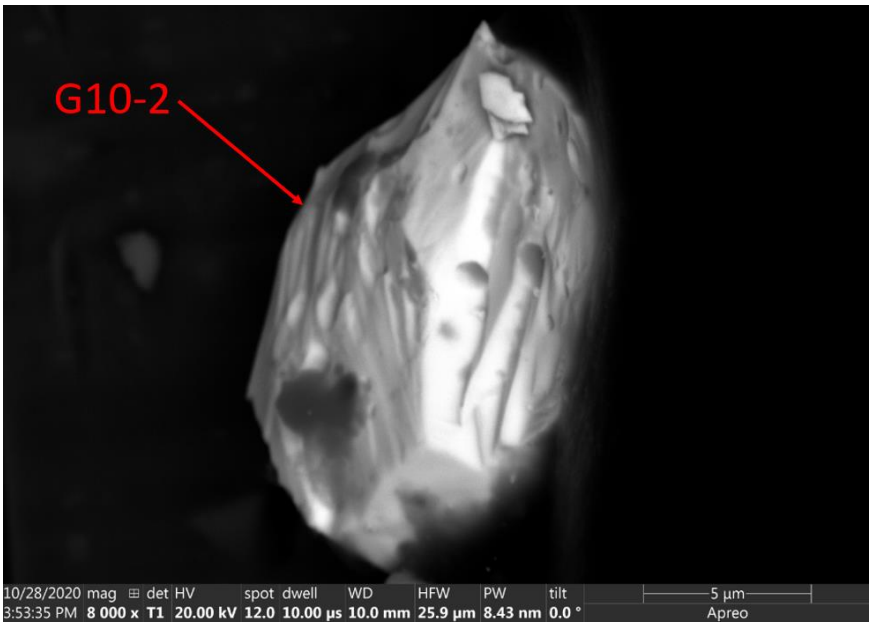

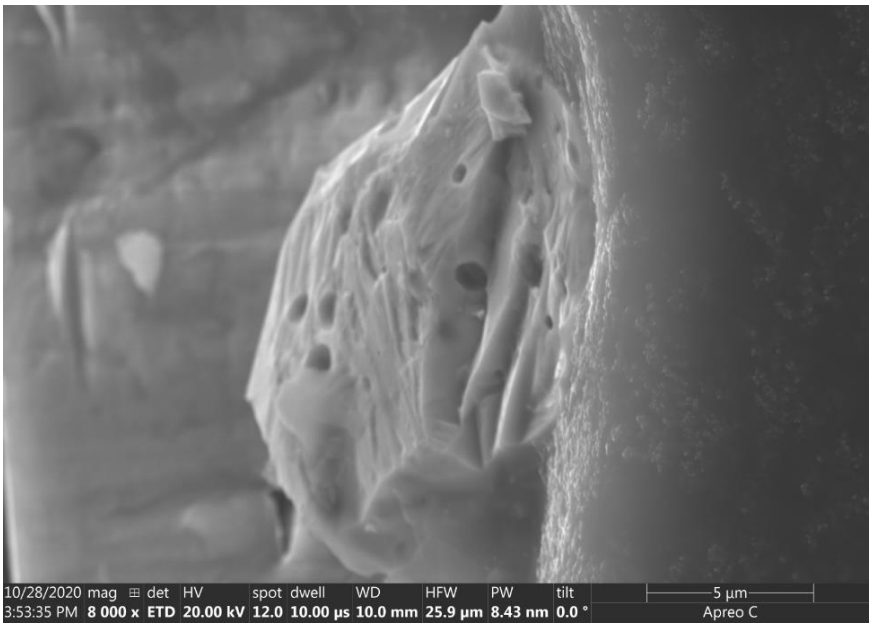

Figure 50. Particle G10-2 SEM Images

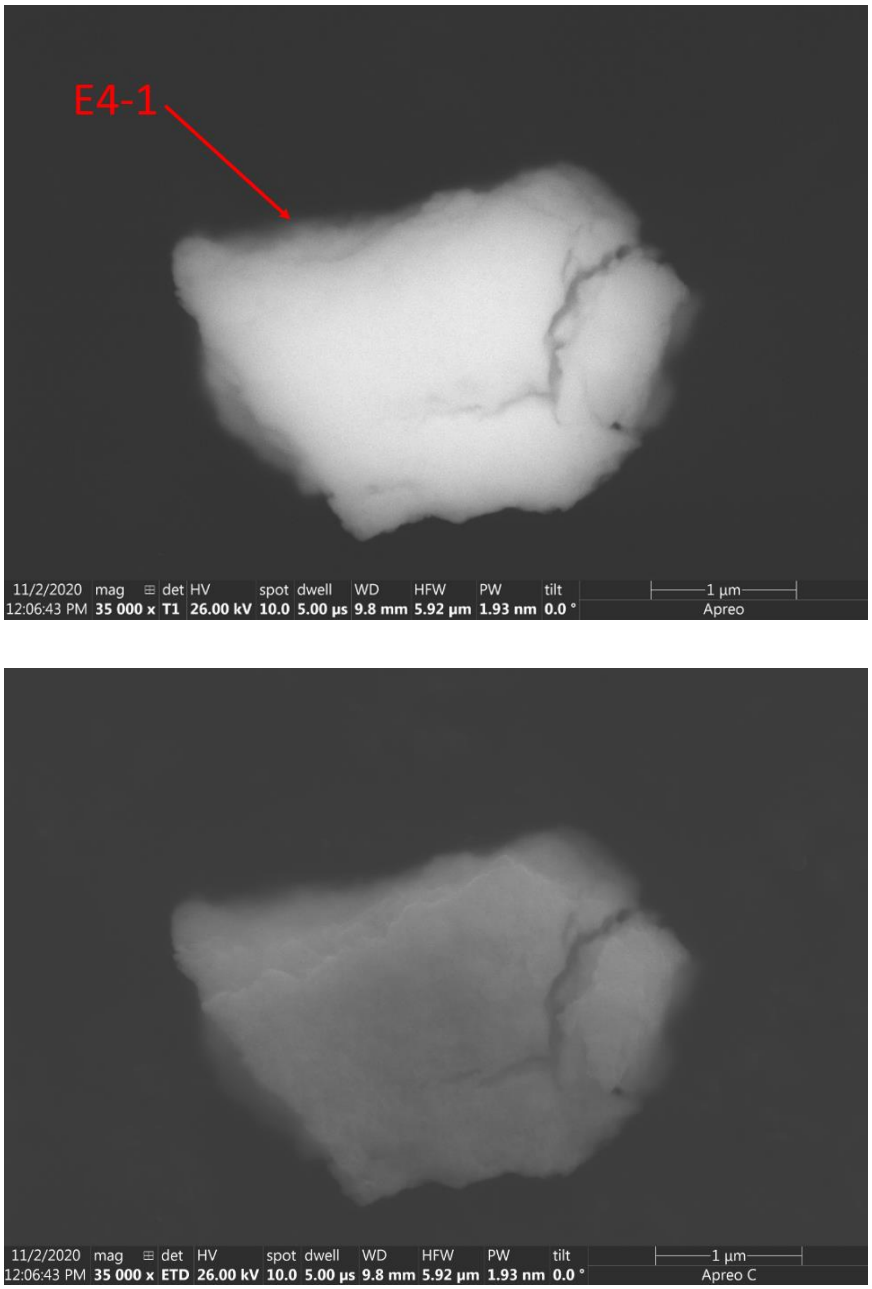

Figure 51. Particle E4-1 SEM Images

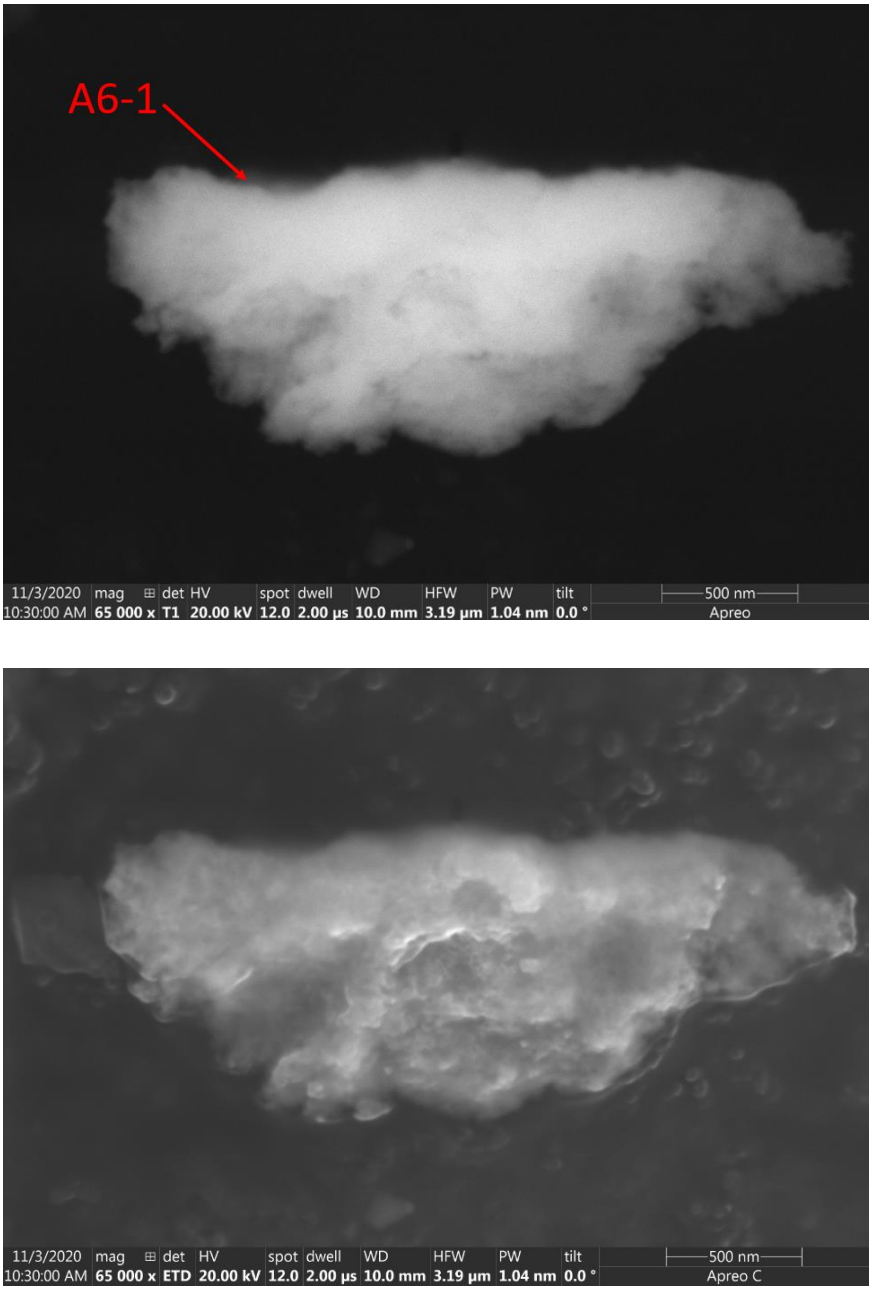

Figure 52. Particle A6-1 SEM Images

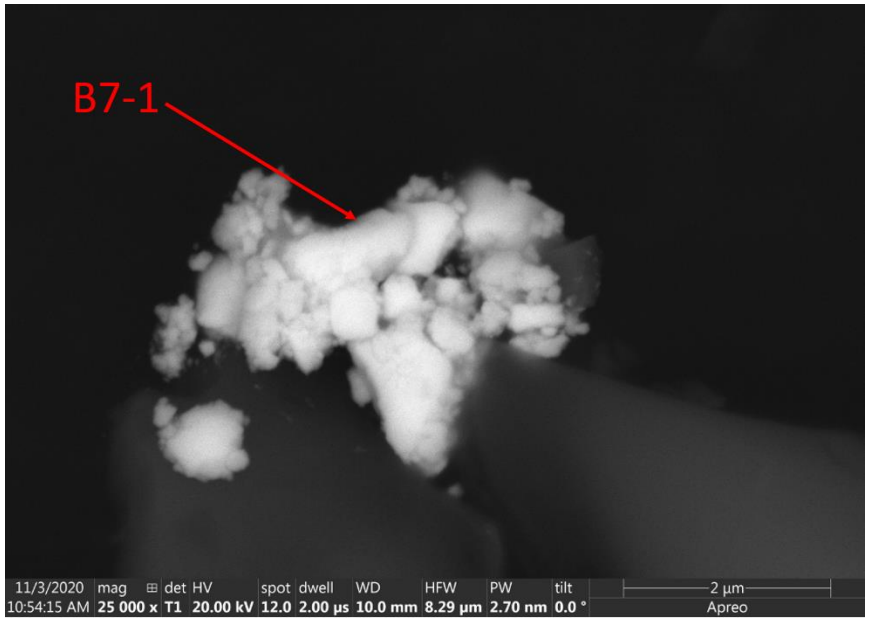

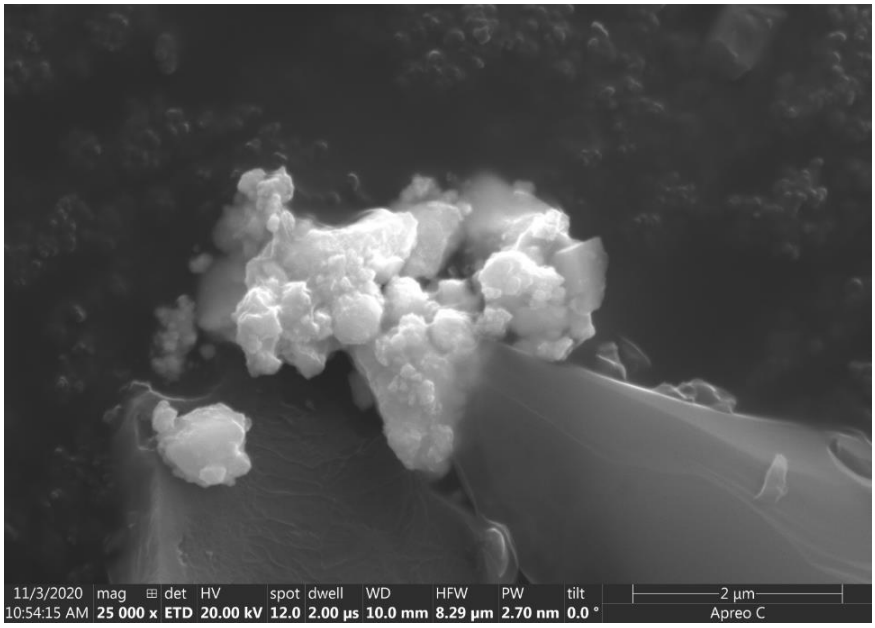

Figure 53. Particle B7-1 SEM Images

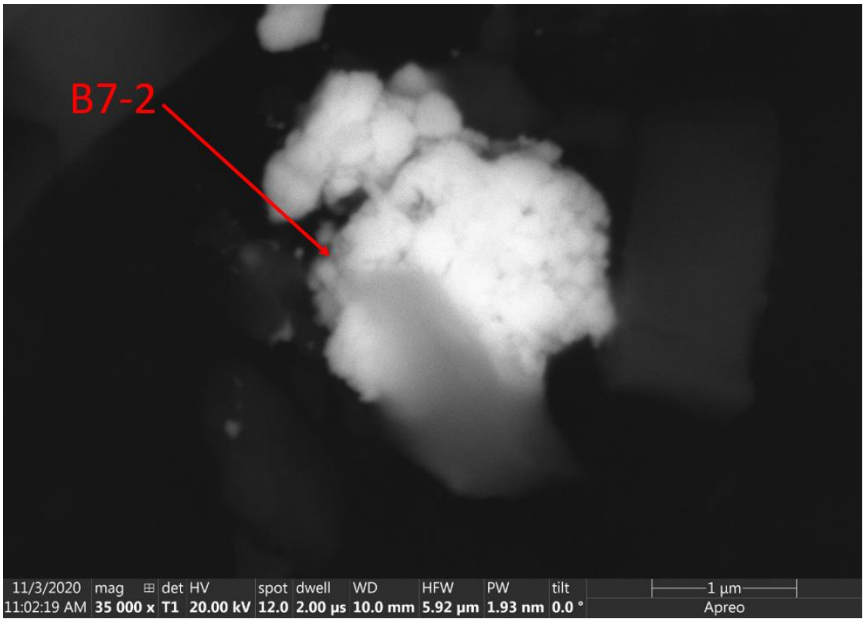

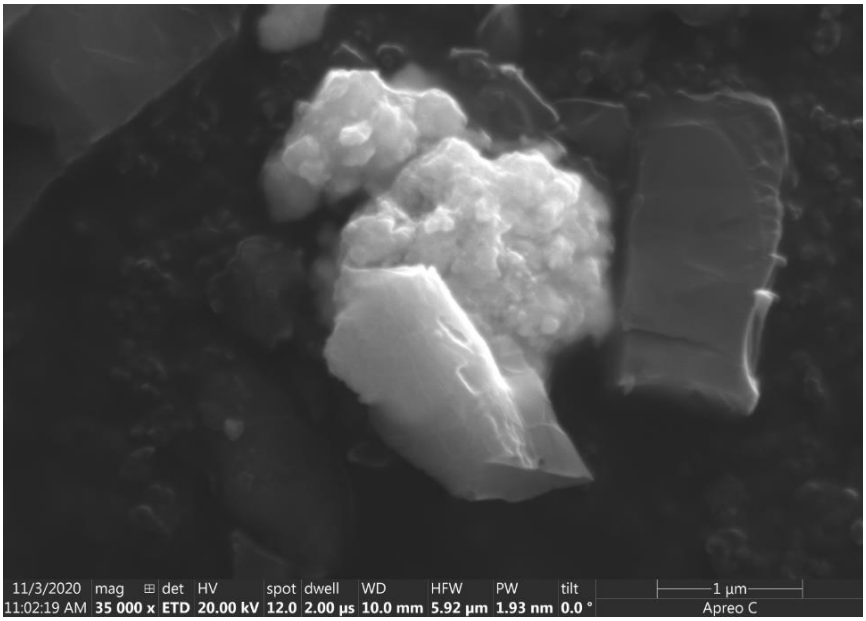

Figure 54. Particle B7-2 SEM Images

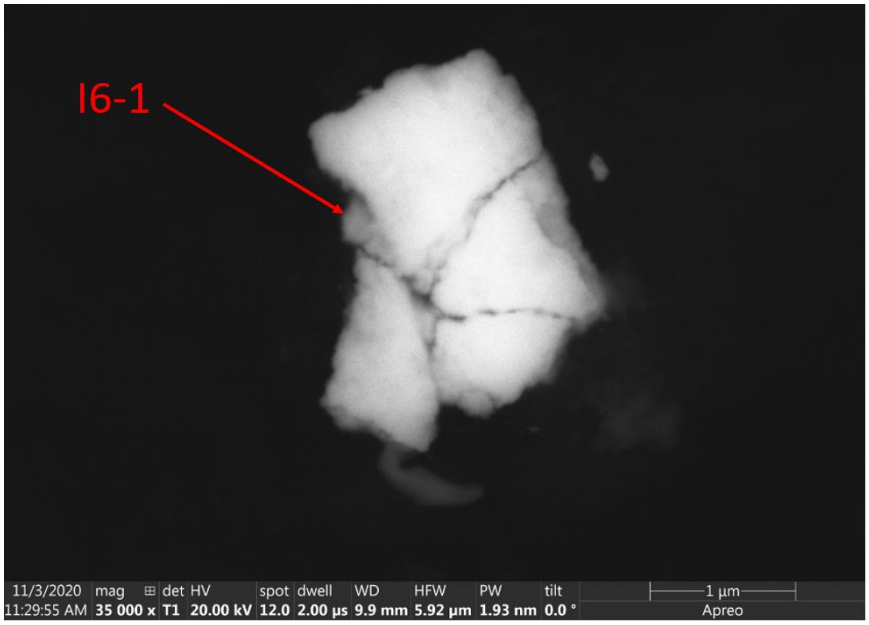

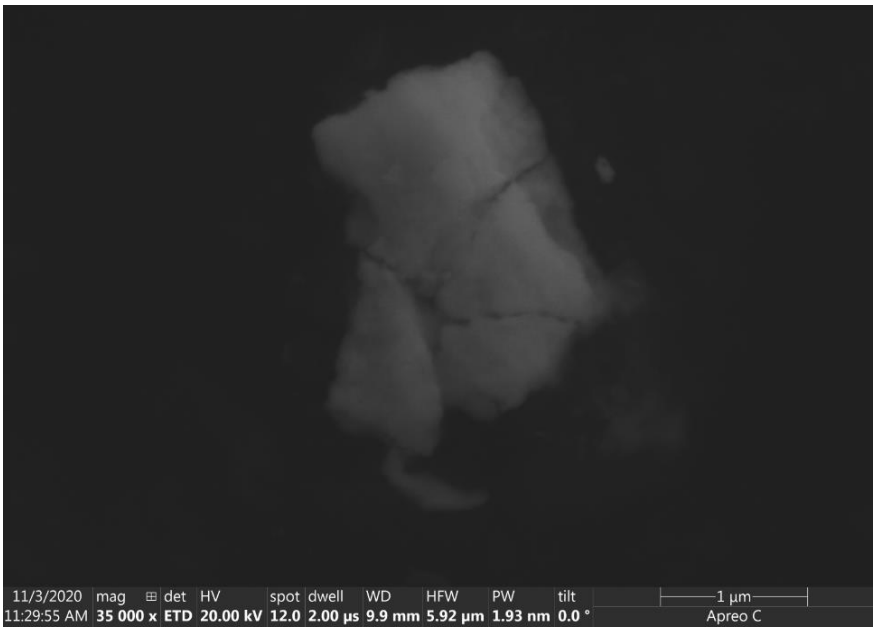

Figure 55. Particle I6-1 SEM Images

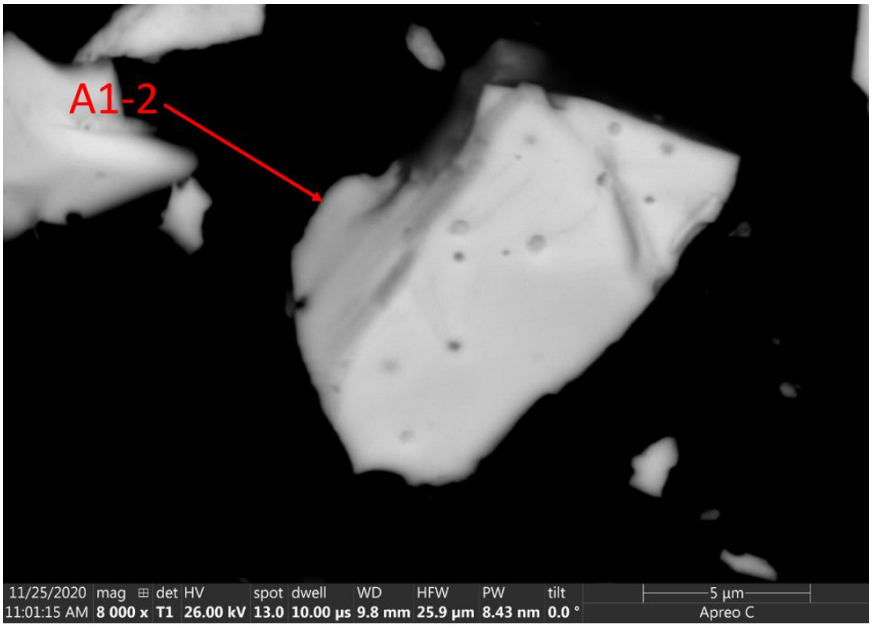

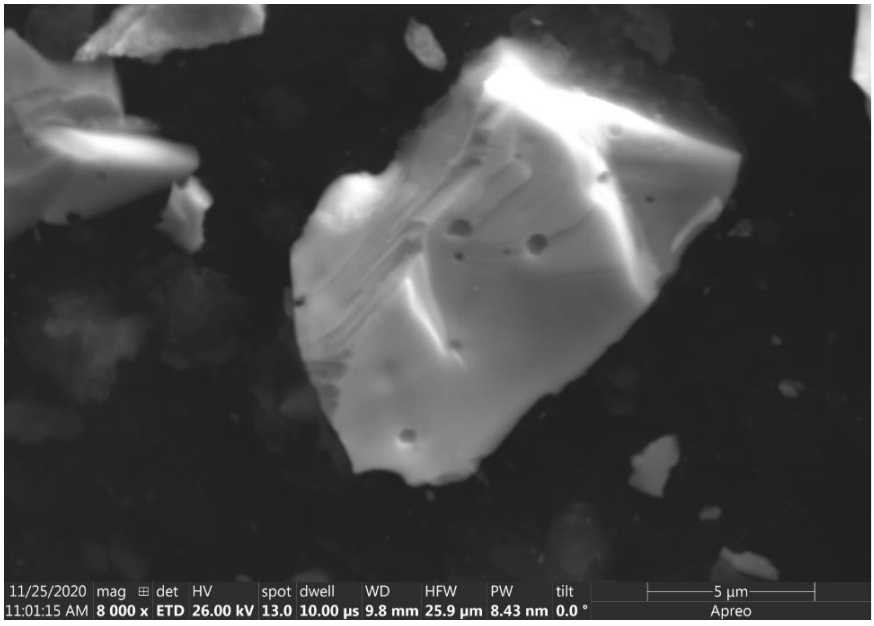

Figure 56. Particle A1-2 SEM Images

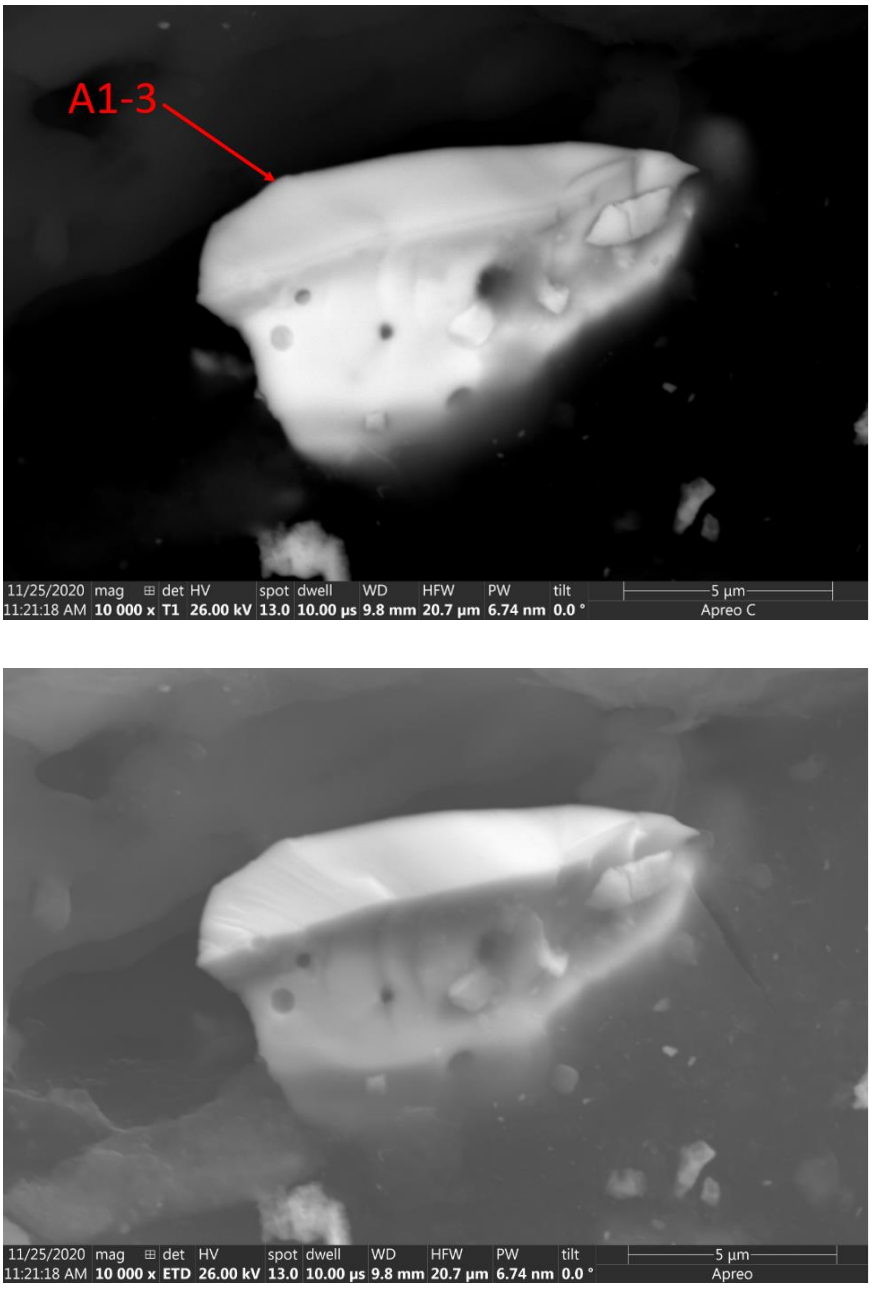

Figure 57. Particle A1-3 SEM Images

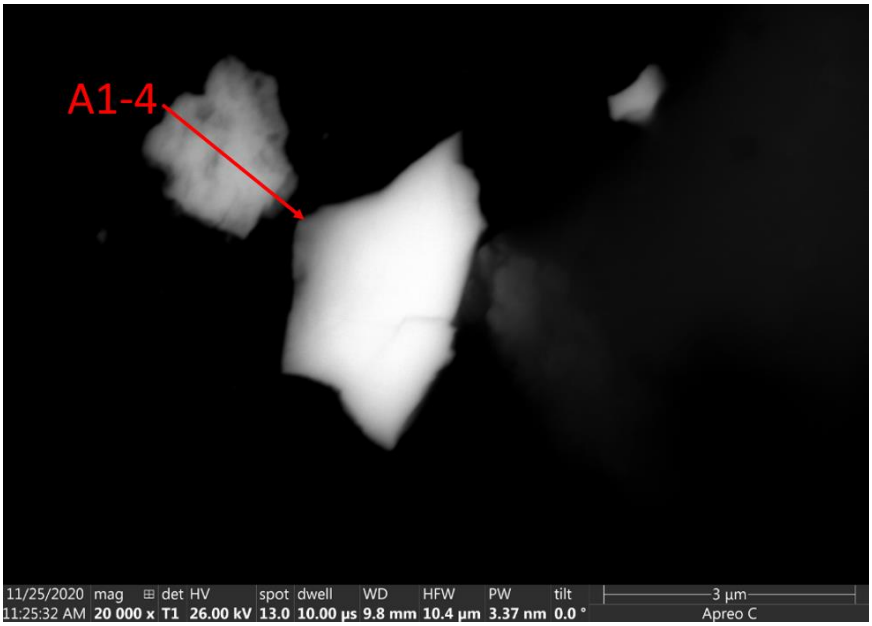

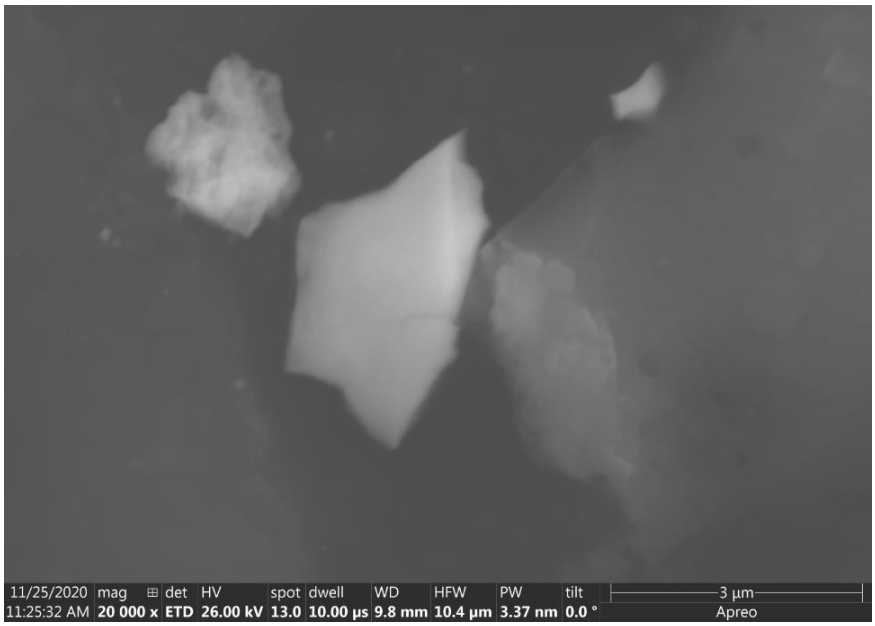

Figure 58. Particle A1-4 SEM Images

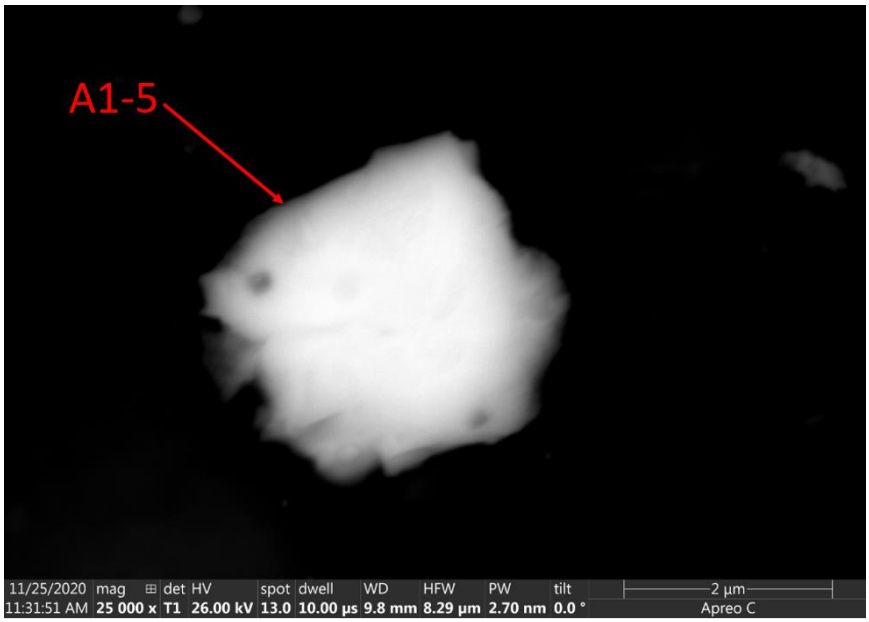

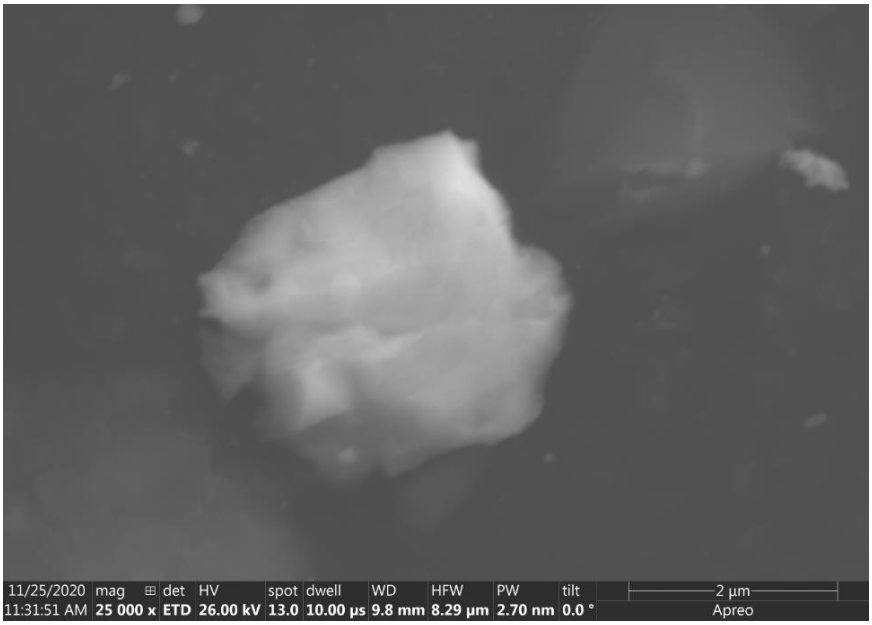

Figure 59. Particle A1-5 SEM Images

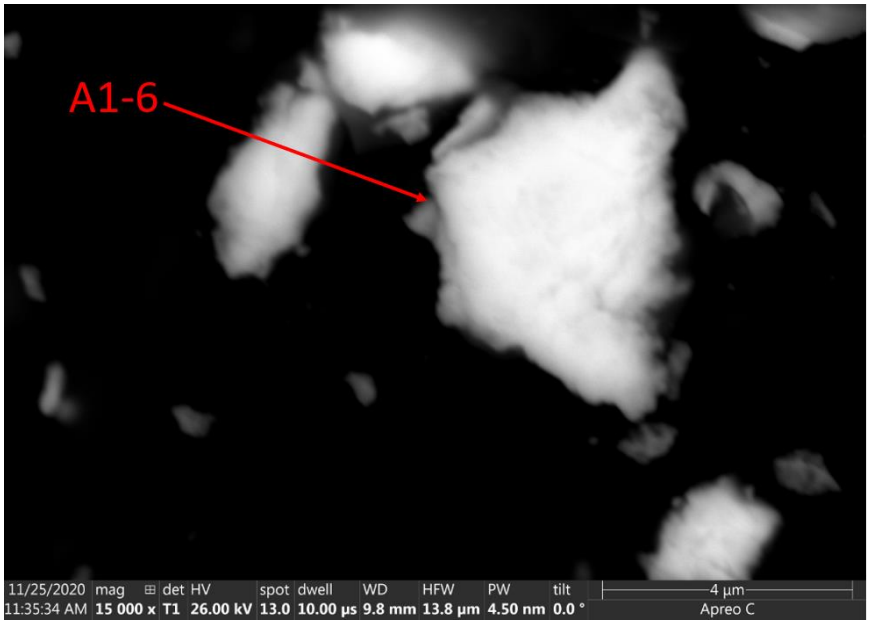

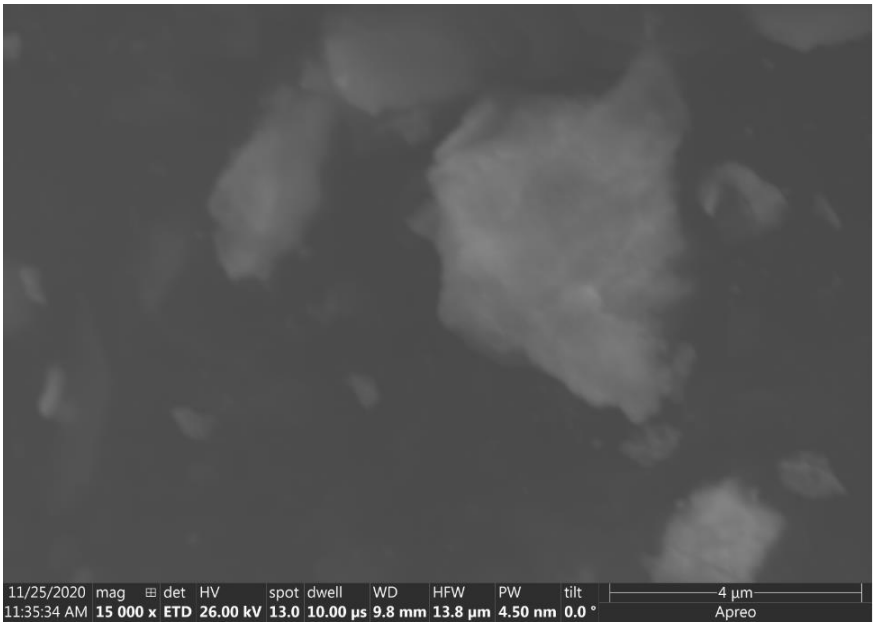

Figure 60. Particle A1-6 SEM Images

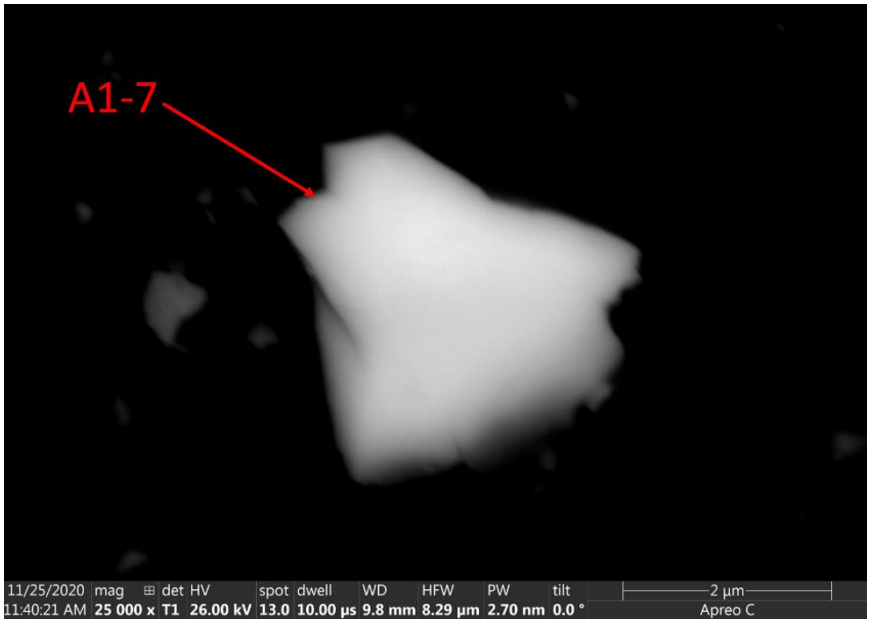

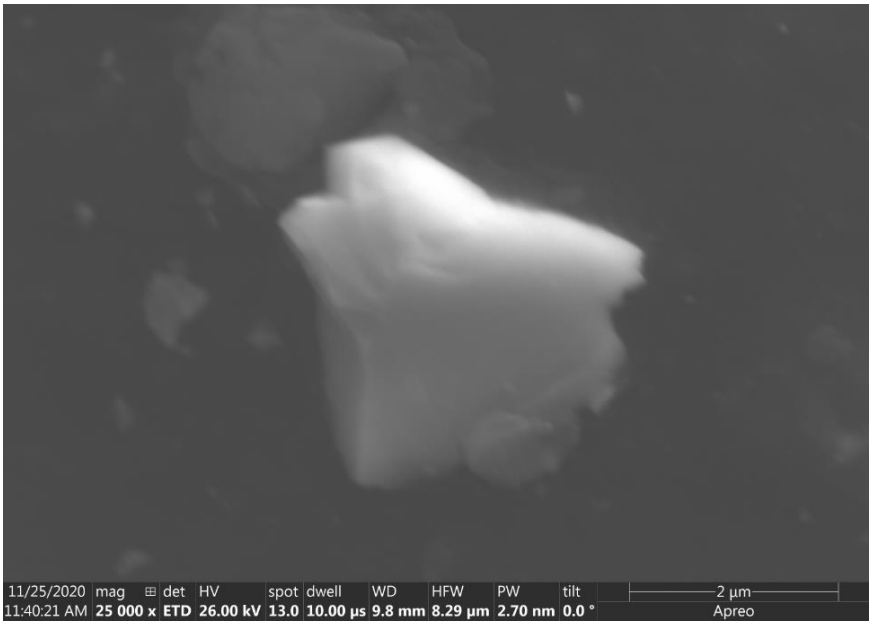

Figure 61. Particle A1-7 SEM Images

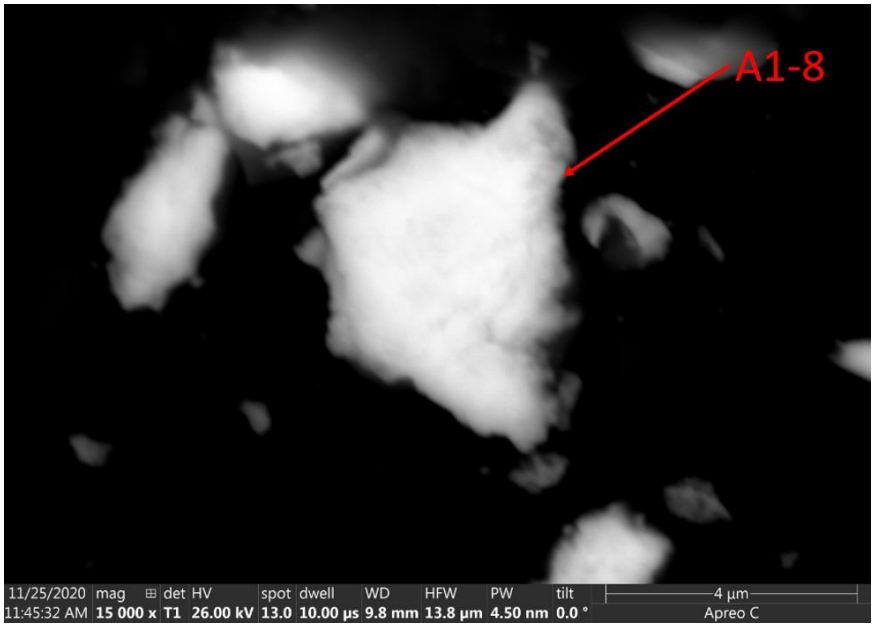

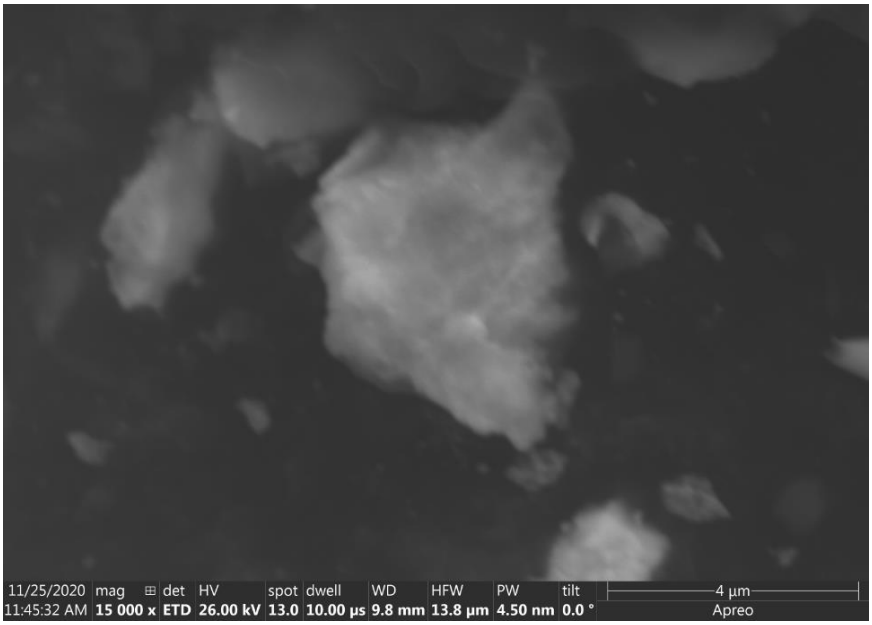

Figure 62. Particle A1-8 SEM Images

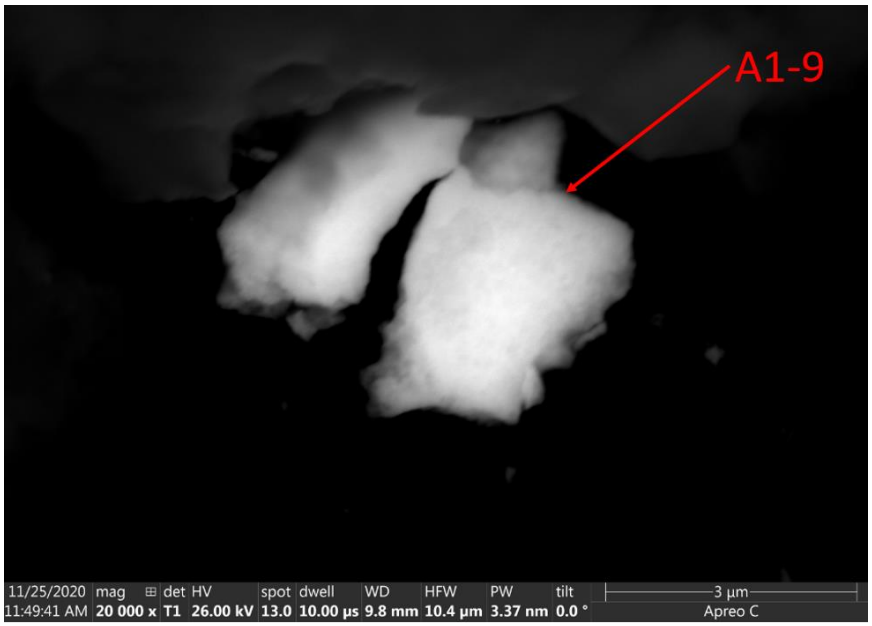

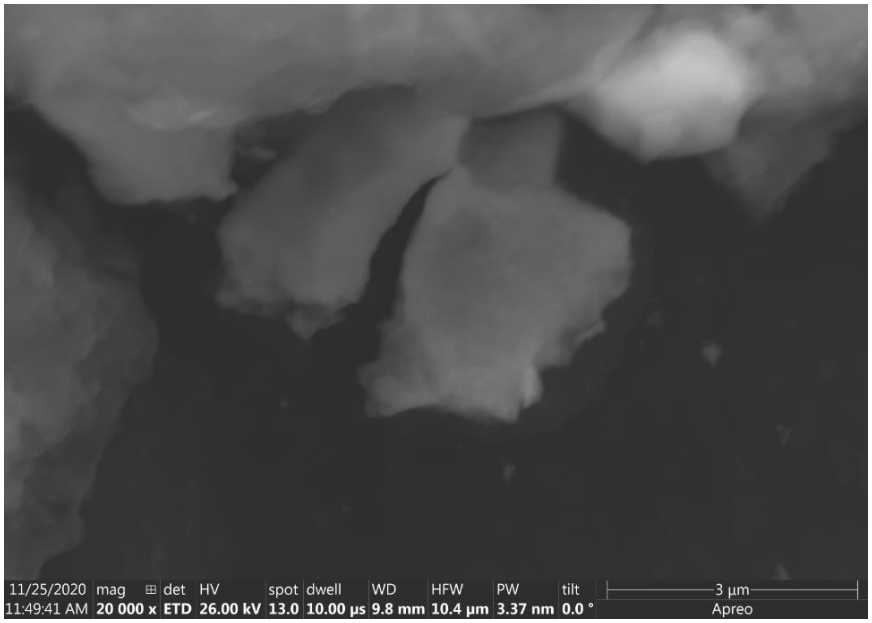

Figure 63. Particle A1-9 SEM Images

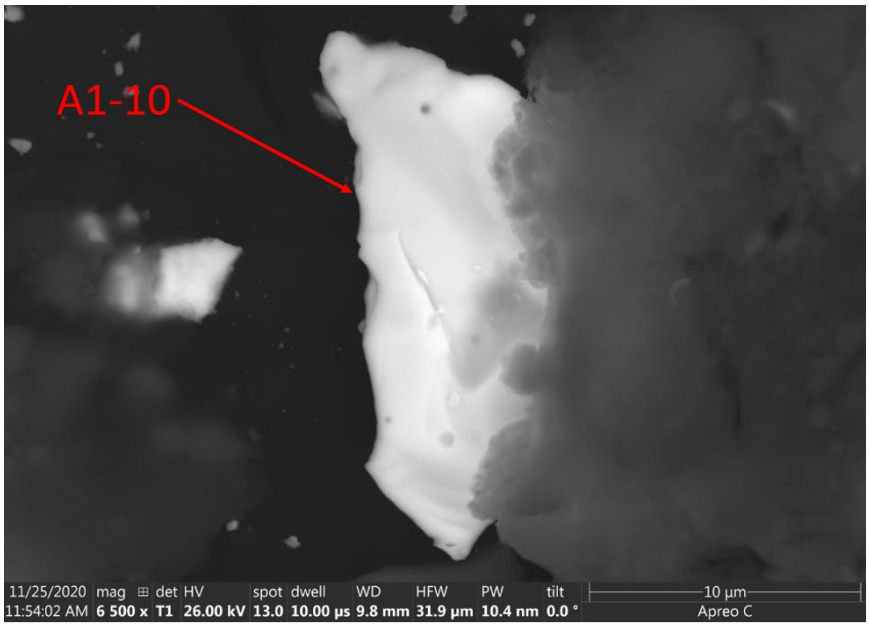

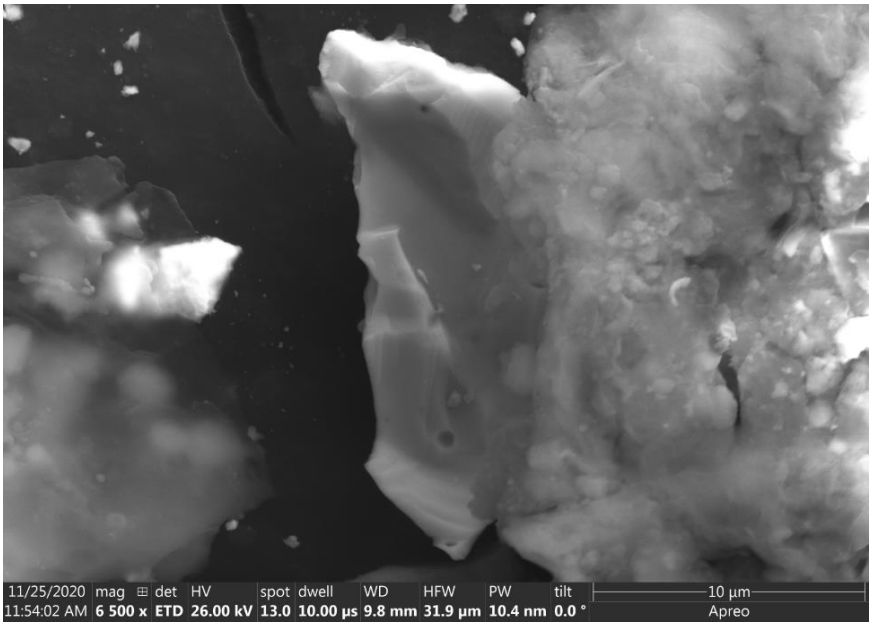

Figure 64. Particle A1-10 SEM Images

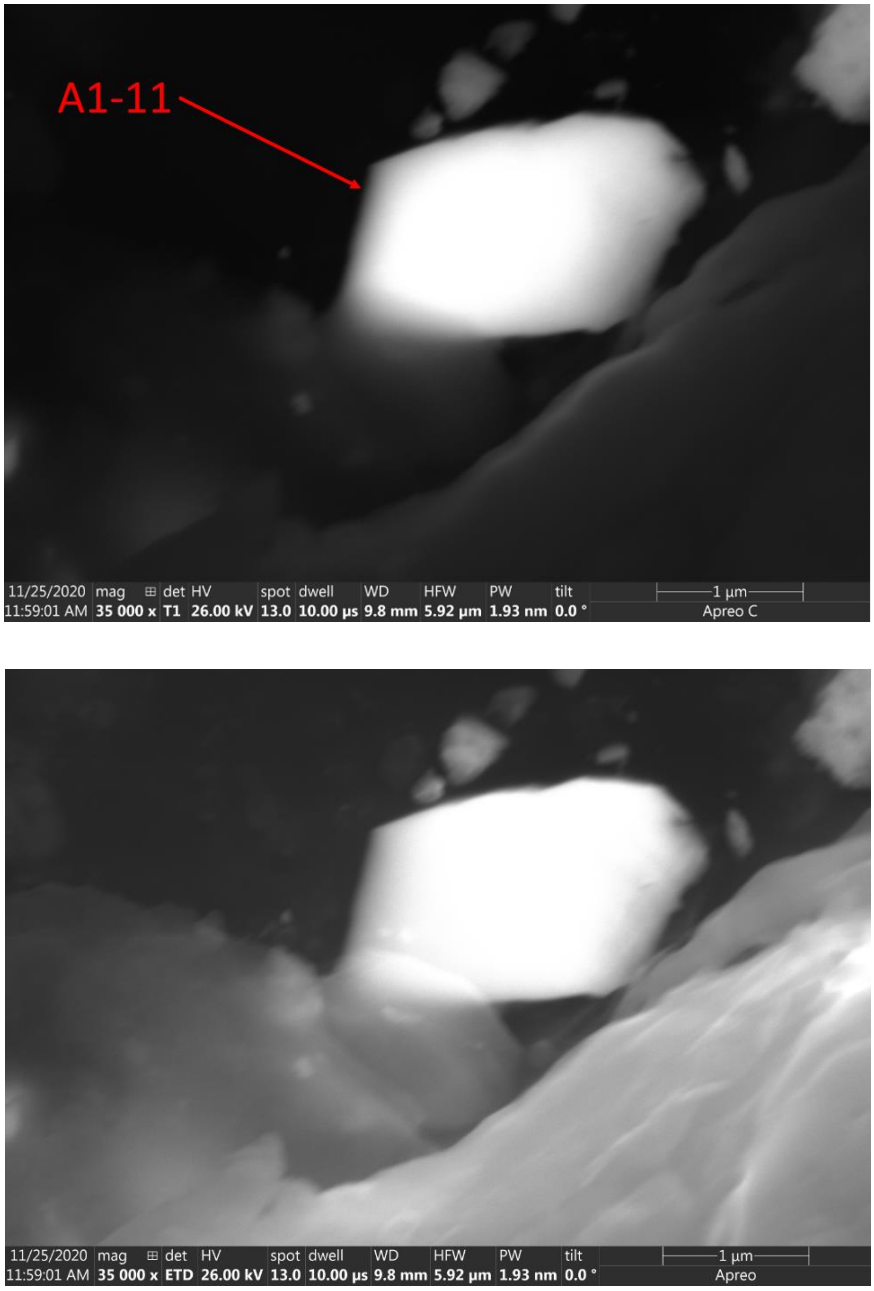

Figure 65. Particle A1-11 SEM Images

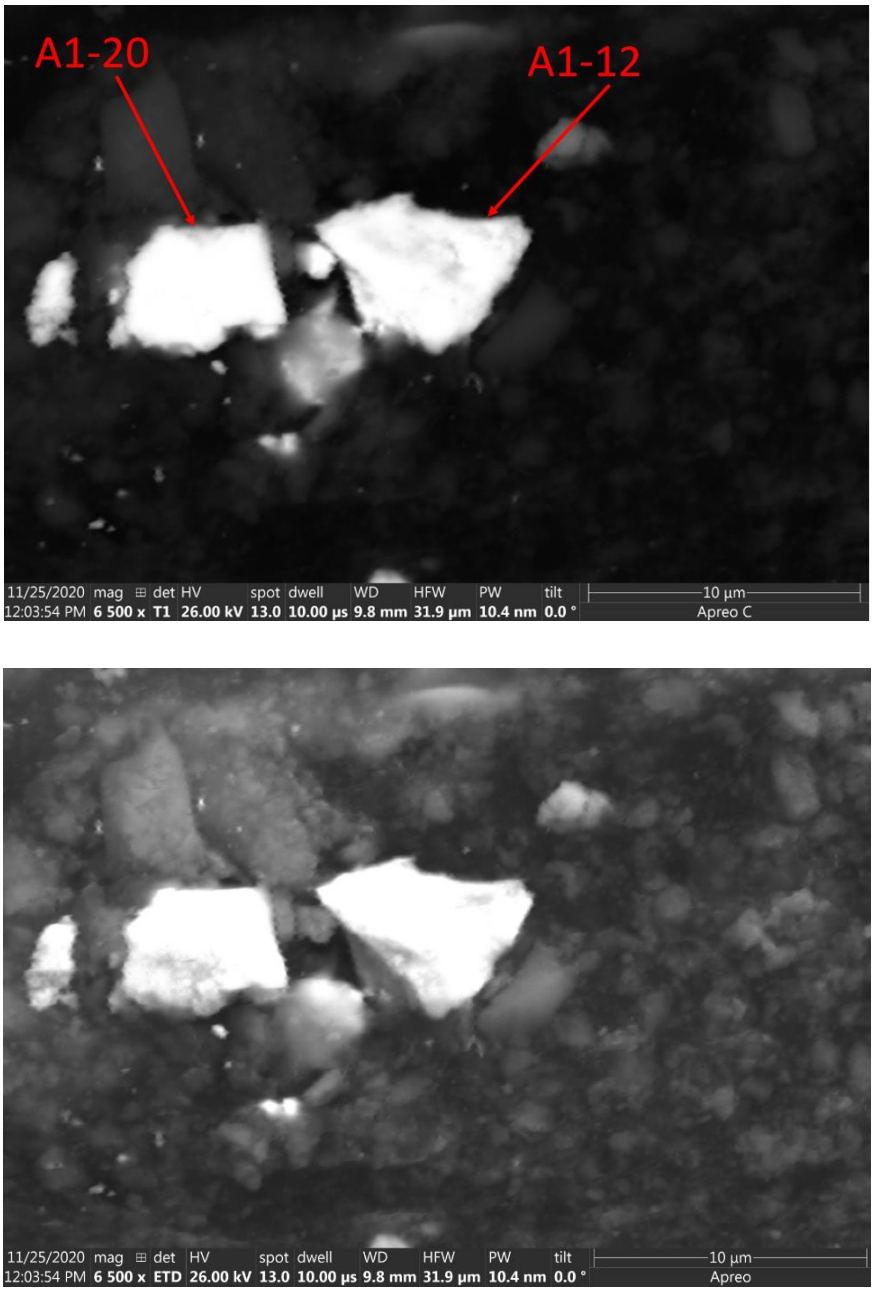

Figure 66. Particles A1-12 and A1-20 SEM Images

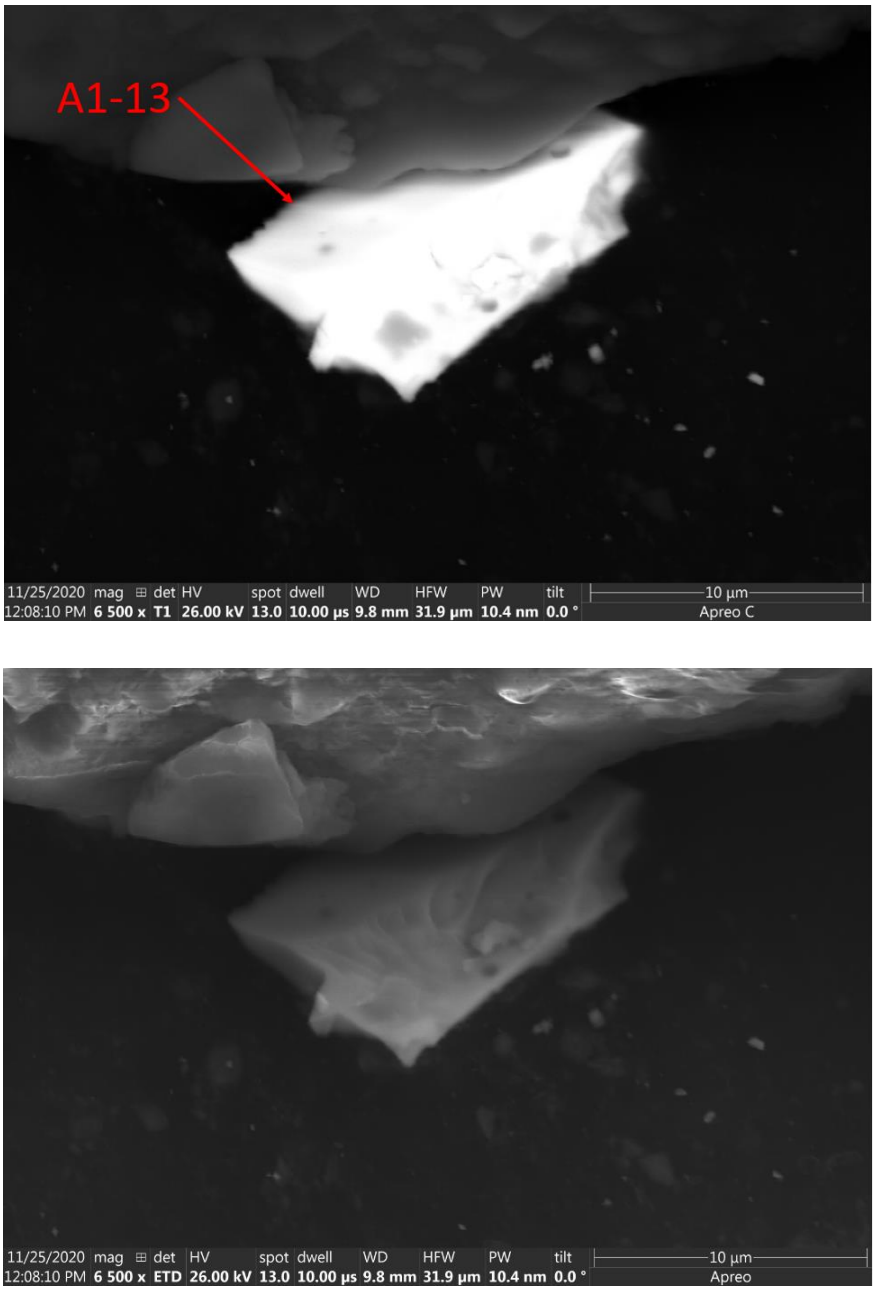

Figure 67. Particle A1-13 SE Image

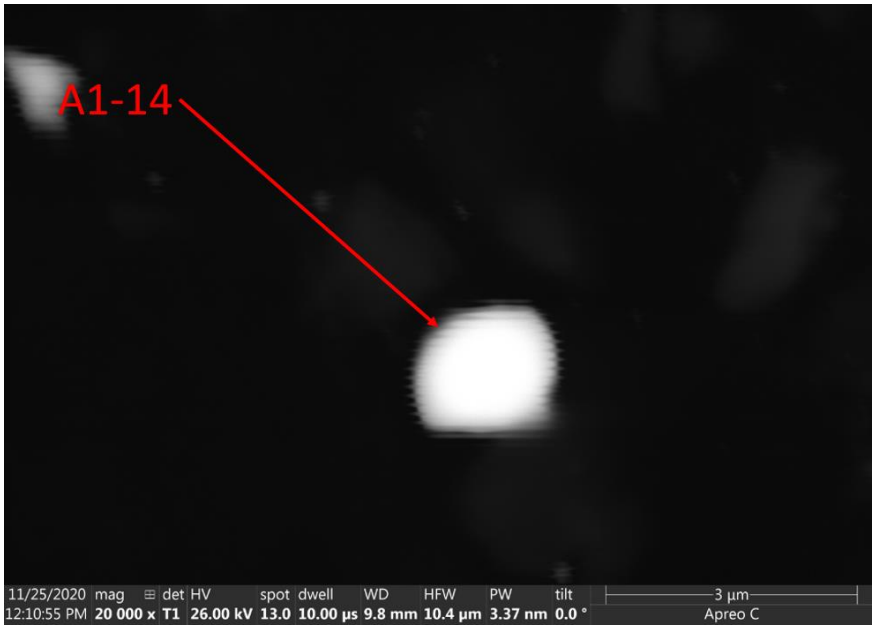

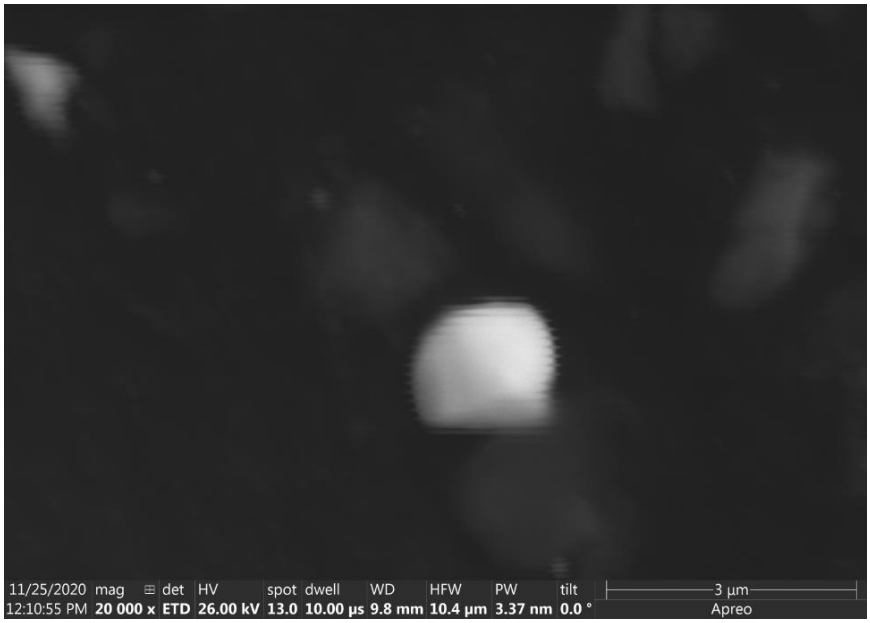

Figure 68. Particle A1-14 SEM Images

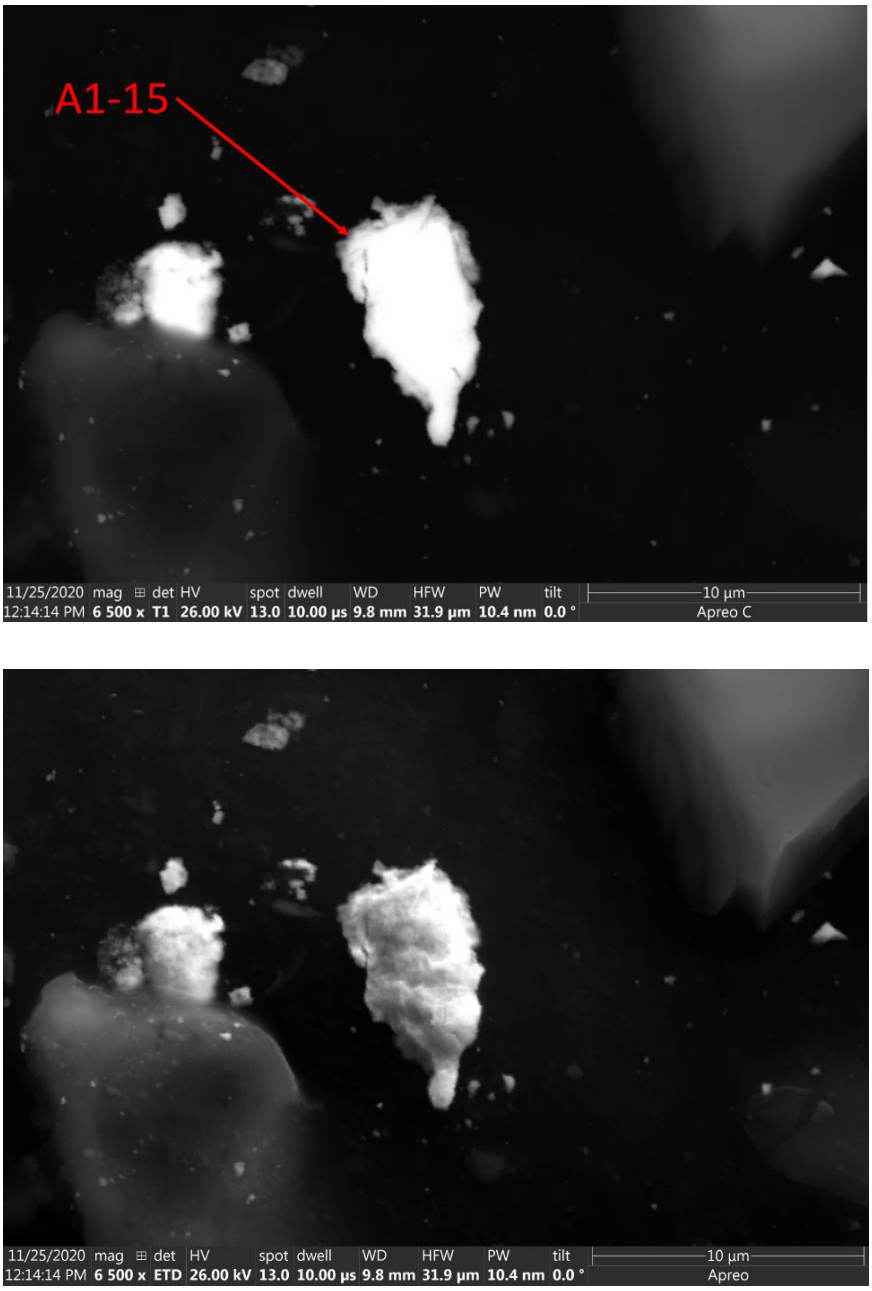

Figure 69. Particle A1-15 SEM Images

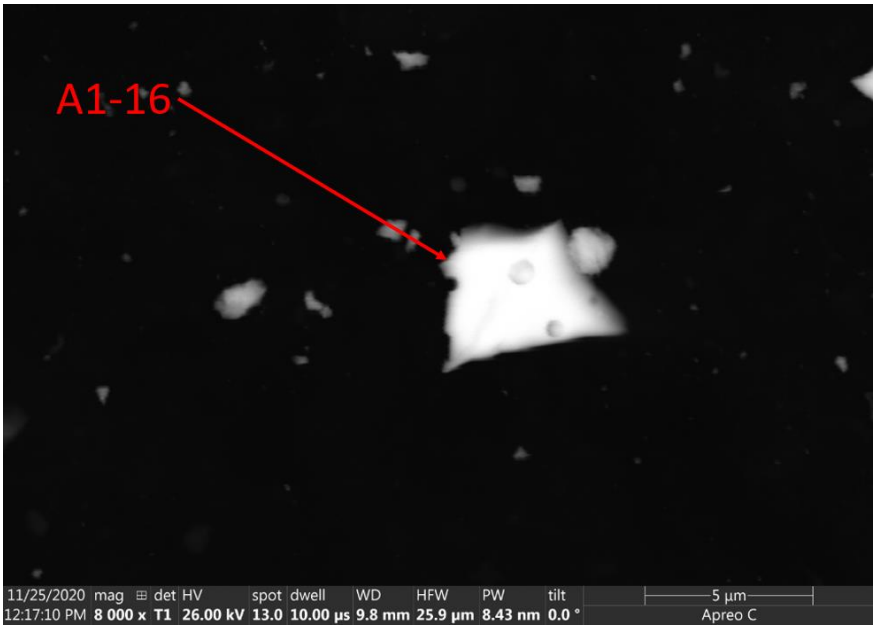

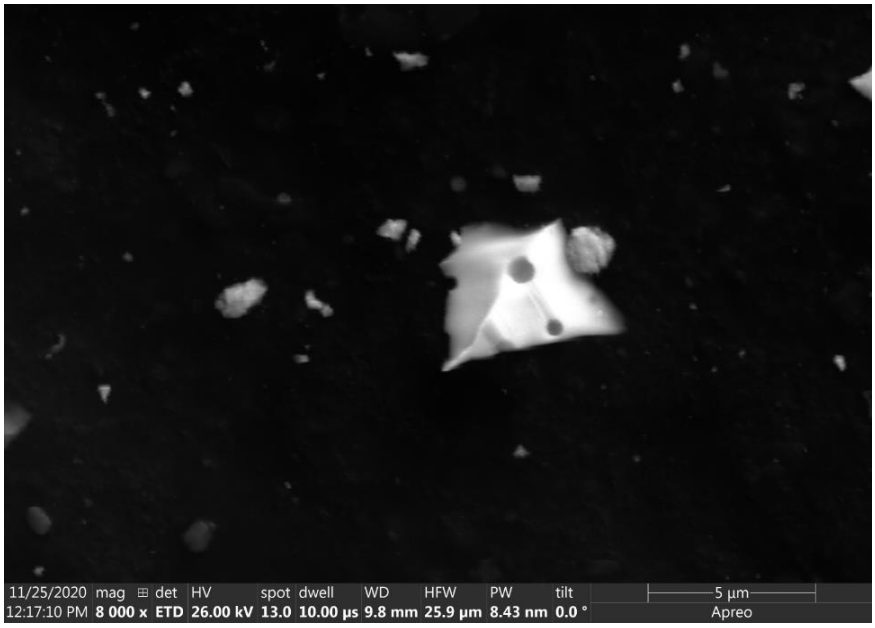

Figure 70. Particle A1-16 SEM Images

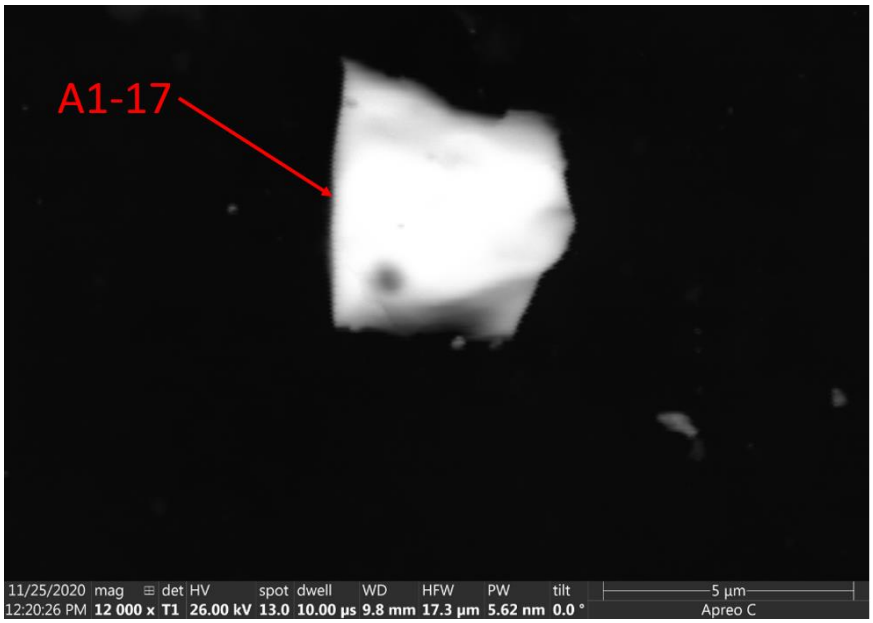

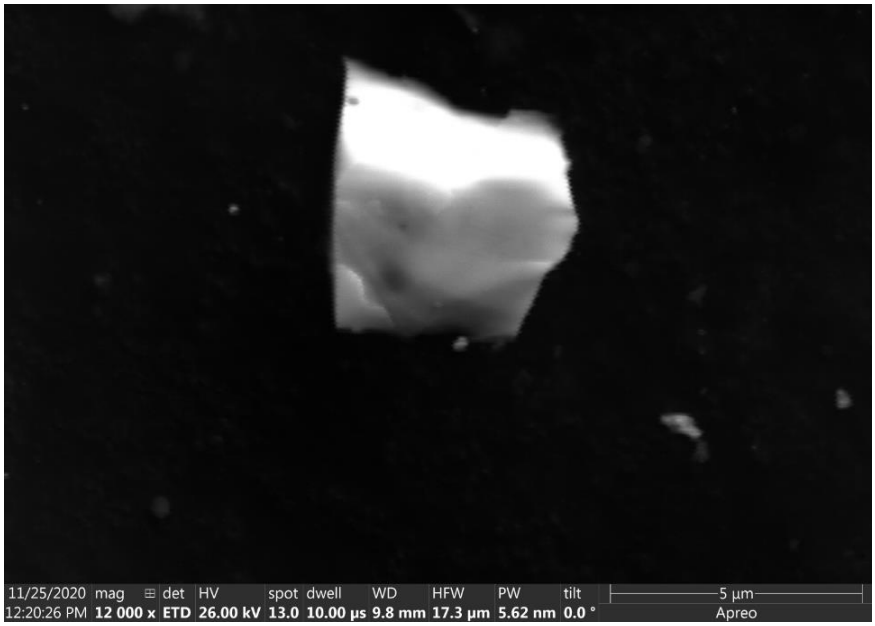

Figure 71. Particle A1-17 SEM Images

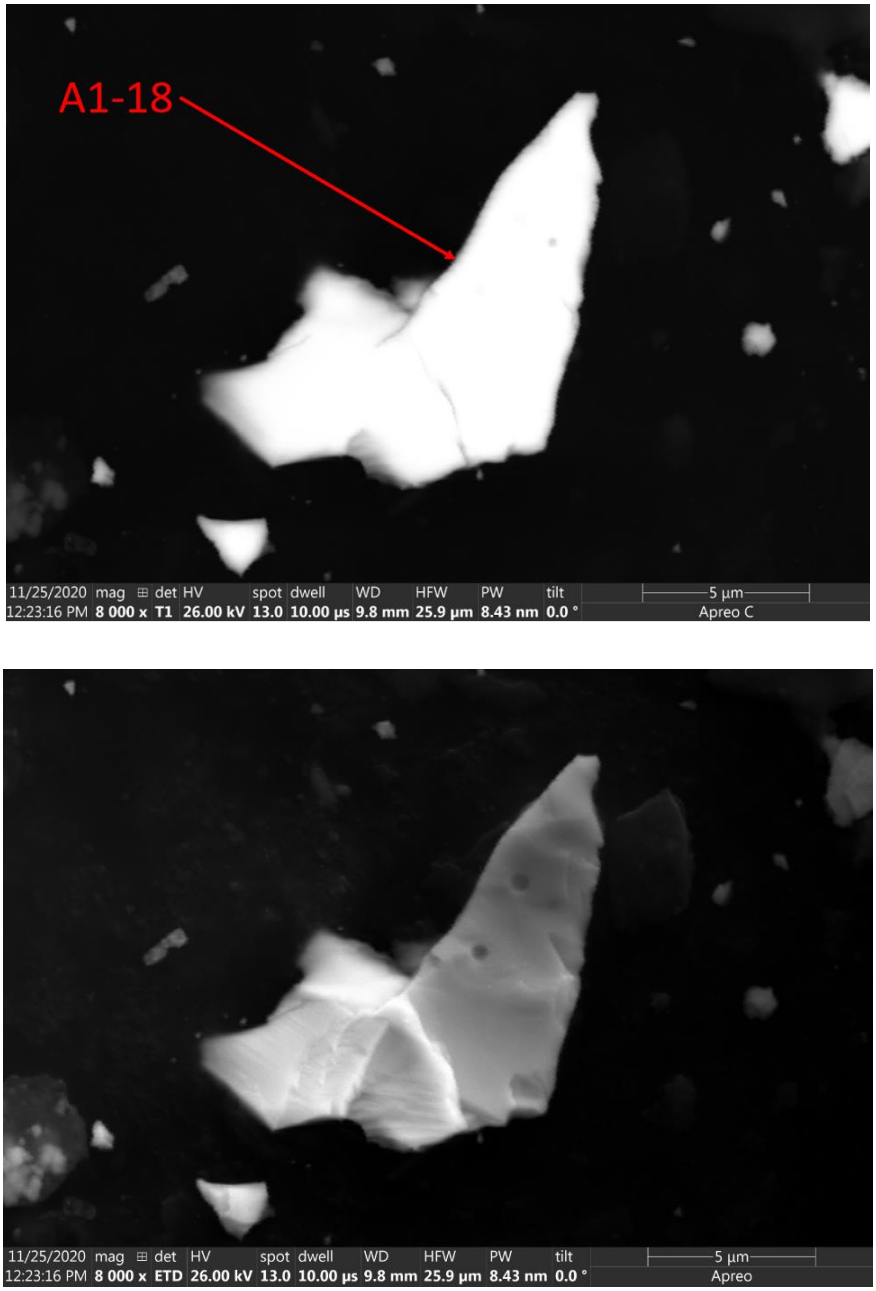

Figure 72. Particle A1-18 SEM Images

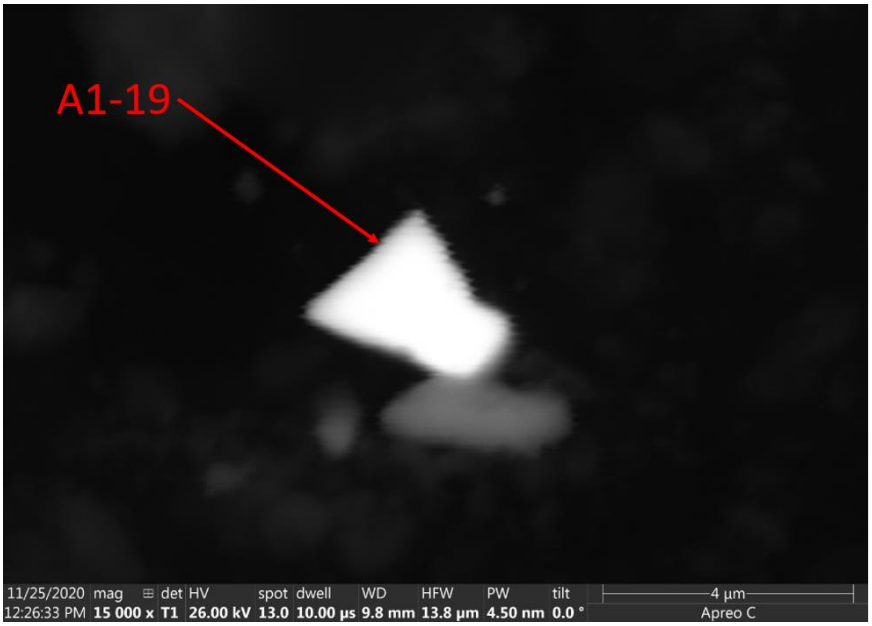

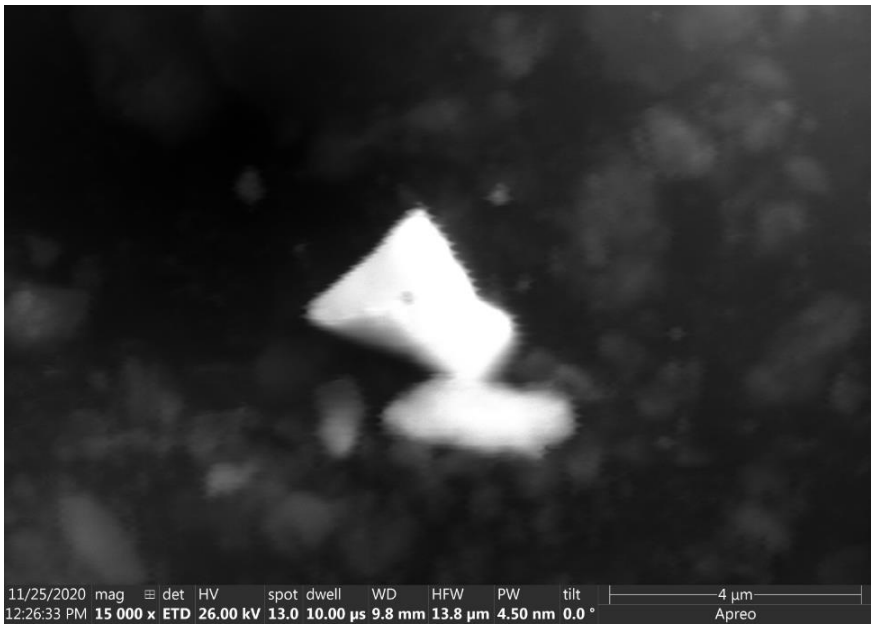

Figure 73. Particle A1-19 SEM Images

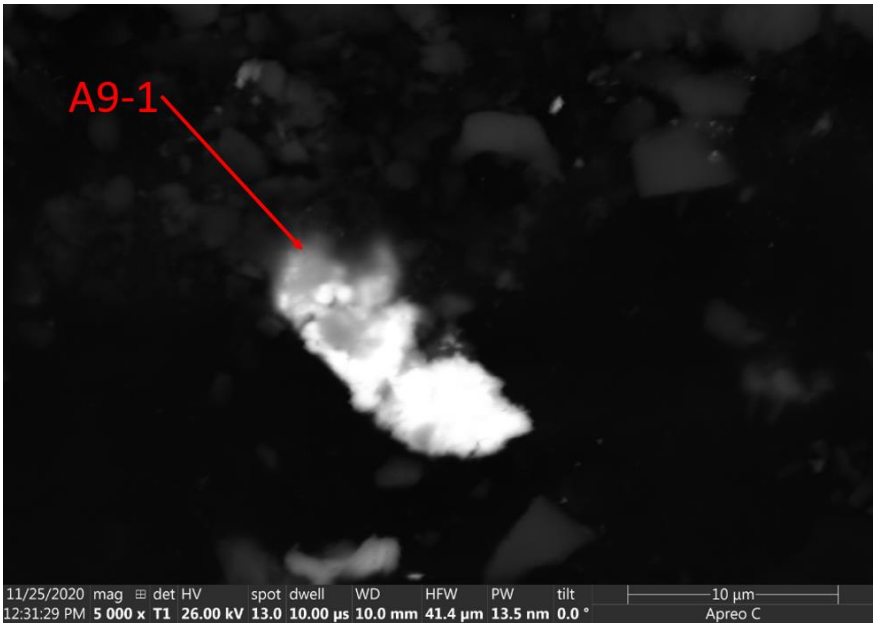

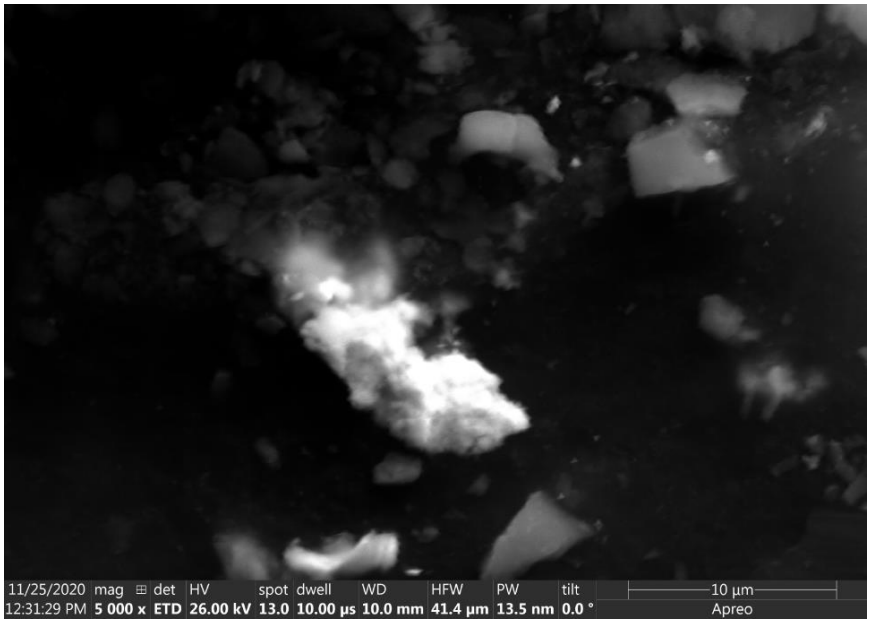

Figure 74. Particle A9-1 SEM Images

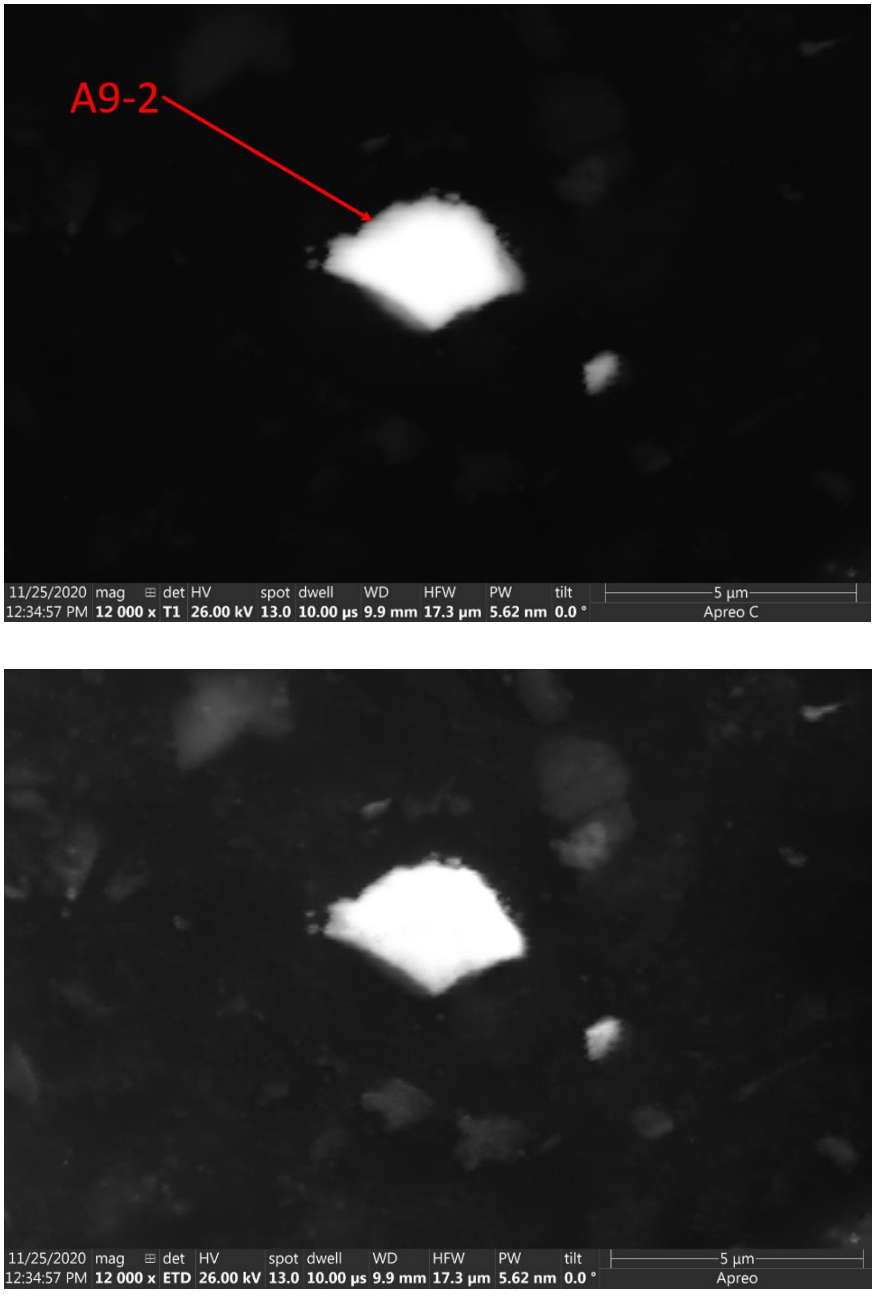

Figure 75. Particle A9-2 SEM Images

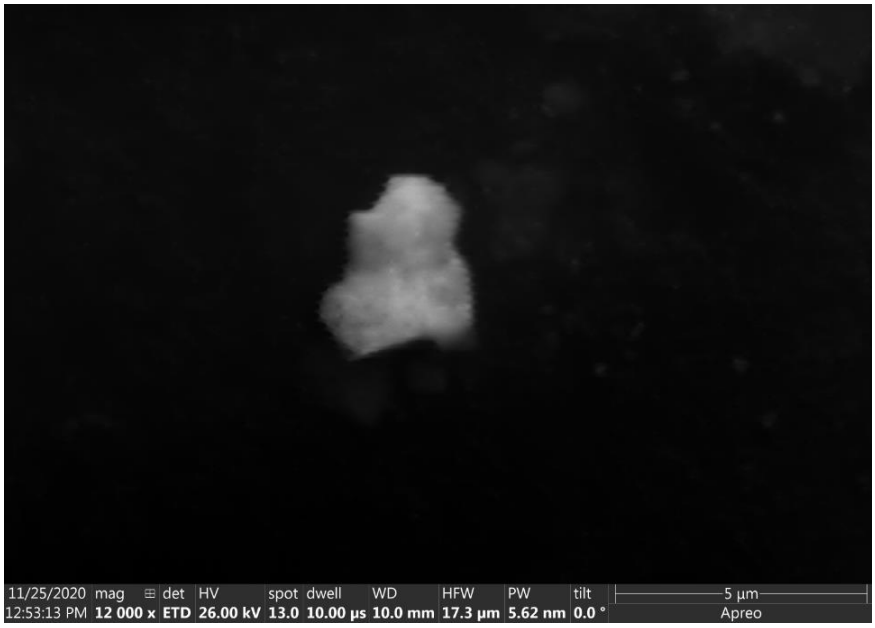

Figure 76. Particle D8-2 SEM Images

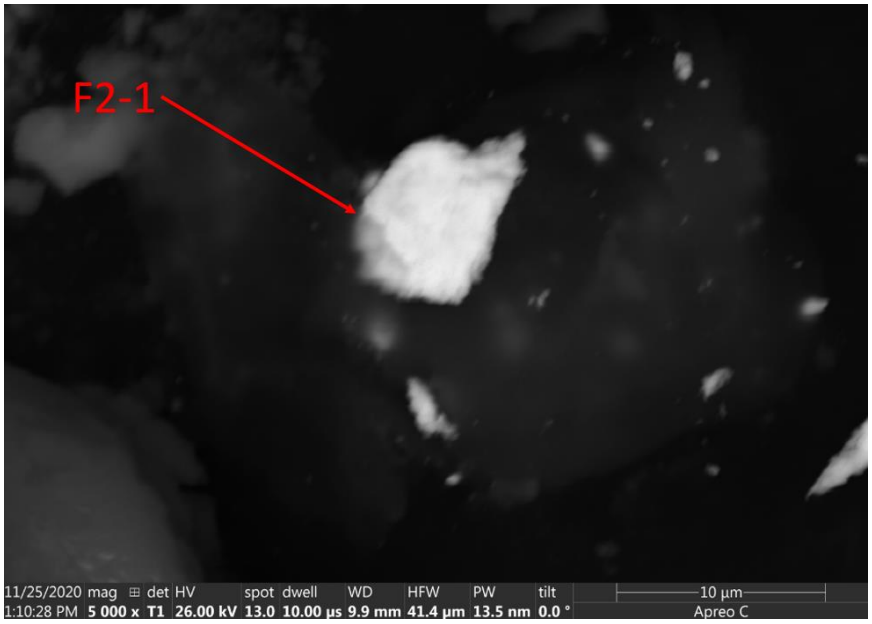

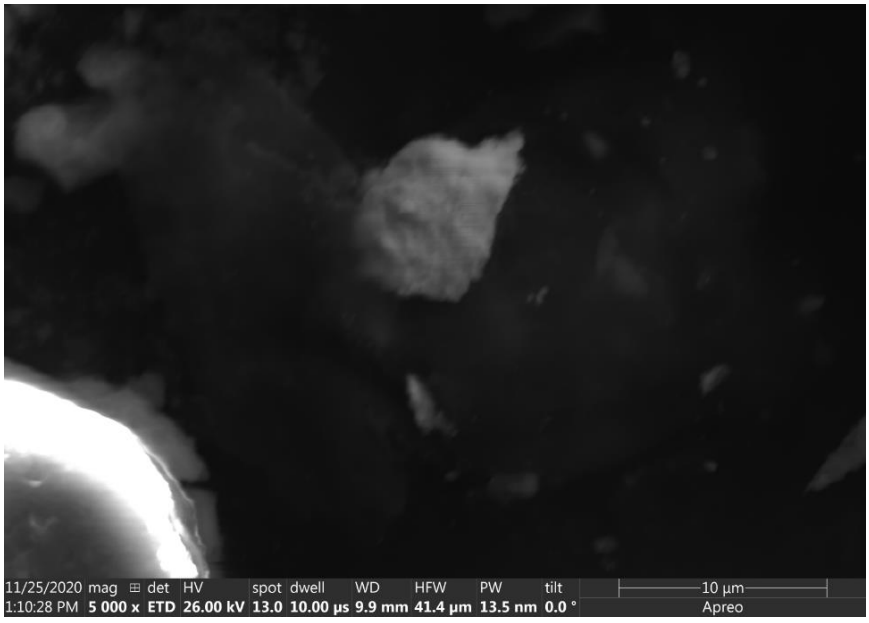

Figure 77. Particle F2-1 SEM Images

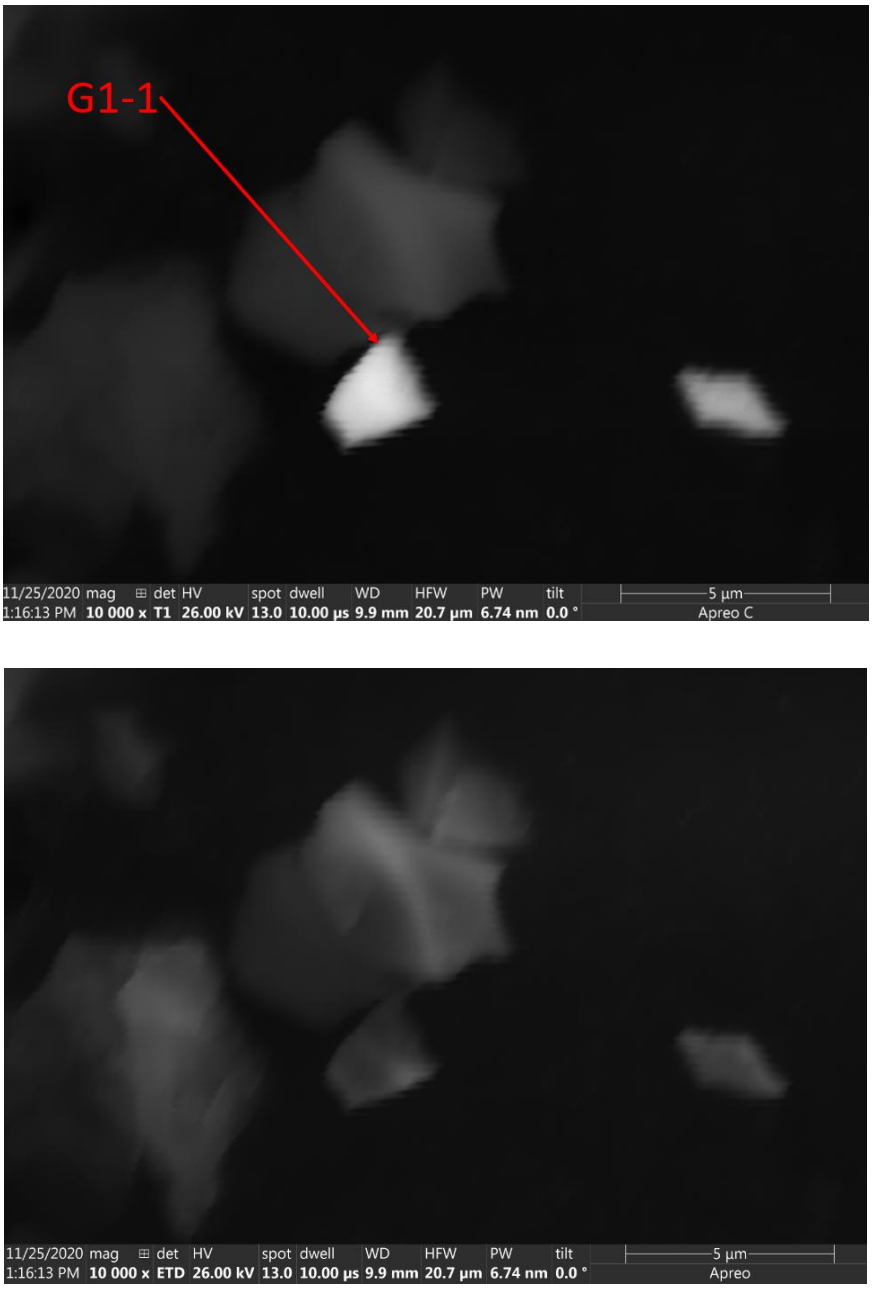

Figure 78. Particle G1-1 SEM Images

Figure 79. Particle I11-1 SEM Images

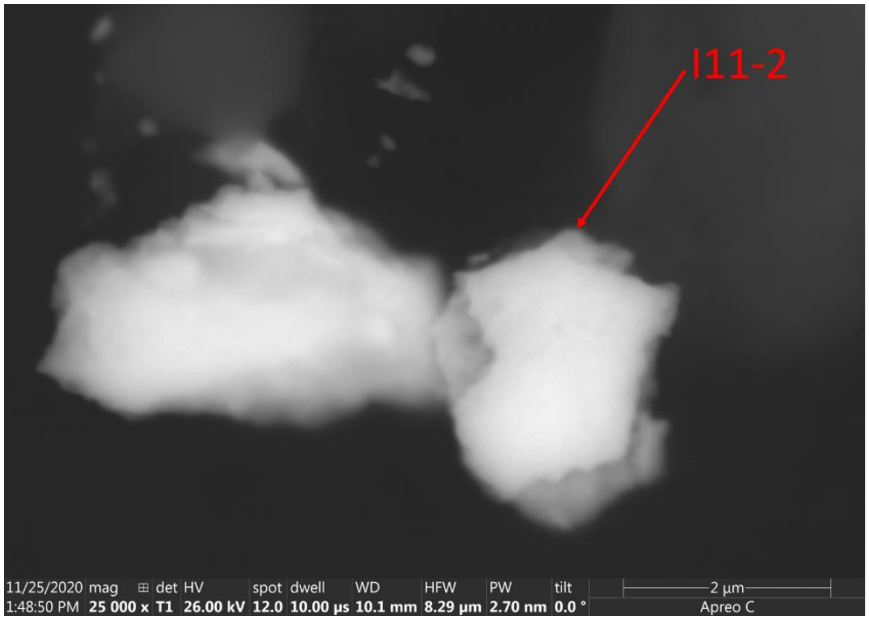

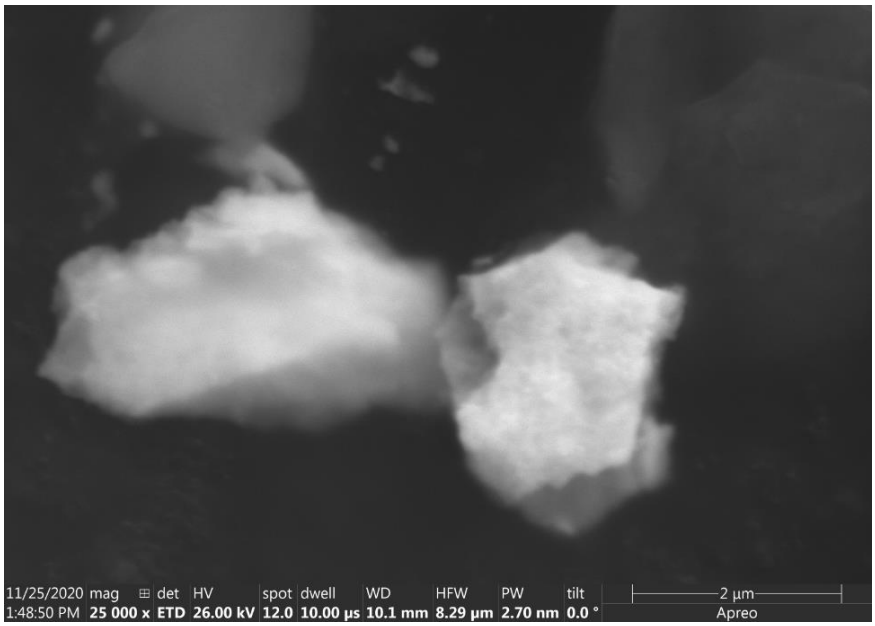

Figure 80. Particle I11-2 SEM Images

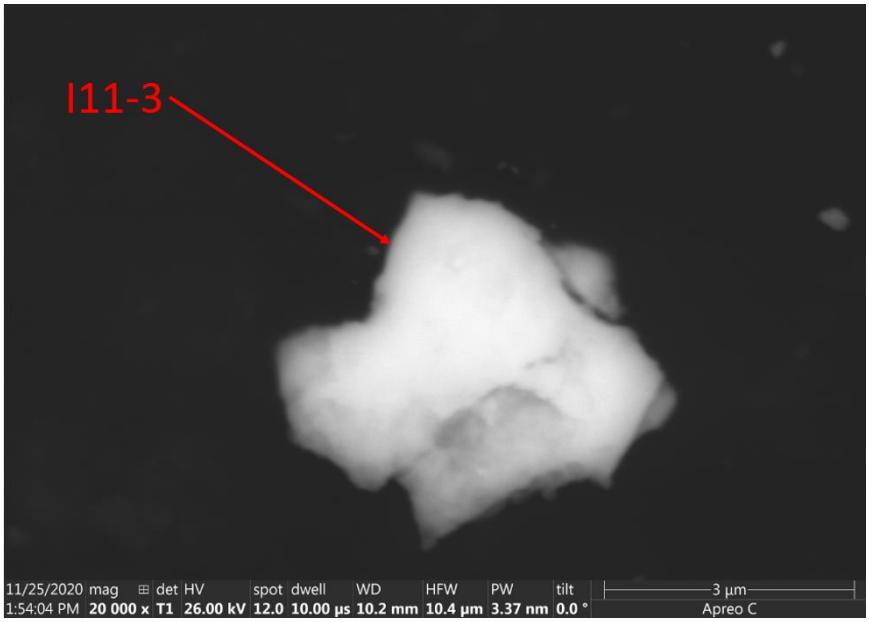

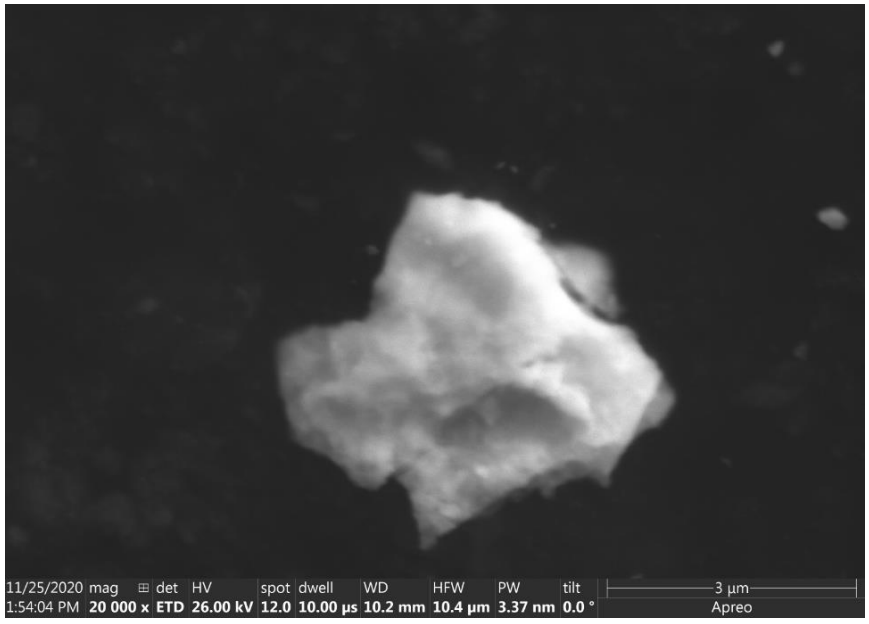

Figure 81. Particle I11-3 SEM Images

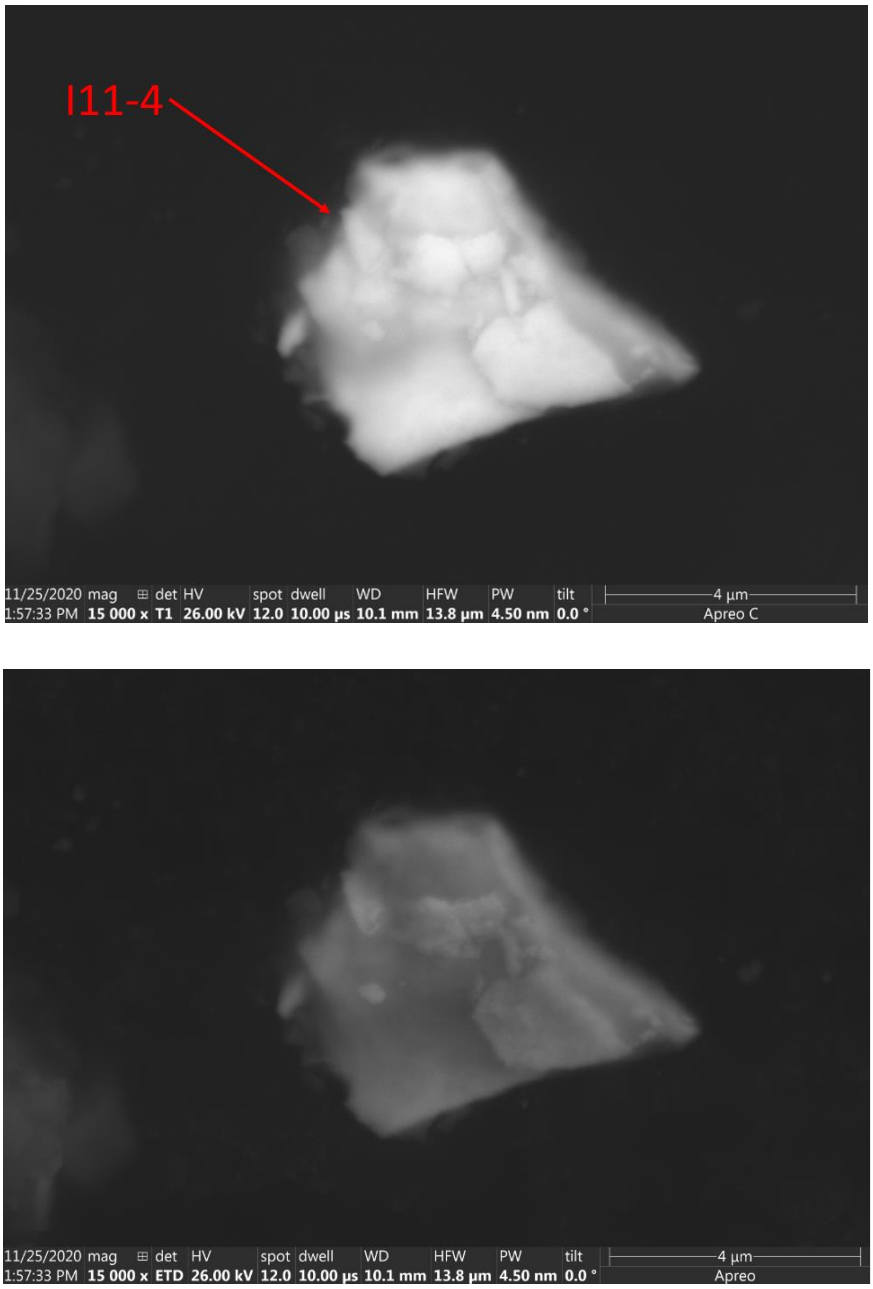

Figure 82. Particle I11-4 SEM Images

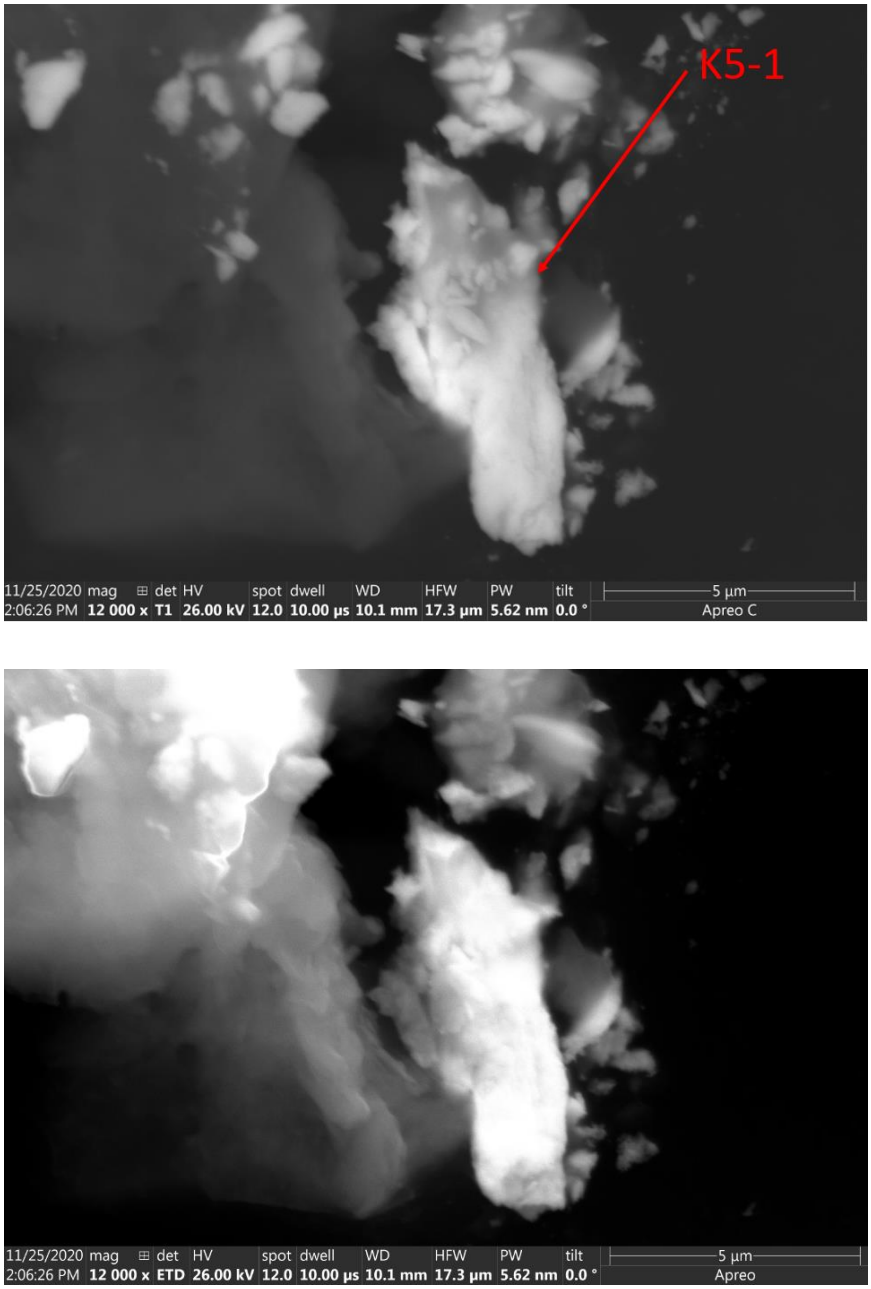

Figure 83. Particle K5-1 SEM Images

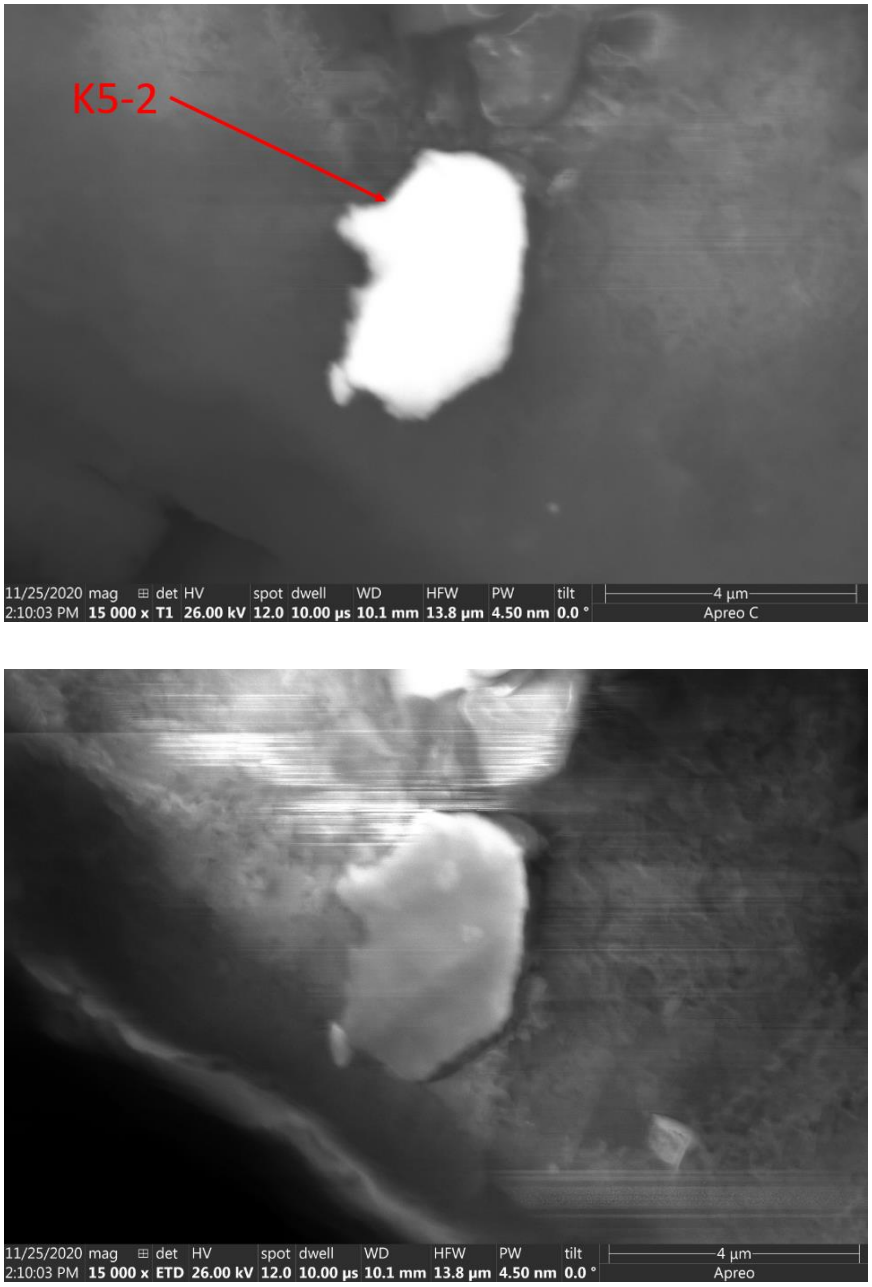

Figure 84. Particle K5-2 SEM Images

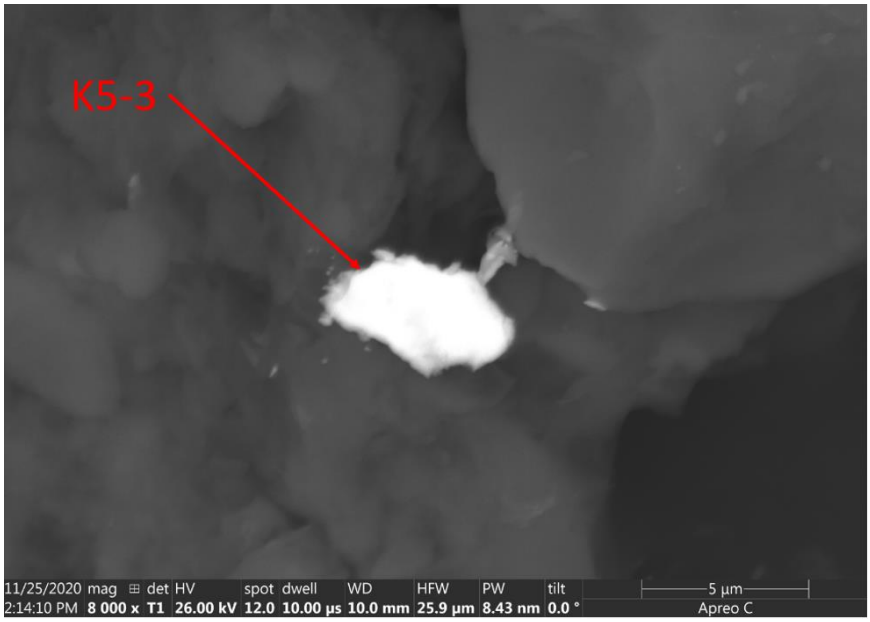

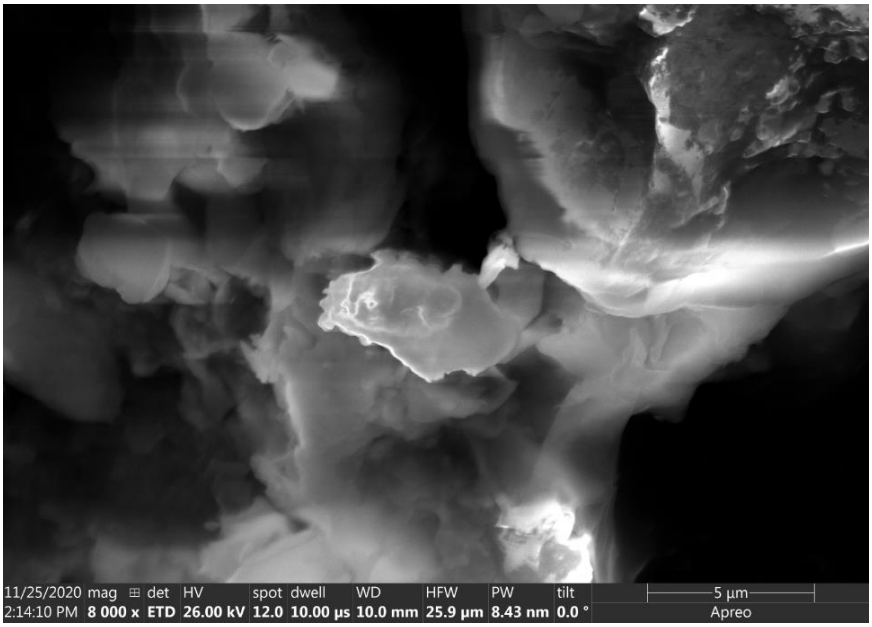

Figure 85. Particle K5-3 SEM Images

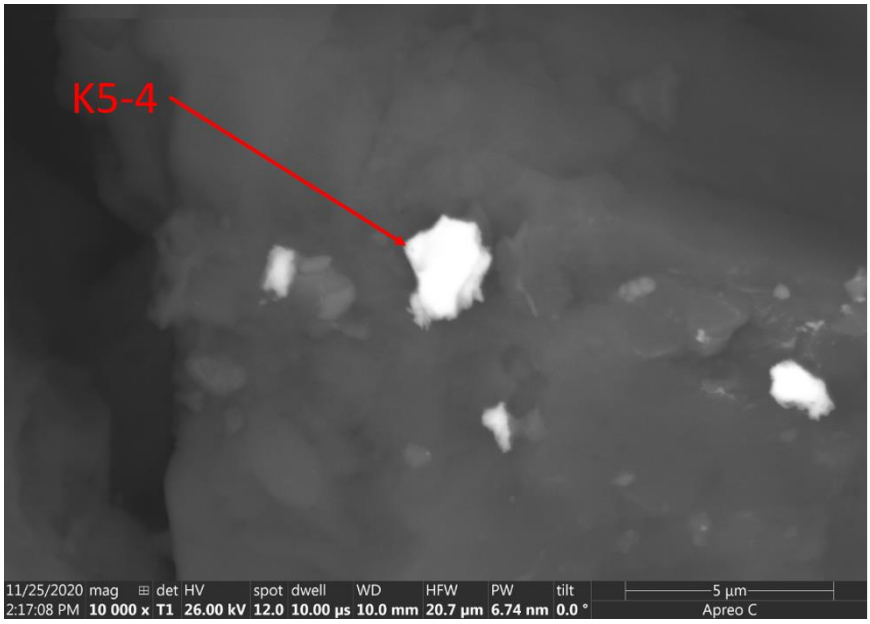

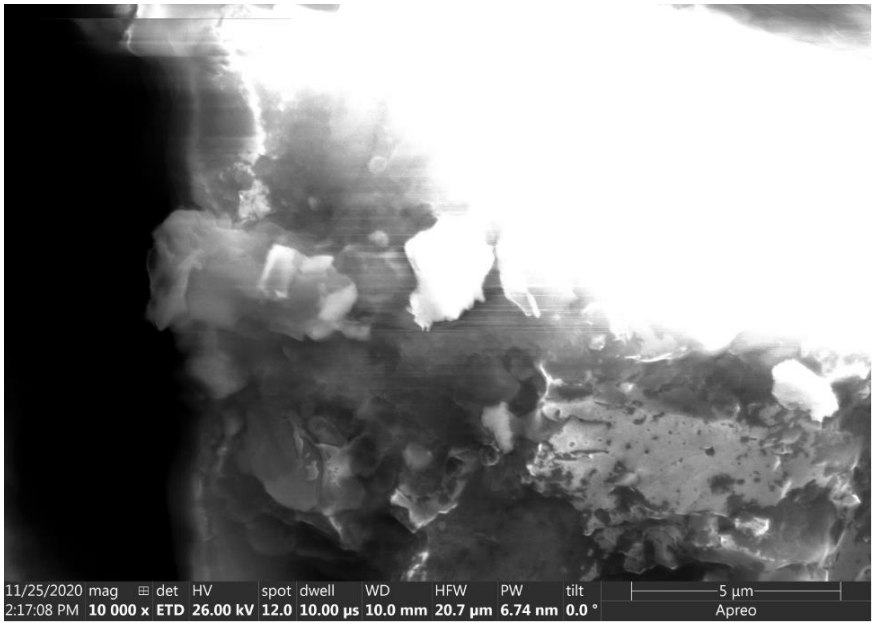

Figure 86. Particle K5-4 SEM Images

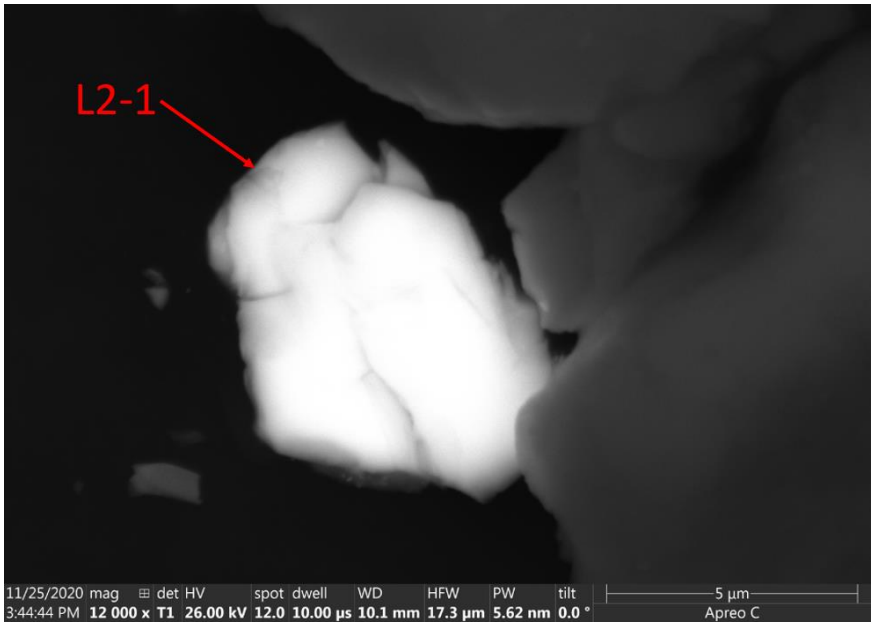

Figure 87. Particle L2-1 BSE Image

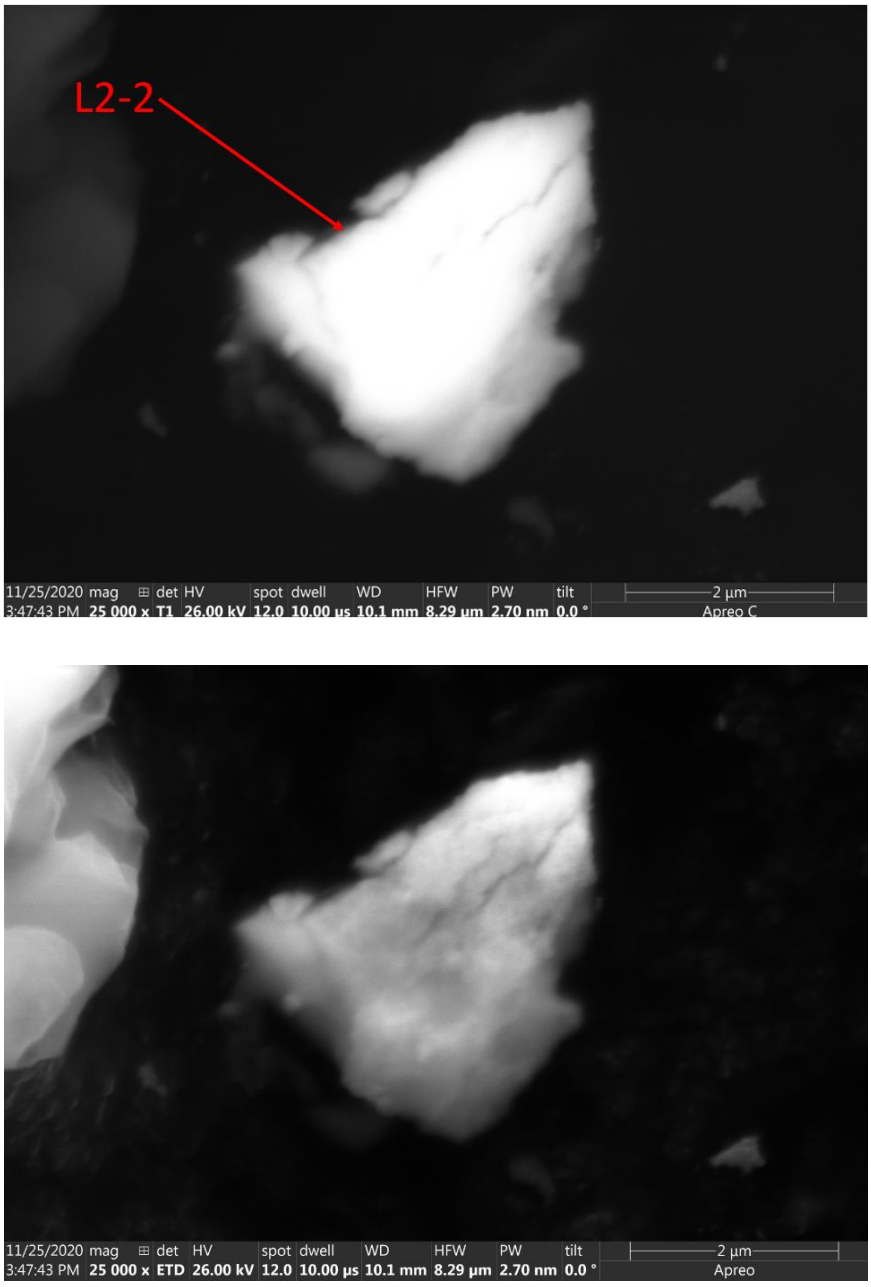

Figure 88. Particle L2-2 SEM Images

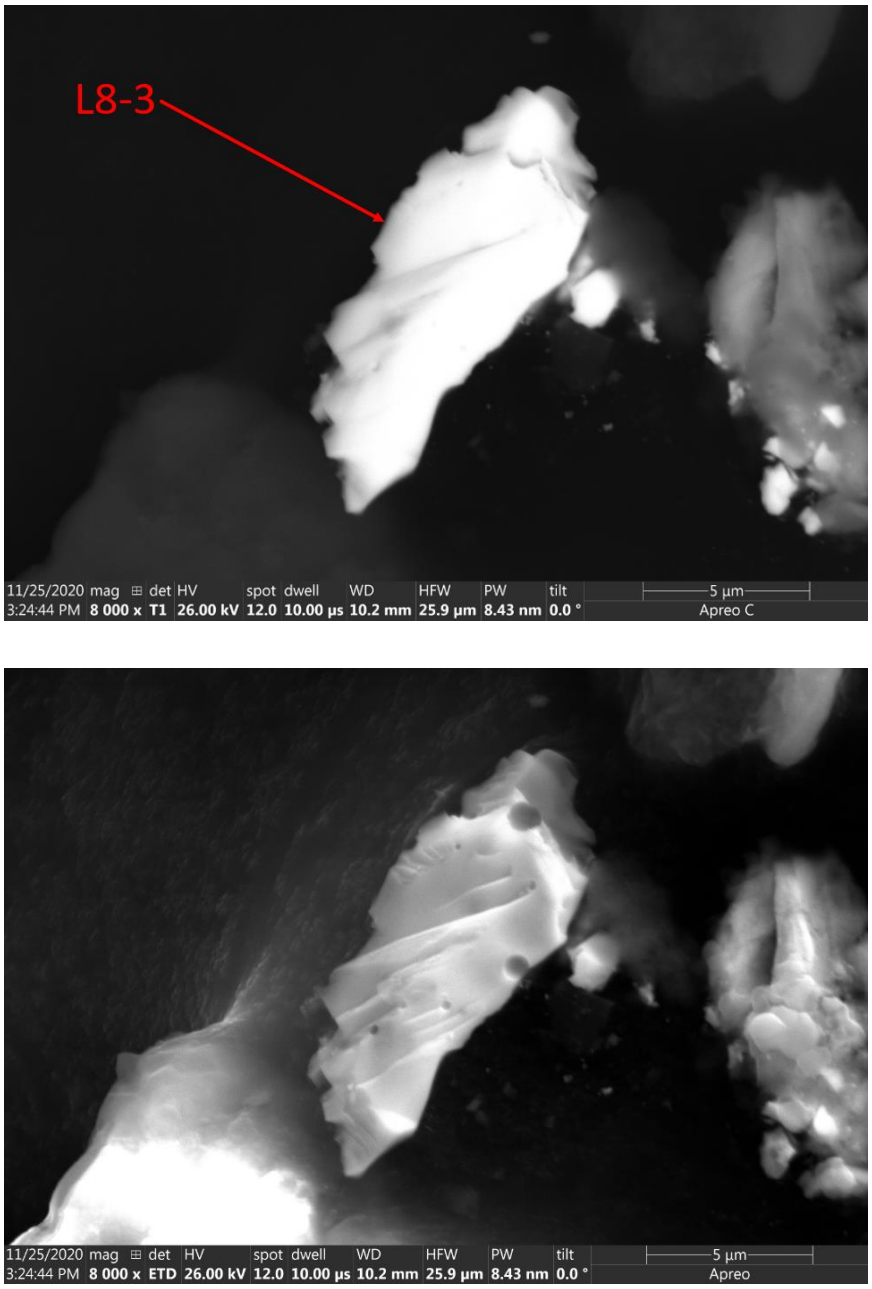

Figure 89. Particle L8-3 SEM Images

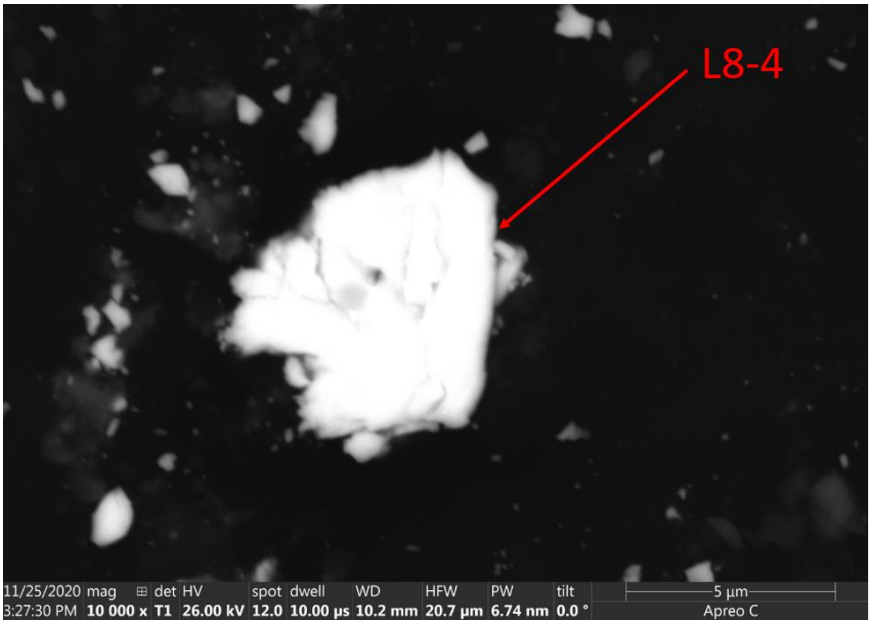

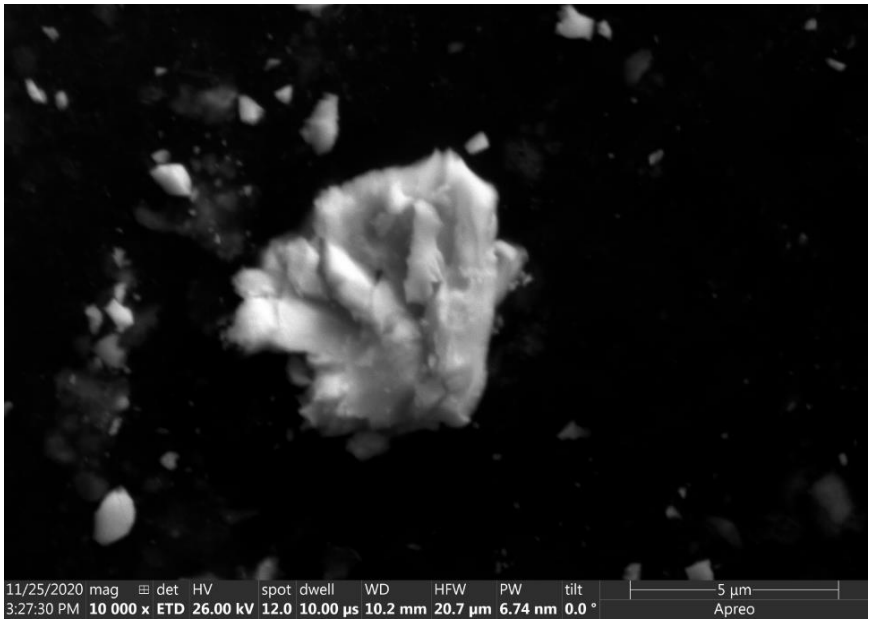

Figure 90. Particle L8-4 SEM Images

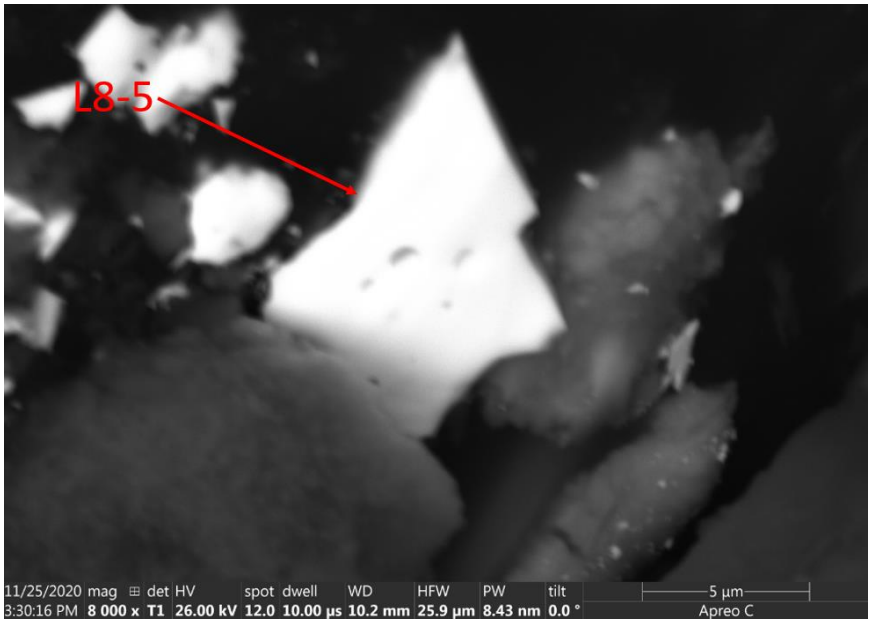

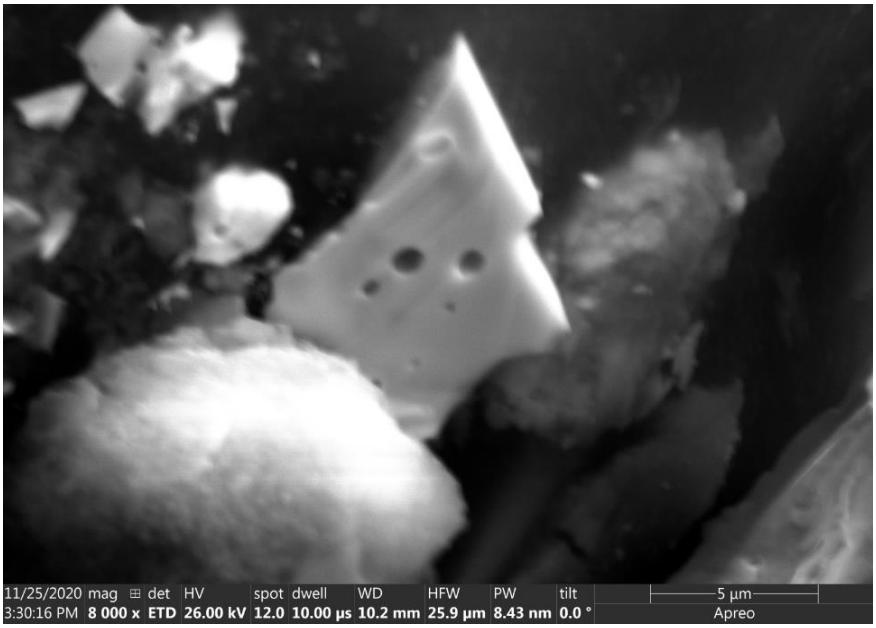

Figure 91. Particle L8-5 SEM Images

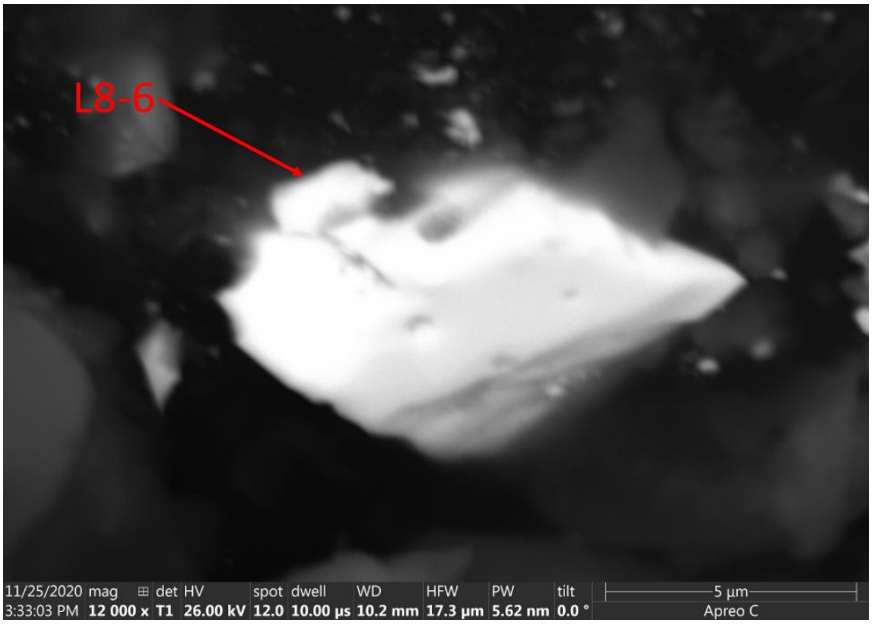

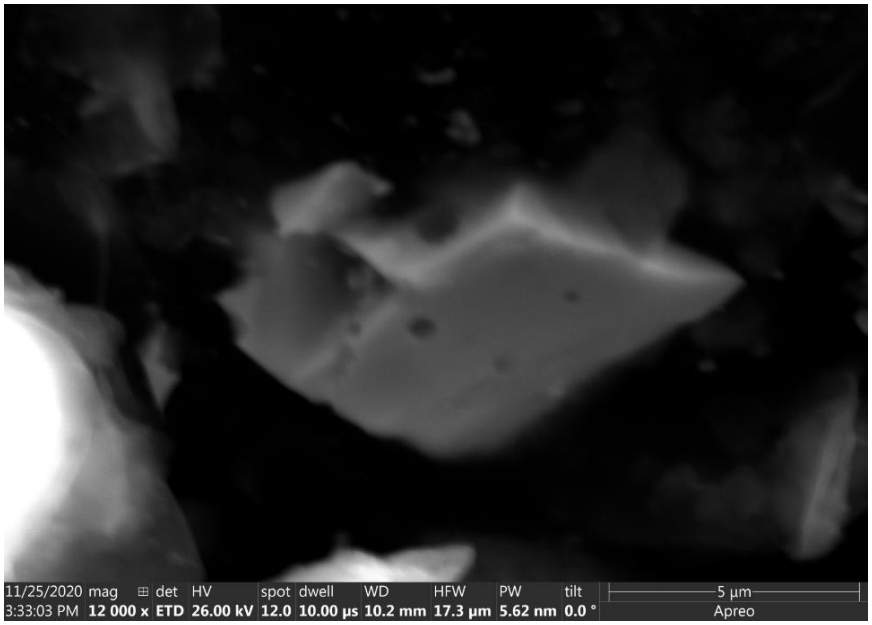

Figure 92. Particle L8-6 SEM Images

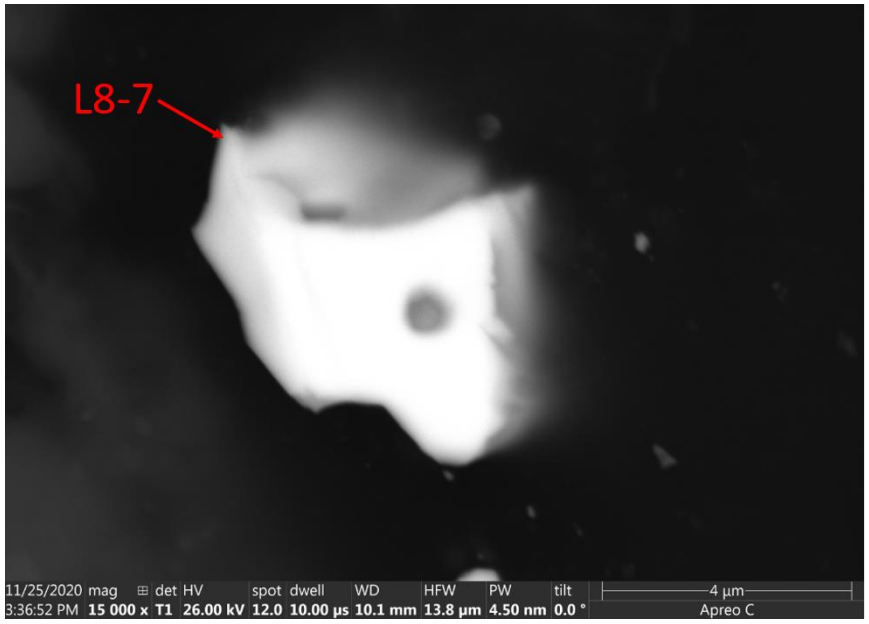

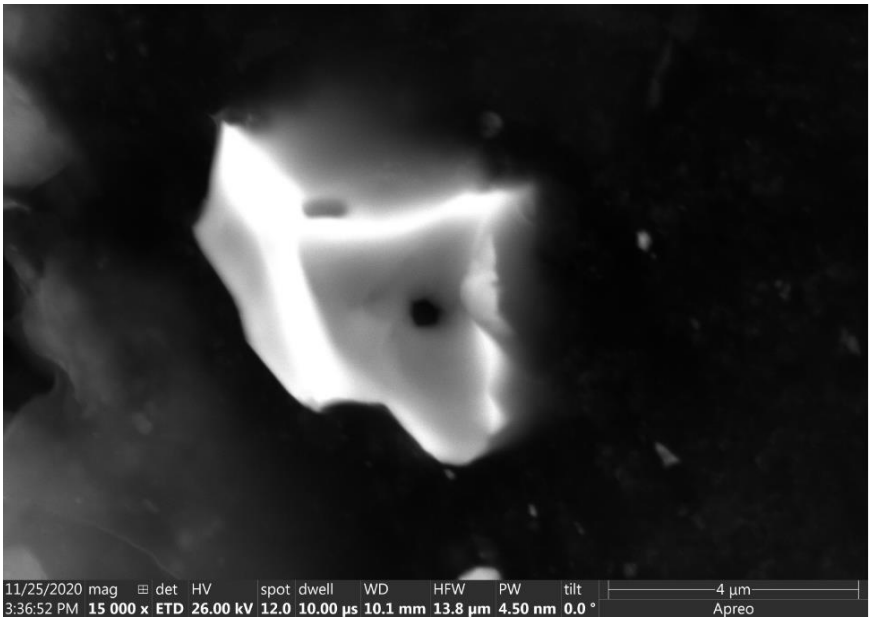

Figure 93. Particle L8-7 SEM Images

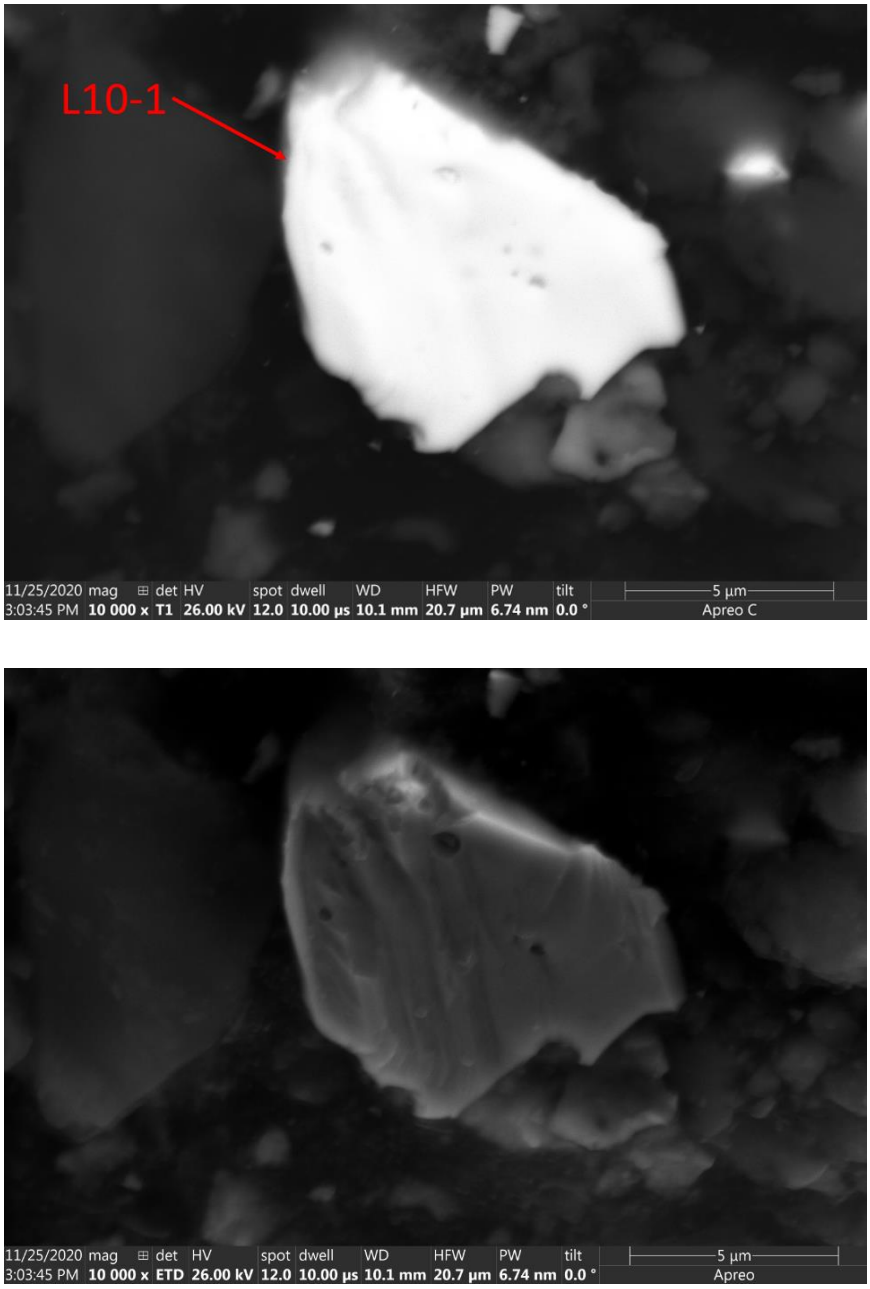

Figure 94. Particle L10-1 SEM Images

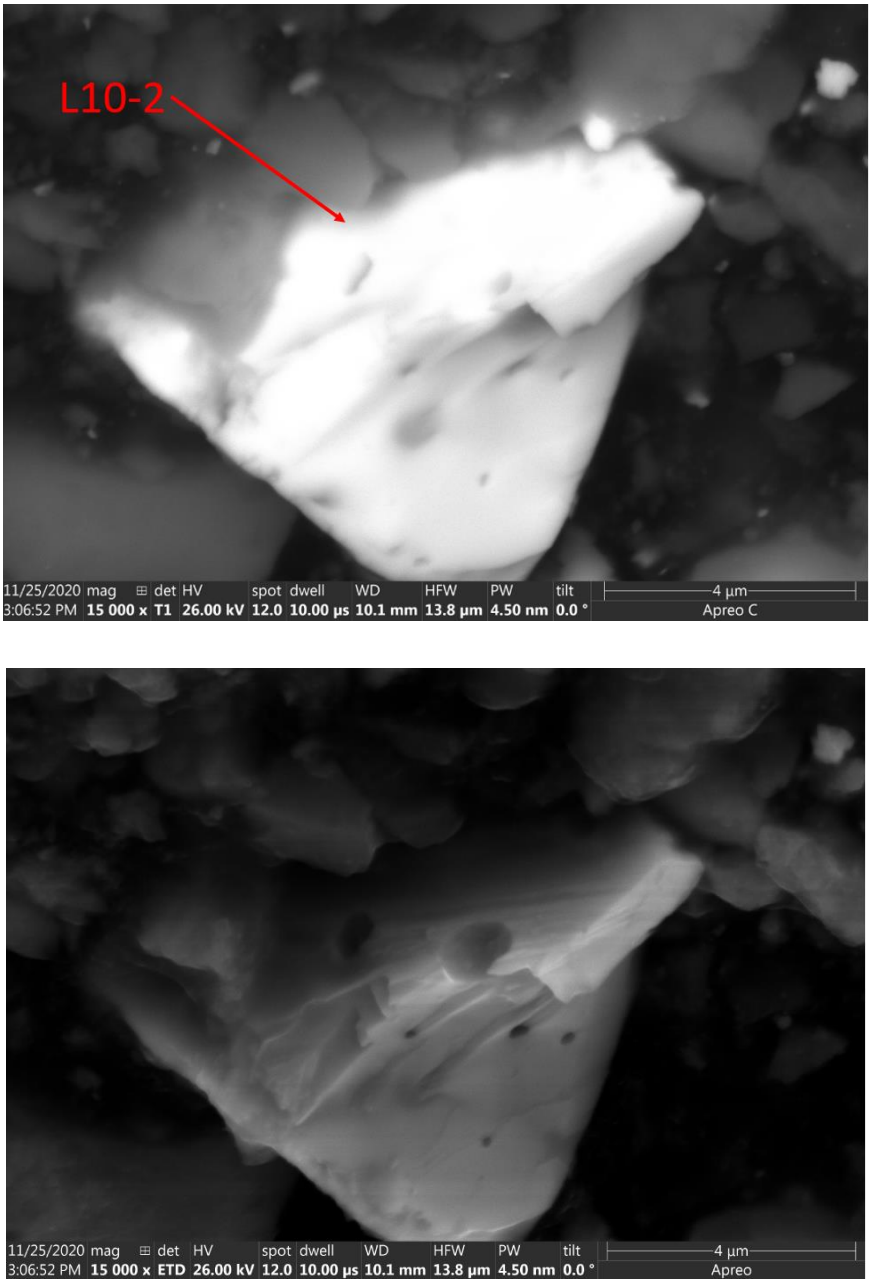

Figure 95. Particle L10-2 SEM Images

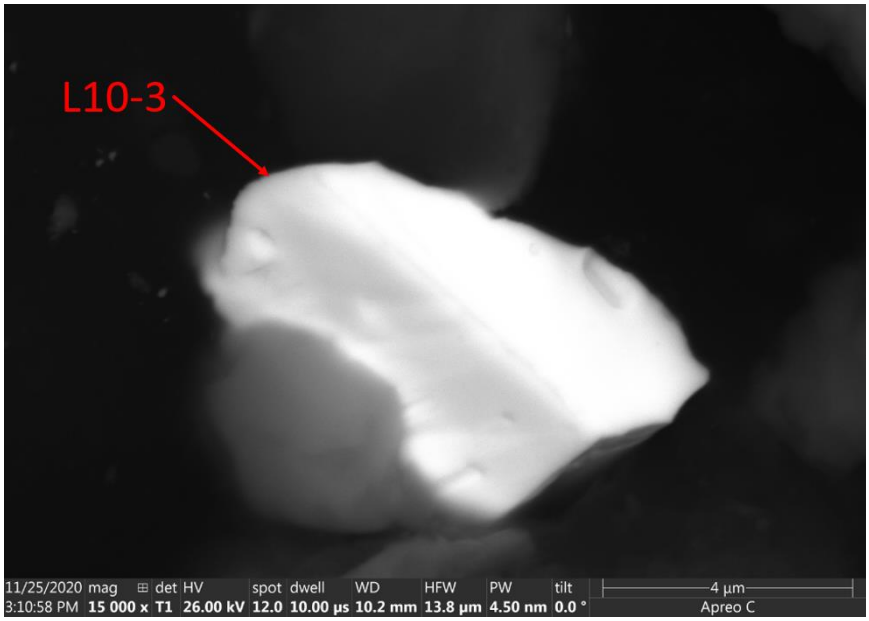

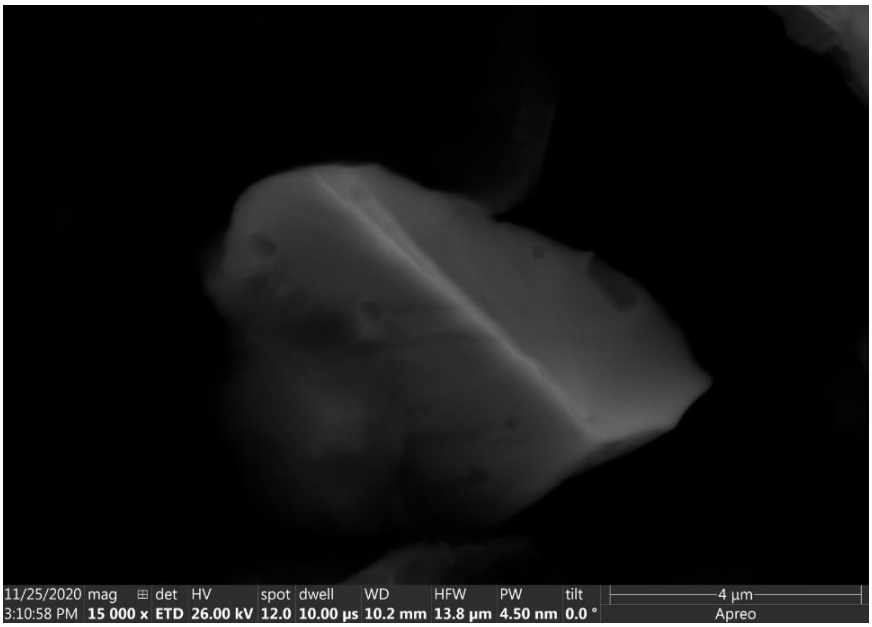

Figure 96. Particle L10-3 SEM Images

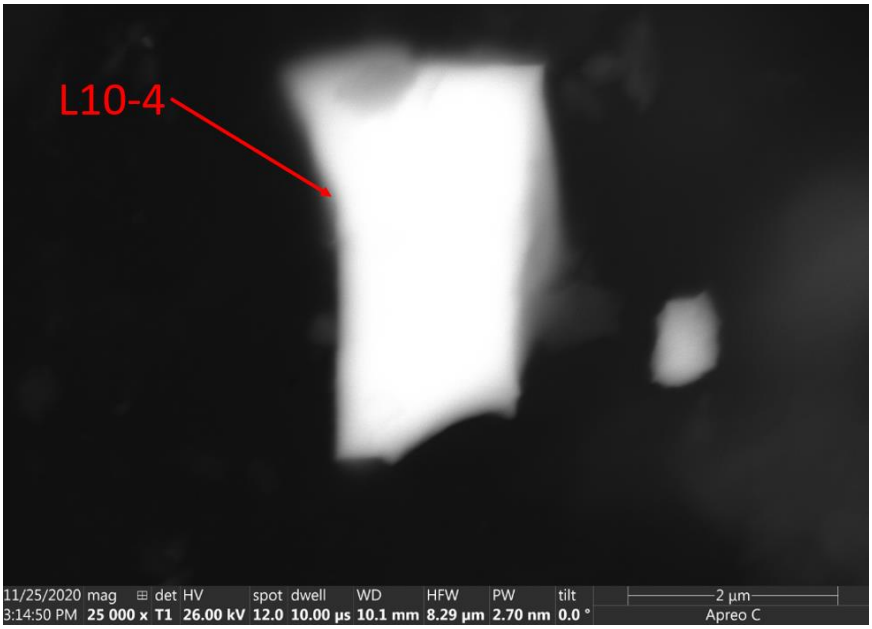

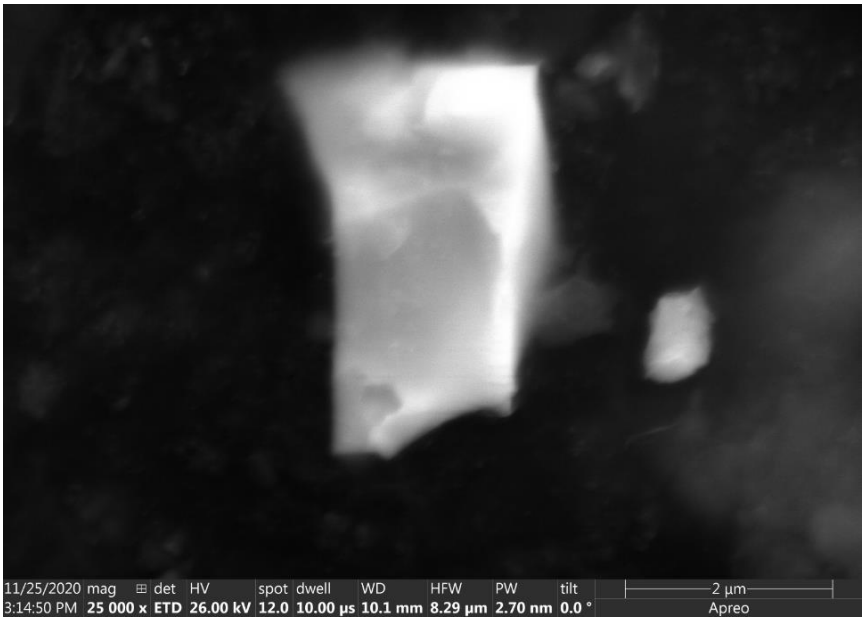

Figure 97. Particle L10-4 SEM Images

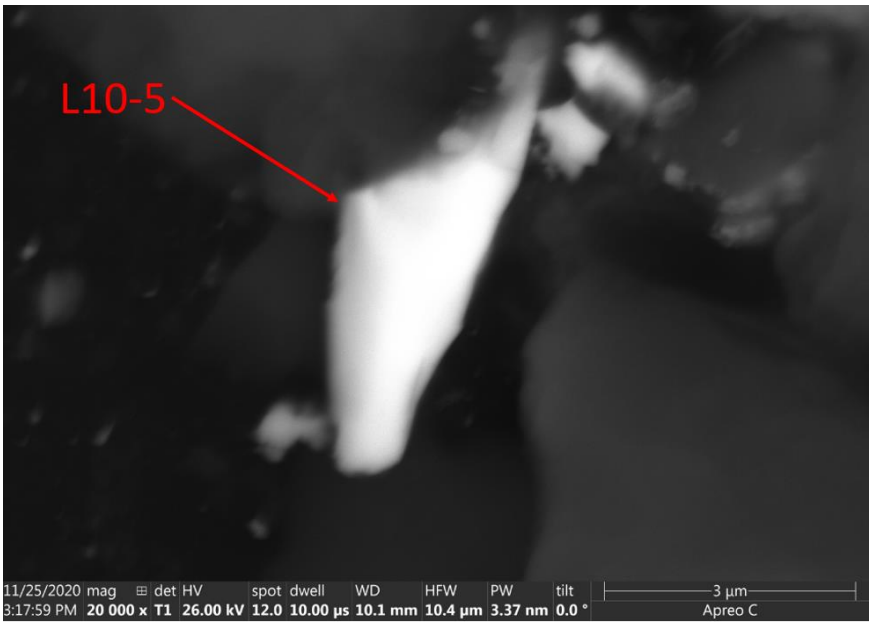

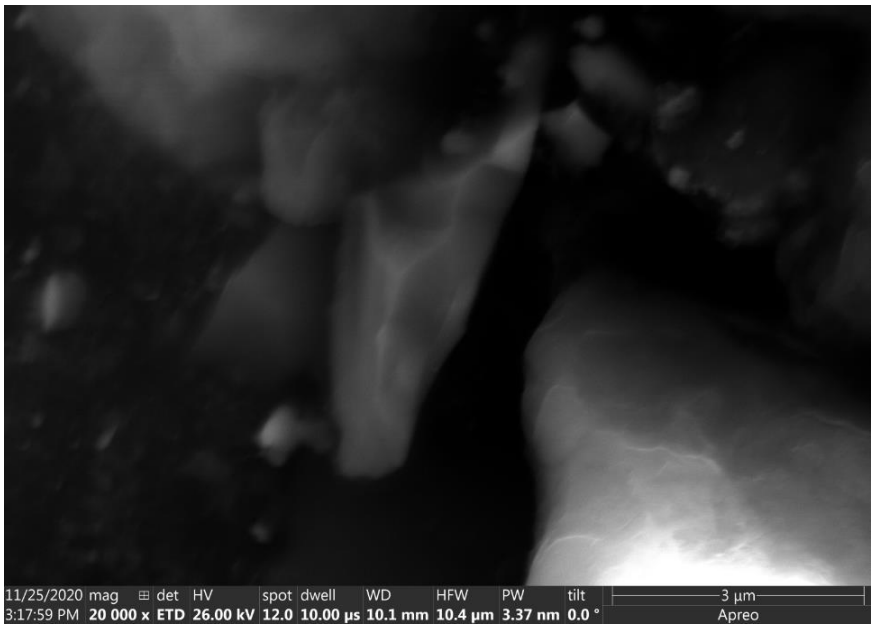

Figure 98. Particle L10-5 SEM Images

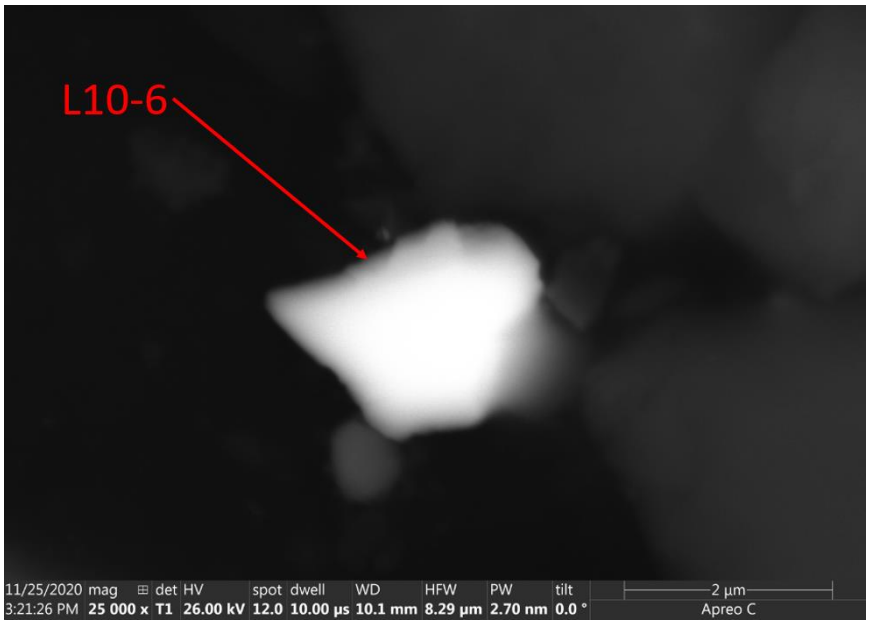

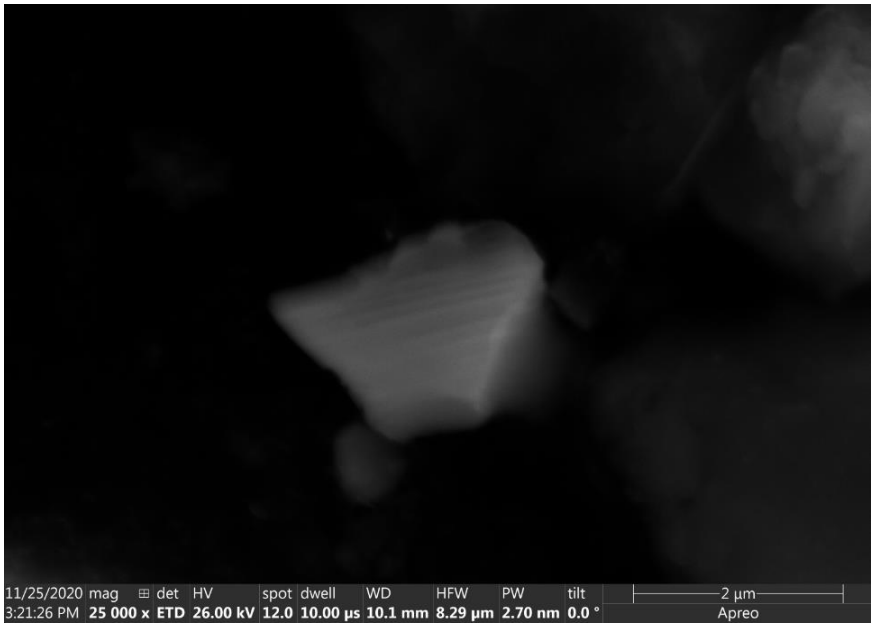

Figure 99. Particle L10-6 SEM Images

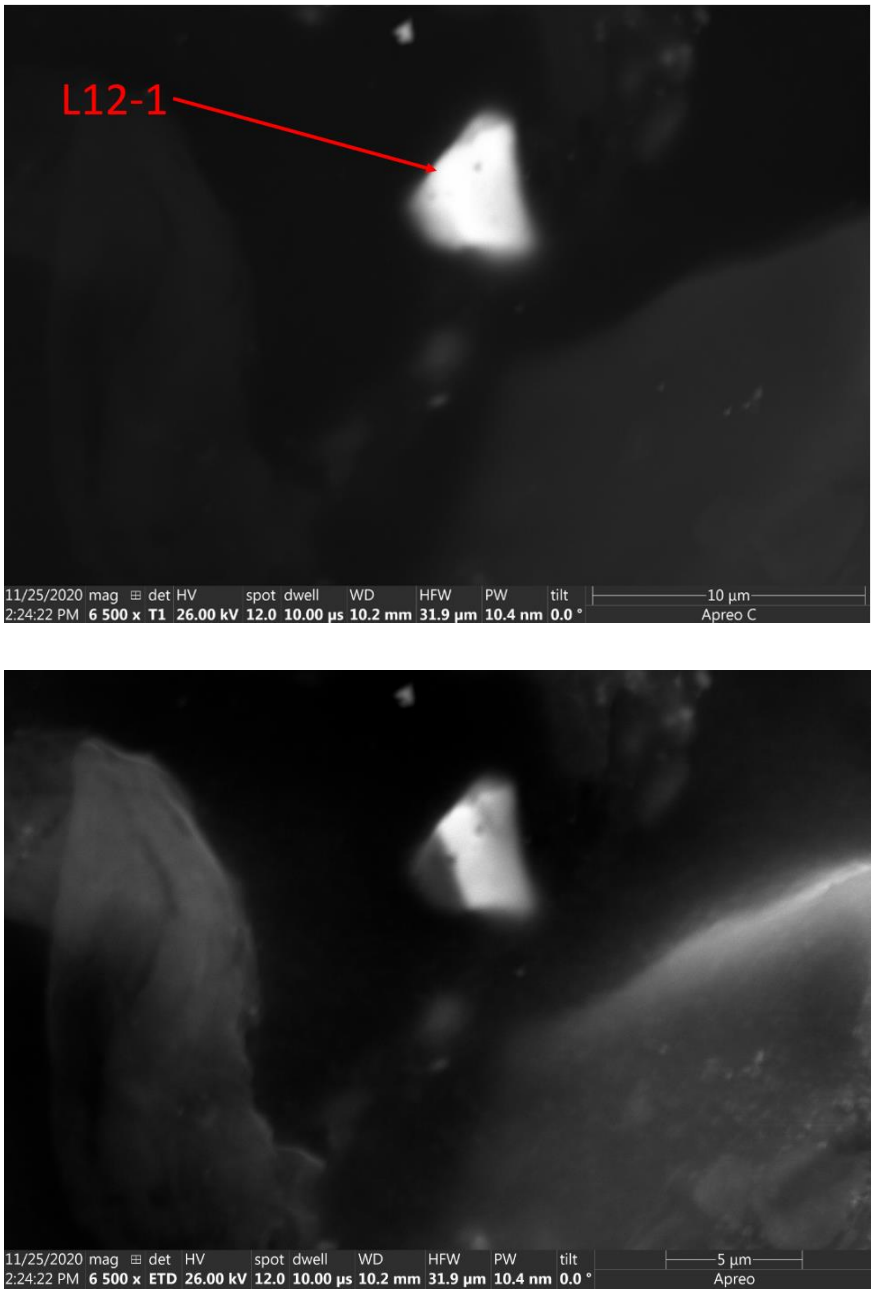

Figure 100. Particle L12-1 SEM Images

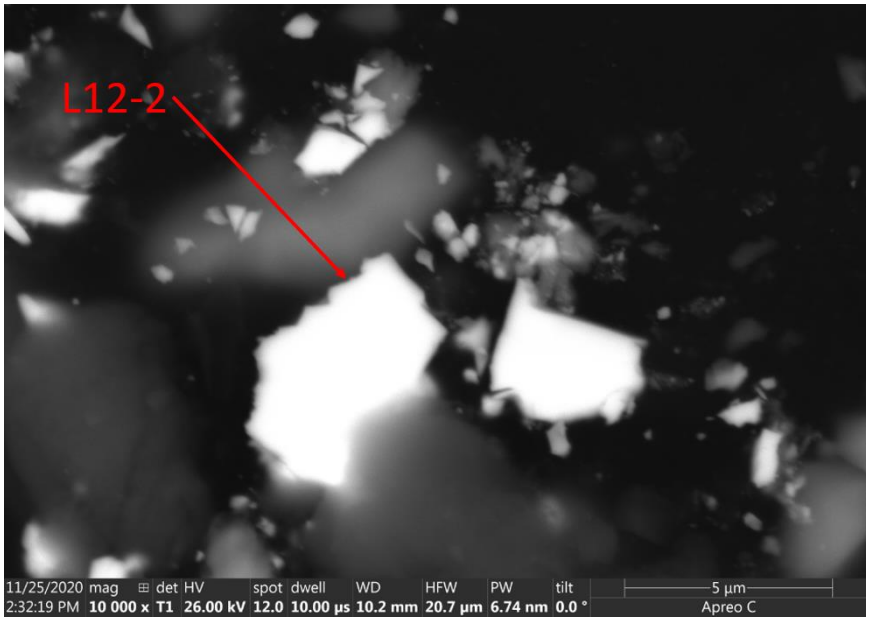

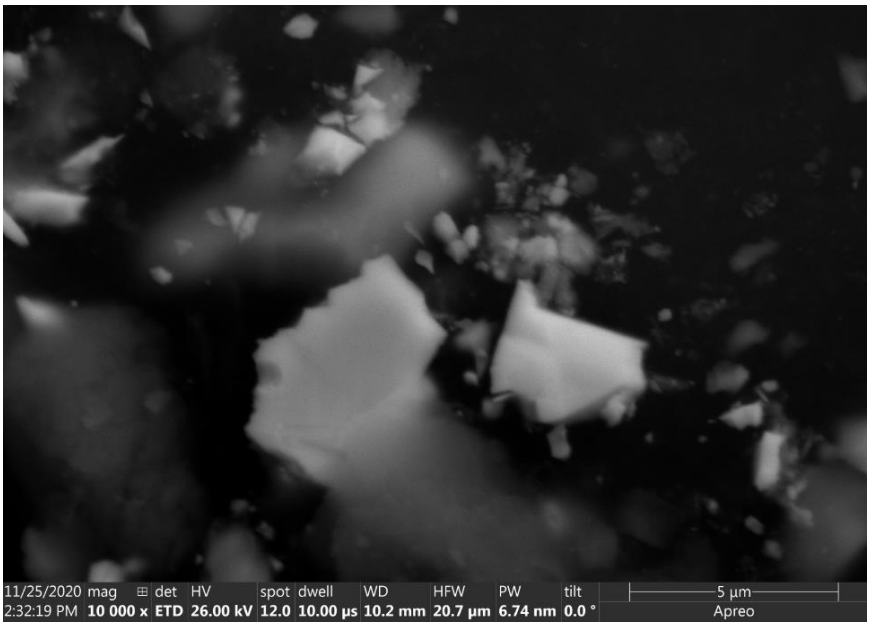

Figure 101. Particle L12-2 SEM Images

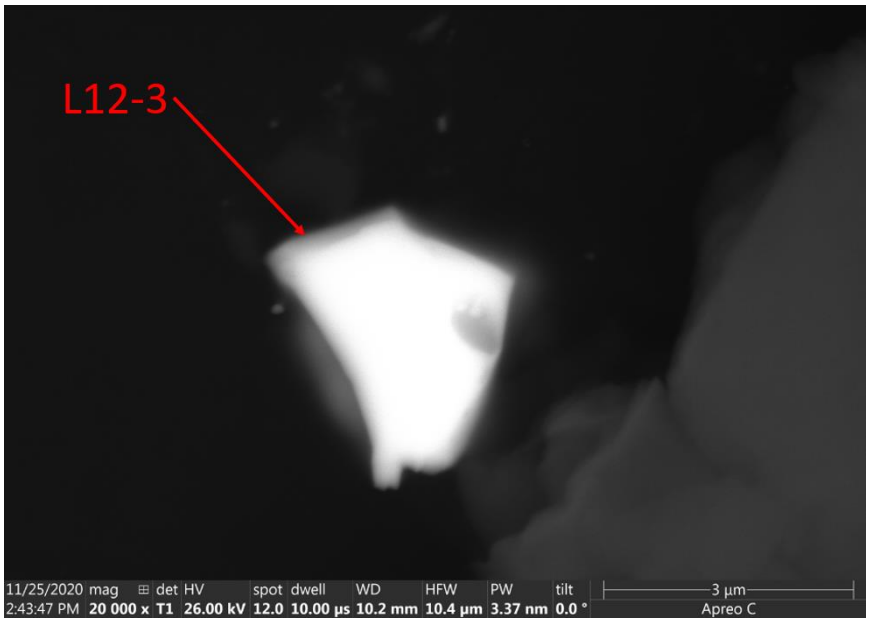

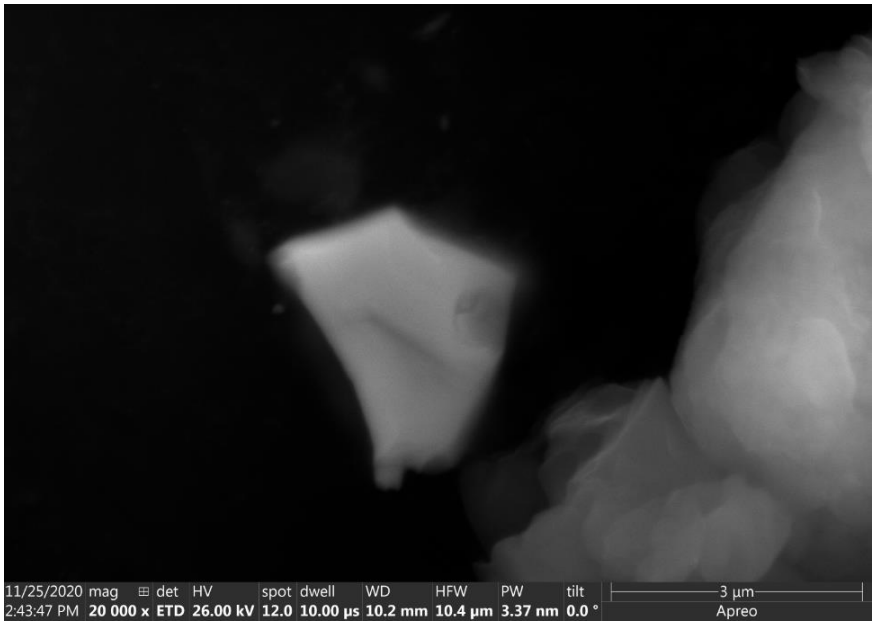

Figure 102. Particle L12-3 SEM Images

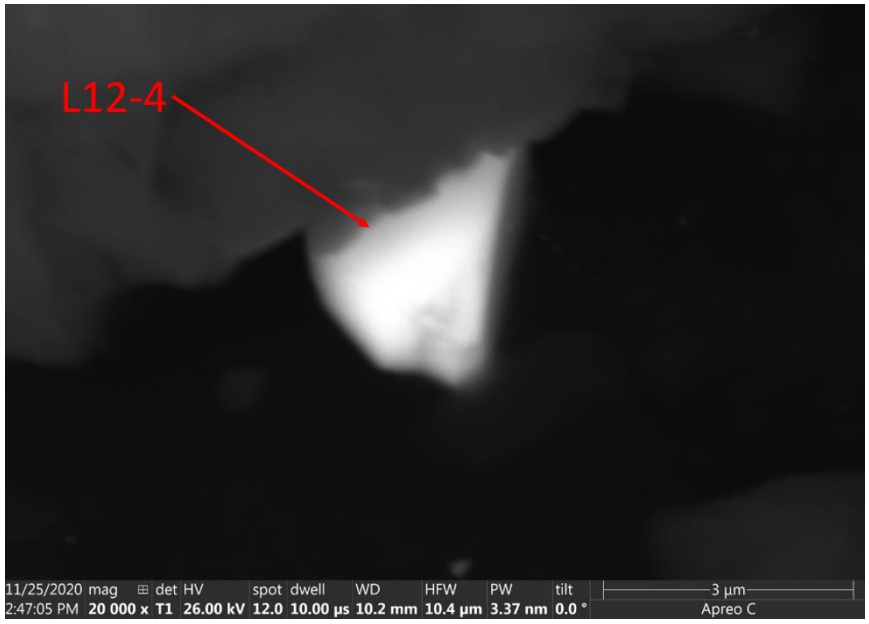

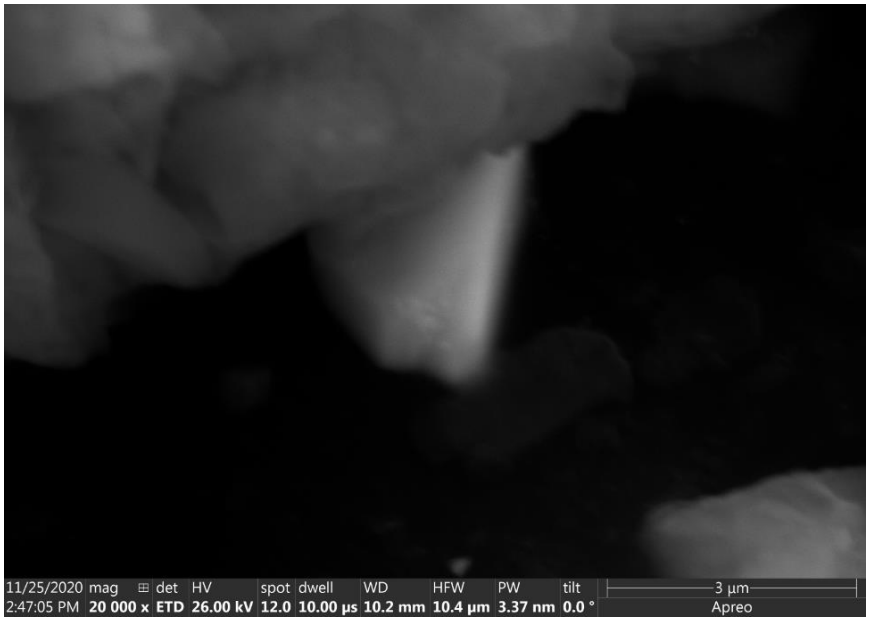

Figure 103. Particle L12-4 SEM Images

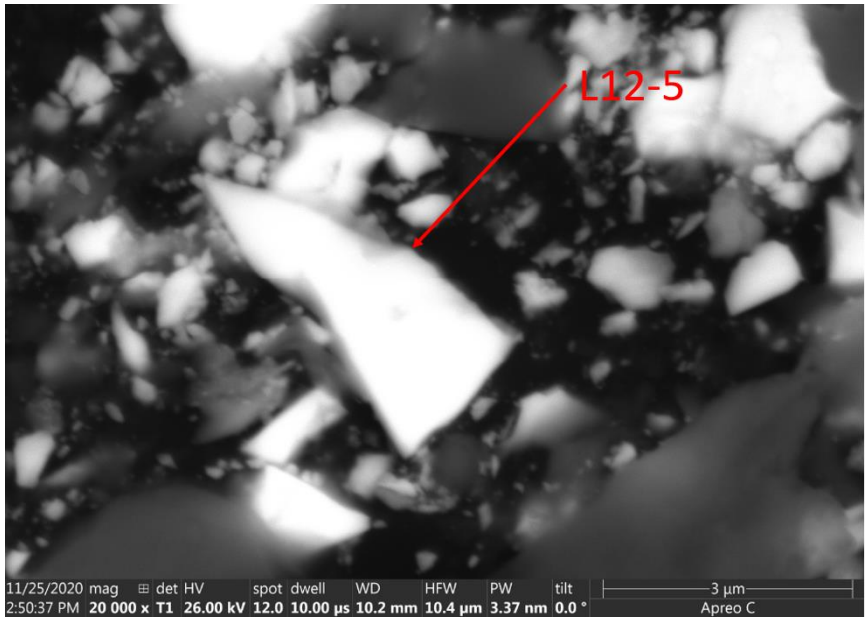

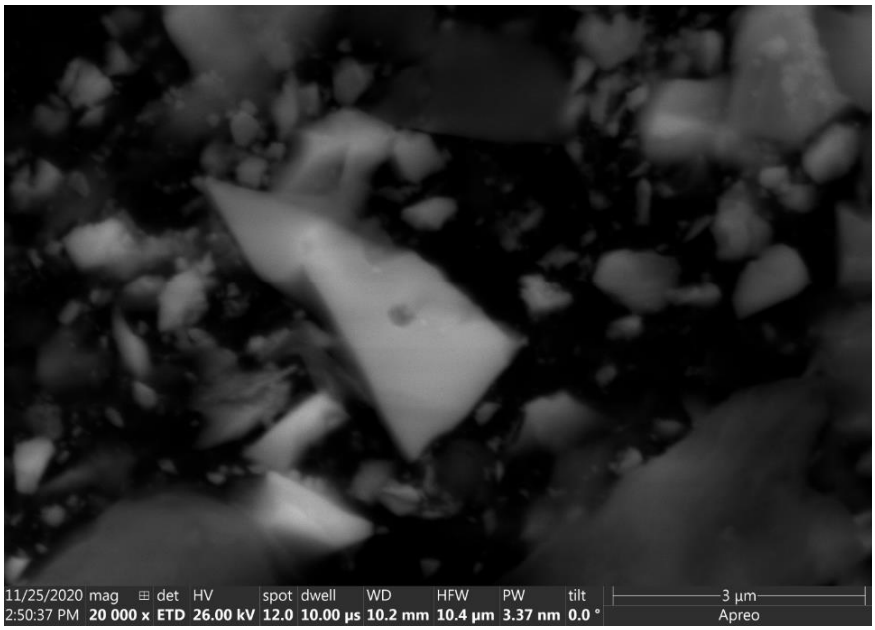

Figure 104. Particle L12-5 SEM Images

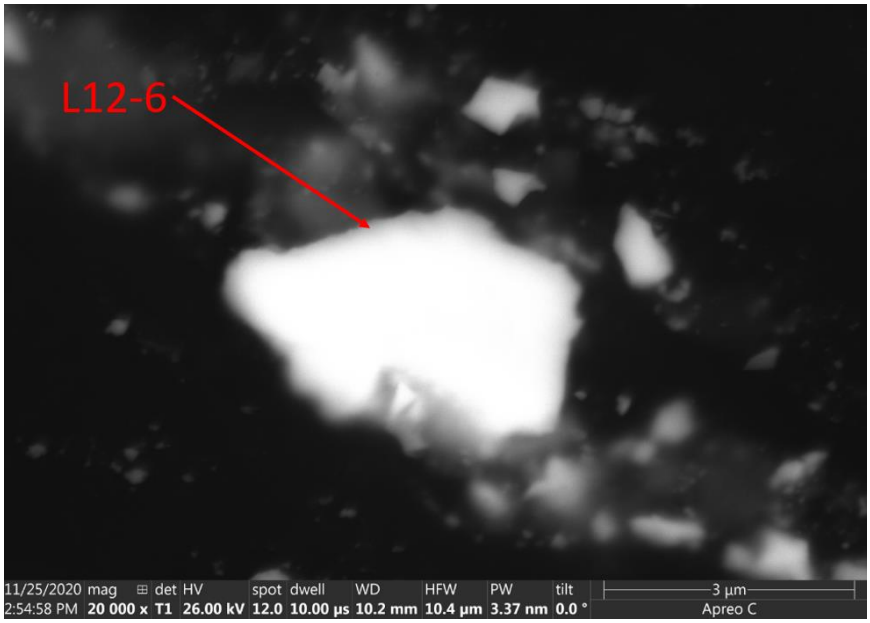

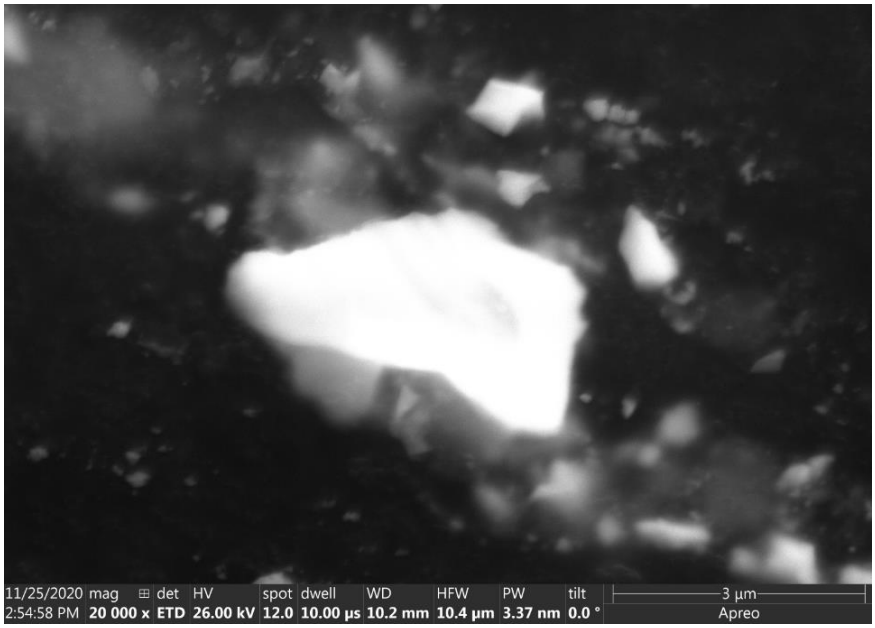

Figure 105. Particle L12-6 SEM Images

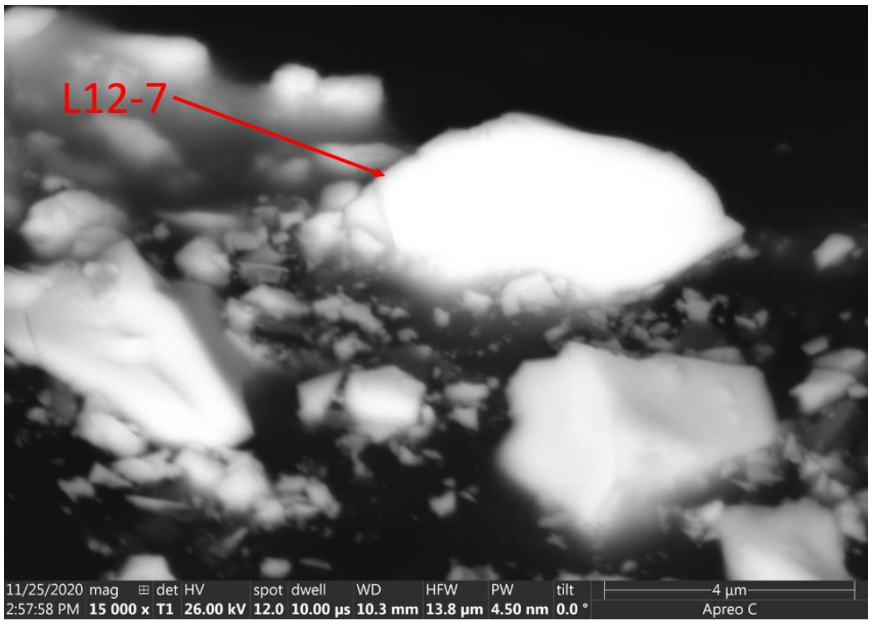

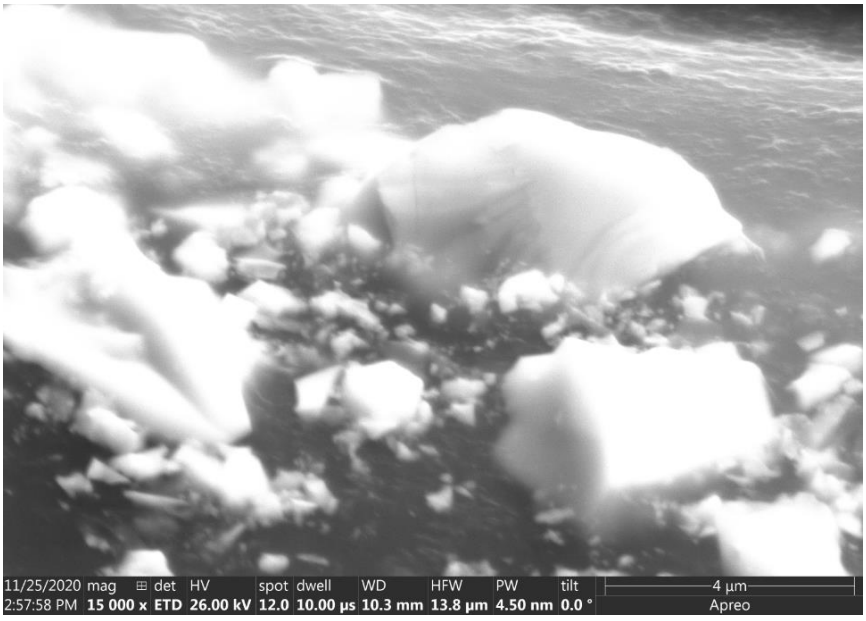

Figure 106. Particle L12-7 SEM Images

Appendix D. HPGe, XRF, and EDS Spectra Repository

The HPGe detector, XRF, and SEM/EDS raw spectra used in this research can be found in a private GitHub repository located at:

https://github.com/BOMARC-Raw-Data/BOMARC_raw_data

To access the repository and the raw spectra therein, contact the author, Dr. Gaiven Varshney of AFIT, or Dr. Abigail Bickley of AFIT for access.

Appendix E. Particle EDS Data

The following tables show the EDS generated qualitative at% composition for all 70 particles analyzed in this research.

Table 24. EDS Data for Particles E4-1 through G10-2

Particle	U	O	Al	Si	Fe	Na	Mg	Cl	Ca	Ni	S	Re	Cu	K	Ti	Cs	F	Zr	V	Cr	Mn
E4-1	20.04	75.80	1.02	2.45	0.69																
A6-1	19.14	70.46	1.84	8.56																	
B7-1	14.90	66.79	0.87	16.64	0.21		2.31					0.07									
B7-2	20.99	67.41	0.42	10.87	0.31																
I6-1	17.39	77.38	0.79	4.08	0.35																
A1-4	15.86	77.72	1.53	4.56	0.33																
A1-5	29.14	55.02	1.39	13.79	0.66																
A1-7	34.92	58.69	1.55	4.15	0.69																
A1-9	17.92	50.62	7.52	16.84	1.96	1.16		0.86						3.11							
A1-11	30.75		12.92	54.67	1.66																
A1-14	67.82		9.18	21.41	1.60																
A1-19	18.65	76.94	1.63	1.96	0.82																
A9-2	17.78	79.58	0.92	1.50	0.23																
D8-2	16.98	78.60	1.23	1.97	1.22																
G1-1	24.75	45.32	3.07	14.35	2.44	2.77		2.41						2.71	2.17						
I11-2	12.83	81.07	1.58	4.17	0.35																
K5-2	8.61	64.03	12.27	14.49	0.60																
K5-4	9.13	74.58	4.06	11.75	0.47																
L2-2	77.37	19.85	0.74	1.62	0.42																
L10-4	96.62		0.75	1.77	0.86																
L10-5	65.67	22.67	2.15	8.54	0.98																
L10-6	73.49	21.06	1.52	3.33	0.60																
L12-3	71.67	22.46	1.55	3.18	0.58					0.57											
L12-4	47.04	29.65	2.91	13.76	2.87		0.35							1.42				2.00			
L12-5	28.10	38.11	4.05	18.11	6.74					2.13				2.75							
L12-6	72.09	23.01	0.71	3.37	0.82																
D8-1	24.30	72.85	1.21	1.28	0.36																
F10-5	41.61	56.52	0.81	1.06																	
F10-6	19.18	75.23	1.13	3.93	0.28					0.25											
A1-6	23.68	72.18	1.39	2.40	0.35																
A1-8	23.74	72.01	1.49	2.41	0.36																
A1-15	22.35	75.33	0.76	1.31	0.27																
A1-16	84.53		4.51	9.49	1.47																
A1-17	19.89	71.78	1.34	6.55	0.44																
A1-20	17.45	79.71	1.26	1.10	0.47																
I11-1	12.83	81.07	1.58	4.17	0.35																
I11-3	20.85	74.92		3.90	0.34																
I11-4	24.14	68.05	1.92	5.36	0.53																
K5-1	13.41	72.95	3.28	8.02	0.77	1.23		0.35													
K5-3	16.77	61.18	4.30	12.90	3.43									1.42							
L2-1	48.83	10.53	2.79	6.53	1.44	1.07								3.79		25.02					
L8-4	79.95	17.74	0.36	1.07	0.88																
L8-6	48.87	31.44	4.94	12.04	1.55	0.91	0.26														
L8-7	77.80	19.08	0.68	2.02	0.42																
L10-2	69.63	19.25	1.38	4.26	5.47																
L10-3	46.96	30.28	2.45	4.78	1.75		0.35							0.45	13.15				0.48		
L12-1	23.43	69.54	0.70	5.71	0.63																
L12-2	80.27	17.28	0.46	1.49	0.50																
L12-7	78.10	18.25	0.45	2.80	0.28					0.12											
F10-1	12.67	75.46	1.54	9.47	0.45					0.42											
F10-2	18.93	71.71	0.91	3.06	0.28					15.86											
F10-3	26.25	65.79	0.98	6.58	0.40																
F10-4	15.50	77.52	1.12	5.28	0.31					0.26											
L8-2	15.36	41.63	2.41	1.60	27.23					6.18										16.02	1.33
G10-2	20.19	51.49	1.57	20.78	0.24	11.57		5.24		0.26	0.47	0.13									

Table 25. EDS Data for Particles A1-2 through G10-1

Particle	U	O	Al	Si	Fe	Na	Mg	Cl	Ca	Ni	S	Re	Cu	K	Ti	Cs	F	Zr	V	Cr	Mn
A1-2	27.47	65.72	1.34	5.19	0.27																
A1-3	20.98	65.18	1.68	6.97	0.49	3.28		1.28					0.15								
A1-10	23.69	68.23	2.44	4.44	0.43			0.78													
A1-12	17.45	79.71	1.26	1.10	0.47																
A1-13	18.70	56.39	2.55	12.22	2.03		1.09		2.62					4.40							
A1-18	21.67	73.44	0.82	3.83	0.24																
A9-1	16.24	68.75	1.70	9.26	1.19	2.41				0.18										0.27	
F2-1	19.54	74.87	1.58	3.67	0.34																
L8-3	76.14	20.44	2.30	0.74	0.37																
L8-5	48.75	26.38	2.94	13.47	1.67	0.28									2.89		3.61				
L10-1	79.80	14.77	1.03	3.44	0.96																
A1-1	26.04	71.38	1.66	0.92																	
L8-1	22.65	74.11	1.03	1.14	1.07																
G6-1	14.77	56.27	1.21	27.08		0.72			1.03		0.27	0.01									
G10-1	28.21	64.85	5.19	1.75																	

Appendix F. Gamma Spectroscopy Spectra

The following figures show the gamma spectroscopy spectra collected using an HPGe detector.

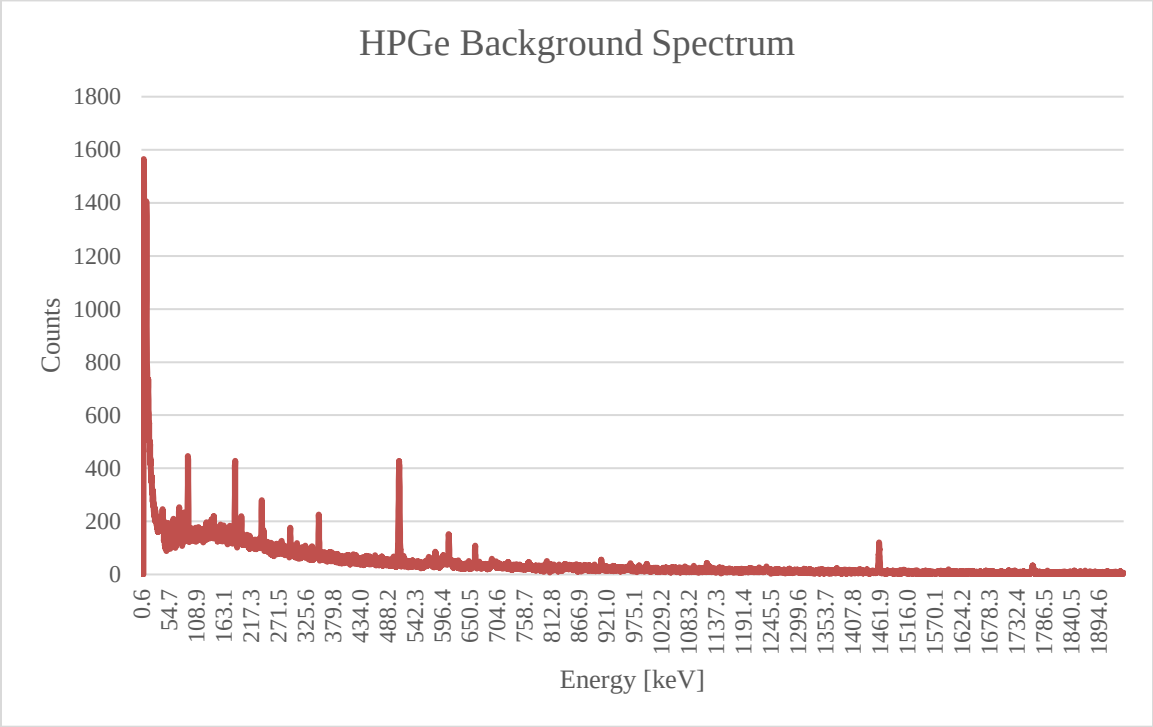

Figure 107. HPGe Background Spectrum

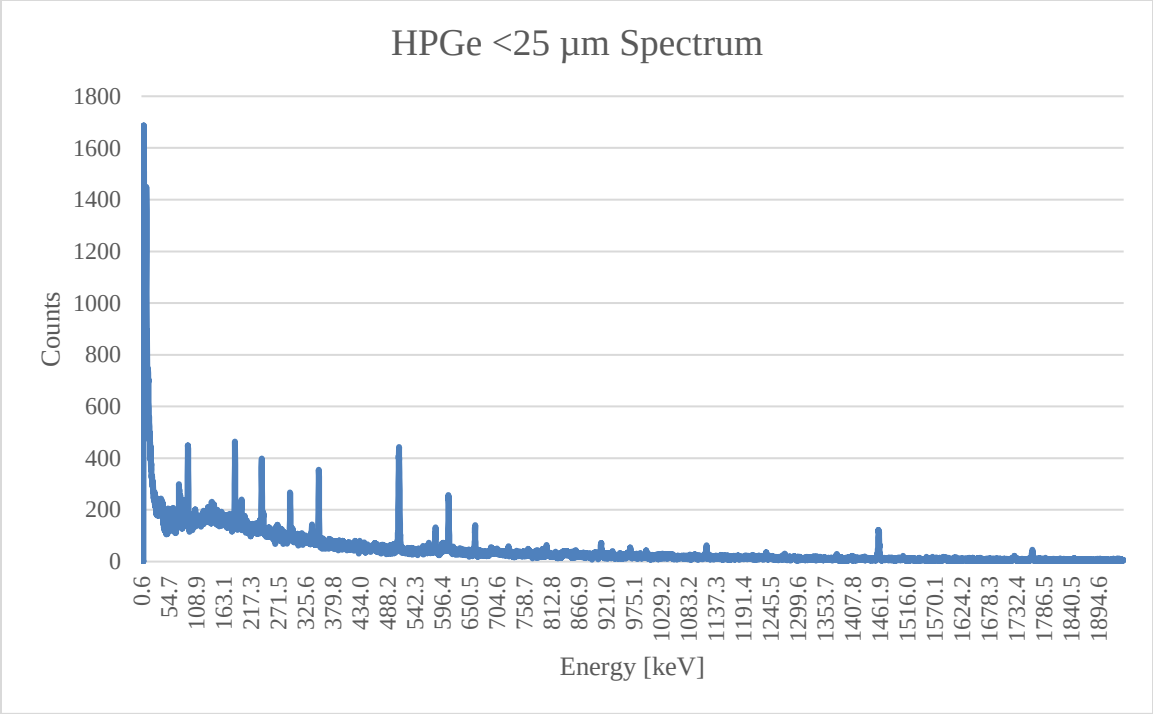

Figure 108. HPGe <25 µm Spectrum

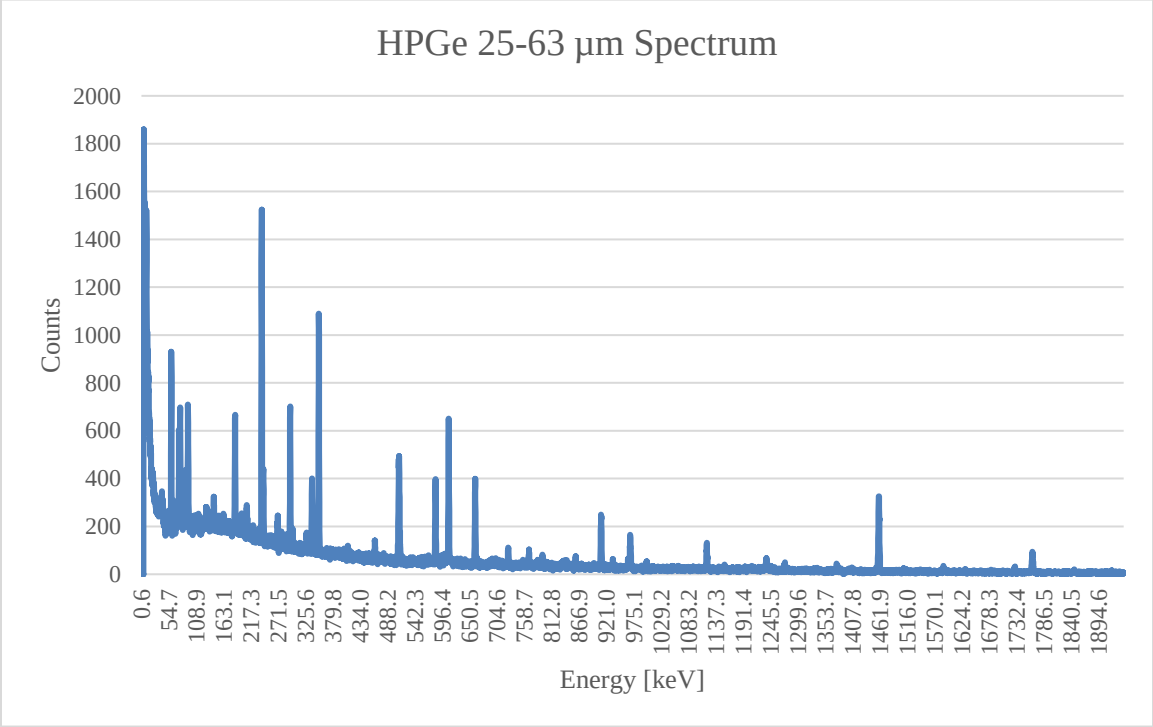

Figure 109. HPGe 25-63 µm Spectrum

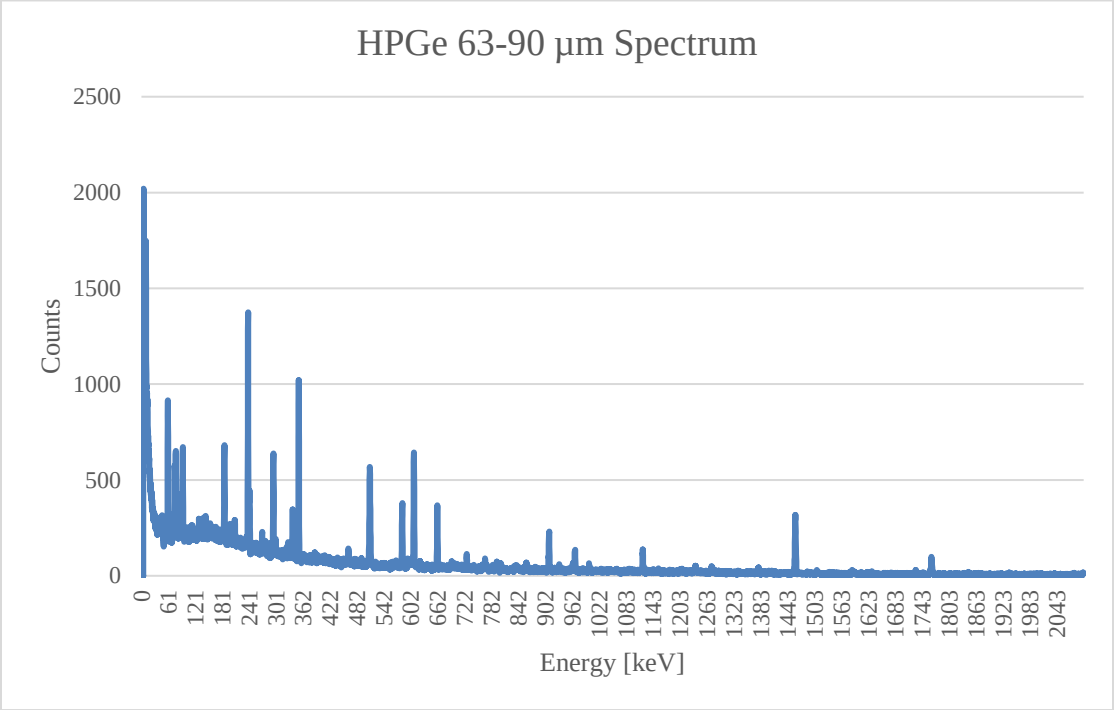

Figure 110. HPGe 63-90 µm Spectrum

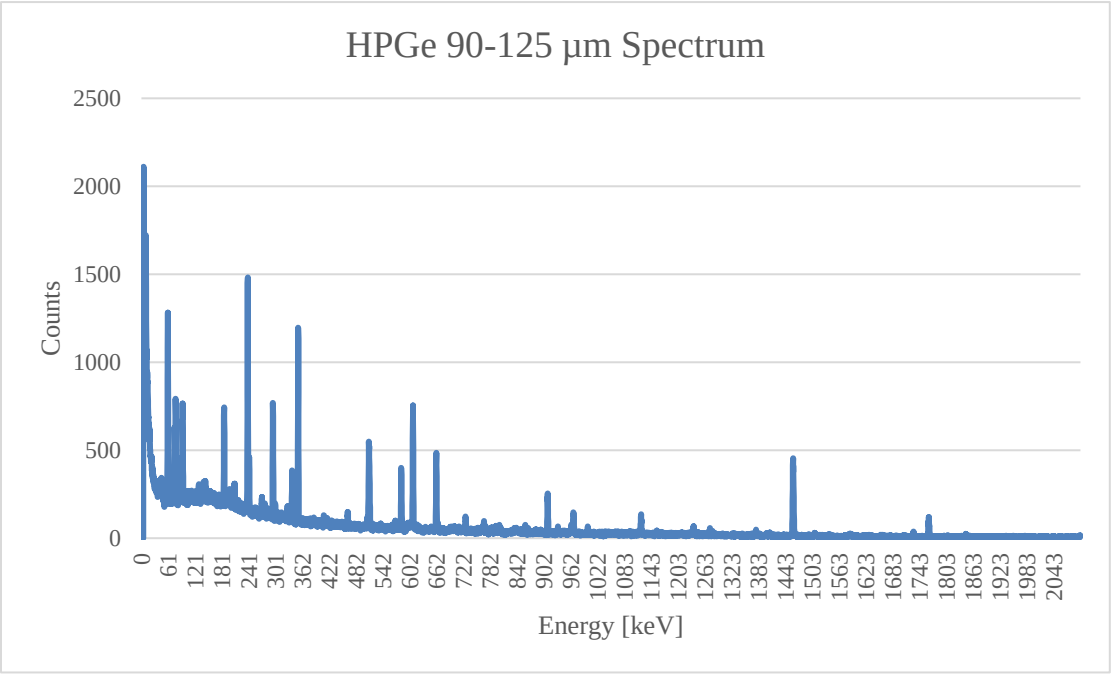

Figure 111. HPGe 90-125 µm Spectrum

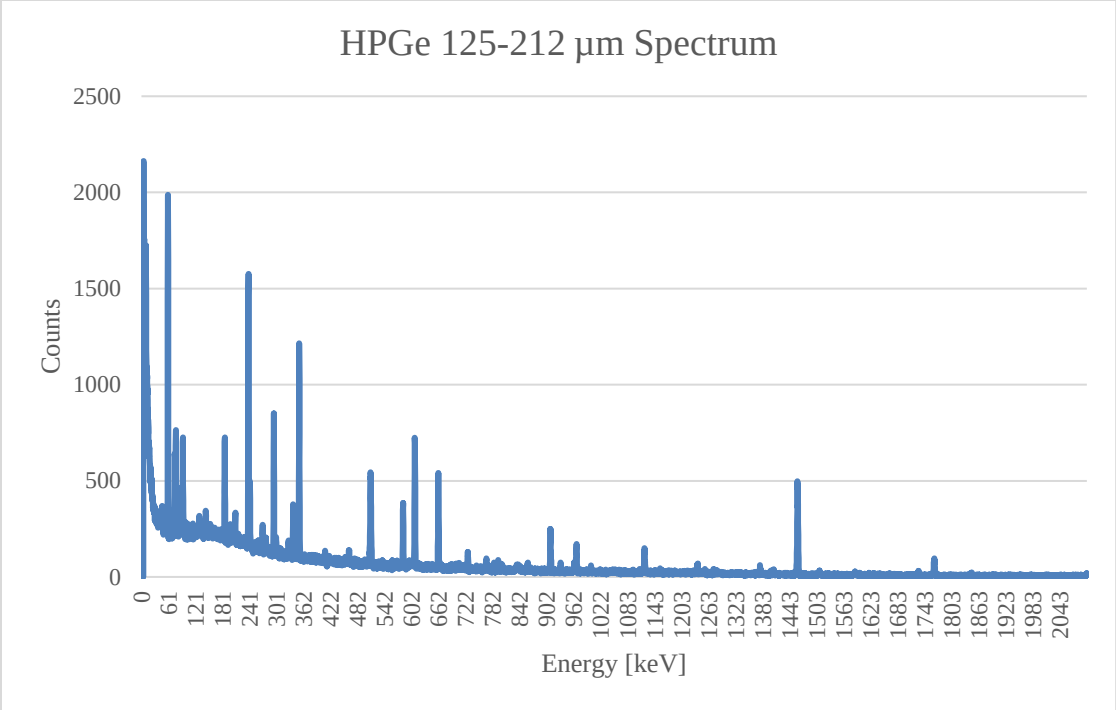

Figure 112. HPGe 125-212 µm Spectrum

Appendix G. XRF Spectra

The following figures show the characteristic X-ray spectra collected using the Horiba XGT-7200V XRF.

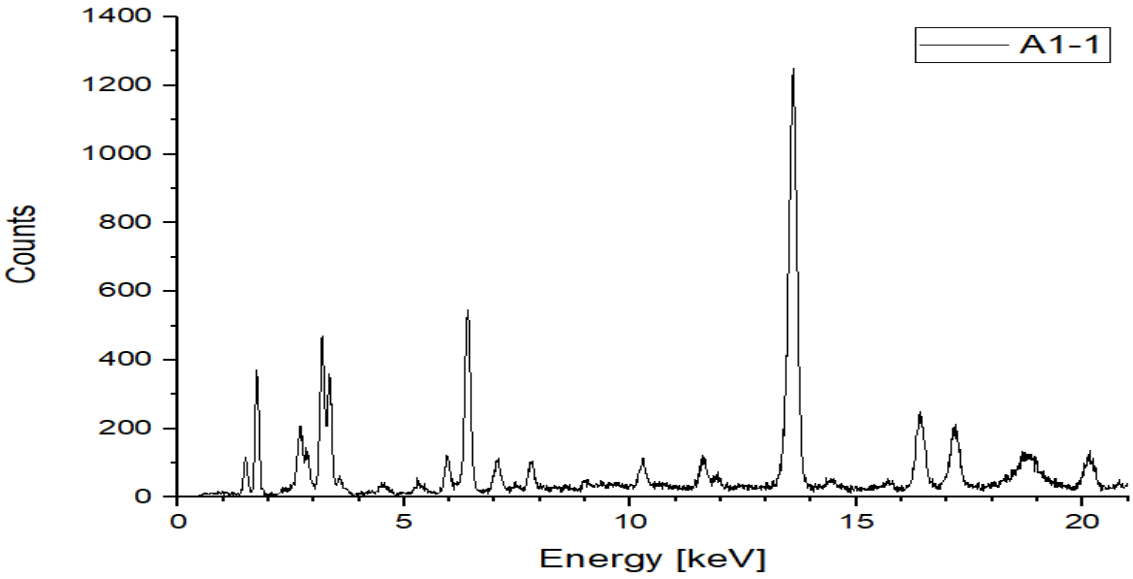

Figure 113. Particle A1-1 XRF Spectrum

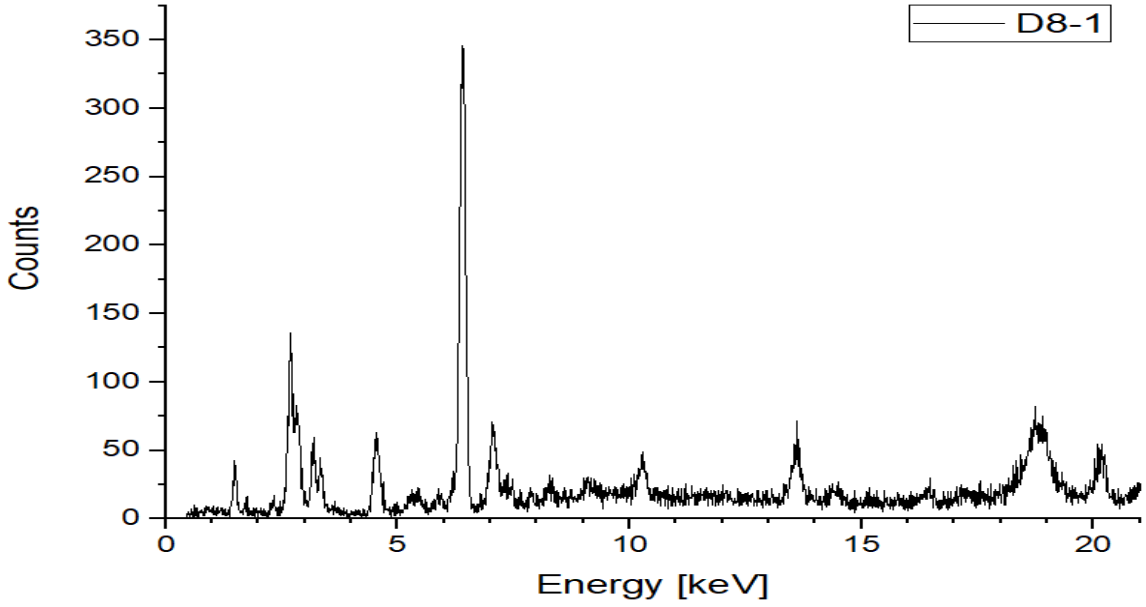

Figure 114. Particle D8-1 XRF Spectrum

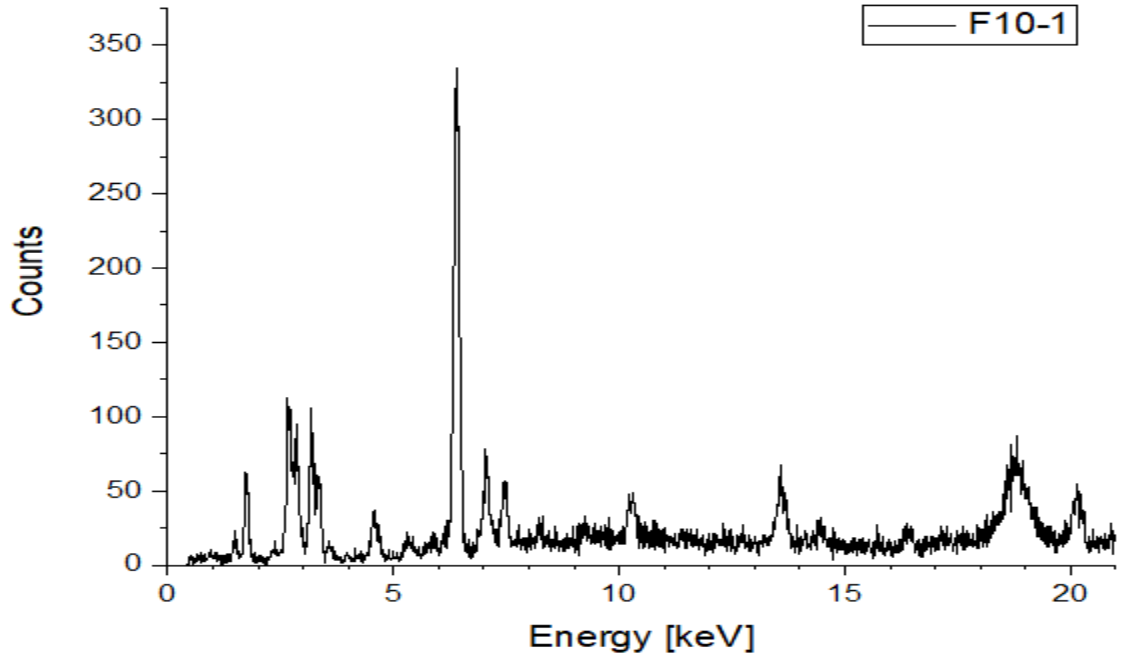

Figure 115. Particle F10-1 XRF Spectrum

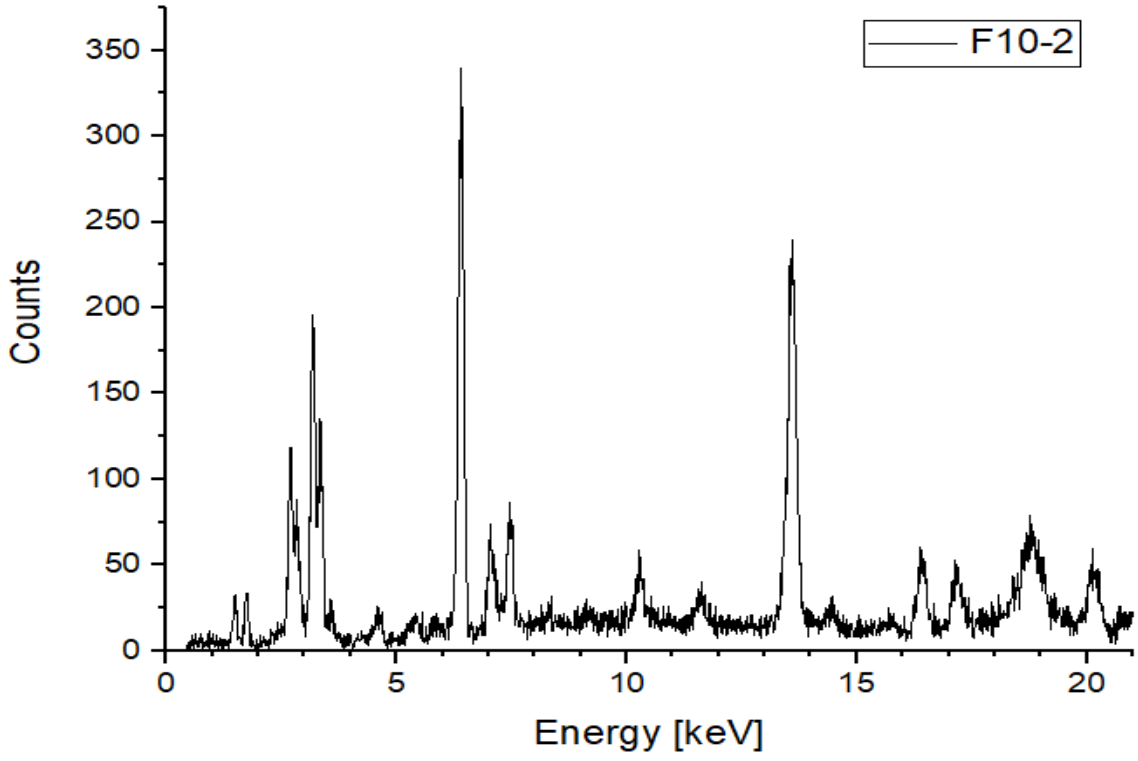

Figure 116. Particle F10-2 XRF Spectrum

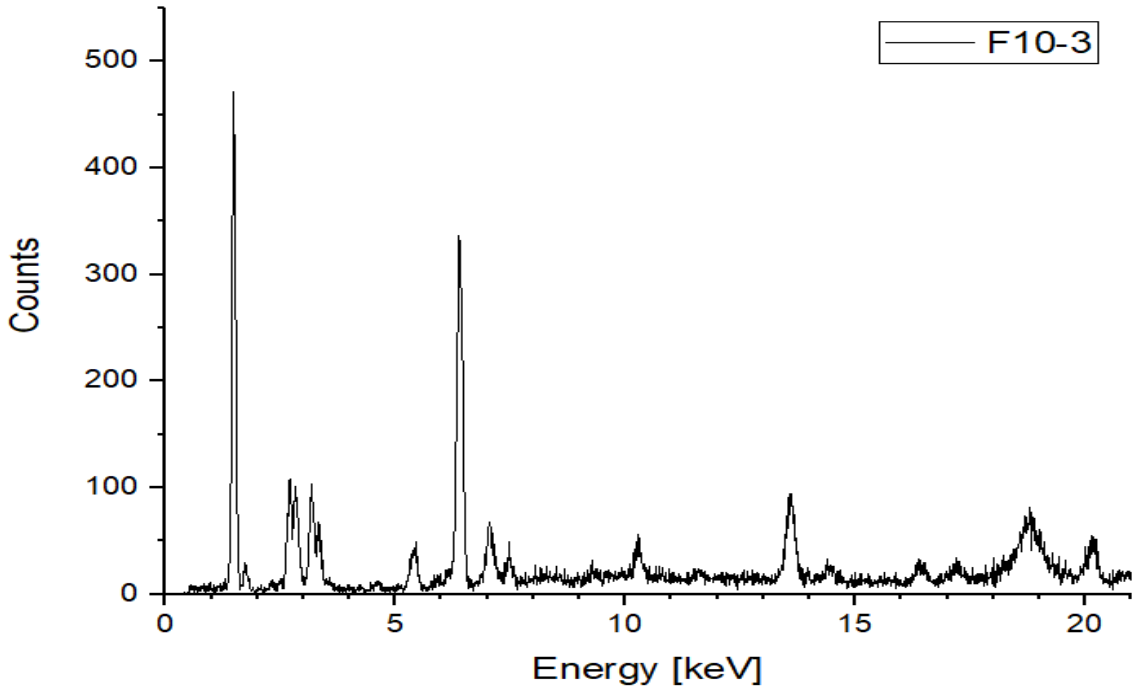

Figure 117. Particle F10-3 XRF Spectrum

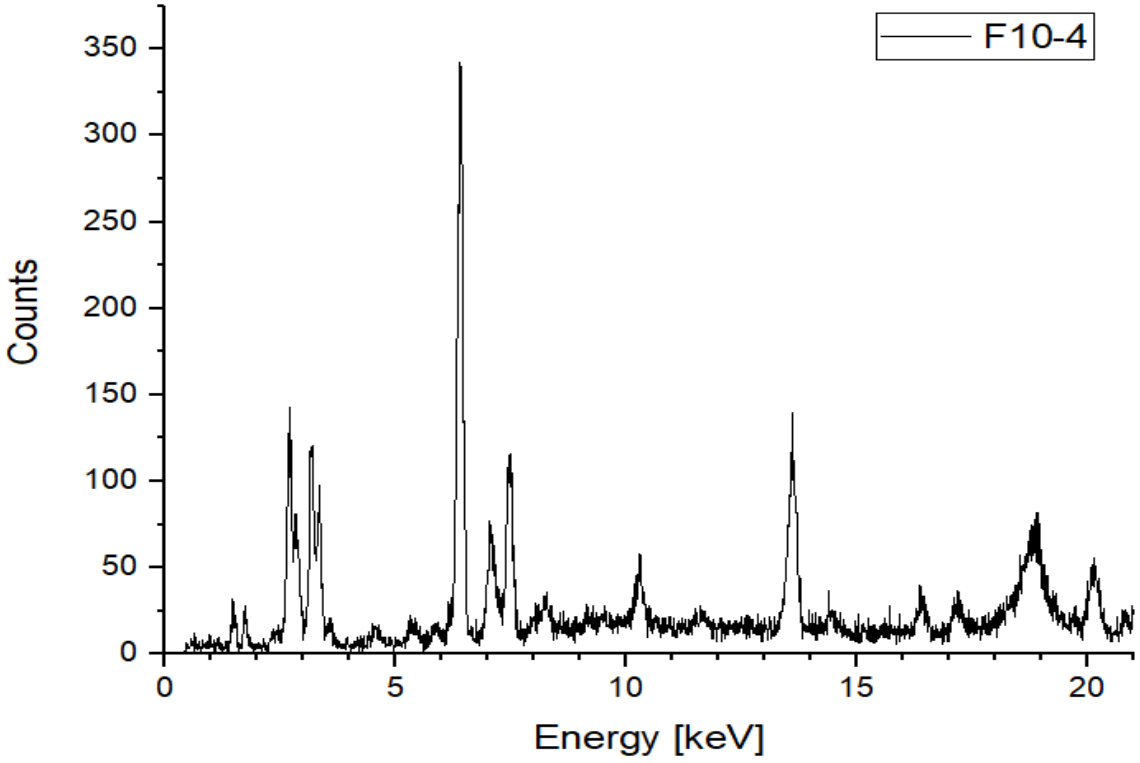

Figure 118. Particle F10-4 XRF Spectrum

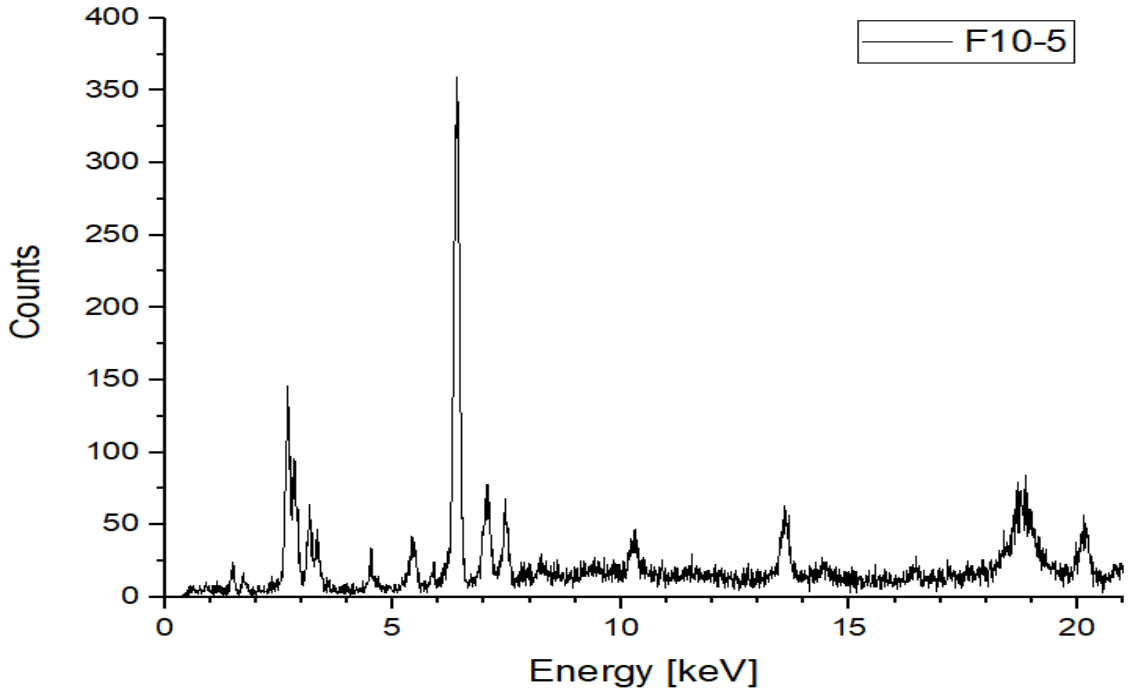

Figure 119. Particle F10-5 XRF Spectrum

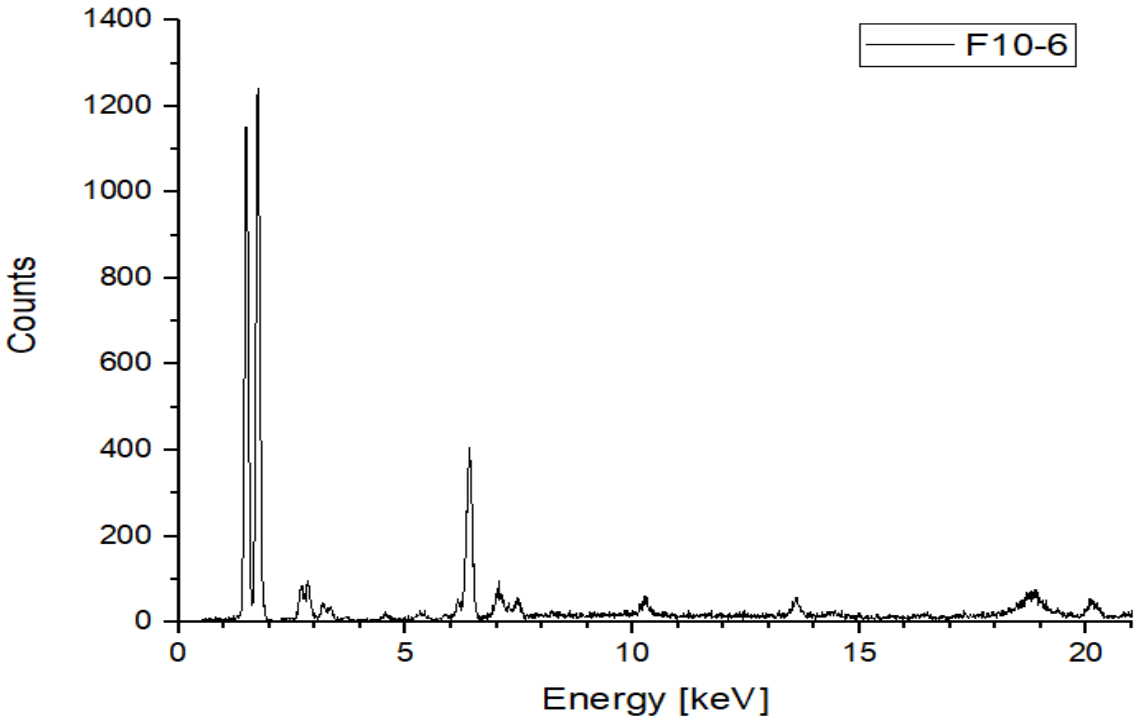

Figure 120. Particle F10-6 XRF Spectrum

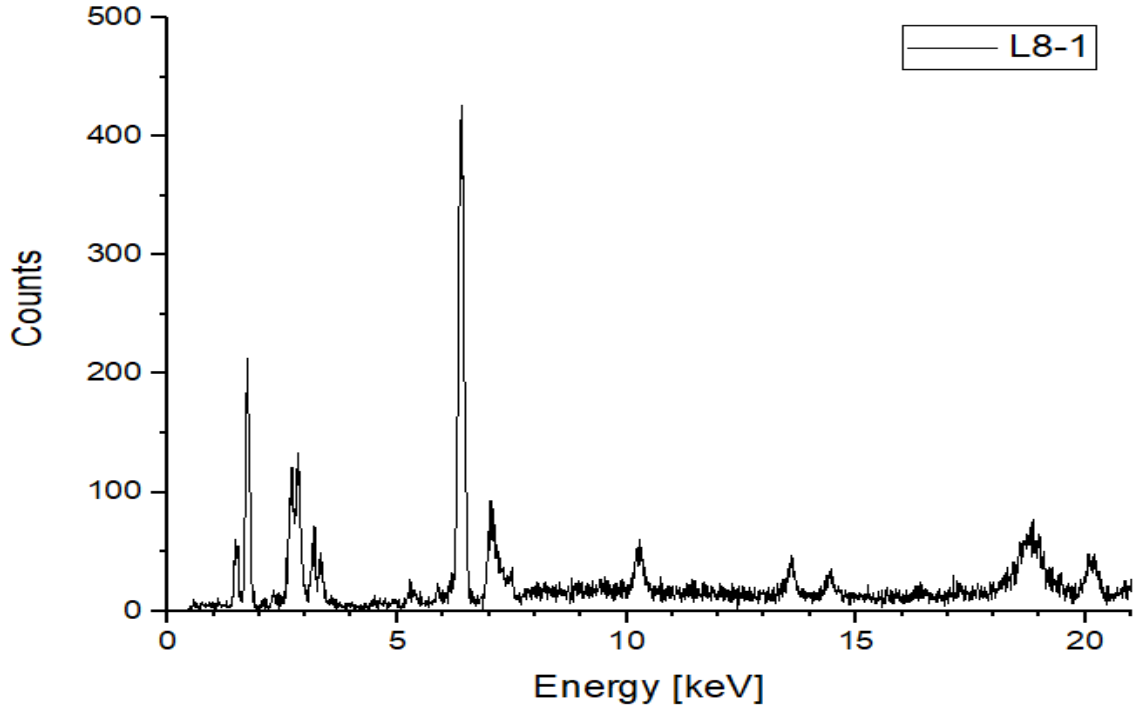

Figure 121. Particle L8-1 XRF Spectrum

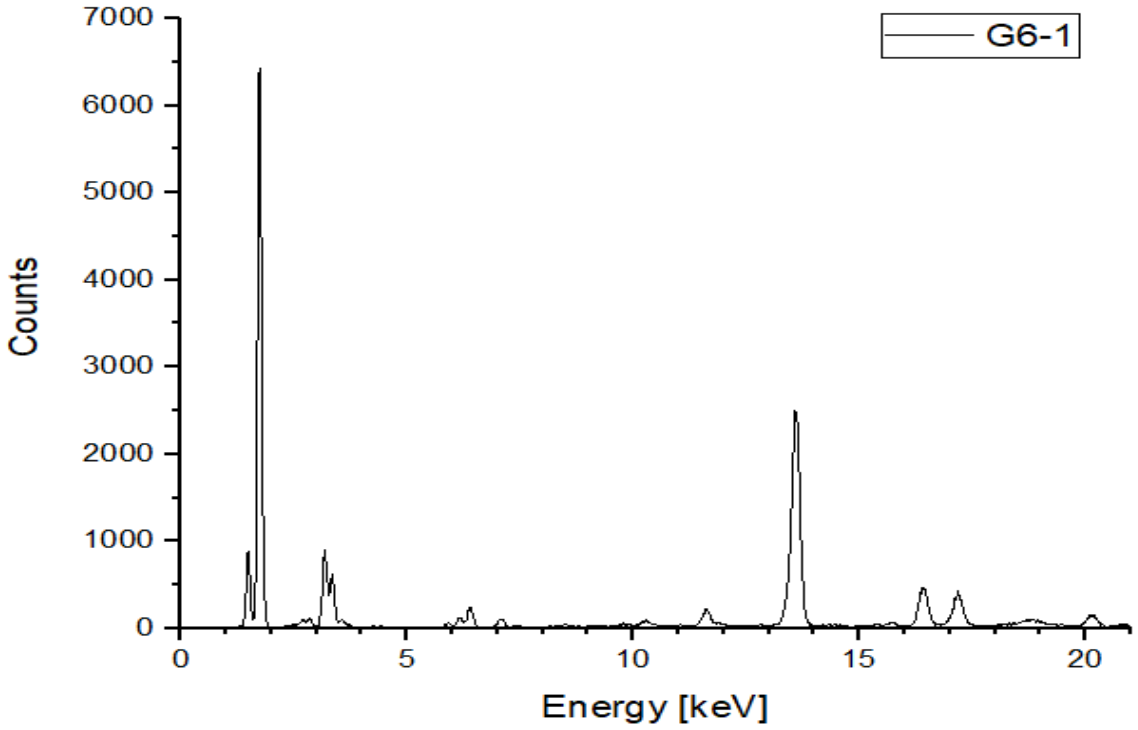

Figure 122. Particle G6-1 XRF Spectrum

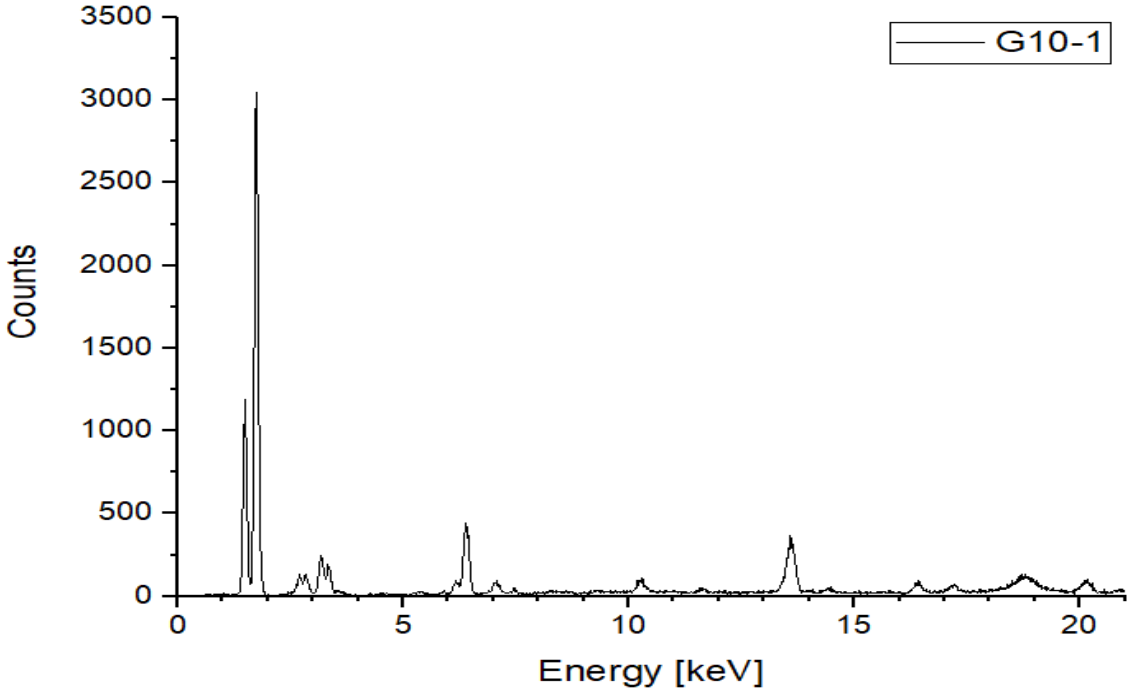

Figure 123. Particle G10-1 XRF Spectrum

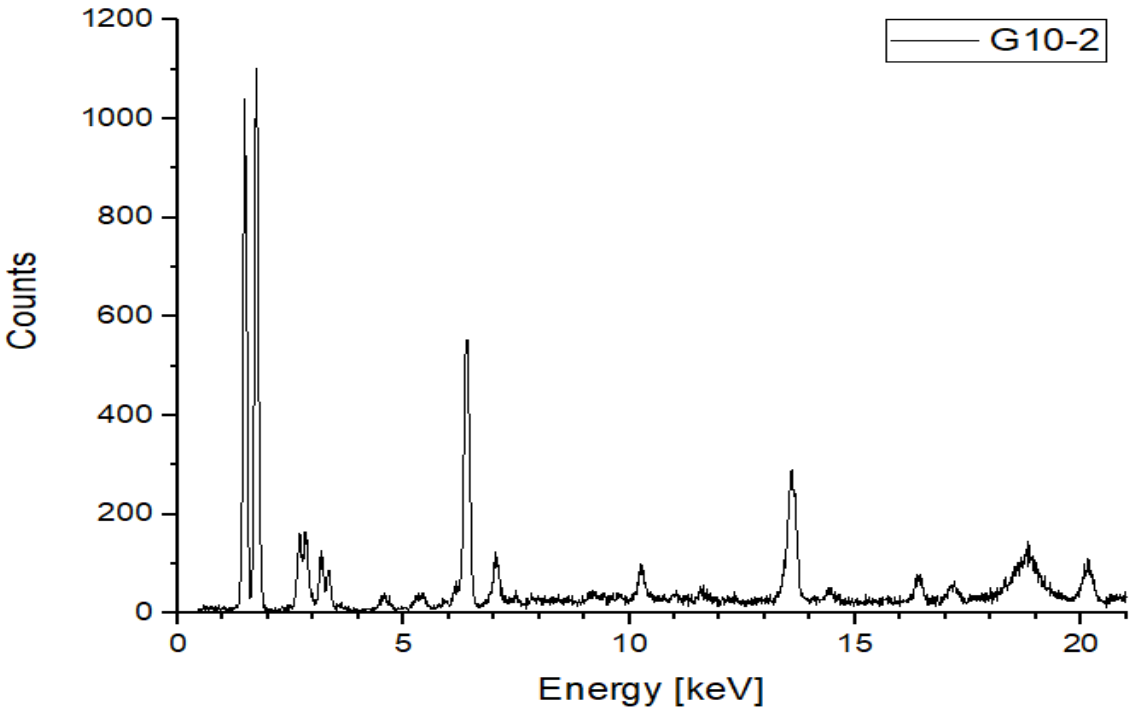

Figure 124. Particle G10-2 XRF Spectrum

Appendix H. EDS Spectra

The following figures show the characteristic X-ray spectra collected using the ThermoFisher Scientific Apreo C SEM microscope with Oxford Instruments Ultim Max 65 EDS.

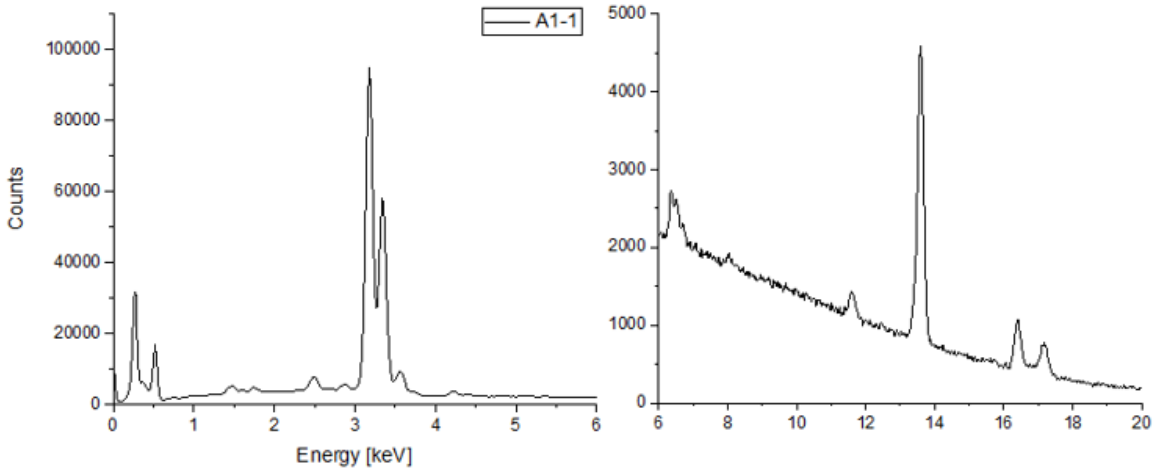

Figure 125. Particle A1-1 EDS Spectrum

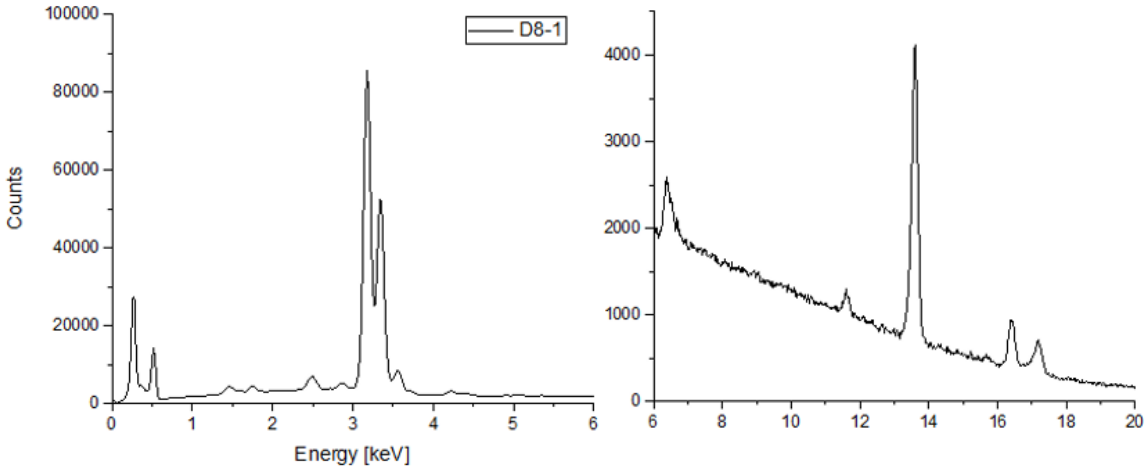

Figure 126. Particle D8-1 EDS Spectrum

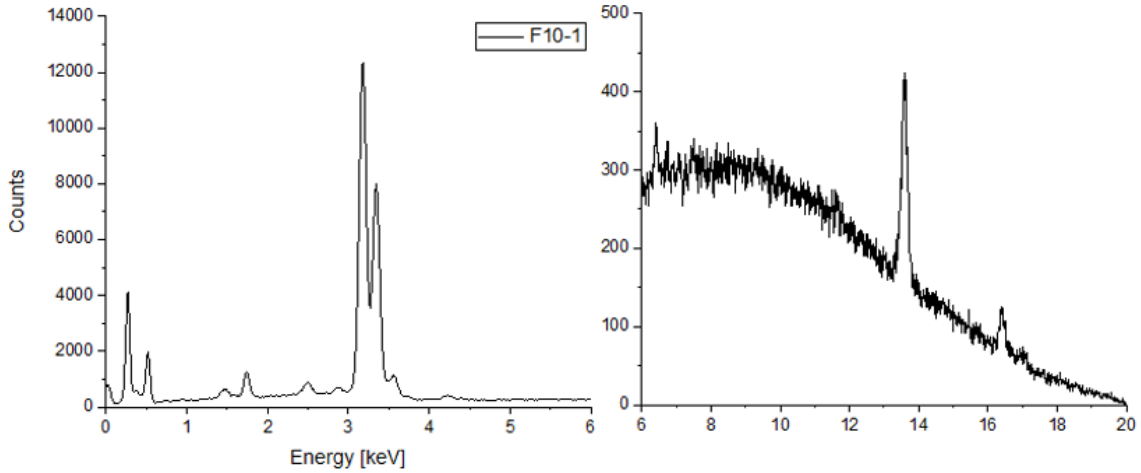

Figure 127. Particle F10-1 EDS Spectrum

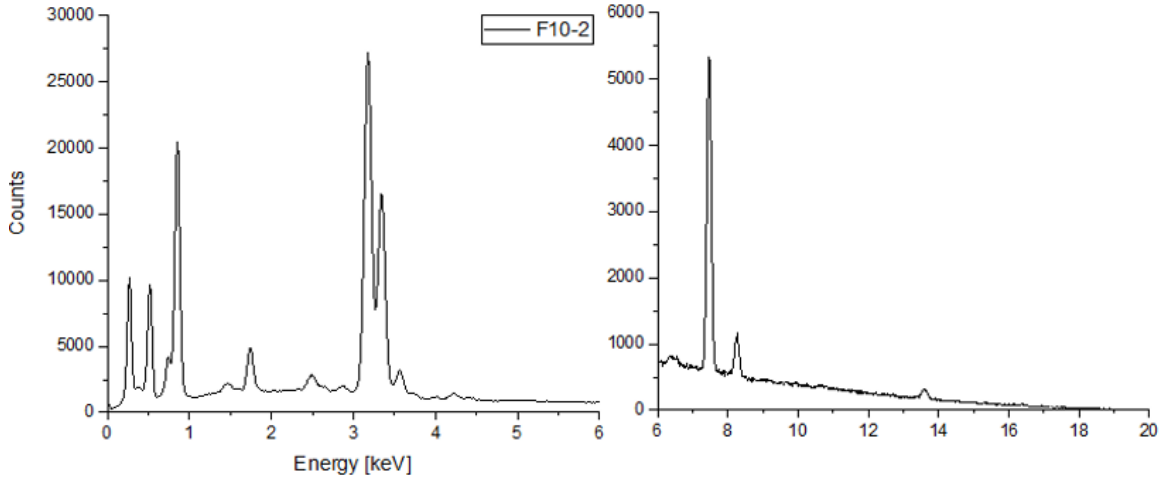

Figure 128. Particle F10-2 EDS Spectrum

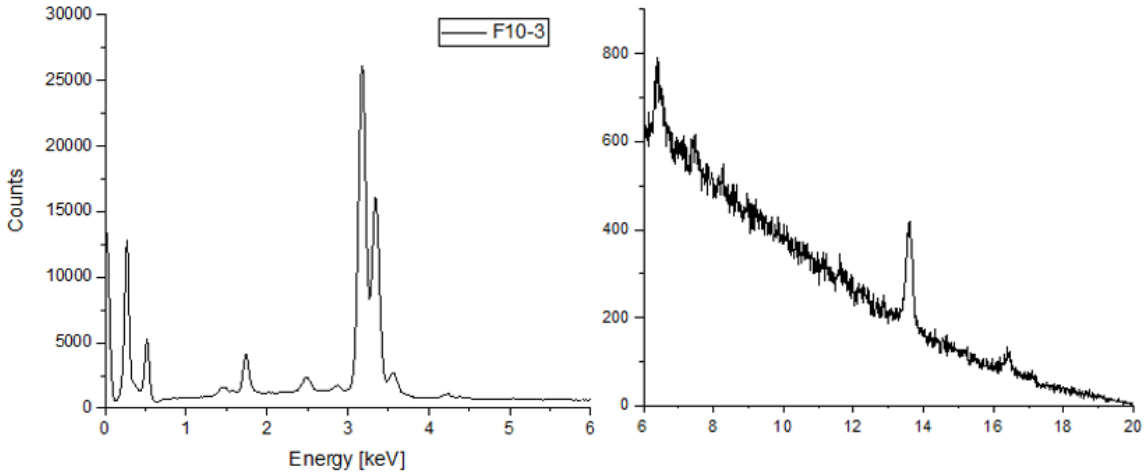

Figure 129. Particle F10-3 EDS Spectrum

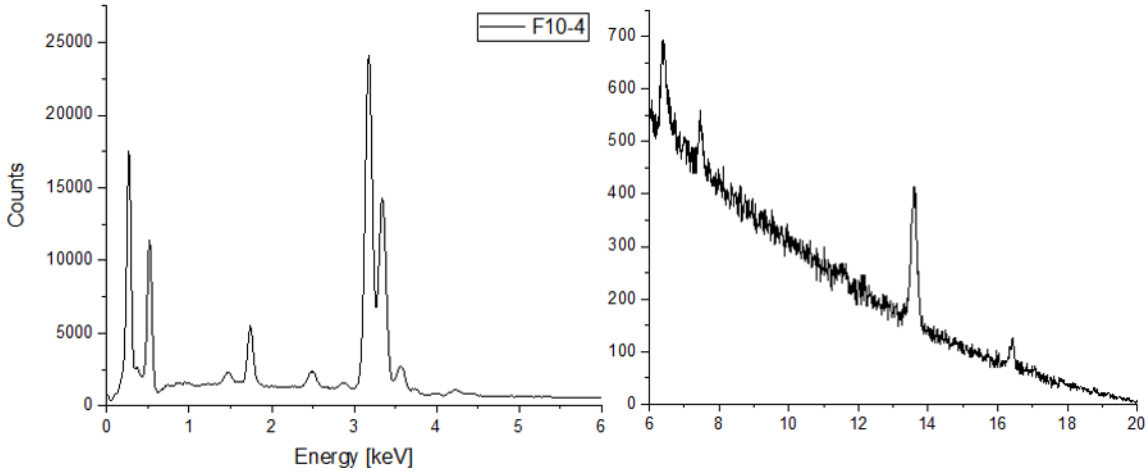

Figure 130. Particle F10-4 EDS Spectrum

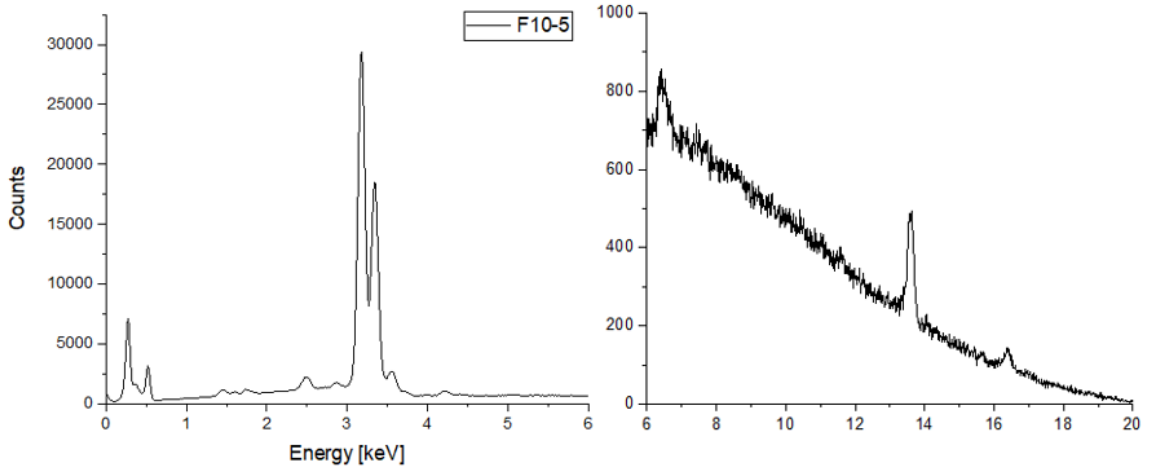

Figure 131. Particle F10-5 EDS Spectrum

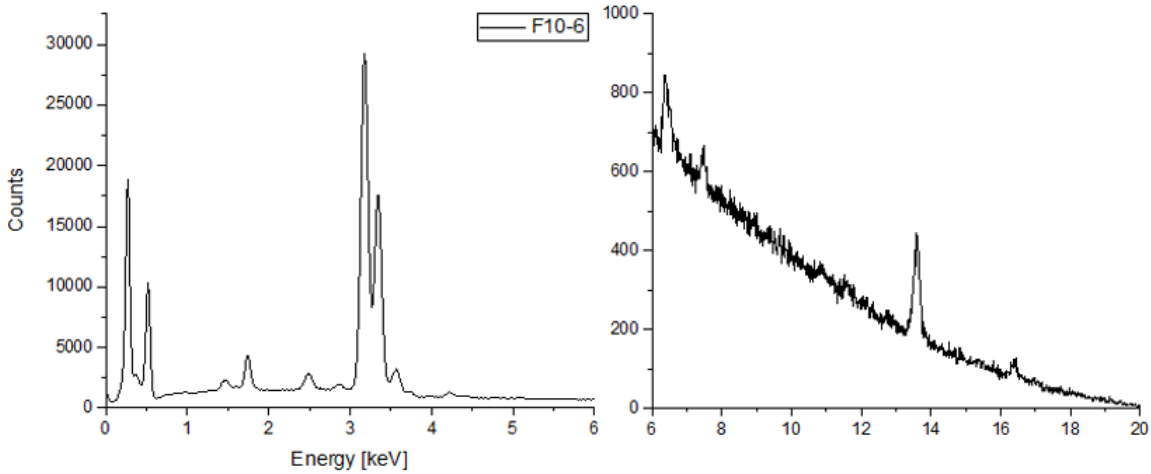

Figure 132. Particle F10-6 EDS Spectrum

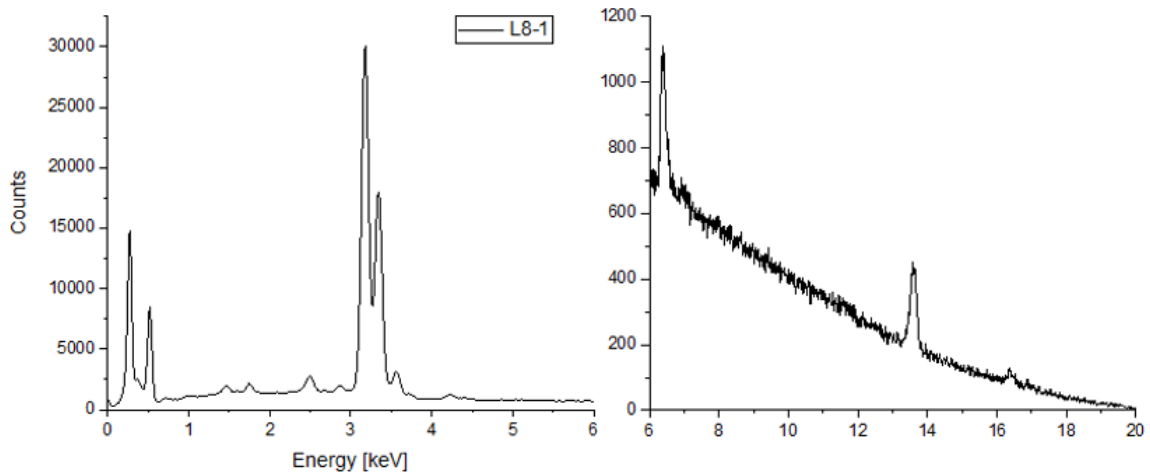

Figure 133. Particle L8-1 EDS Spectrum

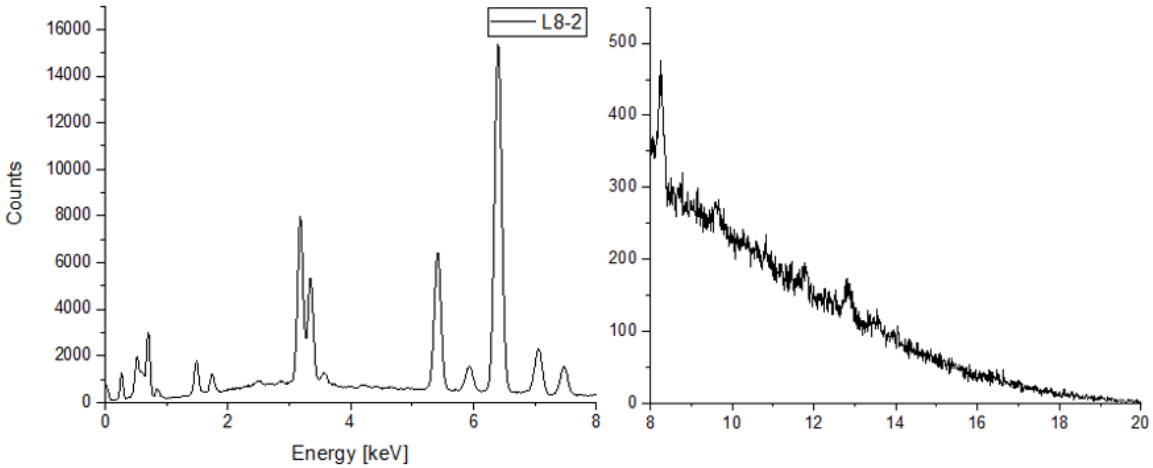

Figure 134. Particle L8-2 EDS Spectrum

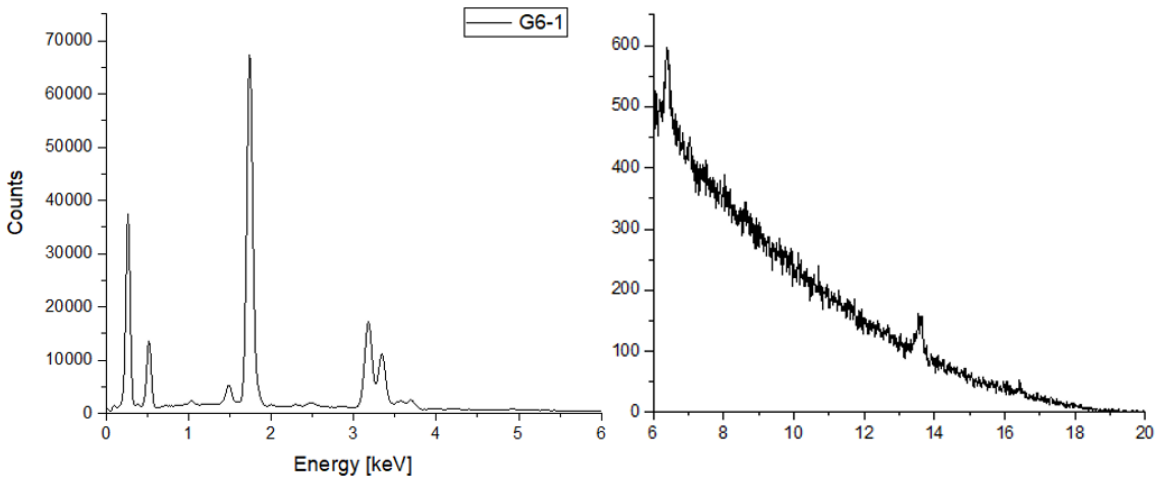

Figure 135. Particle G6-1 EDS Spectrum

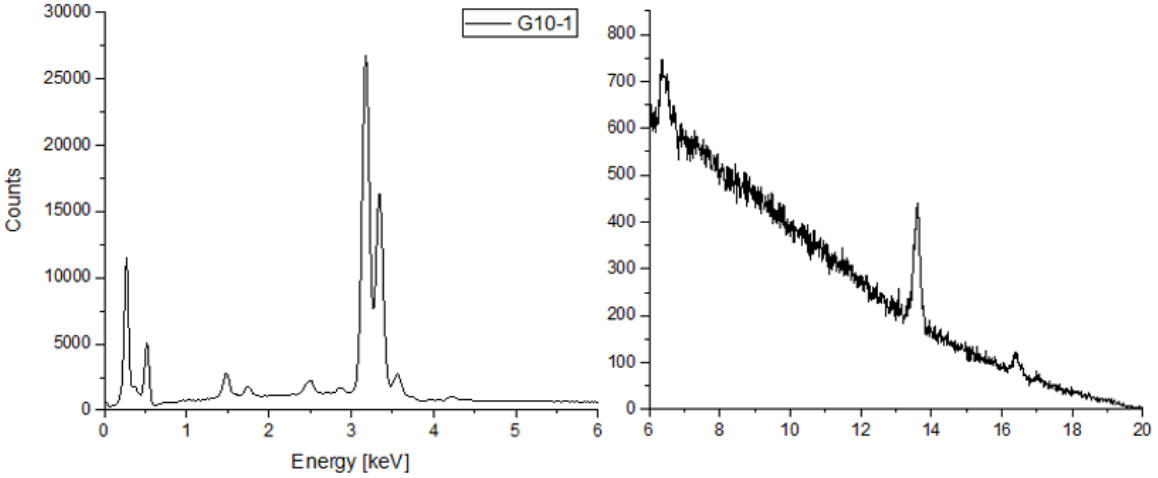

Figure 136. Particle G10-1 EDS Spectrum

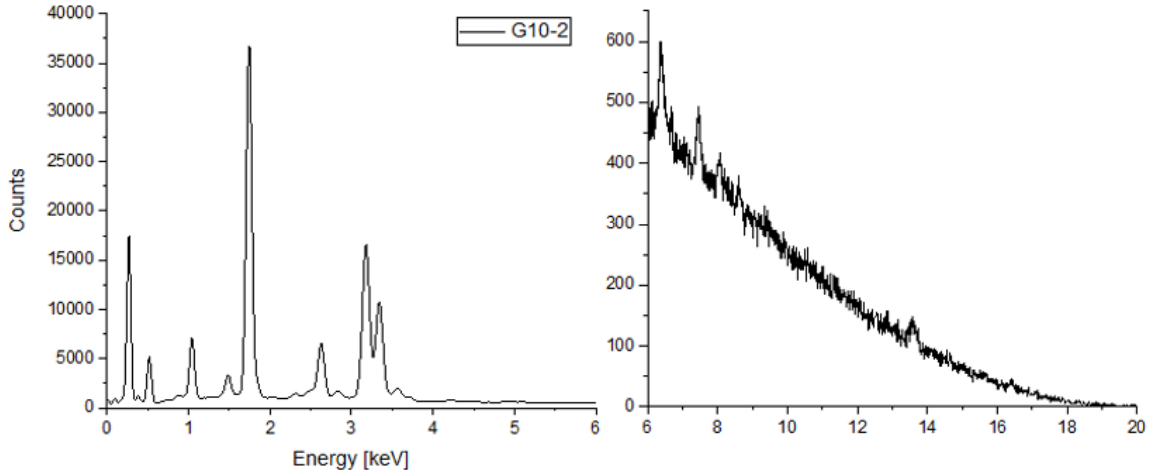

Figure 137. Particle G10-2 EDS Spectrum

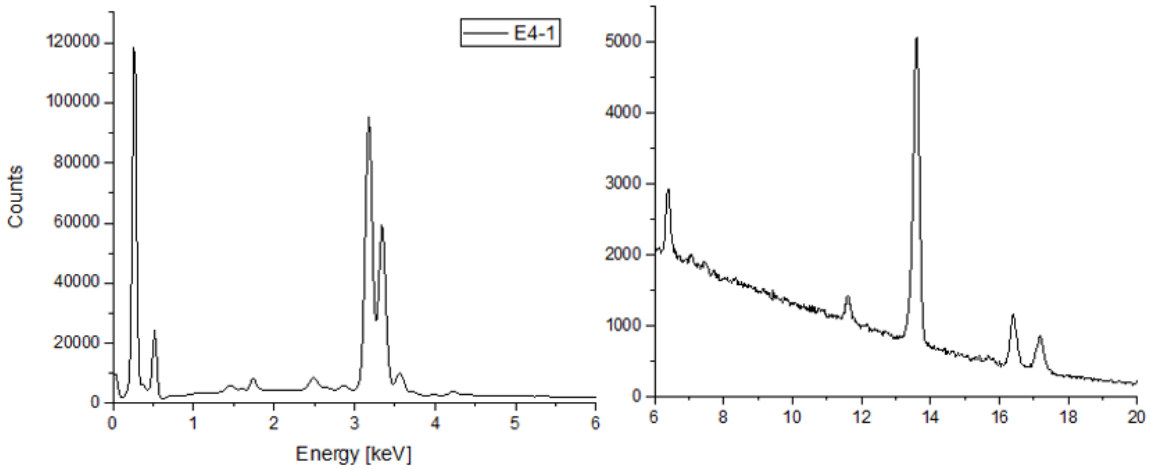

Figure 138. Particle E4-1 EDS Spectrum

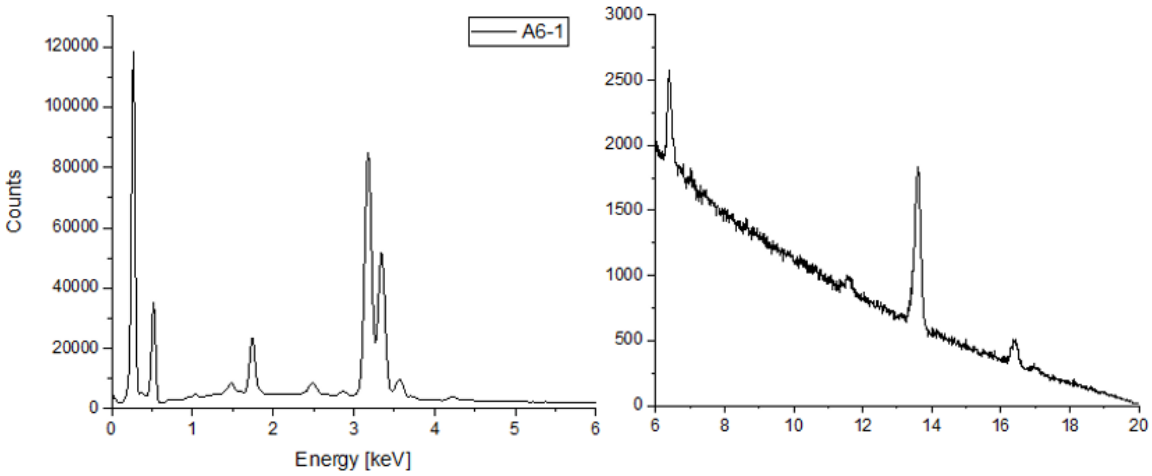

Figure 139. Particle A6-1 EDS Spectrum

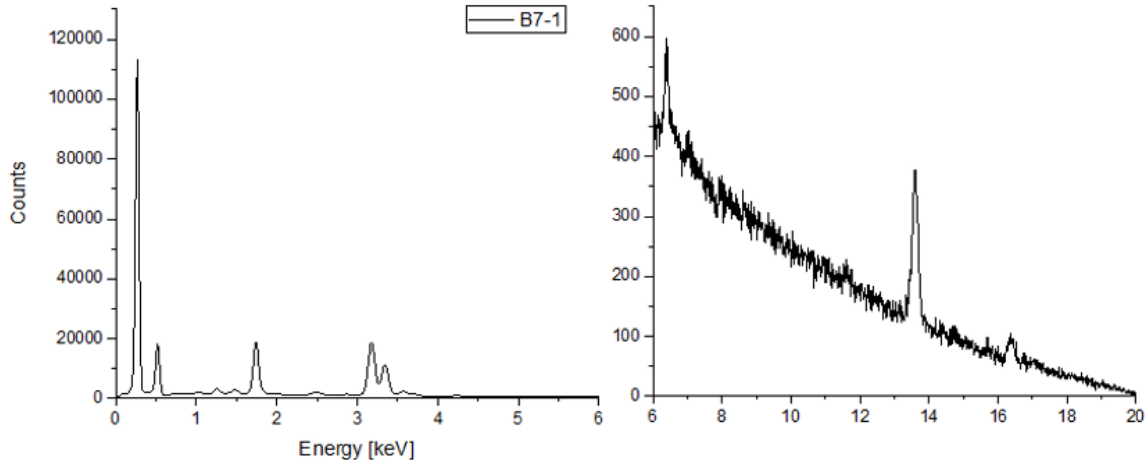

Figure 140. Particle B7-1 EDS Spectrum

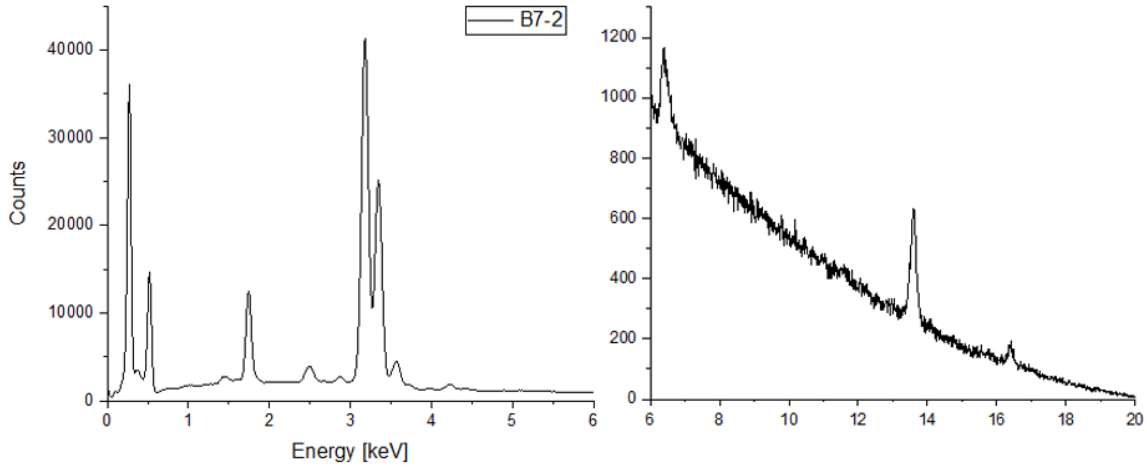

Figure 141. Particle B7-2 EDS Spectrum

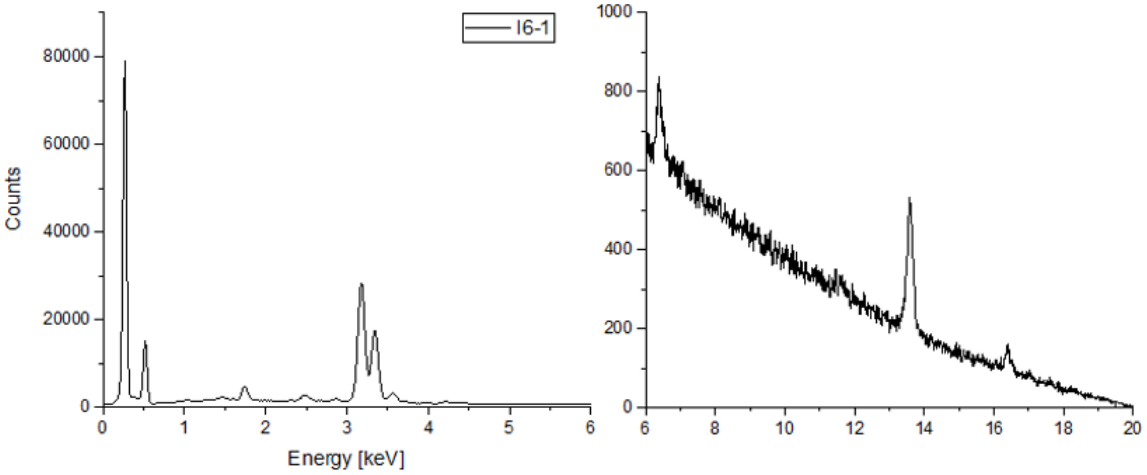

Figure 142. Particle I6-1 EDS Spectrum

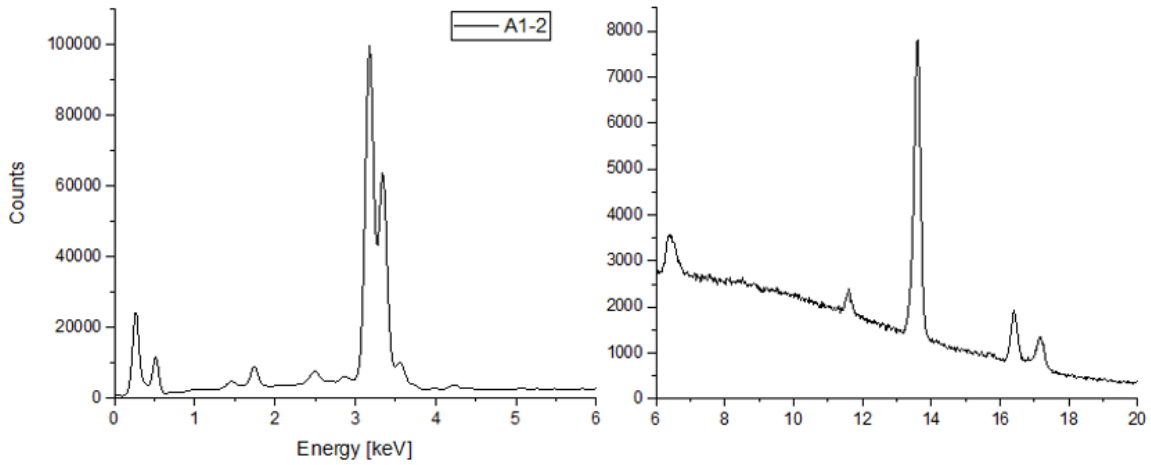

Figure 143. Particle A1-2 EDS Spectrum

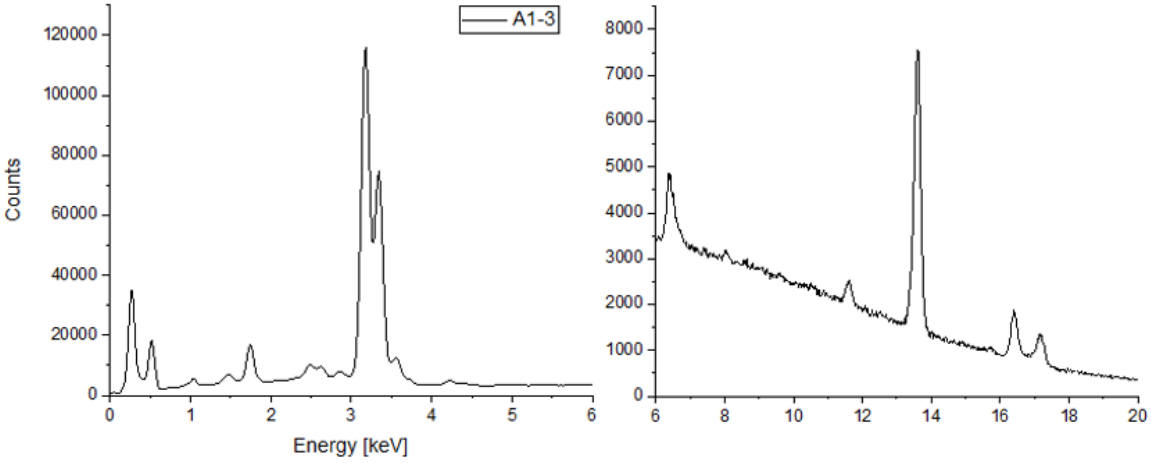

Figure 144. Particle A1-3 EDS Spectrum

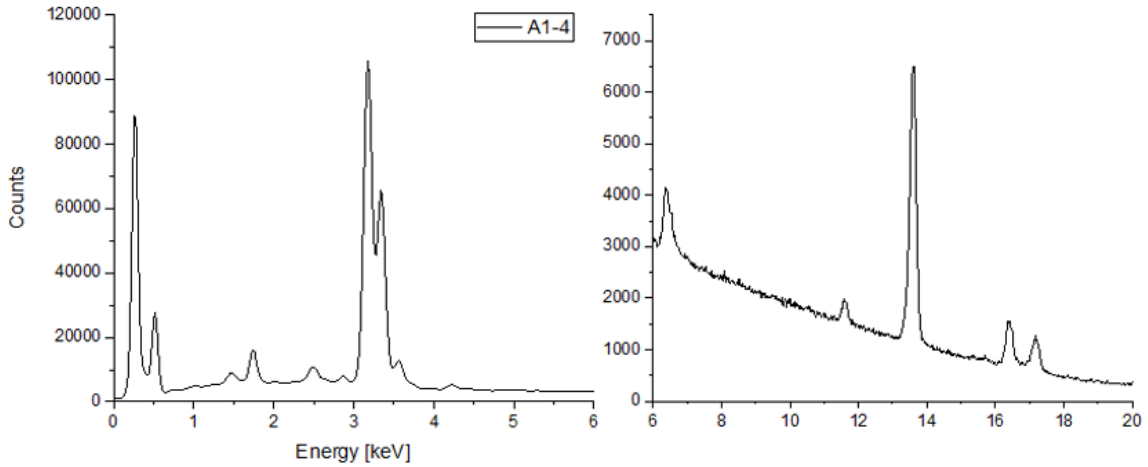

Figure 145. Particle A1-4 EDS Spectrum

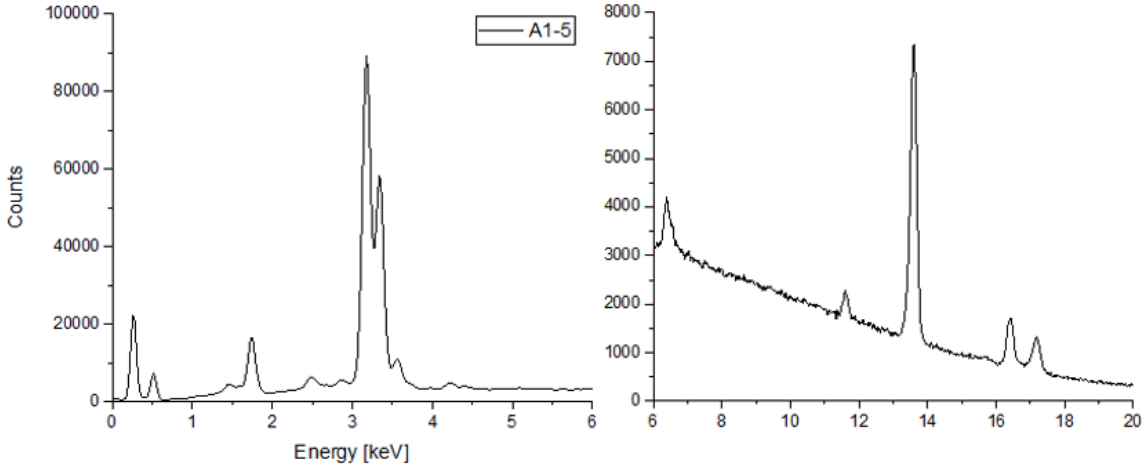

Figure 146. Particle A1-5 EDS Spectrum

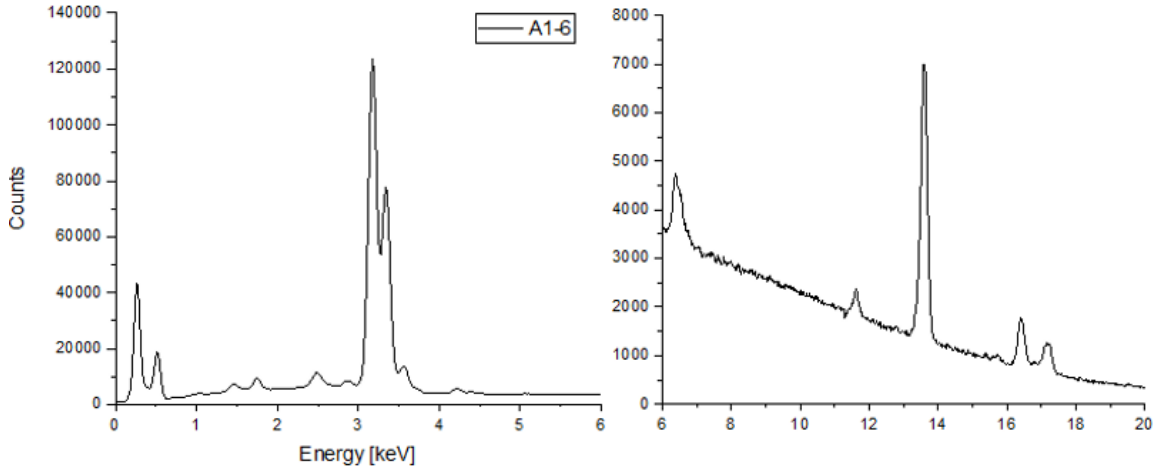

Figure 147. Particle A1-6 EDS Spectrum

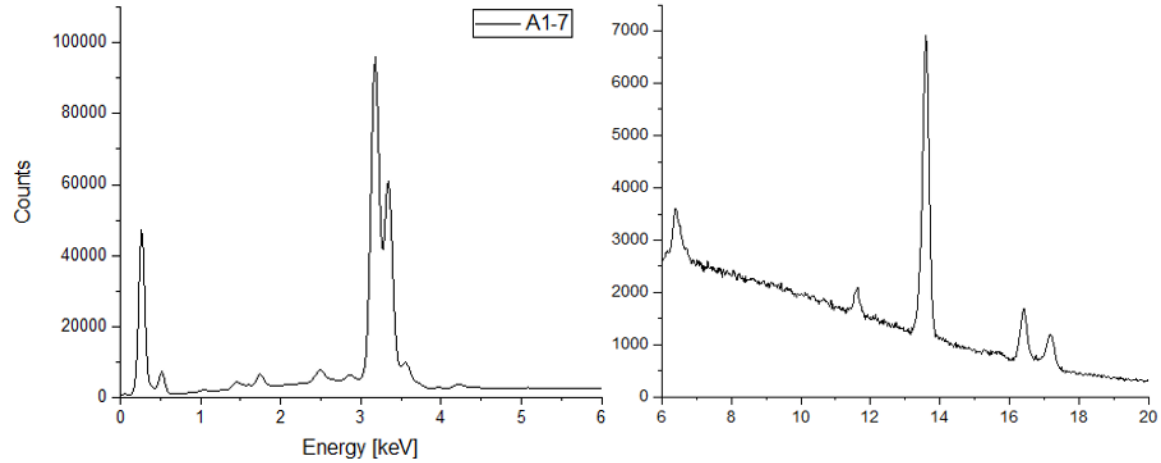

Figure 148. Particle A1-7 EDS Spectrum

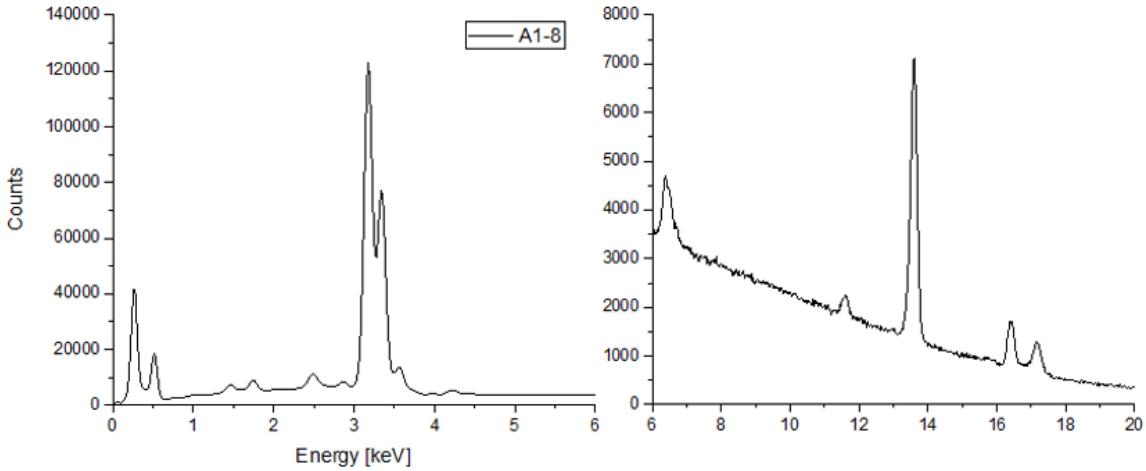

Figure 149. Particle A1-8 EDS Spectrum

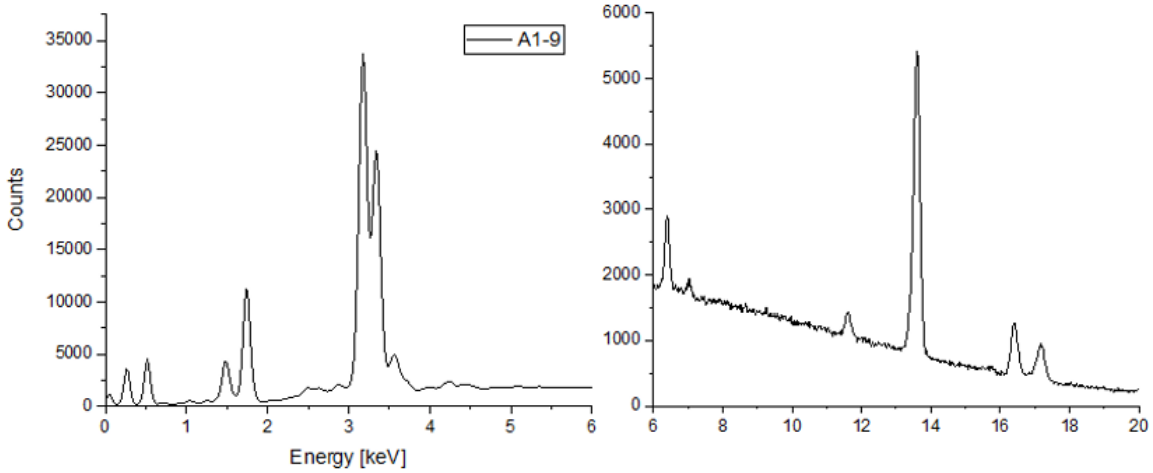

Figure 150. Particle A1-9 EDS Spectrum

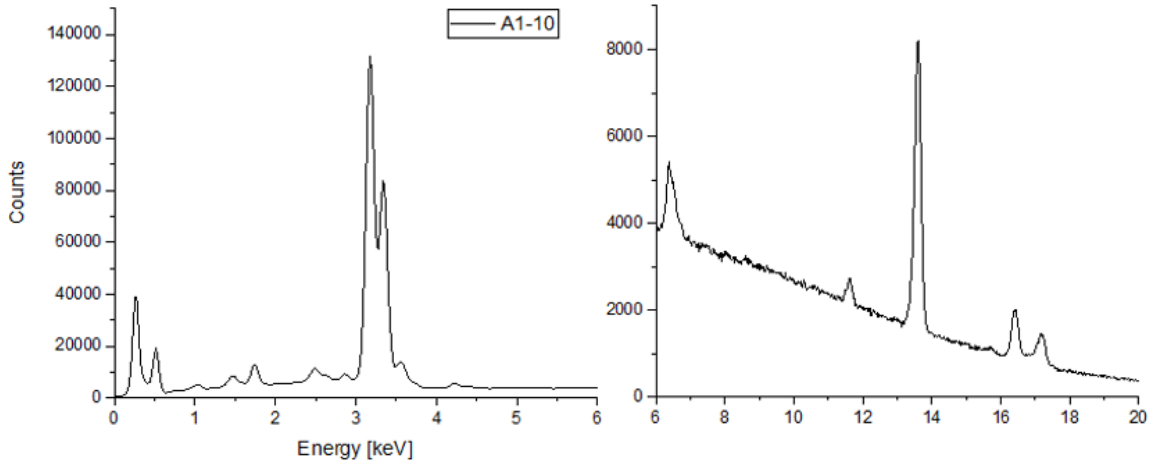

Figure 151. Particle A1-10 EDS Spectrum

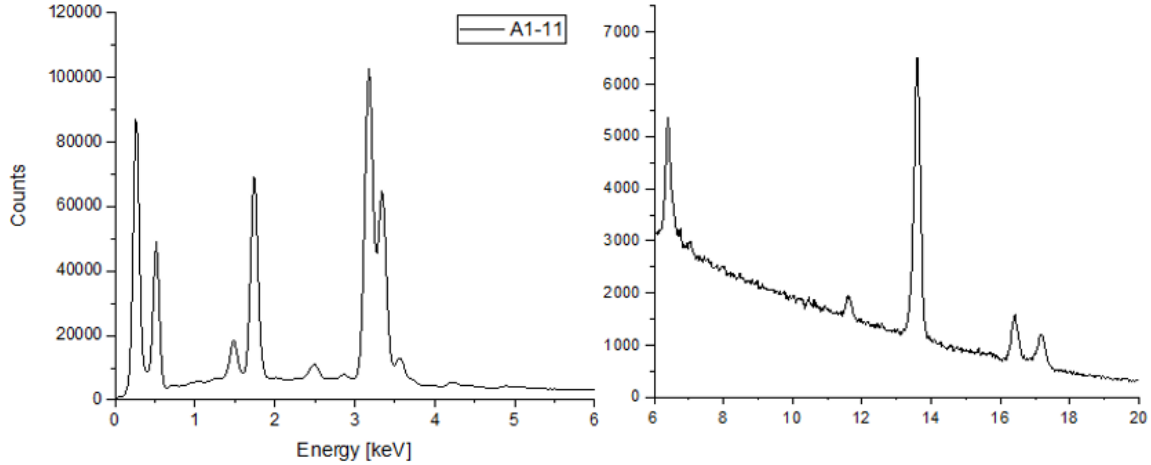

Figure 152. Particle A1-11 EDS Spectrum

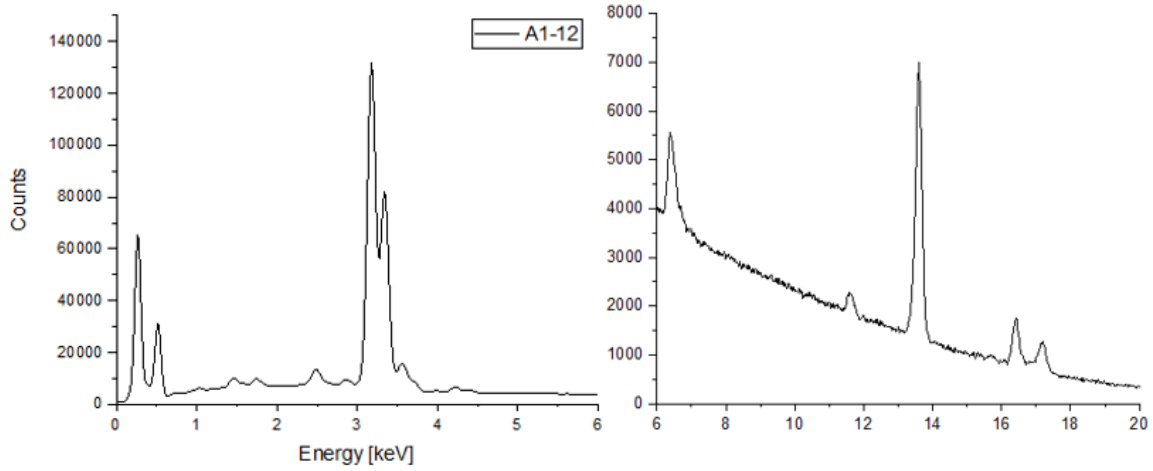

Figure 153. Particle A1-12 EDS Spectrum

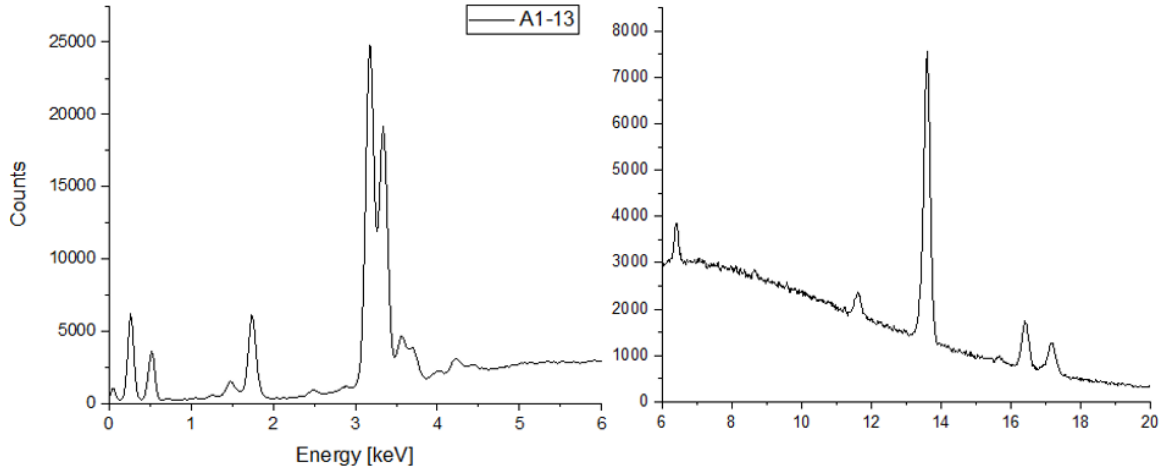

Figure 154. Particle A1-13 EDS Spectrum

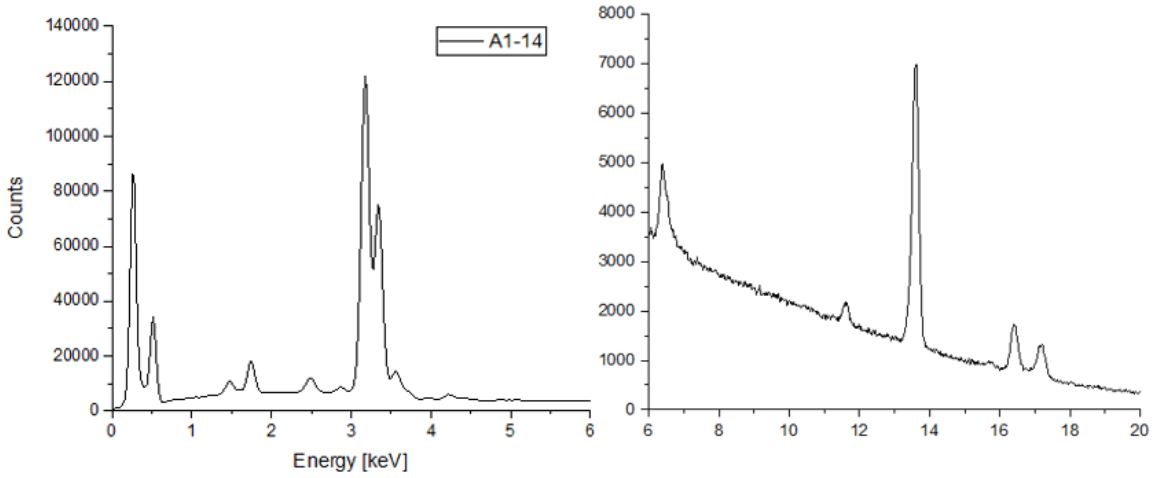

Figure 155. Particle A1-14 EDS Spectrum

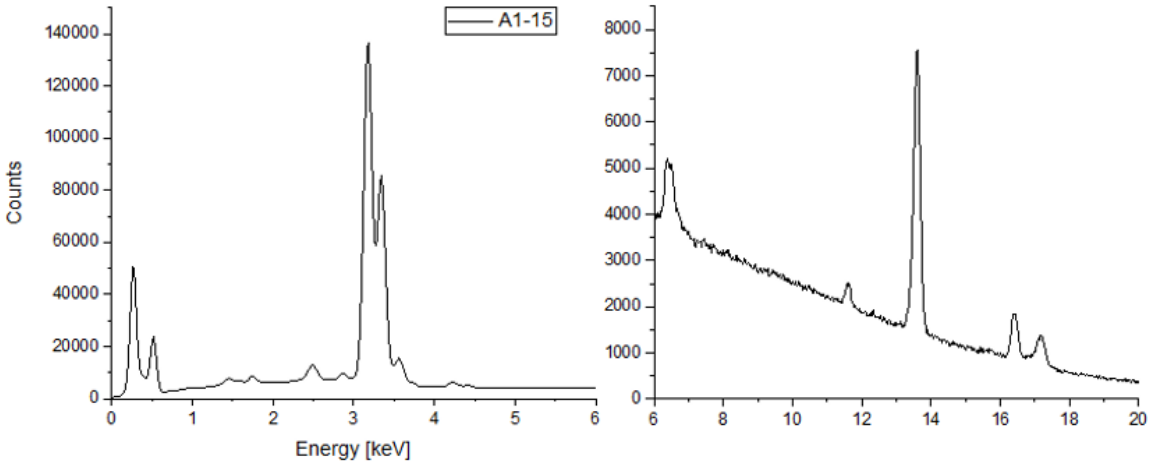

Figure 156. Particle A1-15 EDS Spectrum

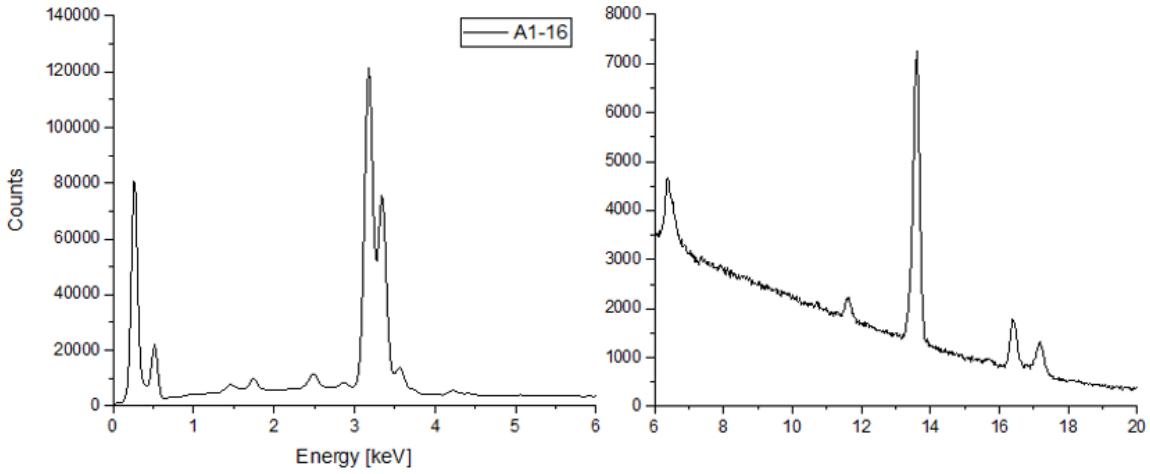

Figure 157. Particle A1-16 EDS Spectrum

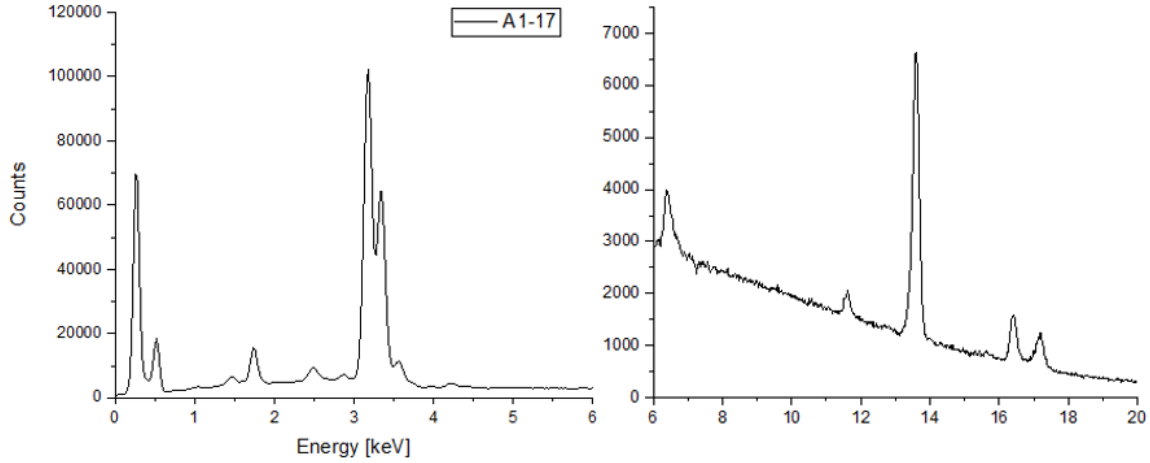

Figure 158. Particle A1-17 EDS Spectrum

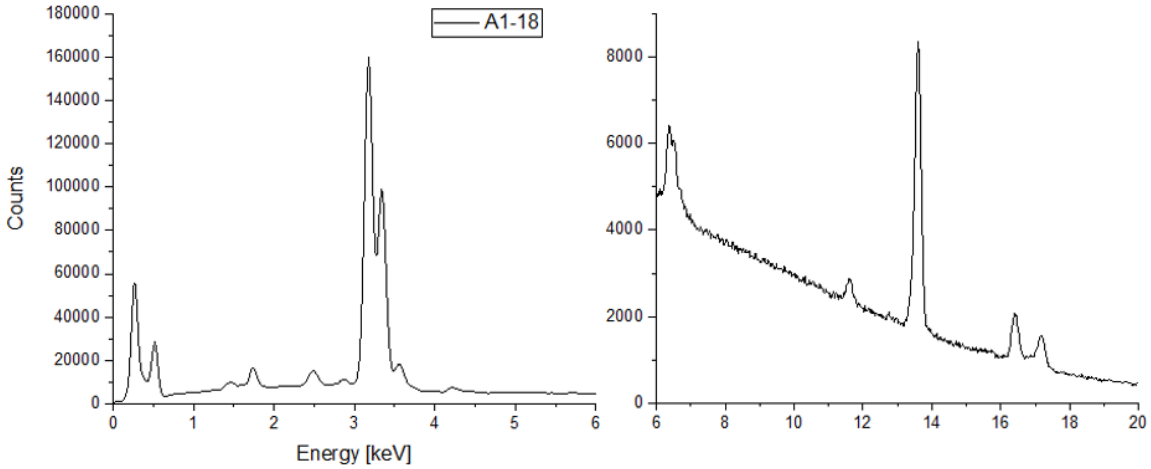

Figure 159. Particle A1-18 EDS Spectrum

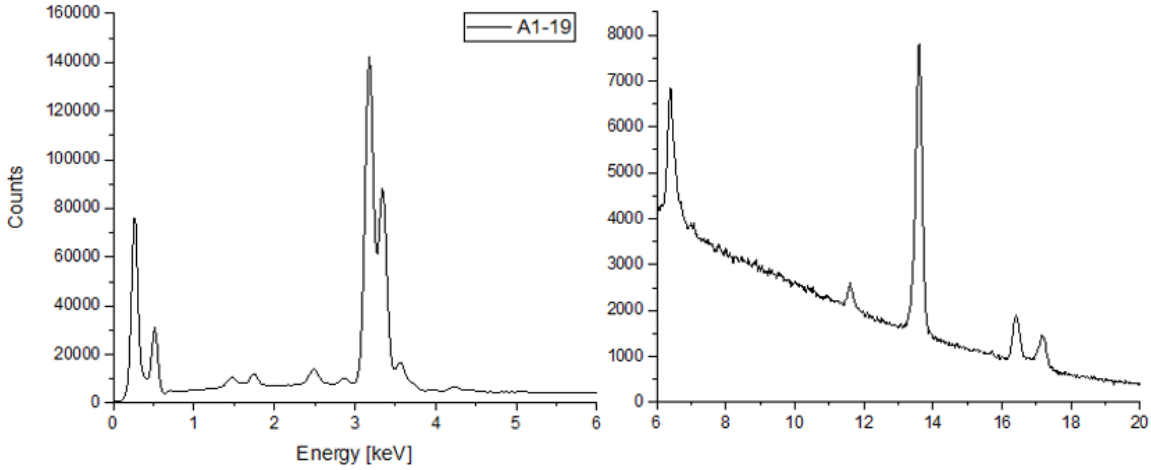

Figure 160. Particle A1-19 EDS Spectrum

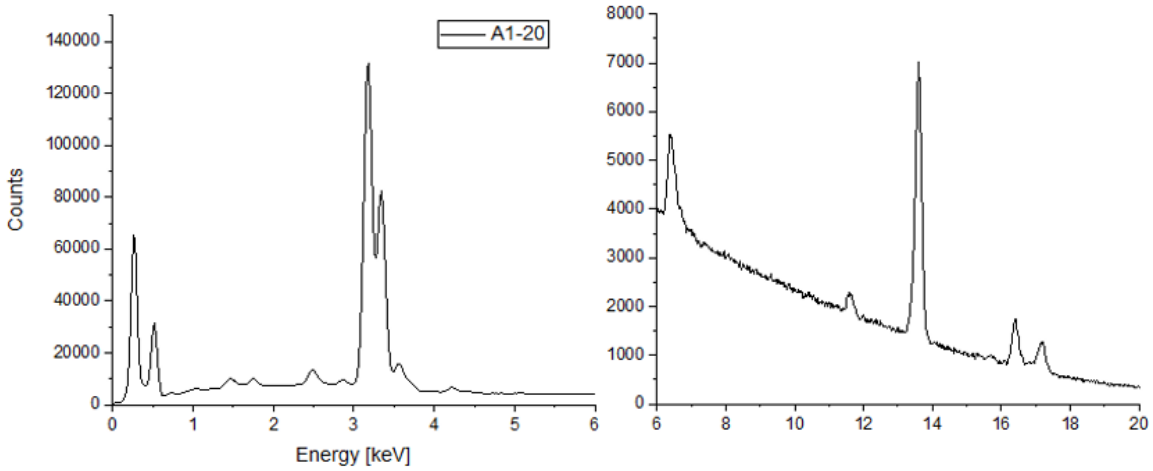

Figure 161. Particle A1-20 EDS Spectrum

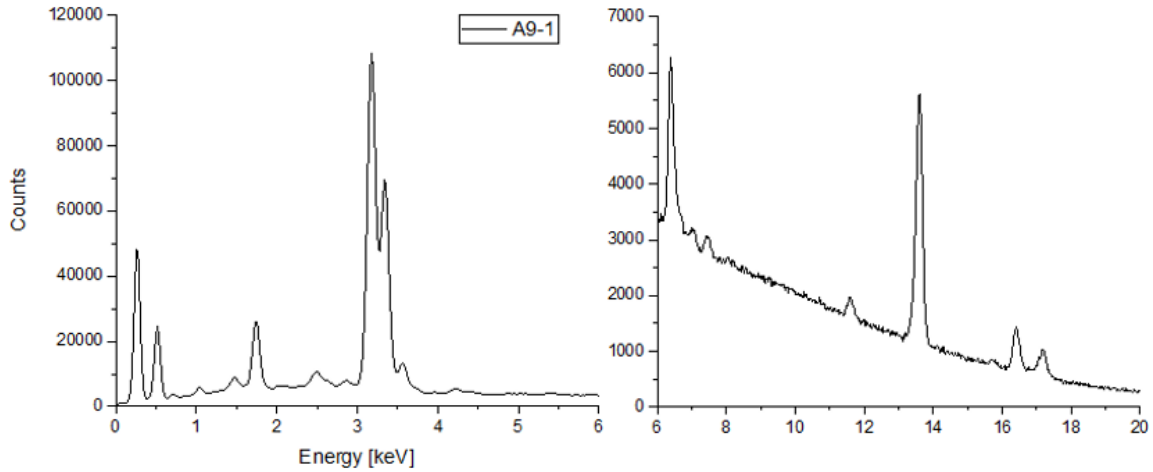

Figure 162. Particle A9-1 EDS Spectrum

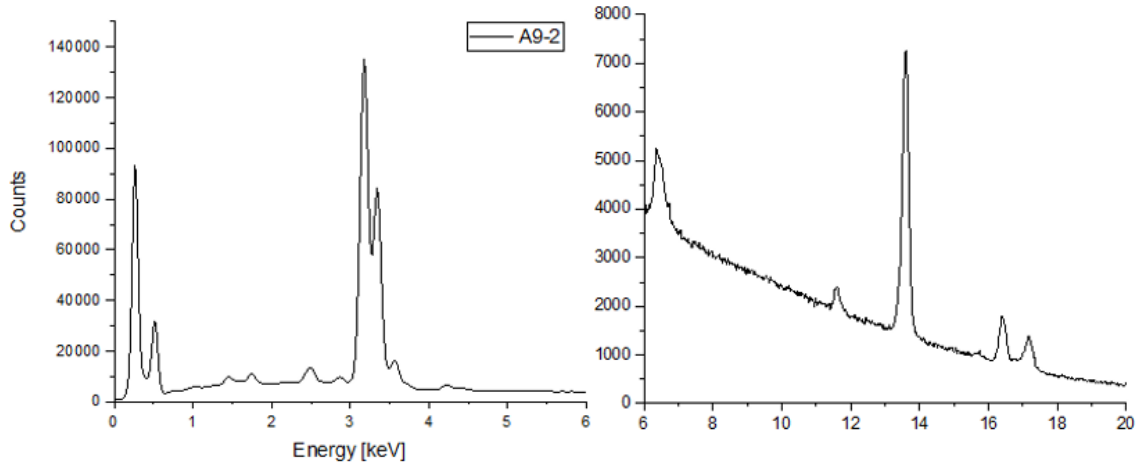

Figure 163. Particle A9-2 EDS Spectrum

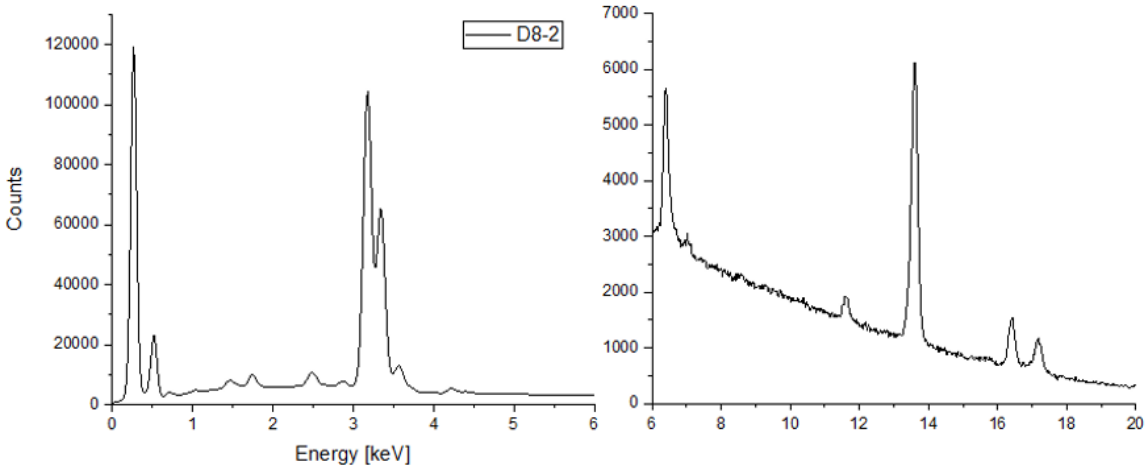

Figure 164. Particle D8-2 EDS Spectrum

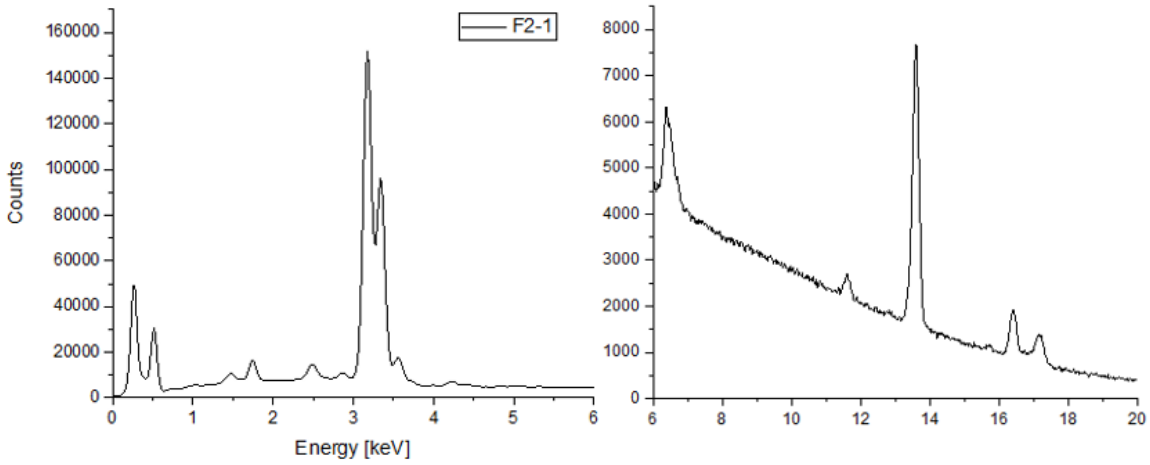

Figure 165. Particle F2-1 EDS Spectrum

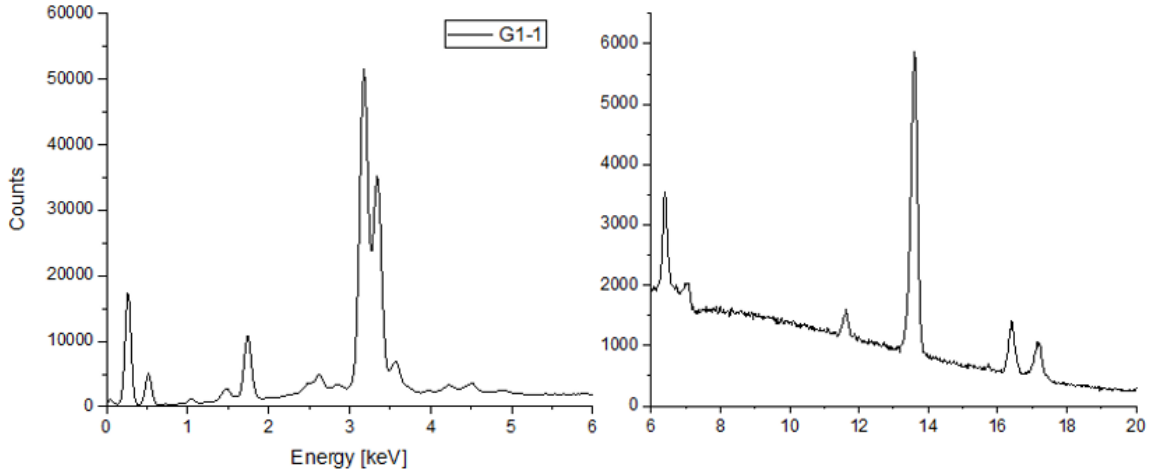

Figure 166. Particle G1-1 EDS Spectrum

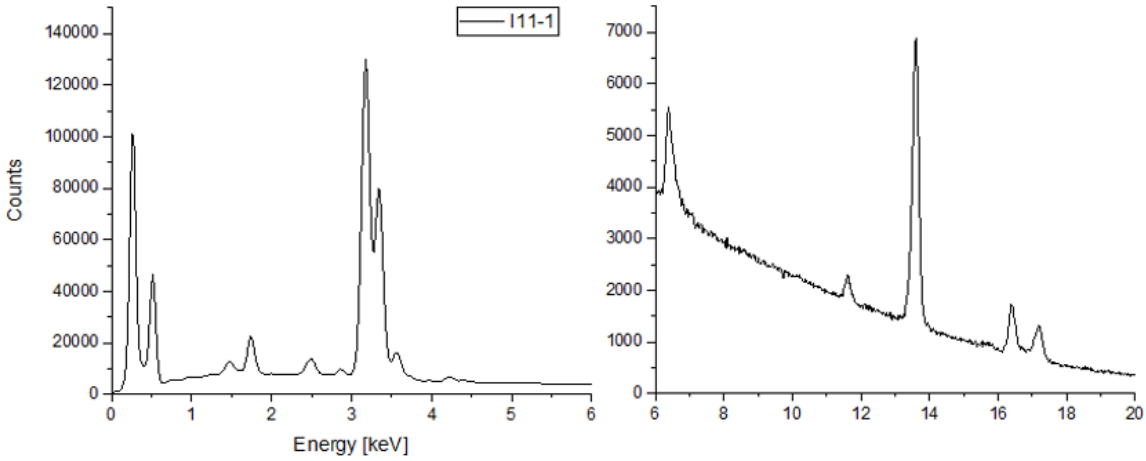

Figure 167. Particle I11-1 EDS Spectrum

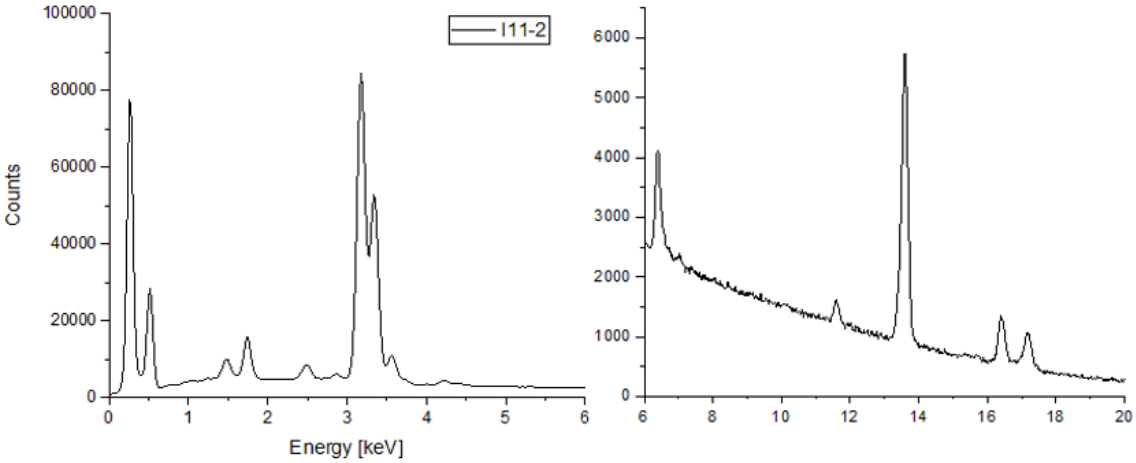

Figure 168. Particle I11-2 EDS Spectrum

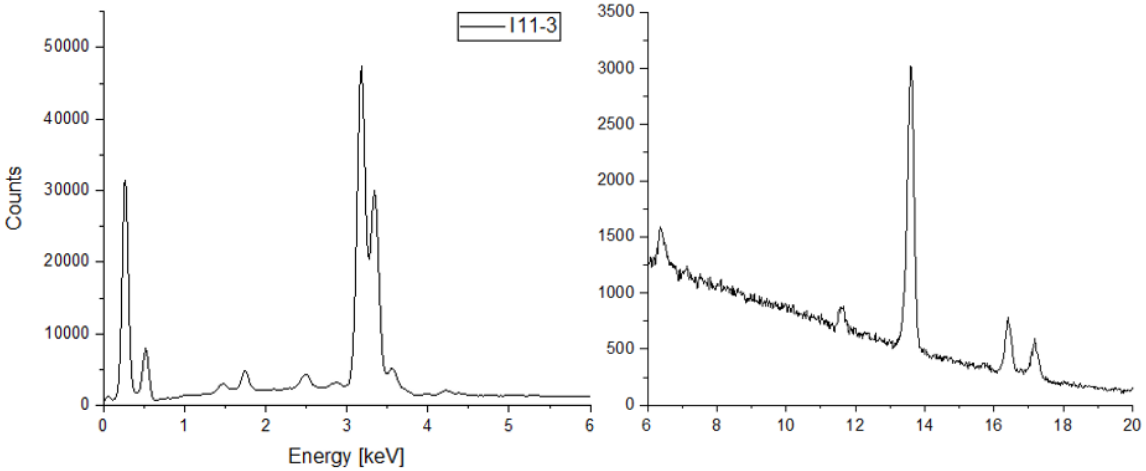

Figure 169. Particle I11-3 EDS Spectrum

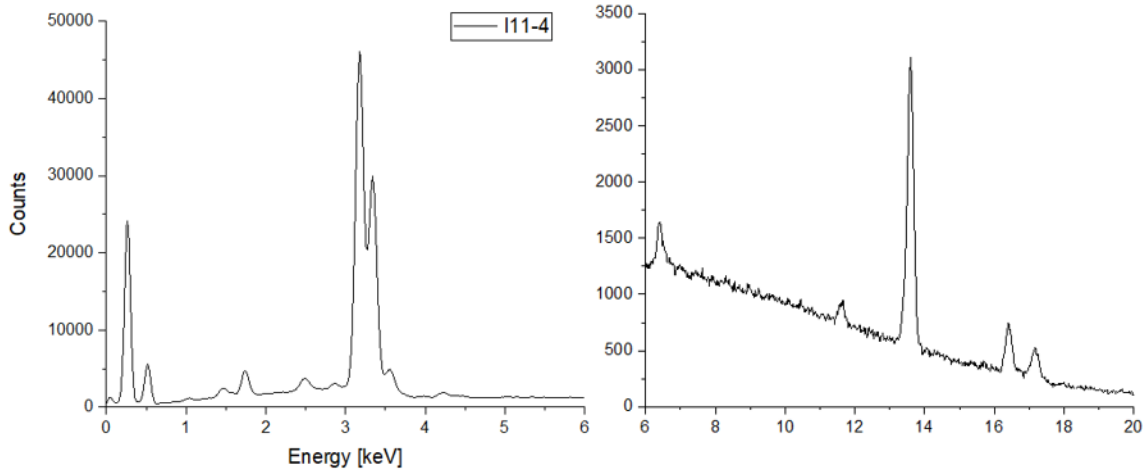

Figure 170. Particle I11-4 EDS Spectrum

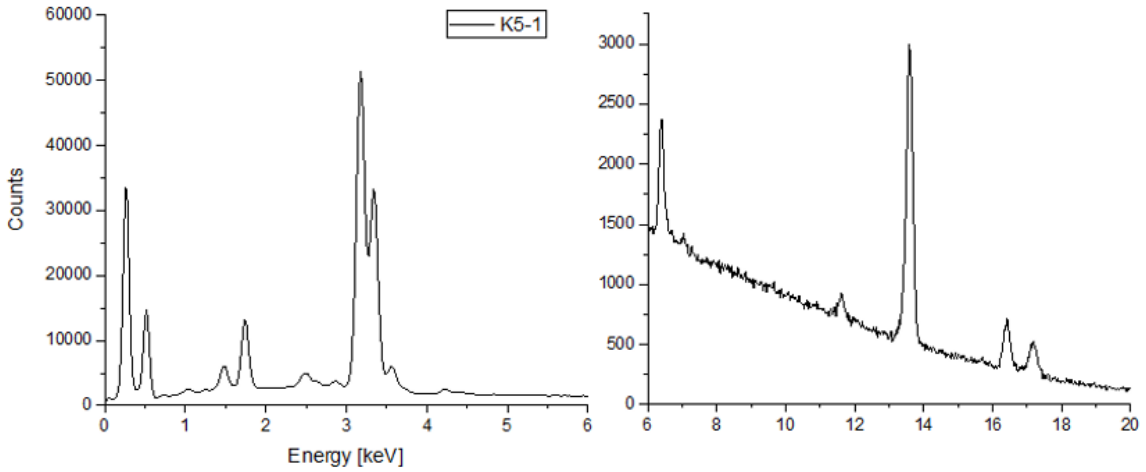

Figure 171. Particle K5-1 EDS Spectrum

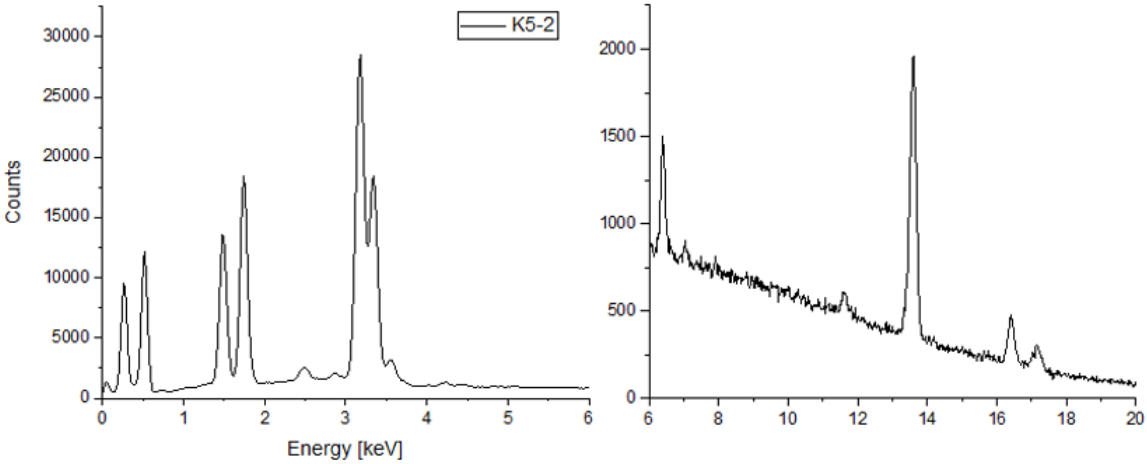

Figure 172. Particle K5-2 EDS Spectrum

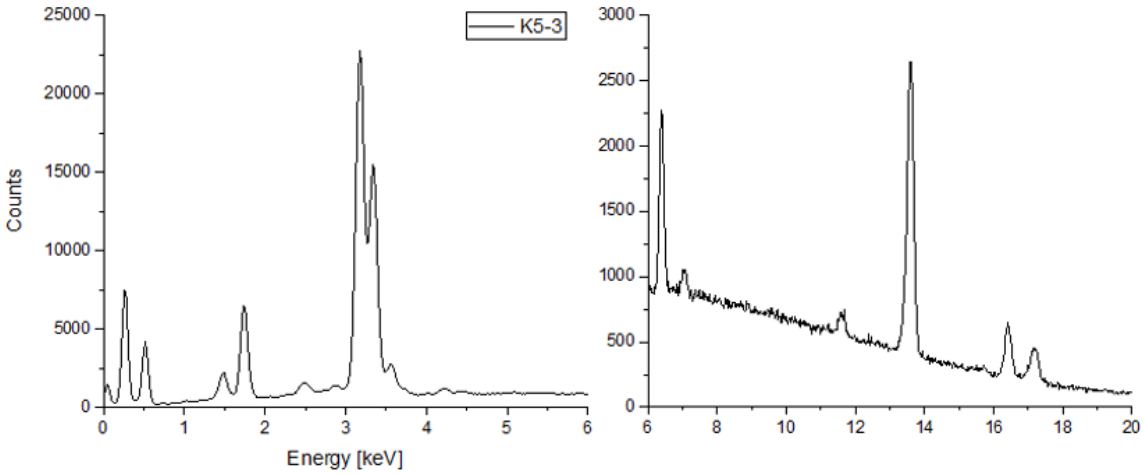

Figure 173. Particle K5-3 EDS Spectrum

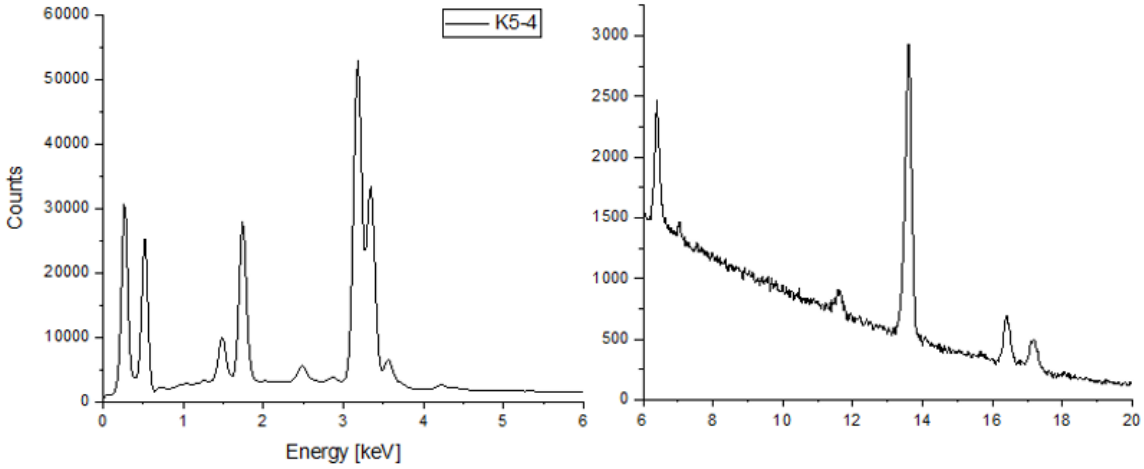

Figure 174. Particle K5-4 EDS Spectrum

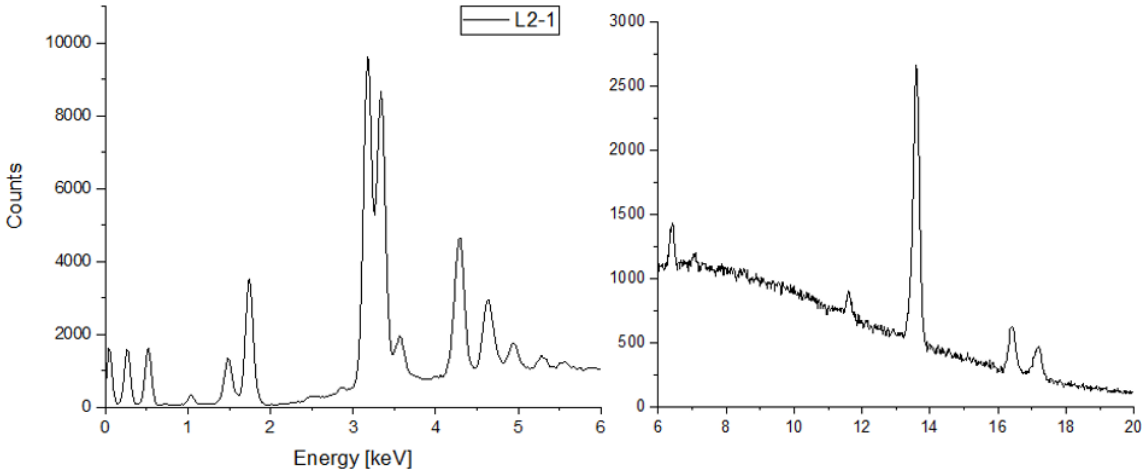

Figure 175. Particle L2-1 EDS Spectrum

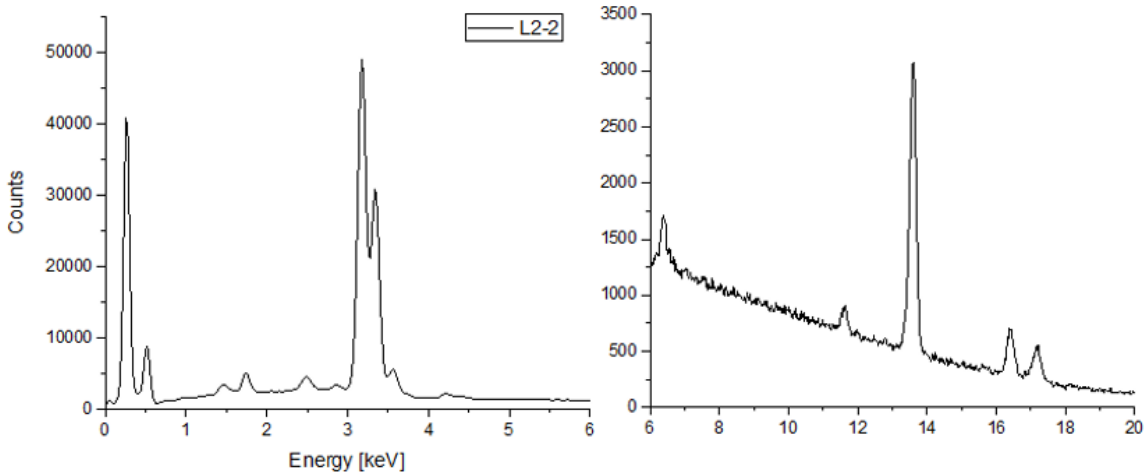

Figure 176. Particle L2-2 EDS Spectrum

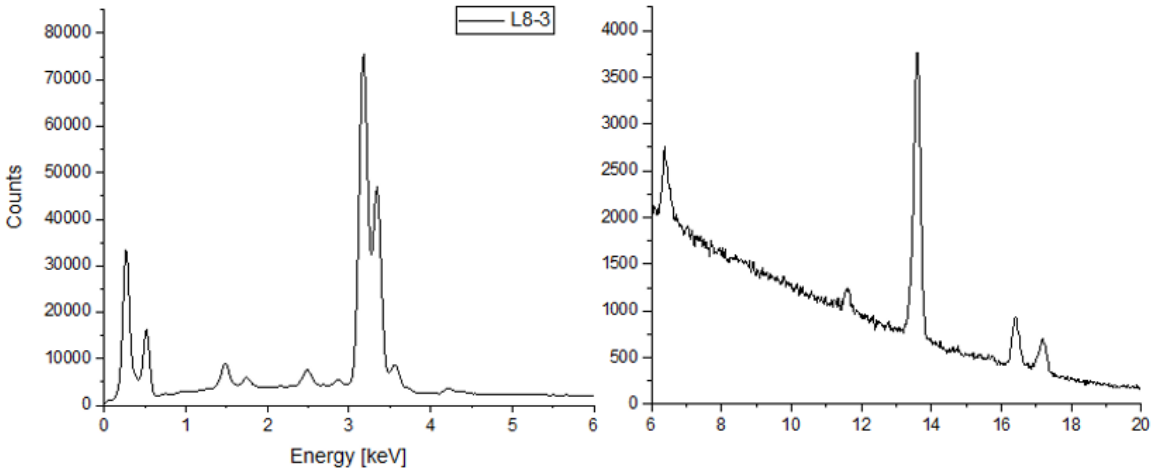

Figure 177. Particle L8-3 EDS Spectrum

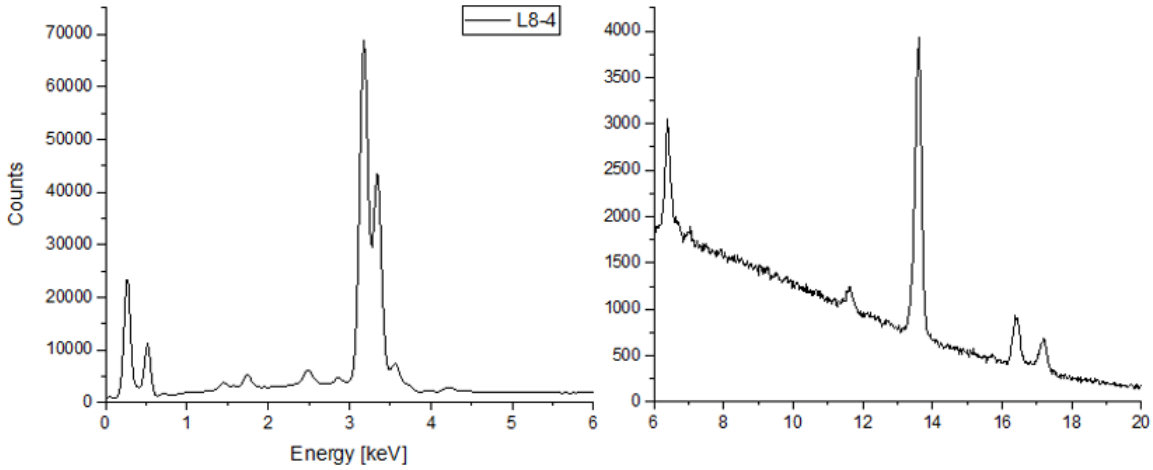

Figure 178. Particle L8-4 EDS Spectrum

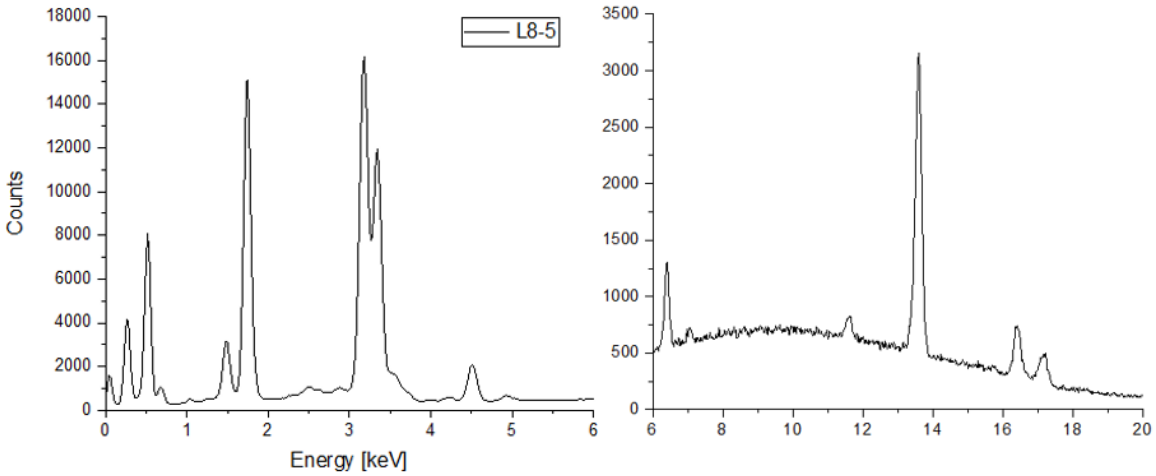

Figure 179. Particle L8-5 EDS Spectrum

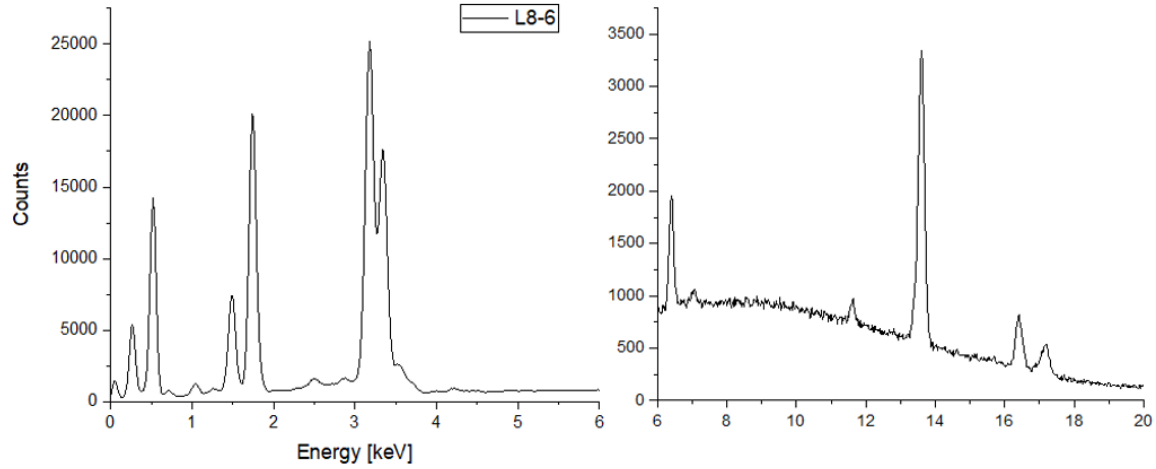

Figure 180. Particle L8-6 EDS Spectrum

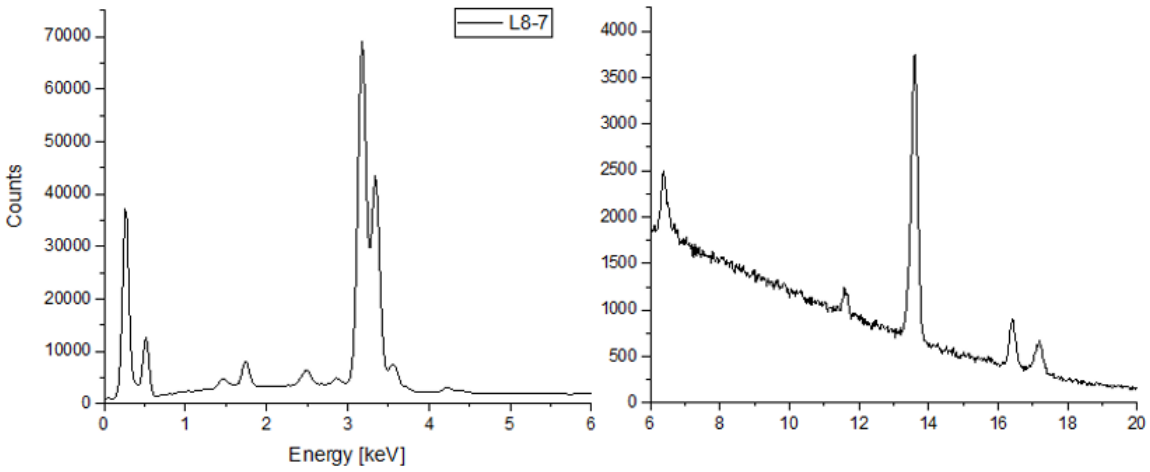

Figure 181. Particle L8-7 EDS Spectrum

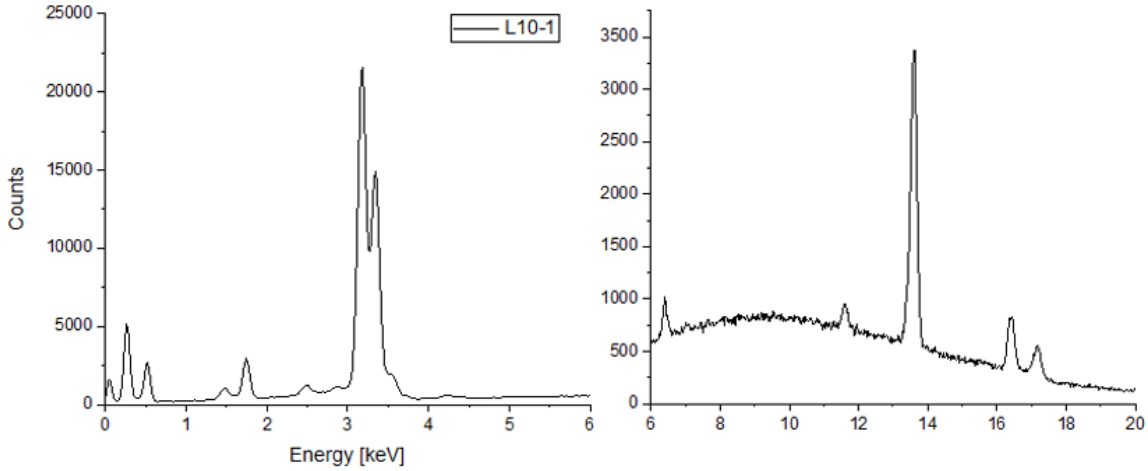

Figure 182. Particle L10-1 EDS Spectrum

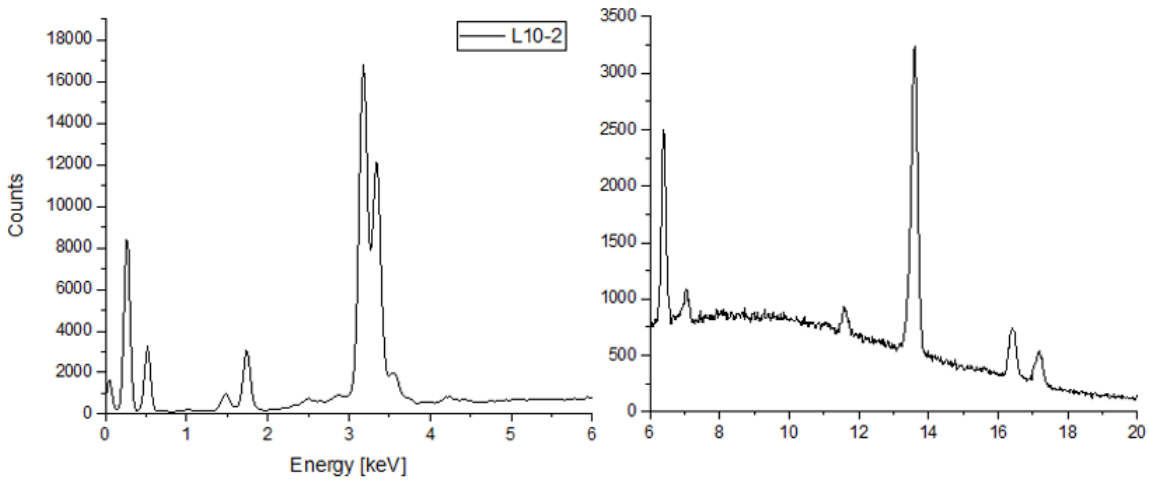

Figure 183. Particle L10-2 EDS Spectrum

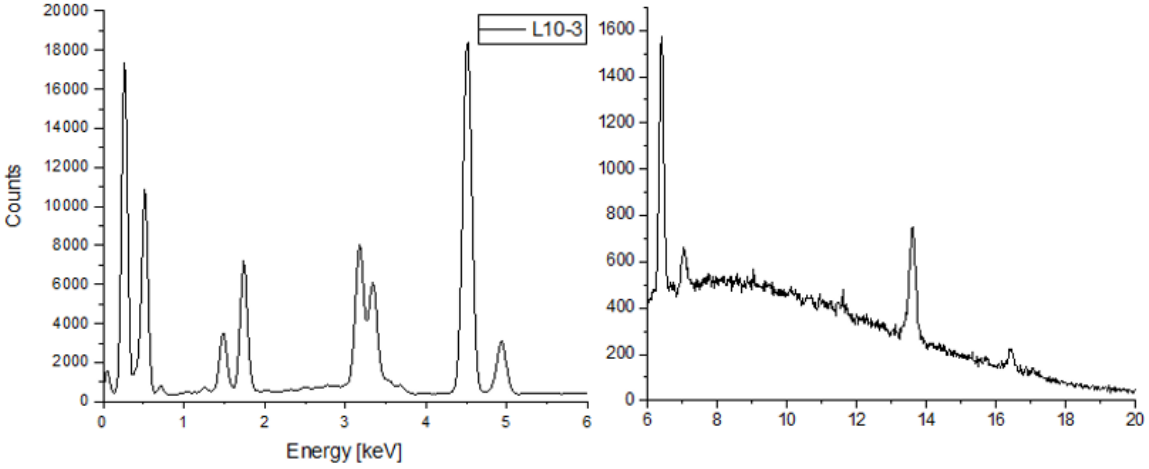

Figure 184. Particle L10-3 EDS Spectrum

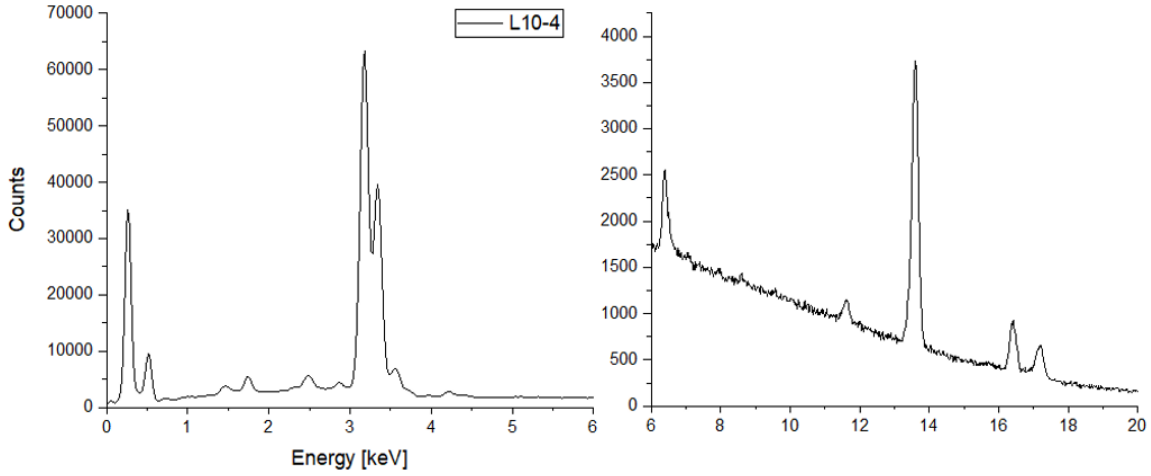

Figure 185. Particle L10-4 EDS Spectrum

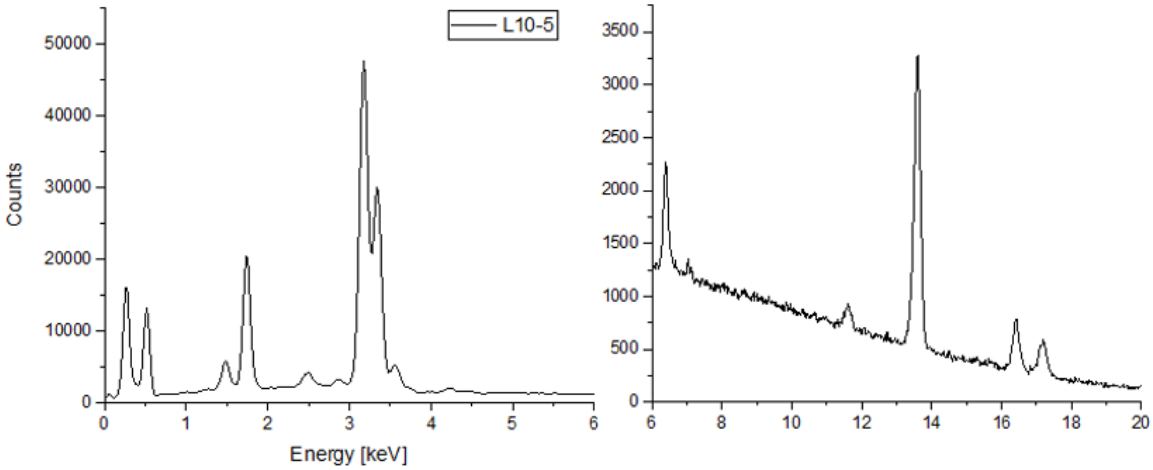

Figure 186. Particle L10-5 EDS Spectrum

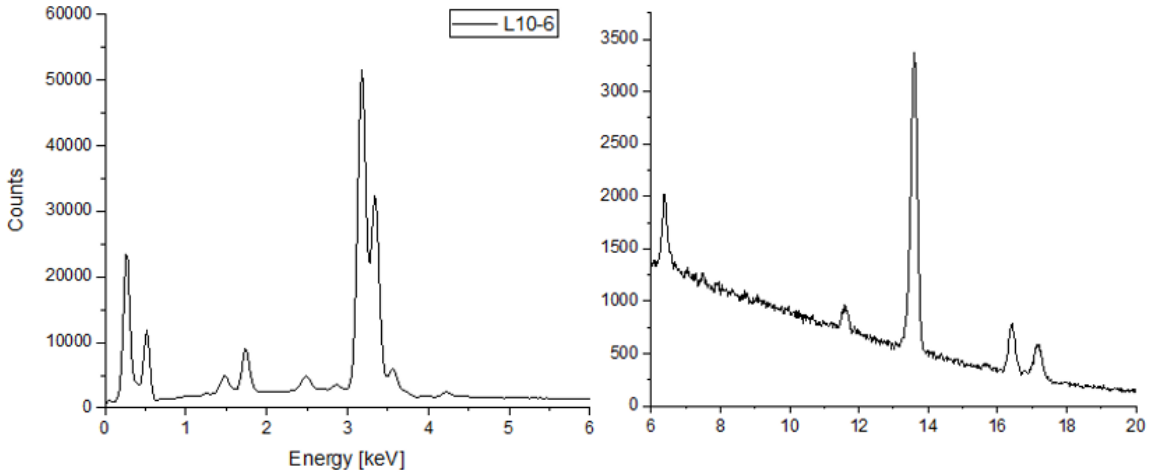

Figure 187. Particle L10-6 EDS Spectrum

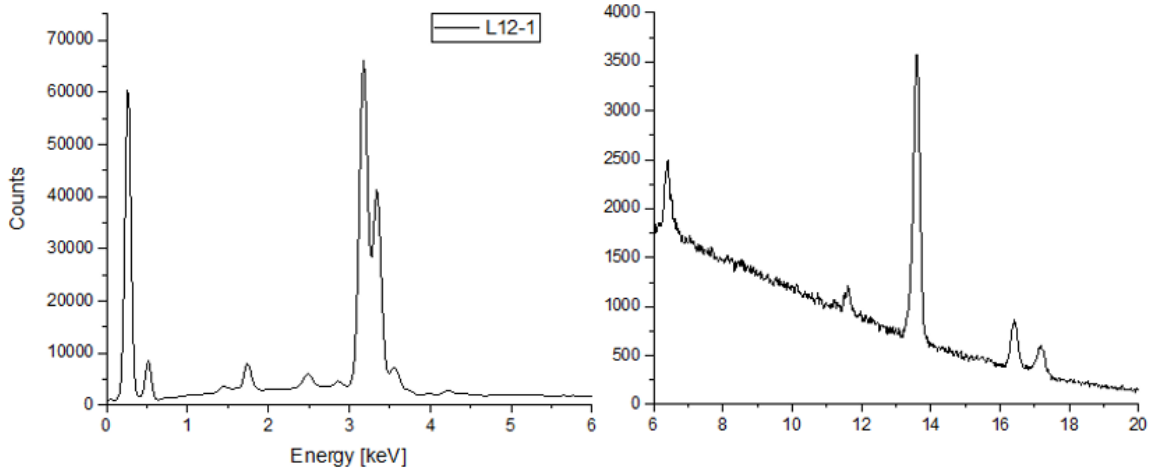

Figure 188. Particle L12-1 EDS Spectrum

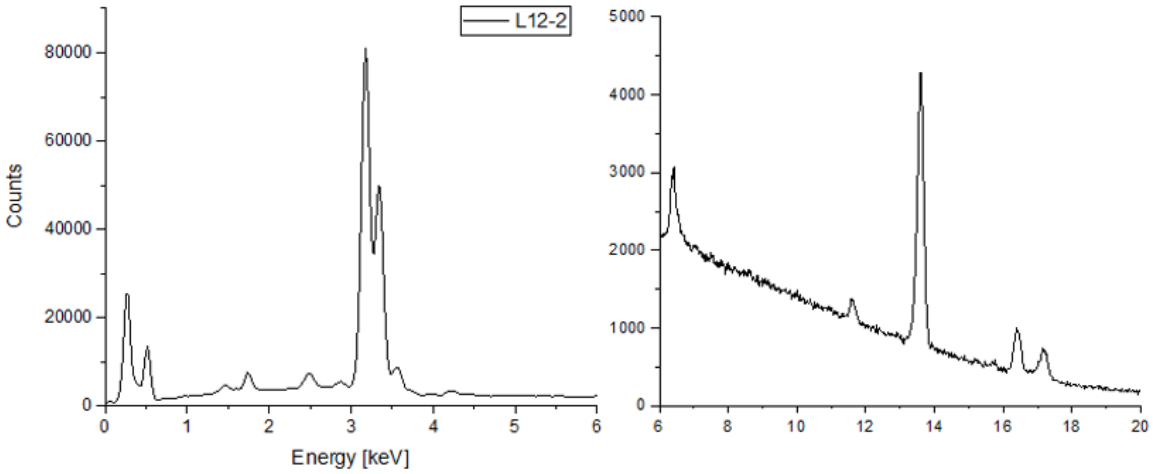

Figure 189. Particle L12-2 EDS Spectrum

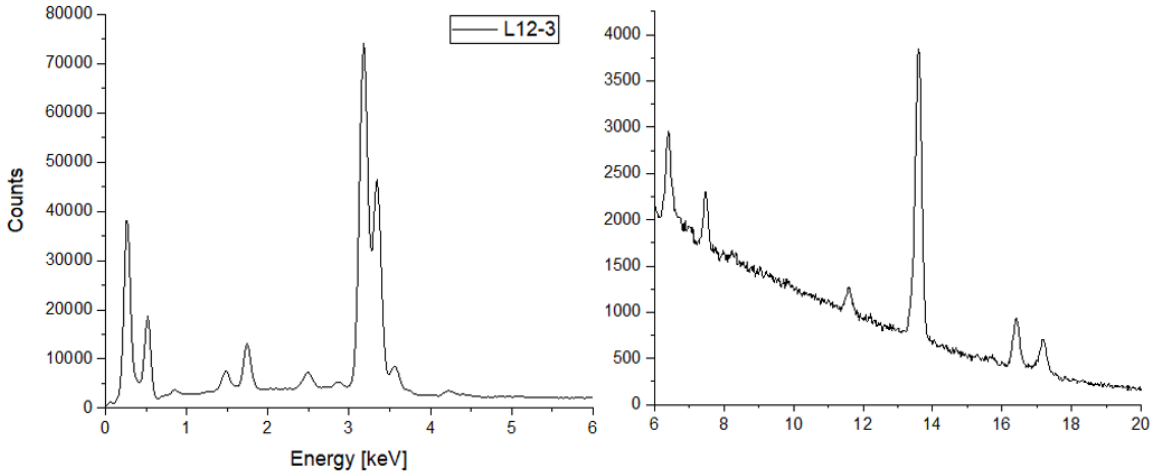

Figure 190. Particle L12-3 EDS Spectrum

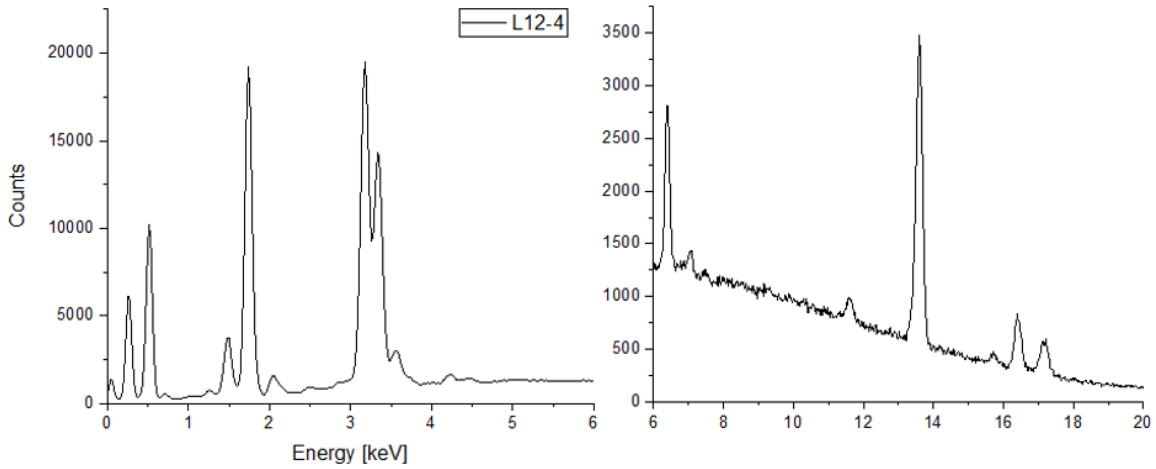

Figure 191. Particle L12-4 EDS Spectrum

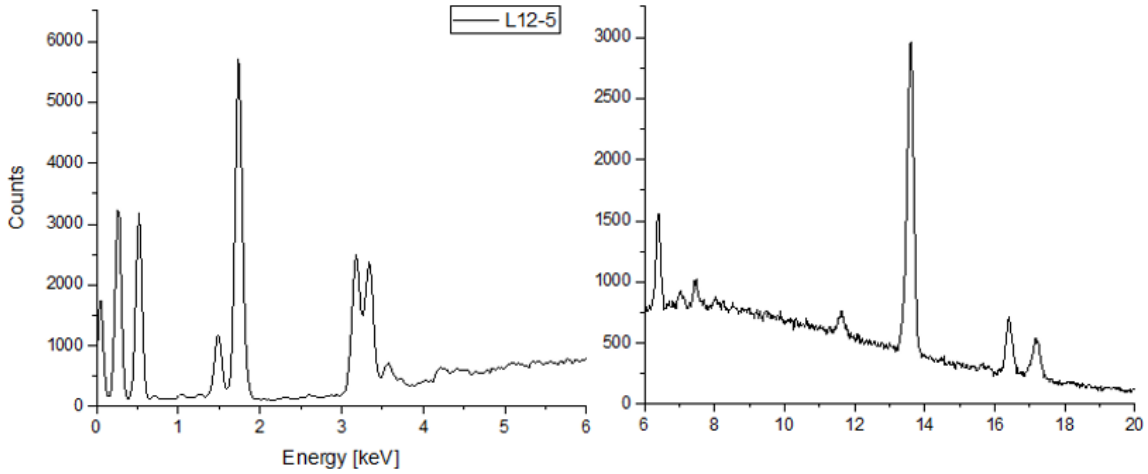

Figure 192. Particle L12-5 EDS Spectrum

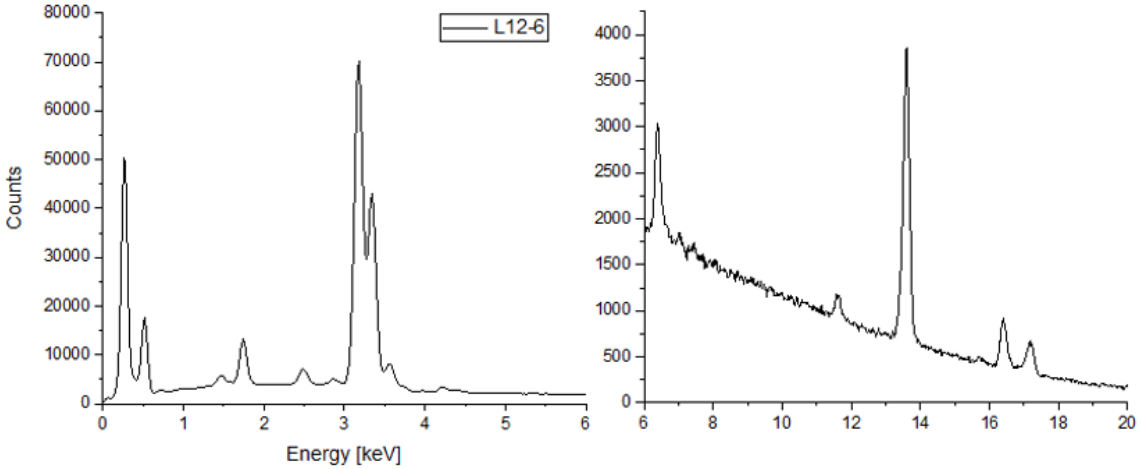

Figure 193. Particle L12-6 EDS Spectrum

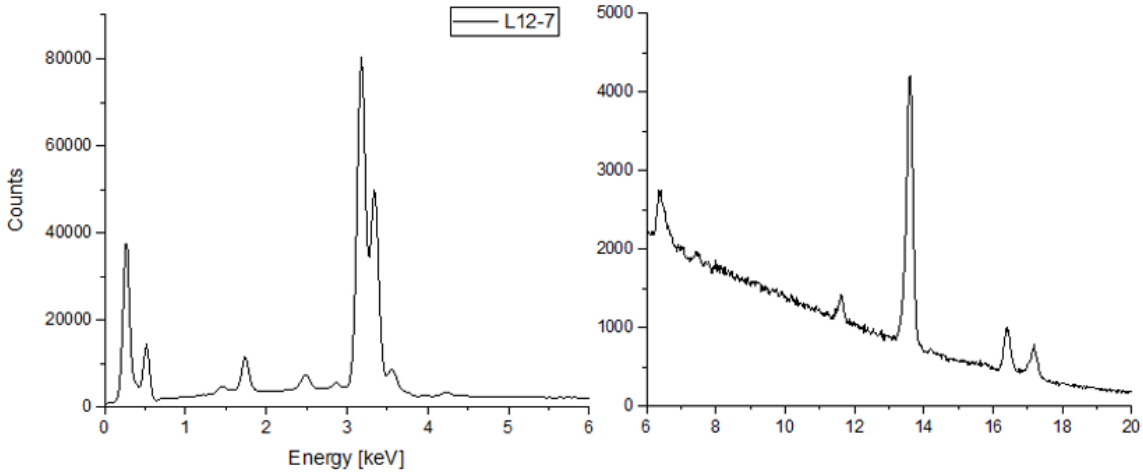

Figure 194. Particle L12-7 EDS Spectrum

Bibliography

1. Cezeaux, Jason. *Characterization of Particles Formed During Non-Critical Nuclear Weapons Accidents*. PhD dissertation, AFIT/ENP/18-S-021. Air Force Institute of Technology (AU), Wright-Patterson AFB OH, September 2018.

2. International Atomic Energy Agency, Radioactive Particles in the Environment: Sources, Particle Characterization and Analytical Techniques, IAEA-TECDOC-1663, IAEA, Vienna (2011).

3. B.Salbu, V. Kashparov, O.C. Lind, R. G.Tenorio, M.P. Johansen, D.P. Child, P. Roos, and C. Sancho, "Challenges associated with the behaviour of radioactive particles in the environment" Journal of Environmental Radioactivity, Volume 186,2018,101-115.

4. W. Clemens and D.K. Gupta (Eds), Radionuclides in the Environment, Springer International Publishing, 2015.

5. S. E. Rademacher and J. L. Hubbell, "Boeing Michigan Aeronautical Research Center (BOMARC) Missile Shelters and Bunkers Scoping Survey Workplan," Air Force Institute for Operational Health Surveillance Directorate, Brooks AFB, 2007.

6. Gostic, Richard C. *Characterization of plutonium particles originating from the BOMARC accident – 1960*. Ph.D. dissertation. University of Las Vegas, Las Vegas NV, 2010.

7. Bowen, James M. *Physicochemical characterization of discrete weapons grade plutonium metal particles originating from the 1960 BOMARC incident*. Ph.D. dissertation. University of Cincinnati, Cincinnati OH, 2013.

8. U.S. Geological Survey. *Radiochemical Sampling and Analysis of Shallow Ground Water and Sediment at the BOMARC Missile Facility, East-Central New Jersey, 1999-2000*. Scientific Investigations Report 2005-5062. Reston: Government Printing Office, 2005.

9. M. H. Lee, Y. Y. Yoon, S. B. Clark and S. E. Glover, "Distribution and Geochemical Association of Actinides in a Contaminated Soil as a Function of Grain Size," Radiochim. Acta, vol. 92, no. 1, pp. 671-675, 2004.

10. Greb, Matthew A. *Magnetic Separation of Soil Contaminated with Weapon Grade Plutonium*. MS thesis, AFIT/ENP/14-M-13. School of Engineering Management, Air Force Institute of Technology (AU), Wright-Patterson AFB OH, March 2014.

11. Nuclear Regulatory Commission. *Radiological and Chemical Properties of Uranium*. ML 11227A233. Oak Ridge: Oak Ridge Institute for Science and Education, 2012.

12. "Gamma-Ray Spectrum Catalog of Isotopes." *Radiochemistry*. Idaho National Engineering and Environmental Laboratory, 2003. Retrieved on 12 December 2020.

13. Los Alamos National Laboratory. *Plutonium Isotopic Composition by Gamma-Ray Spectroscopy: A Review*. Report Series LA-10750-MS; No. 813. Los Alamos: Government Printing Office, 1986.

14. Tsoulfanidis, Nicholas, and Sheldon Landsberger. *Measurement & Detection of Radiation* (4th edition). New York: CRC Press, 2015.

15. Weisstein, Eric W. "Solid Angle." *MathWorld*. Wolfram Research, Inc. 1999. Retrieved on 13 December 2020.

16. Shattan, Michael B. Assistant Professor, Air Force Institute of Technology, Wright-Patterson AFB OH. Personal Correspondence. 14 December 2020.

17. Krane, Kenneth S. *Introductory Nuclear Physics*. Hoboken: John Wiley & Sons, Inc., 1988.

18. Knoll, Glenn F. *Radiation Detection and Measurement* (4th Edition). Hoboken: John Wiley & Sons, Inc., 2010.

19. Bickley, Abigail A. Assistant Professor, Air Force Institute of Technology, Wright-Patterson AFB OH. Personal Correspondence. 16 June 2020.

20. Wirth, Karl, and Andy Barth. "X-Ray Fluorescence (XRF)." *Carleton College*. Science Education Resource Center, Carleton. 21 January 2020. Retrieved on 14 December 2020.

21. Nanakoudis, Antonis. "What is SEM? Scanning Electron Microscopy Explained." *ThermoFisher Scientific*. 14 November 2019. Retrieved 14 December 2020.

22. Gleichmann, Nicole. "SEM vs TEM." *Technology Networks*. 25 February 2020. Retrieved 14 December 2020.

23. "Scanning Electron Microscopy." *NanoScience Instruments*. 2020. Retrieved 14 December 2020.

24. Goldstein, Joseph I. et al. *Scanning Electron Microscopy and X-Ray Microanalysis* (4th Edition). New York: Springer Nature, 2018.

25. Peterson, George G. Post-Doctural Researcher, Air Force Institute of Technology, Wright-Patterson AFB OH. Personal Correspondence. 4 December 2020.

26. "Radioactive Decay." *Environmental Protection Agency*. 28 May 2019. Retrieved 15 December 2020.

27. Goldstein, Joseph I. et al. *Scanning Electron Microscopy and X-Ray Microanalysis* (3rd Edition). New York: Springer Nature, 2003.

28. *MAESTRO-32*. Version 6.0, ORTEC, Windows 2000, disk. Computer software. Advanced Measurement Technology, Inc., Oak Ridge TN, 2006.

29. *Genie 2000 Spectroscopy Software*. Version 3.1, Canberra, Windows 2000, disk. Computer software. Canberra Inudstries, Inc., Meriden CT, 2006.

30. "X-Ray Mass Attenuation Coefficients." *National Institute of Standards and Technology.* 11 December 2019. Retrieved 16 December 2020.

31. "List of Commonly Observed Gamma Energies." *University of Ljubljana*. Retrieved 23 June 2020.

32. Chaparro, Orland M. *Heterogeneity Effects in Plutonium Contaminated Soil*. MS thesis, AFIT/ENV/09-M-01. School of Engineering Management, Air Force Institute of Technology (AU), Wright-Patterson AFB OH, March 2009.

33. "Table of Nuclides." *Korea Atomic Energy Research Institute*. Retrieved 15 December 2020.

34. "Model 43-89 Alpha-Beta Detector." *Ludlum Measurements, Inc.* Retrieved 2 July 2020.

35. *Ultim Max.* Dealer Product Catalog. High Wycombe: Oxford Instruments NanoAnalysis & Asylum Research, no date.

36. "XGT-7200 X-Ray Analytical Microscope." *Horiba, Ltd.* Retrieved 30 July 2020.

37. *Image J*. Version 1.53e, NIH. Computer software. National Institutes of Health, Washington DC, 2019.

38. *OriginPro 2020*. Version b, OriginLab, Windows 10. Computer software. OriginLab Corporation, Northampton MA, 2020.

39. Basunia, *M.S. Nuclear Data Sheets 107, 3323*. National Nuclear Data Center, Upton, 2006.

40. Congressional Research Service. *Nuclear Weapon "Pit" Production: Options to Help Meet a Congressional Requirement*. Report Series 7-5700; No. R44033. Washington: Government Printing Office, 2015.

41. Gostic, Richard C. GG-13, Air Force Technical Applications Center, Patrick AFB FL. Personal Correspondence. 5 November 2020.

42. Bevins, James E. Assistant Professor, Air Force Institute of Technology, Wright-Patterson AFB OH. Personal Correspondence. 9 November 2020.

43. "Uranium Gamma Spectrometry." *Physics Open Lab.* 29 January 2016. Retrieved 8 January 2021.

44. "Isotopes of Plutonium." *Periodictable.com*. Element Collection, Inc. Retrieved 8 January 2021.

45. Environmental Protection Agency. *EPA Facts About Cesium-137*. Washington: Government Printing Office, 2002.

46. Tamasi, A.L., L.J. Cash, C. Eley, R.B. Porter, D.L. Pugmire, A. R. Ross, C.E. Ruggiero, L. Tandon, G.L. Wagner, J.R. Walensky, A.D. Wall, and M.P. Wilkerson. "A Lexicon for Consistent Description of Material Images for Nuclear Forensics." Journal of Radioanalytical and Nuclear Chemistry, 1611-1619, 2016.

47. *AZtec 4.4 User Manual*. Oxford Instruments NanoAnalysis & Asylum Research, High Wycombe, UK, 2020.

48. Beckwith, Thomas G. and others. *Mechanical Measurements* (6th edition). Upper Saddle River: Pearson Prentice Hall, 2007.

49. Varshney, Gaiven, Jason R. Cezeaux, and James C. Petrosky. "Investigation of fissile materials collected from a non-critical nuclear explosion using non-destructive analytical techniques." *Journal of Radioanalytical and Nuclear Chemistry*, 318:505-513 (April 2018).

50. Runde, Wolfgang, S.D. Conradson, D.W. Efurd, N. Lu, C.E. VanPelt, and C.D. Tait, "Solubility and sorption of redox-sensitive radionuclides (Np, Pu) in J-13 water from the Yucca Mountain site: comparison between experiment and theory," Applied Chemistry, vol. 17, pp. 837-853, 2001.

51. Goodwin, Brice, "Calculated uranium solubility in groundwater: implications for nuclear fuel waste disposal," Canadian Journal of Chemistry, vol. 60, pp. 1759-1766, 1982.

REPORT DOCUMENTATION PAGE

Form Approved
OMB No. 074-0188

PLEASE DO NOT RETURN YOUR FORM TO THE ABOVE ADDRESS.

1. REPORT DATE *(DD-MM-YYYY)*	2. REPORT TYPE	3. DATES COVERED *(From – To)*
25-03-2021	Graduate Research Paper	June 2019 – March 2021

TITLE AND SUBTITLE
Characterization and Analysis of BOMARC Accident Debris

5a. CONTRACT NUMBER

5b. GRANT NUMBER

5c. PROGRAM ELEMENT NUMBER

6. AUTHOR(S)

Heffelfinger, Aaron J., MAJ

5d. PROJECT NUMBER

5e. TASK NUMBER

5f. WORK UNIT NUMBER

7. PERFORMING ORGANIZATION NAMES(S) AND ADDRESS(S)

Air Force Institute of Technology
Graduate School of Engineering and Management (AFIT/EN)
2950 Hobson Way, Building 640
WPAFB OH 45433-7765

8. PERFORMING ORGANIZATION REPORT NUMBER

AFIT-ENP-MS-21-M-121

9. SPONSORING/MONITORING AGENCY NAME(S) AND ADDRESS(ES)
Department of Homeland Security

10. SPONSOR/MONITOR'S ACRONYM(S)
DHS

11. SPONSOR/MONITOR'S REPORT NUMBER(S)

12. DISTRIBUTION/AVAILABILITY STATEMENT
Distribution Statement A. Approved for Public Release; Distribution Unlimited

13. SUPPLEMENTARY NOTES
This work is declared a work of the U.S. Government and is not subject to copyright protection in the United States.

14. ABSTRACT

Accidents involving nuclear weapons, such as the Boeing Michigan Aeronautical Research Center (BOMARC) accident in 1960, always pose a significant risk of allowing particles composed of nuclear materials to enter the environment. These particles often differ in characteristics and can be of greatly varying sizes. Gamma ray analysis was conducted on the soil sample and radioisotopes within the sample were identified. Two non-destructive methods for locating actinide bearing particles within the sample were testing, resulting in 70 actinide bearing particles ranging from 1-34 microns being identified. These 70 particles underwent both morphological and elemental characterization, indicating uranium and other elements.

15. SUBJECT TERMS
BOMARC, Nuclear Forensics, Actinide Remediation, SEM/EDS Particle Analysis

16. SECURITY CLASSIFICATION OF:			17. LIMITATION OF ABSTRACT	18. NUMBER OF PAGES	19a. NAME OF RESPONSIBLE PERSON
a. REPORT	b. ABSTRACT	c. THIS PAGE			Dr. Gaiven Varshney, AFIT/ENP
U	U	U	UU	234	19b. TELEPHONE NUMBER *(Include area code)* (937) 255-3636 x4574 gaiven.varshney@afit.edu

Standard Form 298 (Rev. 8-98)
Prescribed by ANSI Std. Z39-18